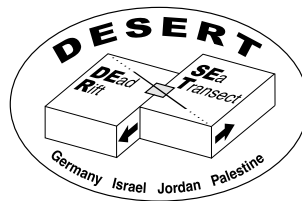Nils Maercklin

Seismic structure of the Arava Fault, Dead Sea Transform

Dissertation
zur Erlangung des akademischen Grades
Doktor der Naturwissenschaften (Dr. rer. nat.)
in der Wissenschaftsdisziplin Geophysik

eingereicht an der
Mathematisch-Naturwissenschaftlichen Fakultät
der Universität Potsdam

Potsdam im Januar 2004

Gutachter:
Prof. Dr. Michael Weber (GeoForschungsZentrum Potsdam & Universität Potsdam)
Prof. Dr. Frank Scherbaum (Universität Potsdam)
Prof. Dr. Wolfgang Rabbel (Christian-Albrechts-Universität Kiel)

Tag der Disputation: 2.07.2004

Abstract

The Dead Sea Transform (DST) is a prominent shear zone in the Middle East. It separates the Arabian plate from the Sinai microplate and stretches from the Red Sea rift in the south via the Dead Sea to the Taurus-Zagros collision zone in the north. Formed in the Miocene ∼17 Ma ago and related to the breakup of the Afro-Arabian continent, the DST accommodates the left-lateral movement between the two plates. The study area is located in the Arava Valley between the Dead Sea and the Red Sea, centered across the Arava Fault (AF), which constitutes the major branch of the transform in this region.

A set of seismic experiments comprising controlled sources, linear profiles across the fault, and specifically designed receiver arrays reveals the subsurface structure in the vicinity of the AF and of the fault zone itself down to about 3–4 km depth. A tomographically determined seismic P velocity model shows a pronounced velocity contrast near the fault with lower velocities on the western side than east of it. Additionally, S waves from local earthquakes provide an average P-to-S velocity ratio in the study area, and there are indications for a variations across the fault. High-resolution tomographic velocity sections and seismic reflection profiles confirm the surface trace of the AF, and observed features correlate well with fault-related geological observations.

Coincident electrical resistivity sections from magnetotelluric measurements across the AF show a conductive layer west of the fault, resistive regions east of it, and a marked contrast near the trace of the AF, which seems to act as an impermeable barrier for fluid flow. The correlation of seismic velocities and electrical resistivities lead to a characterisation of subsurface lithologies from their physical properties. Whereas the western side of the fault is characterised by a layered structure, the eastern side is rather uniform. The vertical boundary between the western and the eastern units seems to be offset to the east of the AF surface trace.

A modelling of fault-zone reflected waves indicates that the boundary between low and high velocities is possibly rather sharp but exhibits a rough surface on the length scale a few hundreds of metres. This gives rise to scattering of seismic waves at this boundary. The imaging (migration) method used is based on array beamforming and coherency analysis of P-to-P scattered seismic phases. Careful assessment of the resolution ensures reliable imaging results.

The western low velocities correspond to the young sedimentary fill in the Arava Valley, and the high velocities in the east reflect mainly Precambrian igneous rocks. A 7 km long subvertical scattering zone (*reflector*) is offset about 1 km east of the AF surface trace and can be imaged from 1 km to about 4 km depth. The reflector marks the boundary between two lithological blocks juxtaposed most probably by displacement along the DST. This interpretation as a lithological boundary is supported by the combined seismic and magnetotelluric analysis. The boundary may be a strand of the AF, which is offset from the current, recently active surface trace. The total slip of the DST may be distributed spatially and in time over these two strands and possibly other faults in the area.

Zusammenfassung

Ein transversales Störungssystem im Nahen Osten, die *Dead Sea Transform* (DST), trennt die Arabische Platte von der Sinai-Mikroplatte und erstreckt sich von Süden nach Norden vom Extensionsgebiet im Roten Meer über das Tote Meer bis zur Taurus-Zagros Kollisionszone. Die sinistrale DST bildete sich im Miozän vor $\sim$17 Ma und steht mit dem Aufbrechen des Afro-Arabischen Kontinents in Verbindung. Das Untersuchungsgebiet liegt im Arava Tal zwischen Totem und Rotem Meer, mittig über der Arava Störung (*Arava Fault*, AF), die hier den Hauptast der DST bildet.

Eine Reihe seismischer Experimente, aufgebaut aus künstlichen Quellen, linearen Profilen über die Störung und entsprechend entworfenen Empfänger-Arrays, zeigt die Untergrundstruktur in der Umgebung der AF und der Verwerfungszone selbst bis in eine Tiefe von 3–4 km. Ein tomographisch bestimmtes Modell der seismischen Geschwindigkeiten von *P*-Wellen zeigt einen starken Kontrast nahe der AF mit niedrigeren Geschwindigkeiten auf der westlichen Seite als im Osten. Scherwellen lokaler Erdbeben liefern ein mittleres *P*-zu-*S* Geschwindigkeitsverhältnis und es gibt Anzeichen für Änderungen über die Störung hinweg. Hoch aufgelöste tomographische Geschwindigkeitsmodelle bestätigen der Verlauf der AF und stimmen gut mit der Oberflächengeologie überein.

Modelle des elektrischen Widerstands aus magnetotellurischen Messungen im selben Gebiet zeigen eine leitfähige Schicht westlich der AF, schlecht leitendes Material östlich davon und einen starken Kontrast nahe der AF, die den Fluss von Fluiden von einer Seite zur anderen zu verhindern scheint. Die Korrelation seismischer Geschwindigkeiten und elektrischer Widerstände erlaubt eine Charakterisierung verschiedener Lithologien im Untergrund aus deren physikalischen Eigenschaften. Die westliche Seite lässt sich durch eine geschichtete Struktur beschreiben, wogegen die östliche Seite eher einheitlich erscheint. Die senkrechte Grenze zwischen den westlichen Einheiten und der östlichen scheint gegenüber der Oberflächenausprägung der AF nach Osten verschoben zu sein.

Eine Modellierung von seismischen Reflexionen an einer Störung deutet an, dass die Grenze zwischen niedrigen und hohen Geschwindigkeiten eher scharf ist, sich aber durch eine raue Oberfläche auf der Längenskala einiger hundert Meter auszeichnen kann, was die Streuung seismischer Wellen begünstigte. Das verwendete Abbildungsverfahren (Migrationsverfahren) für seismische Streukörper basiert auf *Array Beamforming* und der Kohärenzanalyse *P*-zu-*P* gestreuter seismischer Phasen. Eine sorgfältige Bestimmung der Auflösung sichert zuverlässige Abbildungsergebnisse.

Die niedrigen Geschwindigkeiten im Westen entsprechen der jungen sedimentären Füllung im Arava Tal, und die hohen Geschwindigkeiten stehen mit den dortigen präkambrischen Magmatiten in Verbindung. Eine 7 km lange Zone seismischer Streuung (*Reflektor*) ist gegenüber der an der Oberfläche sichtbaren AF um 1 km nach Osten verschoben und lässt sich im Tiefenbereich von 1 km bis 4 km abbilden. Dieser Reflektor markiert die Grenze zwischen zwei lithologischen Blöcken, die vermutlich wegen des horizontalen Versatzes entlang der DST nebeneinander zu liegen kamen. Diese Interpretation als lithologische Grenze wird durch die gemeinsame Auswertung der seismischen und magnetotellurischen Modelle gestützt. Die Grenze ist möglicherweise ein Ast der AF, der versetzt gegenüber des heutigen, aktiven Asts verläuft. Der Gesamtversatz der DST könnte räumlich und zeitlich auf diese beiden Äste und möglicherweise auch auf andere Störungen in dem Gebiet verteilt sein.

Contents

1. Introduction

Transform faults constitute conservative plate boundaries, where the relative movement of adjacent plates is primarily horizontal and tangential to the fault. Such a movement is referred to as strike-slip motion. Transform faults or large scale strike-slip faults cut the continental crust in several regions of the world. Besides the Dead Sea Transform (DST) in the Middle East, examples of transform faults which displace continental lithosphere are the San Andreas Fault in California, the Alpine Fault in New Zealand, the West Fault Zone in Chile, and the North Anatolian Fault System in Turkey.

In contrast to the relatively simple structure of oceanic fracture zones, continental transform faults are considerably more complex. This reflects the differences in strength and thickness between oceanic and continental lithosphere. Furthermore, this reflects the inhomogeneous nature of the continental crust, which may contain ancient lines of weakness along which ruptures occur preferentially (e.g. Kearey and Vine, 1995). The strike of faults therefore may depart from a simple linear trend, and the curvature of strike-slip faults gives rise to zones of compression and extension. This results in structures like pressure ridges and pull-apart basins like the prominent Dead Sea basin at the DST (e.g. Garfunkel, 1981).

Upper-crustal fault zones are structurally complex and lithologically heterogeneous zones of brittle deformation (e.g. Chester *et al.*, 1993; Schulz and Evans, 2000; Ben-Zion and Sammis, 2003). Due to the transform motion at strike-slip faults, different lithological units with different physical properties may be juxtaposed at the actual fault trace. Moreover, faults control the subsurface fluid flow, e.g. brines or meteoric waters, either by localising the flow in the fault zone or by impeding a cross-fault flow (Caine *et al.*, 1996). Three architectural elements are discriminated commonly for brittle fault zones in low-porosity rocks (e.g. Caine *et al.*, 1996; Ben-Zion and Sammis, 2003). These elements are the host rock, the damage zone, and the fault core. The host rock or protolith is the unfaulted rock bounding the fault-related structures. The damage zone consists of minor faults and fractures, fracture networks, or other subsidiary structures, which are all related to the main faulting process. Most of the fault displacement is localised at the fault core. It is rarely developed as a discrete slip surface but often found to be composed of various cataclastic rocks. The transition from the damage zone to the host rock is gradual. Therefore, its width is often defined as the region, where the fracture density is above a certain threshold value (Janssen *et al.*, 2002). The widths of damage zones observed at large fault zones range from metres to several hundreds of metres, whereas the fault core typically extends just over several centimetres. However, large, long-lived fault zones have a complex displacement history and accumulate many different slip events, resulting in a complex network of faults of many sizes (Wallace and Morris, 1986).

Results of field studies and experimental fracture work suggest that fault growth processes obey the same laws over a broad range of scales (Bonnet *et al.*, 2001, and references therein). Such scaling laws include the cumulative fault displacement to fault length ratio, the relation of fault width and fault length, and the fault size to the distribution of earthquake occurrence frequency (Scholz *et al.*, 2000; Stirling *et al.*, 1996). The scaling laws are important for seismic hazard assessment, because the earthquake energy release is related to the dimensions of the rupture plane and the slip magnitude (Stacey, 1992; Scholz and Gupta, 2000).

In general, structural geology studies are restricted to surface expressions of faults, and the subsurface continuation of a certain fault is often poorly constrained from such studies. Geophysical investigations can reveal the deeper structure of fault zones. For example, earthquake hypocentres may cluster along a fault plane, and fault-plane solutions provide information on the slip direction of an earthquake at a fault. Geophysical imaging methods employ the different physical properties of rocks or lithological units (e.g. Telford *et al.*, 1990). Variations of subsurface densities or magnetisations can be measured at the surface and used to constrain the (modelled) subsurface structure. Although covering a broad range of values, different rock types are characterised by different velocities of seismic compressional and shear waves (P and S waves), and especially the presence of subsurface fluids affects the electrical resistivity (Schön, 1996, and references therein). Furthermore, seismic waves can be reflected or scattered at layer boundaries or subvertical discontinuities such as faults (e.g. Yilmaz, 2001), and seismic waves may be guided in a subvertical low-velocity zone related to the damage zone of a fault (e.g. Ben-Zion, 1998).

In this thesis I apply seismic methods to image the subsurface structure around the Arava Fault (AF), which constitutes a major segment of the Dead Sea Transform (DST) system. The DST is a prominent shear zone in the Middle East. It links the compressional regime at the Alpine-Himalayan mountain belt, stretching from the Mediterranean to Indonesia, and the extension at the Afro-Arabian rift system, which is the largest continental rift system on Earth. The DST separates the Arabian plate from the Sinai microplate and stretches from the Red Sea Rift in the south to the Taurus-Zagros collision zone in the north (see figure 2.1, page 7). The transform is related to the breakup of the Afro-Arabian continent and accommodates the left-lateral (sinistral) movement between the two plates (Freund *et al.*, 1970; Garfunkel, 1981). The total amount of displacement is ∼105 km, and present relative motion between the African and Arabian plate is between 3–4 mm a^{-1} (e.g. Klinger *et al.*, 2000b).

The relative simplicity of the DST, especially in the Arava Valley between the Dead Sea and the Red Sea, puts this transform in marked contrast to other large transform systems like the North Anatolian Fault system in the middle of an orogenic belt and the San Andreas Fault system, which is influenced by repeated accretional episodes and the interaction with a triple junction (DESERT Group, 2000). Therefore, the DST provides a natural laboratory to study transform faults, a key structural element of plate tectonics besides subduction and rifting. Furthermore, paleoseismological studies (e.g. Amiran *et al.*, 1994), and instrumental earthquake studies in the past decades demonstrate that several damaging earthquakes occured along the DST. Thus, it poses a considerable seismic hazard to the neighbouring countries.

Seismics, Seismology	Electromagnetics	Potential fields	Petrology, Geothermics
Wide-angle refl./refraction	Magnetotellurics	Magnetic data	Petrology
Near-vertical reflection	Time-domain EM	Gravimetry	Geothermics
Controlled source array			
Passive array			
Thermomechanical modelling and integrative interpretation			

Table 1.1: Subprojects in the frame of the international and multidisciplinary DESERT research project. Members of the DESERT Group and their institutional affiliations are listed in section A.4.

To study structure and dynamics of the DST, the DESERT (Dead Sea Rift Transect) project started with field work in the beginning of the year 2000 (DESERT Group, 2000). The DESERT project is an international and multidisciplinary research effort with participants from Germany, Israel, Jordan, and the Palestine Territories (see also section A.4). The various experiments conducted in the frame of DESERT focus on the segment of the DST in the Arava Valley between the Dead Sea and the Red Sea. At this location the strike-slip displacement seems to be concentrated on a distinct and continuous master fault and to be undisturbed by extensional structures at the Dead Sea and the Red Sea. Thus, general questions on the structure and evolution of large shear zones can be addressed by geophysical investigations in this region.

The DESERT project comprises several different geophysical and geological investigations on a broad range of scales from regional studies, including the entire crust and upper mantle, via detailed studies of the shallow crust to small-scale studies at the AF itself. The applied methods include controlled-source and passive seismology, electromagnetics and geoelectrics, potential field analysis and modelling, petrological and geothermal investigations, surface geological field work, and remote sensing (satellite imagery). The independent results of these different subprojects are included in an integrative interpretation and constitute constraints for thermo-mechanical modelling of the dynamics of the DST (Sobolev *et al.*, 2003). Table 1.1 summarises the subprojects of DESERT.

The passive seismic array and a wide-angle seismic reflection and refraction survey aim to image seismic velocities, seismic anisotropy, and discontinuities of the entire crust and upper mantle along and around an up to 270 km long profile across the DST (DESERT Group, 2002, 2004; Rümpker *et al.*, 2003). A regional density model of this area has been developed by Götze *et al.* (2002). The near-vertical seismic reflection survey revealed crustal structures along the central 100 km along the profile (DESERT Group, 2004), and an electrical resistivity image on a regional scale comes from magnetotelluric measurements concentrated east of the transform (Weckmann *et al.*, 2003). These regional scale studies are supplemented by smaller scale experiments in the vicinity of the Arava Fault (AF), the main fault trace of the DST in this region. The target volume of these experiments comprises the upper 3–5 km of the crust in an area of about 10×10 km, centered on the AF to detect possible along-strike variations. Field work has been completed for the seismic Controlled Source Array (CSA)

project, a magnetotelluric survey along several profiles (Ritter *et al.*, 2001; Schmidt, 2002), and a local gravity survey (Götze *et al.*, 2002).

The subject of this thesis is the analysis, modelling, and interpretation of seismic data acquired during the Controlled Source Array (CSA) subproject of DESERT, and the relation of seismic results to other geophysical and geological observations. Essentially, the CSA comprises a set of several small scale seismic experiments located in the same area. The study area is the vicinity of the AF, the principal target of these experiments. The CSA aims to image the three-dimensional structure of the upper crust around the AF, to determine its shape and location, and to determine properties of the fault zone itself. Furthermore, the CSA provides a dataset for the development of methods to image steeply dipping structures like faults. The imaged subsurface lithological structure and the architecture of the fault zone itself provides constraints on the tectonic evolution of the AF. Additional aspects are the relation of deeper structures to the present surface trace of the AF and its relation to other fault strands observed in the study area. The small scale CSA and magnetotelluric projects reveal along-strike variations of the AF and link the deeper crustal structure imaged geophysically (e.g. DESERT Group, 2004) with geological and neotectonic studies at the DST (e.g. Galli, 1999; Klinger *et al.*, 2000b).

Structure of the thesis

The following chapters are structured according to applied methods and the subsets of data analysed or discussed. The seismic and magnetotelluric methods are introduced at the beginning of individual chapters, where appropriate. In general, obtained results from the different methods are also briefly dicussed in the respective chapters.

Chapter 2 gives an overview of the tectonic setting and the evolution of the DST in the Middle East. A more detailed description concentrates on structural studies at faults in the Arava Valley, and on igneous rocks and the sedimentary sequence in the main study area.

Various seismic experiments conducted as part of the DESERT project are introduced in chapter 3. The main part of this chapter deals with the Controlled Source Array (CSA) experiments. This includes experiment design, data acquisition, initial data processing, and aspects of data quality.

The next three chapters cover processing, modelling, and inversion of various seismic phases observed in CSA data. Chapter 4 contains the inversion of first arrival traveltimes for the subsurface P velocity structure on different scales. After an explanation of the tomographic inversion method and its resolution, the determined velocity structure is presented, discussed, and partly related to regional gravity observations in the area.

Secondary seismic phases from local earthquakes and controlled-source data constrain the P-to-S velocity ratio (v_p/v_s ratio) in the study area, the cross-fault structure, and the trace of the AF. The analysis and modelling of these phases is described in chapter 5, and the phases

considered are S waves, waves reflected at the fault zone, and reflections from subhorizontal layer boundaries. A study on waves guided in a fault-related low-velocity layer is published separately by Haberland *et al.* (2003b).

After some general considerations on single scattering of seismic waves, chapter 6 explains a developed migration technique to image the three-dimensional spatial distribution of scatterers in the subsurface and includes a comprehensive discussion of the resolution of this method. The imaged distribution of scatterers in the study area is related to the boundary between two different lithological units, and its location bares implications for the present surface trace of the AF.

Chapter 7 merges seismic and magnetotelluric results in the study area. After an overview of the magnetotelluric method and the magnetotelluric experiment in the Arava Valley, this chapter describes the correlation of seismic velocities and electrical resistivities to characterise different lithologies.

Finally, chapter 8 integrates all obtained results. I summarise the results presented in previous chapters, discuss their releation to other geophysical or geological observations in the study area, relate the observations to the situation at other large transform faults, and conclude with geologic and tectonic implications.

The appendix collects technical details like relevant computer codes and coordinates of presented cross-sections or depth slices.

2. Tectonics and geology

The Dead Sea Transform (DST) is a prominent shear zone in the Middle East. It separates the Arabian plate from the Sinai microplate, an appendage of the African plate, and stretches from the Red Sea rift in the south via the Dead Sea to the Taurus-Zagros collision zone in the north (figure 2.1). Formed in the Miocene ~17 Ma ago and related to the breakup of the Afro-Arabian continent, the DST accommodates the sinistral movement between the two plates (Freund *et al.*, 1970; Garfunkel, 1981). Section 2.1 describes the evolution and the current tectonic and geological setting of the DST, the seismicity in the area, the slip rate along the transform, and some hydrological aspects. A more detailed view on the local tectonics and surface geology of the study area follows in section 2.2.

2.1 Regional setting

The continental crust crossed by the DST was consolidated after the Late Proterozoic Pan-African orogeny. During most of the Phanerozoic, the region remained a stable platform. A cover of mostly marine sediments accumulated during several depositional cycles until Late Eocene times, and igneous activity was sparse in this period (Bender, 1968; Garfunkel, 1981, 1997; Garfunkel and Ben-Avraham, 1996). Some rifting events occurred probably in the Permian, and also in Triassic and Early Jurassic times. These events were related to the eastern Mediterranean branch of the Neo-Thetys and shaped its passive continental margin. In the Late Cretaceous the closure of the neighbouring part of the Neo-Thetys was accompanied by mild compressional deformation. The resulting structures are known as the Syrian arc fold belt, which stretches from western Sinai in the southwest to the Palmyrides in the northeast (figure 2.1). The Syrian arc includes a bundle of NNE–SSW to ENE–WSW trending folds and a group of roughly E–W trending lineaments of aligned folds and faults along which some right-lateral shearing took place. The latter is referred to as central Negev-Sinai shear belt (Bartov, 1974) and extends across Sinai and the central Negev to about 200 km east of the Dead Sea.

The continental breakup phase began in the Oligocene at 30–25 Ma with widespread, pre-dominantly basaltic volcanism (Garfunkel, 1981, and references therein). Major rifting and faulting followed in the Miocene around ~17 Ma and led to the detachment of Arabia from Africa. Their separation created the Red Sea, which opens as a propagating rift (see e.g. Kearey and Vine, 1995) with incipient seafloor spreading in its southern and some deep
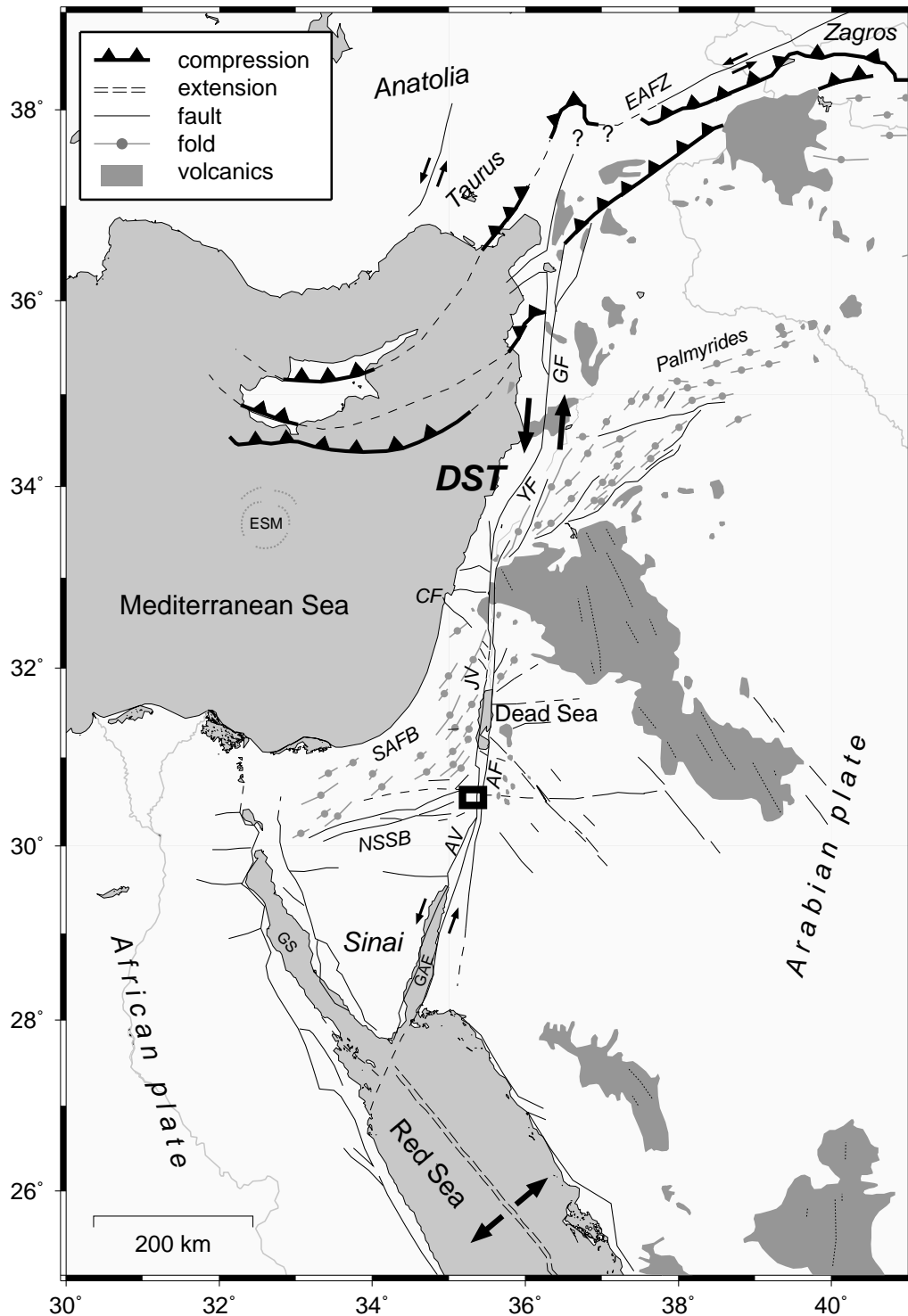
Figure 2.1: *Tectonic setting of the Dead Sea Transform (DST) in the Middle East, compiled after Garfunkel (1981, 1997); Salamon et al. (1996). Arrows indicate directions of relative motion at faults, and a black box marks the study area. Abbreviations: AV – Arava Valley, AF – Arava Fault, CF – Carmel Fault, EAFZ – East Anatolian fracture zone, ESM – Eratosthenes Seamount, GAE – Gulf of Aqaba/Elat, GF – Ghab Fault, GS – Gulf of Suez, JV – Jordan Valley, NSSB – Negev-Sinai shear belt, SAFB – Syrian arc fold belt (including Palmyrides), YF – Yammouneh Fault.*

extensional basins in its northern part. With respect to Sinai, the Arabian plate rotates counterclockwise around a pole at about 33° N, 24° E (Girdler, 1990), but also other locations seem to be feasible (see e.g. Klinger *et al.*, 2000b). The kinematics of the Arabian-African plate separation at the Red Sea requires a left-lateral motion of about 100 km parallel to the DST, but a part of the motion was accommodated by the opening of the Gulf of Suez (McKenzie *et al.*, 1970; Joffe and Garfunkel, 1987; LePichon and Gaulier, 1988). Faulting and ongoing seismicity indicate continuing activity of both lines (van Eck and Hofstetter, 1990; Garfunkel and Ben-Avraham, 1996).

The total amount of 105 km left-lateral motion along the DST is obtained by matching the sedimentary cover and some basement units (Quennell, 1958, 1959; Freund *et al.*, 1970). Matching the lineaments of the central Negev-Sinai shear belt (figure 2.1) yielded the most accurate value (Quennell, 1959; Bartov, 1974). Further evidence comes from magnetic anomaly patterns across the transform (Hatcher *et al.*, 1981), and regional plate kinematics provides an independent estimate of motion as mentioned above. However, across the northern segment of the DST ophiolite nappes, thrust onto the edge of the Arabian platform in the Late Cretaceous, are offset just 80 km. Garfunkel (1981) explains this difference with the non-rigidity of the lands bordering that segment of the transform.

Whereas the total slip along the DST is known, the history of motion is not that well constrained. The youngest rocks affected by the entire offset are 20–25 Ma old (Miocene) dikes, which are found at the Gulf of Aqaba/Elat (Eyal *et al.*, 1981). Thus, the transform motion must have begun later. According to Garfunkel and Ben-Avraham (1996) igneous activity and local subsidence along the transform suggest some 18 Ma. The history of the Red Sea opening provides another constraint because of the corresponding transform motion along the DST. The Red Sea was already an evaporite-filled basin by the end of the Miocene (5 Ma), subsequent opening was considerably less than half of the total amount (e.g Izzeldin, 1987), and most of the opening of the Gulf of Suez was achieved already before the Late Miocene (e.g. Garfunkel, 1997). Moreover, magnetic anomalies record an opening of the Red Sea of 75 km in the last 5 Ma, which is only a fraction of the total amount (Garfunkel and Ben-Avraham, 1996), and the opening seems to have accelerated in the Middle or Late Miocene (Izzeldin, 1987; LePichon and Gaulier, 1988). These observations lead to a slip along the DST of about 40 km or less in the last 5 Ma (Plio-Pleistocene), and thus, most of the offset must have occurred earlier (Joffe and Garfunkel, 1987). From Miocene to recent times, another phase of igneous activity produced mainly volcanic fields consisting of basalts (figure 2.1), but on a regional scale, there is no obvious relation between their extent and the DST (Garfunkel, 1997).

Today, the DST system consists of at least six major overlapping, left-stepping strike-slip faults with deep rhomb-shaped depressions between each fault pair (Garfunkel, 1981, 1997; Girdler, 1990). These depressions extend from three deeps in the Gulf of Aqaba/Elat in the south to the Lake Tiberias in the north. The largest one is the Dead Sea basin with a current water-level more than 400 m below the mean sea level. All these depressions are interpreted as pull-apart basins due to transtension at transform offsets and related to the left-

lateral movement along the DST. The basins are partly filled with sediments, which reach a maximum thickness of about 10 km under the Lisan diapir in the Dead Sea basin (ten Brink *et al.*, 1990; Garfunkel, 1997; Hassouneh, 2003). The basins as well as the narrow Arava and Jordan Valleys (figure 2.1) are typically bounded by normal faults, which reminds of a typical extensional rift structure (e.g. see Kearey and Vine, 1995). However, the presence of major strike-slip faults and regional plate kinematics clearly demonstrate the transform character of the DST. Between the Gulf of Aqaba/Elat and the Dead Sea the Arava Fault (AF) constitutes the major branch of the DST and takes up most of the slip (Garfunkel, 1981; Atallah, 1992). There, the transform strikes between about N12°E and N20°E. North of the Dead Sea, the DST continues with the Jordan Valley Fault. The simple structure of the DST changes between latitude 33° N and 35° N (figure 2.1), where the transform bends to the right, leading to transpressional structures. Within this restraining bend, the transform system comprises several distinct fault branches, which trend roughly parallel to the strike of the Palmyrides fold range (Garfunkel, 1981; Girdler, 1990; Gomez *et al.*, 2003). There, the lateral slip of the DST appears to be distributed over these branches (Walley, 1988; Gomez *et al.*, 2003), and scattered seismicity suggests that this region is still tectonically active (Chaimov *et al.*, 1990; Salamon *et al.*, 1996). Because the faults observed there do not seem to accomodate the total lateral slip, the Palmyrides represent some internal deformation of the Arabian plate. The northernmost DST segment (Ghab Fault) trends approximately N5°E and extends to the Tauros-Zagros collision zone between Arabia and Anatolia. Central Anatolia, bounded by the East Anatolian fracture zone in the southeast, moves coherently with minor internal deformation to the west (McClusky *et al.*, 2000).

Several geophysical studies revealed the deeper structure of the eastern Mediterranean, the DST system, and Arabia (Arabo-Nubian shield). Whereas the crust of the eastern Mediterranean is assumed to be partly underlain by typical oceanic crust with thicknesses smaller than 10 km (Ginzburg *et al.*, 1979; Makris *et al.*, 1983; Rybakov *et al.*, 1997; Ben-Avraham *et al.*, 2002), the continental crust of Arabia reaches thicknesses between 35 km and 40 km (El-Isa *et al.*, 1987; Al-Zoubi and Ben-Avraham, 2002). From the Mediterranean coast in the northwest across the DST to the southeast, the depth of the crust-mantle boundary (Moho) increases linearily from about 25 km to 38 km with only minor undulations beneath the surface expression of the DST (DESERT Group, 2004). Evidence for a lithospheric-scale transform displacement at the DST comes from seismic anisotropy (Rümpker *et al.*, 2003) and thermo-mechanical modelling (Sobolev *et al.*, 2003). Within the relatively cold and strong lithosphere at the DST, the shear strain is localised in a narrow (20–40 km) vertical decoupling zone, which extends through the crust and upper mantle. Additionally, Sobolev *et al.* (2003) explained the observed uplift of the eastern flank of the DST with less than 4 km of transform-perpendicular extension, as suggested previously by Garfunkel (1981). The regional scale topography structure across the DST is discussed for example by Wdowinski and Zilberman (1997).

Most of the major and moderate earthquakes in the region occur at the geologically documented plate boundaries (Salamon *et al.*, 1996). Their frequency-magnitude relationship is commonly described by $\log N = a - b M_L$ with the local magnitude M_L and the correspond-

ing number of earthquakes N (Gutenberg and Richter, 1954). For the DST, b-values are typically found in the range from 0.80 to 1.07 (van Eck and Hofstetter, 1989; Marco *et al.*, 1996; Salamon *et al.*, 1996). Shapira and Feldmann (1987) determined a-values between 3.2 and 3.5 for earthquakes of $2 \leq M_L \leq 4$, and they state that a b-value of 0.8 is most likely the same along the DST. From a 50 ka paleoseismic record, Marco *et al.* (1996) estimated a recurrence interval of 1.6 ka for earthquakes with $M_L \geq 5.5$ in the Dead Sea basin and found temporal clustering at periods of 10 ka. An analysis of seismicity in the 20*th* century (Salamon *et al.*, 1996) and geomorphological studies (Klinger *et al.*, 2000a) lead to potential recurrence intervals of 385 a and about 200 a, respectively, for earthquakes with a moment magnitude $M_W = 7$ along the DST.[1] Four strong historic earthquakes hit the segment of the DST south of the Dead Sea in the years 1068, 1212, 1293, and 1458 A. D. (Ambraseys *et al.*, 1994; Klinger *et al.*, 2000a). These earthquakes are corroborated in sedimentary records (Ken-Tor *et al.*, 2001). During the 20*th* century most of the seismic moment at the DST was released by a few large earthquakes (Salamon *et al.*, 2003), which record the predominant strike-slip motion of the transform: September 1918 in the northern segment, July 1927 in the northern Dead Sea basin (both with $M_L = 6.2$), and November 1995 in the Gulf of Aqaba/Elat ($M_W = 7.2$). Nevertheless, the current seismicity of the southern DST section is rather small (Salamon *et al.*, 1996), although recent activity there is indicated by offset gullies and alluvial fans (Klinger *et al.*, 2000a). The current microearthquake activity in the area south of the Yammouneh Fault (figure 2.1) is concentrated along three fault zones: the Carmel Fault, the central Negev-Sinai shear belt, and mainly along the DST (van Eck and Hofstetter, 1989). These earthquakes tend to cluster in or near tensional structures at fault offsets and pull-apart basins, e.g. at the Gulf of Aqaba/Elat and the Dead Sea basin, again illustrating the relative seismic quiescence of the study area in the central Arava Valley. During the one week recording period of this study, two microearthquakes occured there (section 5.2).

Recent estimates of the current slip rate along the southern segment of the DST range from 1 mm a^{-1} to more than 10 mm a^{-1} (Gardosh *et al.*, 1990; Ginat *et al.*, 1998; Klinger *et al.*, 2000b; Pe'eri *et al.*, 2002). These estimates are based on geomorphological observations, precise geodetic measurements, and plate kinematic considerations. From 15 km translocated Plio-Pleistocene drainage systems Ginat *et al.* (1998) inferred an average slip rate of 3–7.5 mm a^{-1}, which is consistent with the 4±2 mm a^{-1} determined by Klinger *et al.* (2000b) from offset Pleistocene alluvial fans in the Arava Valley. Continuous Global Positioning System (GPS) monitoring west of the DST and the assumption of a locked-fault model lead to a relative motion of 2.6±1.1 mm a^{-1} (Pe'eri *et al.*, 2002). This estimate is an independent confirmation of the geomorphologically determined values given above. Recently, a slightly higher slip rate was determined by McClusky *et al.* (2003) from GPS measurements on a larger scale. Their model predicts 5.8±1 mm a^{-1} left-lateral slip on the southern segment of the DST. But this value does not account for the movement of the Sinai subplate and may reflect active opening of the Gulf of Suez rift.

---

[1] Note the different magnitude definitions used: local magnitude M_L versus moment magnitude M_W.

The Precambrian basement in the vicinity of the DST represents the northwestern part of the Arabo-Nubian shield and consists of mainly juvenile Late Proterozoic rocks (Bender, 1968; Stoeser and Camp, 1985; Stern, 1994). The Arabo-Nubian Shield was formed by accretion of several microplates (terranes) comprising intra-oceanic arc sequences, granitoids, as well as oceanic and continental fragments. A Cambrian volcano-sedimentary succession usually overlies the Precambrian basement. Coarse-grained clastics are restricted to fault-bounded basins and fine-grained clastics are found in large areas around the southern segment of the DST (Weissbrod and Sneh, 2002). The DESERT Group (2004) constructed a 100 km long, NW-SE trending geological profile across the study area (figure 2.1) down to about 3 km depth. West of the DST, the 1.5–2 km thick Phanerozoic is dominated by Cretaceous and Tertiary rocks underlain mainly by Triassic sequences thinning out towards the DST. Towards the north, the thickness of the Phanerozoic increases to about 4 km on the western shoulder of the Arava Valley (e.g. Garfunkel and Ben-Avraham, 1996). East of the DST, Lower Cretaceous rocks unconformably overlie Ordovician and Cambrian sandstones, and on the eastern shoulder of the Arava Valley Precambrian basement rocks crop out. In general, the Phanerozoic sequence is thicker on the western shoulders of the Arava and Jordan Valleys than on their eastern sides.

2.2   Local setting

The study area is located in the Arava Valley between the Dead Sea and the Red Sea (black box in figure 2.1), centered across the Arava Fault (AF), which is the major branch of the Dead Sea Transform (DST) in this area (section 2.1). The Arava Valley is a large depression of variable width, filled with Quaternary clastic sediments. The topography in the central part of the study area varies smoothly between 50 m below (northwest) and about 100 m above sea level (south and east). The heights of the valley shoulders reach a few hundreds of metres in the west and more than 1500 m above sea level in the east.

Geomorphologically, the eastern shoulder typically shows a rugged topography with steep slopes, comprising mainly Precambrian volcanics and Cambrian sandstones in the east, and Cretaceous sandstones in the northeast (figure 2.2). Large alluvial fans developed at the entrances to steep-sided wadis along the foot of the escarpment. The fans are littered with flashflood ravines and large boulders and can extend several kilometres from the wadi mouth. Major wadis, such as Wadi Finan, are oriented NW-SE, presumably reflecting tectonic control. The wadis are up to 600 m wide and accumulated up to 25 m alluvial deposits on their floors (Rabb'a, 1994). The Wadi Qunai follows the trace of the AF in the southern part of the study area . In general, the young sediments have a gentle depositional dip towards the valley centre (Bender, 1968). Isolated rock exposures in the vicinity of the AF show an elongated shape, again reflecting the tectonic regime in the area. Predominantly east of the AF, the valley floor is in parts covered by longitudinal, roughly parallel oriented sand dunes.
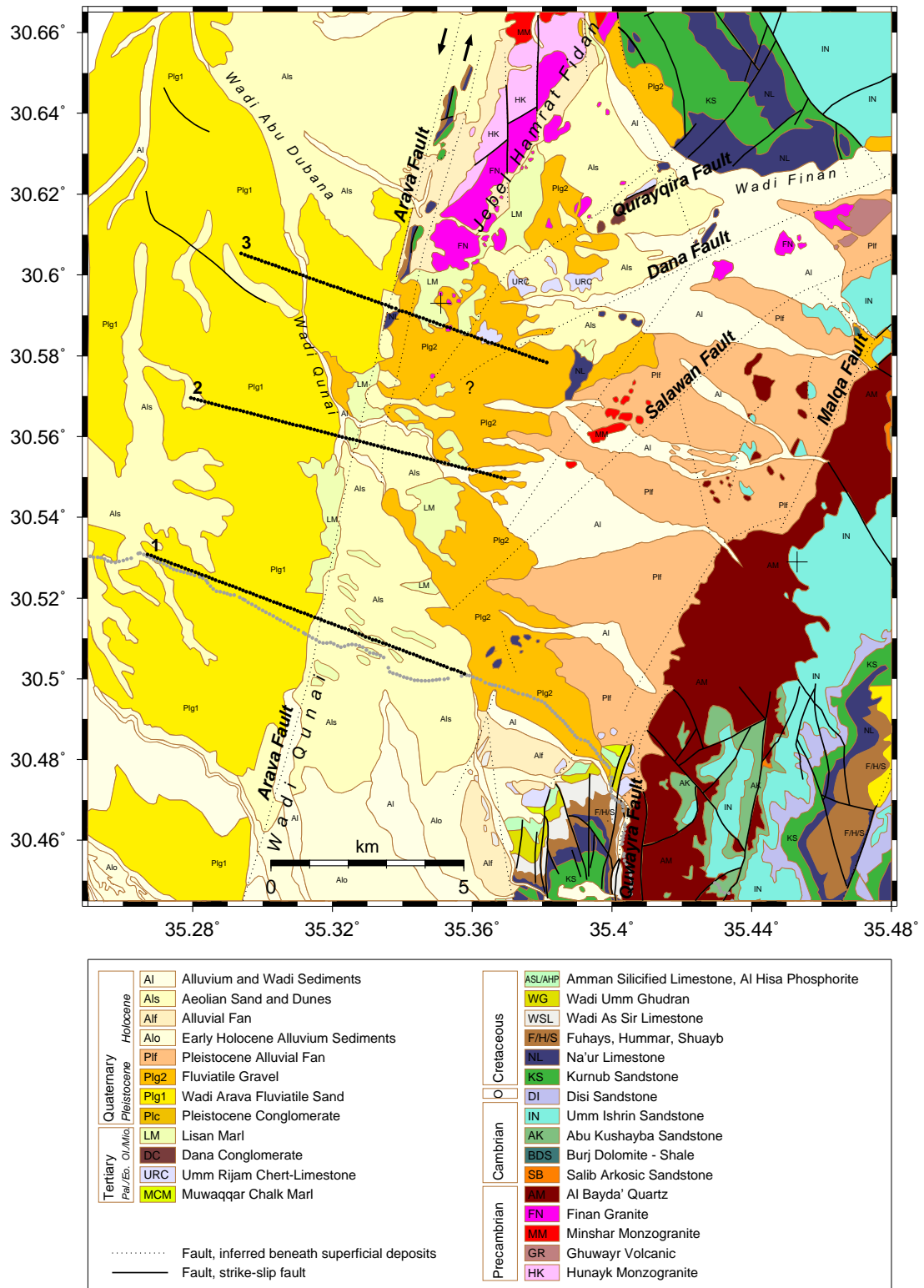
Figure 2.2: *Geological map of the study area after Rabb'a (1991, 1994) north of* $30.5°$ *N and Barjous (1995) in the southern part. The NVR and CSA geophone lines in grey and black are included for better orientation (see section 3.2), and crosses near 30.59° N, 35.35° E and 30.53° N, 35.45° E indicate the ends of a geological cross-section (figure 2.3). Abbreviations of geologic series: Eo – Eocene, Mio – Miocene, Ol – Oligocene, O – Ordovician, Pal – Paleocene.*

2.2.1   Faults and fault-related structures

En-echelon tectonic basins of varying depth, filled with clastic sediments, characterise the region west of the AF (Bartov *et al.*, 1998). One of these basins is the Zofar basin, which makes up the western part of the study area. The basin is bounded to the north by the NW-SE striking Shezaf listric fault. The western and eastern boundaries are defined by the roughly parallel trending Zofar Fault and AF, respectively. Contrary to the left-lateral strike-slip character of the AF, the movement at the Zofar Fault is predominantly normal with the downthrown block to the east (Bartov *et al.*, 1998). The estimation of more than 400 m of displacement is based on stratigraphic markers within the Hazeva Group (see section 2.2.2), water wells drilled on both sides of the fault, and electromagnetic investigations (references in Bartov *et al.*, 1998).

The geological map of the study area (figure 2.2) includes the surface traces of the AF and of other faults in its vicinity. Most of these faults are inferred beneath superficial alluvial and ae-olian sediments. However, the AF is clearly visible on satellite images and aerial photographs as a straight line cutting alluvial fans and downthrown on its western side (Rabb'a, 1994). In the mapped area the AF strikes at N12°–N16° E. Its trace is outlined in the field by sudden changes in drainage courses, offset gullies and alluvial fans, jogs, pressure ridges, small rhomb grabens, water holes, and scarps (Barjous and Mikbel, 1990; Galli, 1999; Klinger *et al.*, 2000a,b). A few kilometres south of the study area, the AF is marked by a 3–10 m high fault scarp, which mainly faces eastward and is strongly degraded at the intersection with the alluvial fan of Wadi Qunai in the southwestern part of the map (Galli, 1999). Near the southernmost geophone line 1 (figure 2.2) the fault trace is hardly recognisable. South of geophone line 2, the Wadi Qunai follows the AF trace, running in an up to 600 m wide depression between the fault scarp on the eastern and an uplifted block on its western side (Galli, 1999). A pressure ridge progressively emerges further north, such that slices of Cretaceous sandstones and limestones are uplifted and squeezed along the fault plane. The ridge coincides with a bend of the fault trace to the right (see also Garfunkel, 1981). The length of the ridge is about 9 km with a maximum width of 700 m, and it terminates in the northern part of the map (figure 2.2), west of the elongated mountain ridge Jebel Hamrat Fidān (Galli, 1999). The trace of the AF is partly covered by sand dunes, which are mainly confined to the region east of the fault. Because the pressure ridge locally divides two plains with a topographical step of ∼40 m, this structure acts as a wall supporting the accumulation of aeolian sands on one side of the fault. Several springs occur along the fault trace, especially between the geophone lines 2 and 3. The springs are fed from the eastern side with its water table just a few metres below the surface (Galli, 1999).

As stated in section 2.1, the strike-slip AF is the major fault branch at this segment of the DST, taking most of the left-lateral slip (Garfunkel, 1981; Atallah, 1992). Its morphological expression confirms the strike-slip behaviour and indicates Pleistocene to recent activity. But the AF also exhibits some minor normal movement (Barjous and Mikbel, 1990). The downthrown side alternates between the west and the east within Pleistocene to recent deposits. West of the Jebel Hamrat Fidān, the AF achieved a throw of about 700 m, where Upper Cre-
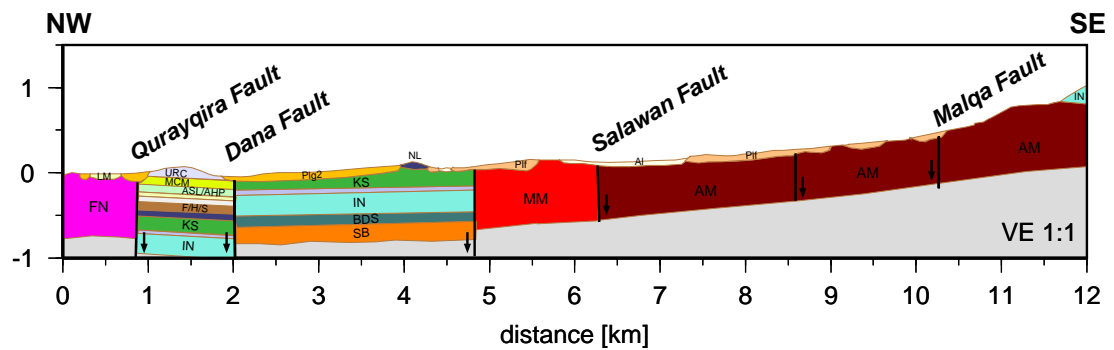
Figure 2.3: *Geological cross-section at the northeastern edge of the study area (Rabb'a, 1991). The ends of this section are indicated by crosses in figure 2.2, and colours and labels are as in that figure. Arrows indicate the downthrow sides of blocks at faults with a normal displacement.*

taceous rocks are adjacent to Pleistocene sediments. Besides that, other faults trending more or less parallel to the AF are observed in the northern part of the mapped area (figure 2.2). A series of small faults is present on the Jebel Hamrat Fidān and display left-lateral strike-slip movements (Rabb'a, 1994). These faults appear as crush zones, which horizontally offset the Precambrian Fidān granites (FN and HK in figure 2.2). Between the pressure ridge out-crops of Cretaceous rocks and the Jebel Hamrat Fidān, Rabb'a (1991) inferred another fault strand parallel to the AF, about 1 km east of it. Furthermore, reflection seismic investigations south of geophone line 3 revealed a subvertical fault about 2 km west of the AF (seismic line VWJ-9; Natural Resources Authority, Jordan).

Faults east of the Jebel Hamrat Fidān are included in a geological cross-section constructed by Rabb'a (1991) and reproduced in figure 2.3. This cross-section trends from the southern tip of the Jebel Hamrat Fidān to the outcropping Precambrian volcanites in the southeast (two crosses in figure 2.2). The Al Quwayra Fault zone in the southeastern corner of the study area is a set of faults trending N5°E. These faults pass about 4 km west of the ancient city of Petra and extend hundreds of kilometres further south (Barjous and Mikbel, 1990). Their northern continuation is referred to as Malqa Fault by Rabb'a (1991, 1994). The Malqa Fault is covered by Pleistocene and Holocene sediments, which are not displaced (Barjous and Mikbel, 1990) and thus indicating that this fault was not active recently. Below the sediments, the Malqa Fault appears to be downthrown to the west (Rabb'a, 1991). Never-theless, the dominant movement along the Al Quwayra Fault zone is strike-slip, as indicated by a vertical fault plane with minor undulations, horizontal slickensides, normal and reverse flower structures, alternating upthrow and downthrow sides, and small-scale drag folds in ad-jacent Upper Cretaceous and Tertiary sediments. Barjous and Mikbel (1990) derived 40 km of left-lateral movement along the Al Quwayra Fault.

The Salawan Fault, the Dana Fault, and the Qurayqira Fault strike roughly SW-NE and ex-tend into the central part of the study area (figure 2.2). The first two faults belong to the most distinctive faults in the region. Their traces are clearly visible on satellite images, and

they form the western end of a W-E striking fault zone, which extends some hundreds of kilometres further to the east (Rabb'a (1994); see also figure 2.1). The Salawan Fault and the Dana Fault define the boundaries of the Dana horst. In the study area, an unnamed fault strand between these two faults separates outcrops of Precambrian Minshar Monzogranite, adjacent to the Salawan Fault, from a downthrown sedimentary sequence of Cambrian and Cretaceous age (figure 2.3). The Salawan Fault seems to be a steeply dipping normal fault downthrown some 200 m to the south and southeast, producing steeply dipping strata in the Cambrian Umm Ishrin Sandstones (Rabb'a, 1994). East of the study area, the normal displacement reportedly reaches about 900 m at the Dana horst (Barjous and Mikbel, 1990; Rabb'a, 1994). There is evidence for an Early Cambrian structural weakness zone along the present W-E trending segment of the Salawan Fault and that this fault was rejuvenated in the Tertiary, which influenced the sedimentation in this period. Field observations indicate right-lateral movement along the Salawan Fault with a total slip of 7 km (Barjous and Mikbel, 1990).

North of the Dana Fault trace, the Qurayqira Fault separates the Precambrian granites of the Jebel Hamrat Fidān from a sequence of mainly Cretaceous and Tertiary deposits (figure 2.3). This sequence constitutes a sagged block between the Qurayqira Fault and the Dana Fault, which is downthrown by about 500 m relative to the sedimentary sequence southeast of it. From surface geological mapping (Rabb'a, 1991), the extent of the Qurayqira Fault towards the AF is constrained by a few small outcrops of Precambrian granites south of the Jebel Hamrat Fidān (figure 2.2), but the continuation of the Dana Fault remained undetermined in that survey.

2.2.2 Igneous and sedimentary rocks

In the study area, igneous rocks are exposed in the north on Jebel Hamrat Fidān, on the eastern escarpment of the Arava Valley, and at some isolated outcrops (figure 2.2). They comprise Late Proterozoic granites, acidic and basic volcanites, and dikes of variable composition (Jarrar *et al.*, 1983; Rabb'a, 1994). Most of the dikes are confined to the plutonites and do not cross the base of the Cambrian succession. The remaining igneous rocks belong to the Aqaba and Arava complexes, which form part of the Arabo-Nubian shield (section 2.1). The Hunayk Monzogranite or Granodiorite (HK in figure 2.2) is exposed on Jebel Hamrat Fidān, has an elongated outcrop pattern and exhibits a rugged and steep topography. This rock unit is medium- to coarse-grained with a porphyritic texture. Rabb'a (1994) suggests an intrusive age of 600–610 Ma. The Hunayk Monzogranite is in sharp contact with the younger, medium-grained Minshar Monzogranite (MM) and the fine-to medium-grained Finan Granite (FN; 540–550 Ma). Several small outcrops of Finan Granite south of Jebel Hamrat Fidān and northwest of the Qurayqira Fault indicate a possible southern continuation of this granite unit below the superficial deposits (see also figure 2.3). The Minshar Monzogranite occurs only on small isolated outcrops northwest of the Salawan Fault. This rock is cut by numerous dikes that made it weak and friable. Its paleosurface is preserved on

which Pleistocene conglomerates rest unconformably. Finally, the Al Bayda' Quartz (AM; Ahaymir volcanic suite) crops out on the eastern escarpment of the Arava Valley. This suite is dominated by massive porphyritic rhyolitic flows with minor intrusions of granitic composition (Rabb'a, 1994). Its age was interpreted to be about 510–570 Ma (Bender, 1968; Rabb'a, 1994). Northwest of the outcrops, the Al Bayda' Quartz extends below Quaternary deposits to the Salawan Fault (figure 2.3).

Sedimentary rocks of Cambrian–Ordovician age belong to the Ram Group (Rabb'a, 1994). Four formations can be distinguished in the study area: Salib Arkosic Sandstone (SB), Burj Dolomite-Shale (BDS), Umm Ishrin Sandstone, and Disi Sandstone (figure 2.2). The Ram Group mainly consists of fluvial, clastic sediments deposited in a braided river environment. They comprise medium- to coarse-grained (arkosic) sandstones, quartz arenite, thin beds of siltstones, and various types of pebbles. Cross-bedding is quite common. An exception is the Burj Dolomite-Shale formation, which was deposited in a shallow marine, subtidal environment. This formation consist of siltstone and fine-grained sandstone, limestone, and dolomite.

The Ram Group is unconformably overlain by the Cretaceous Kurnub Group of fine- to medium-grained sandstones (KS). They were deposited in a fluvial environment ranging from braided rivers (lower KS) to low-velocity meandering (upper KS). Another unconformity separates the Kurnub Group from the Ajlun Group of predominantely carbonate rocks comprising limestone, dolomite, gypsum, calcareous mudstone, and marl. Five formations are present in the study area: Na'ur Limestone (NL), Fuhays, Hummar, Shuayb (F/H/S, undifferentiated), and Wadi As Sir Limestone (WSL). The entire group was deposited in a shallow marine environment. Predominantely of marine origin are also the sediments of the subsequent Belqa Group. This group is of Cretaceous–Tertiary age, and its bottom is marked by an unconformity. The lowermost formation, Wadi Umm Ghudran (WG), exhibits indications for a rapid transgression from a shallow marine to a pelagic environment. Other formations of the Belqa Group in the study area are the Amman Silicified Limestone (ASL/AHP), Muwaqqar Chalk Marl (MCM), Umm-Rijam Chert-Limestone (URC), the Dana Conglomerate (DC), and the Lisan Marl (LM). The Dana Conglomerate was periodically deposited as alluvial fans into a subsiding lake basin, and the Lisan Marl indicates a saline pelagic lake environment with lacustrine facies at the margins of the developing valley along the DST (Rabb'a, 1994). In summary, the sediments of this group comprise chalk, marl, and phosphorite, but quartz sandstone, dolomite, and thin beds of chert are also present.

The Hazeva Group, also known as the Hazeva Formation, lies between the Avedat Group and the Dead Sea Group in the Negev, the Arava Valley, and eastern Sinai (Calvo and Bartov, 2001). Whereas the Eocene Avedat Group was deposited in a marine environment, the Plio-Pleistocene Dead Sea Group includes stratigraphic units restricted only to the valleys along the DST. The Hazeva Group is of Miocene age, and it consists of non-marine conglomerates, sandstones, siltstones, and marls deposited in alluvial, fluvial, and lacustrine environments. Parts of this group correlate with the Dana Conglomerate east of the DST (Bender, 1968; Bartov, 1974; Rabb'a, 1994; Calvo and Bartov, 2001). Five formations build this group,

which are in ascending order Ef'e, Gidron, Zefa, Rotem, and Karkom. The thickness of the entire Hazeva Group increases to the north, towards the Dead Sea basin, with a maximum thickness of 2500 m. In the study area (Zofar basin; see section 2.2.1), only the middle and upper parts of the Rotem formation are present and about 1100 m thick. During most of the depositional period of the Rotem formation, there was no activity along the faults in the Arava Valley, but at the end of that period and during the deposition of the Karkom formation, these faults and probably the central Negev-Sinai shear belt (figure 2.1) began to be active (Calvo and Bartov, 2001). Only the Karkom formation exhibits evidence for syntectonic deposition. The Plio-Pleistocene (2–4 Ma) Arava Formation of the Dead Sea Group is a fluvial-lacustrine unit deposited throughout the Arava Valley and the southern Negev (Avni *et al.*, 2001). Rabb'a (1991) mapped this unit as Wadi Arava Fluviatile Sand (Plg1 in figure 2.2).

Most of the study area is covered by Pleistocene to recent, unconsolidated deposits (figure 2.2). Pleistocene deposits are characterised by poorly-sorted clasts with a matrix of fine sand and siltstone. Holocene alluvial sediments consist of fine- to coarse-grained sand, pebbles and boulders of limestone and basement rocks reflecting the geology of the source region. Alluvial fans with a radiating drainage pattern developed at the eastern valley escarpment and extend for up to about 3 km from the mouths of major wadis. As mentioned above, the study area is in part covered by aeolian sands and dunes. The maximum thickness of these well-sorted, medium-grained sands is about 20 m, and the longitudinal, roughly parallel trending dunes dominate east of the Arava Fault (see also section 2.2.1).

3. Seismic experiments

After an overview of some regional scale seismic investigations in the Arava Valley, this chapter describes data acquisition, initial processing, and data quality of the Controlled Source Array experiments, which provided the seismic data for this study.

3.1 Regional scale seismic experiments

Regional scale seismic experiments include all those with a length scale larger than some tens of kilometers. Within the DESERT project, these experiments are a passive seismological array, a wide-angle seismic reflection-refraction profile, and a near-vertical seismic reflection profile.

The passive seismological array (PAS) consisted of 59 three-component broadband and short period stations, deployed between end of April 2000 and June 2001 (DESERT Group, 2000, 2002). This network crosses the Dead Sea Transform (DST) between the Dead Sea and the Red Sea with an aperture of about 250 km in NW-SE and 150 km in SW-NE direction. Scientific aims include a tomographic study, mapping crustal and upper mantle discontinuities with converted seismic waves (receiver function method), examination of seismic anisotropy, and the analysis of local seismicity (Mohsen *et al.*, 2000). Additionally, SKS phases[1] were observed on 86 stations along a 100 km profile crossing the DST. Rümpker *et al.* (2003) modelled these phases to constrain variations of anisotropic properties in the crust and upper mantle beneath the profile.

The NW-SE trending wide-angle reflection-refraction profile (WRR) is 260 km long and crosses the DST about half-way between the Dead Sea and the Red Sea (figure 3.1). Thirteen shots, including two quarry blasts, were recorded by 99 three-component stations with a spacing of 1–4.5 km. Moreover, 125 vertical geophone groups spaced 100 m along a line across the DST in the Arava valley completed the recording spread (DESERT Group, 2000). As a result, Mechie *et al.* (2000) derived a cross-section of P and S velocities in the crust (DESERT Group, 2004). This model is extended and constrained based on older, mainly N-S trending wide-angle profiles (Ginzburg *et al.*, 1979; Makris *et al.*, 1983; El-Isa *et al.*, 1987).

In the central part of the WRR profile the 100 km near-vertical seismic reflection profile (NVR) is located (figure 3.1). It combines a 90-fold vibroseis and a single-fold chemical

---

[1] SKS is a teleseismic S phase that passed the Earth's outer core as P (e.g. Stacey, 1992).
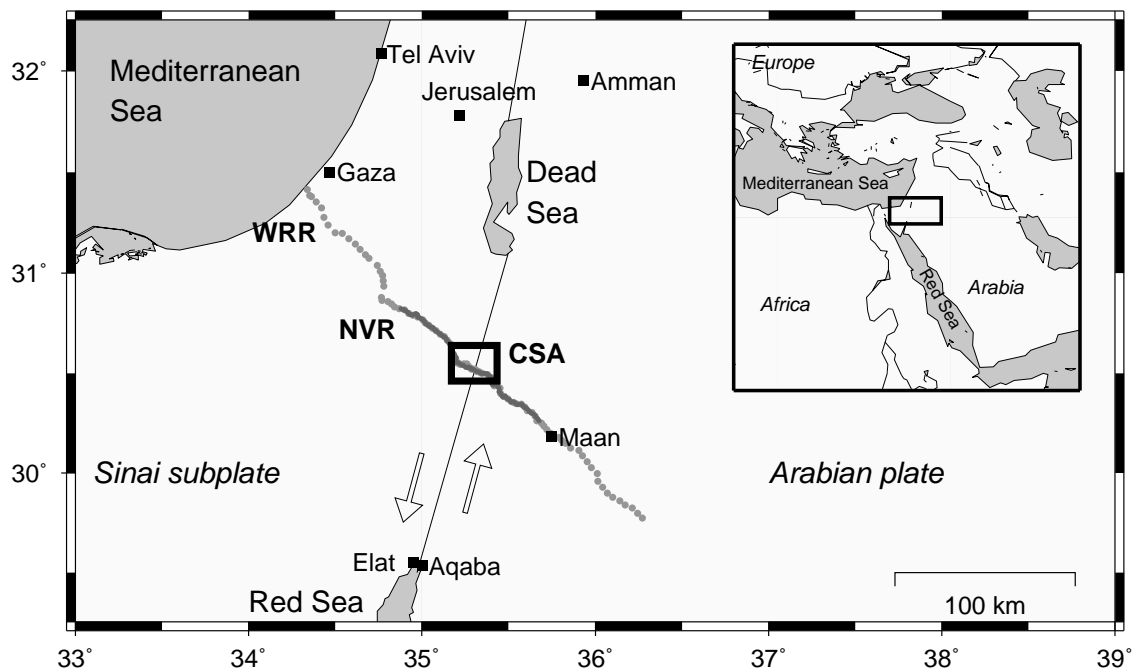
Figure 3.1: *Map of seismic experiments within the DESERT project. The wide-angle reflection-refraction profile (WRR) and the near-vertical reflection profile (NVR) are plotted in grey and black, and the black box indicates the location of the controlled source array experiment (CSA). A black line and arrows mark the Dead Sea Transform with its sinistral plate movement.*

explosion survey with 10 shots (Kesten *et al.*, 2000; DESERT Group, 2000). The vibrator locations are spaced 50 m, and recording was carried out by a roll-along, 180 channel receiver line with a geophone group spacing of 100 m. This leads to a common-midpoint (CMP) interval of 25 m. The results are time- and depth-migrated reflection images covering the entire crust beneath the profile (DESERT Group, 2004). Figure 3.2, bottom, shows a section of this depth-migrated profile across the Arava Fault (AF). Additionally, figure 3.2 includes two more reflection images in the Arava Valley (lines VWJ-6 and VWJ-9), courtesy of the Natural Resources Authority (NRA), Jordan. These images were provided as printed time sections, re-digitised, and finally depth-migrated.[2] Sedimentary reflections, dipping slightly to the north, are clearly visible west of the AF down to about 2–2.5 km depth, whereas the eastern side is characterised by minor reflectivity within the depth range displayed.

Furthermore, Ryberg *et al.* (2001) used the *P* wave first arrival times from NVR data to derive a tomographic image of *P* velocities in the upper 1.5–2 km along the NVR profile (see also Ritter *et al.*, 2003). The tomographic method is outlined in section 4.1.1, and figure 4.8, page 40, shows the *P* velocity structure along a segment of this profile.

---

[2] D. Kesten and M. Stiller, GeoForschungsZentrum Potsdam (2002), personal communication.
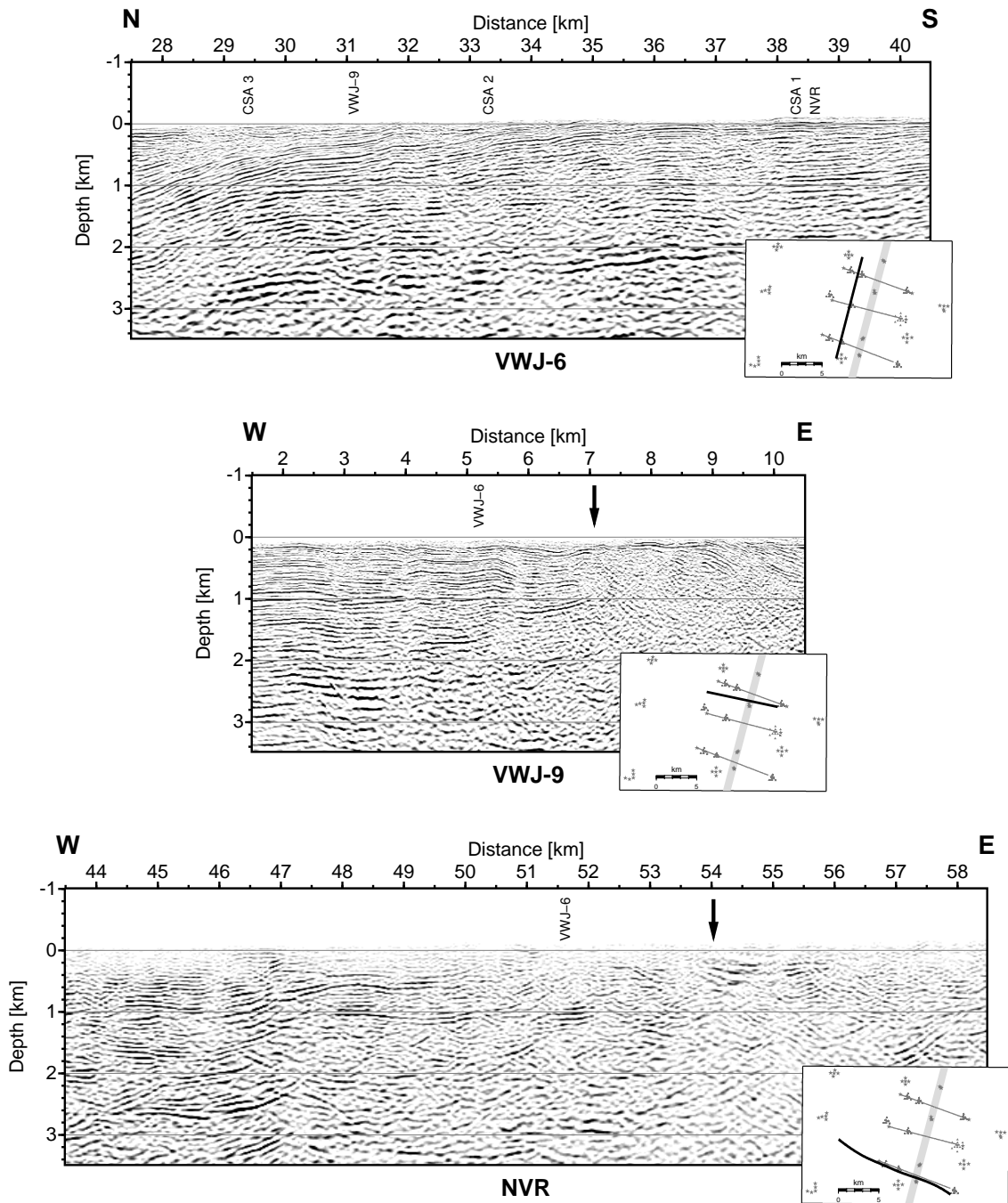
Figure 3.2: *Sections of depth-migrated near-vertical seismic reflection profiles in the Arava Valley. The lines VWJ-6 and VWJ-9 are courtesy of the Natural Resources Authority of Jordan (top panels), and the bottom panel shows a result of the NVR project (DESERT Group, 2004). Arrows indicate the surface trace of the Arava Fault at W-E trending profiles, labels denote intersections of these profiles with each other and with CSA lines, and inset maps mark profile locations with respect to the CSA acquisition geometry (see also figure 3.3). The reflection sections show sedimentary reflections west of the Arava Fault and weak reflectivity east of it.*
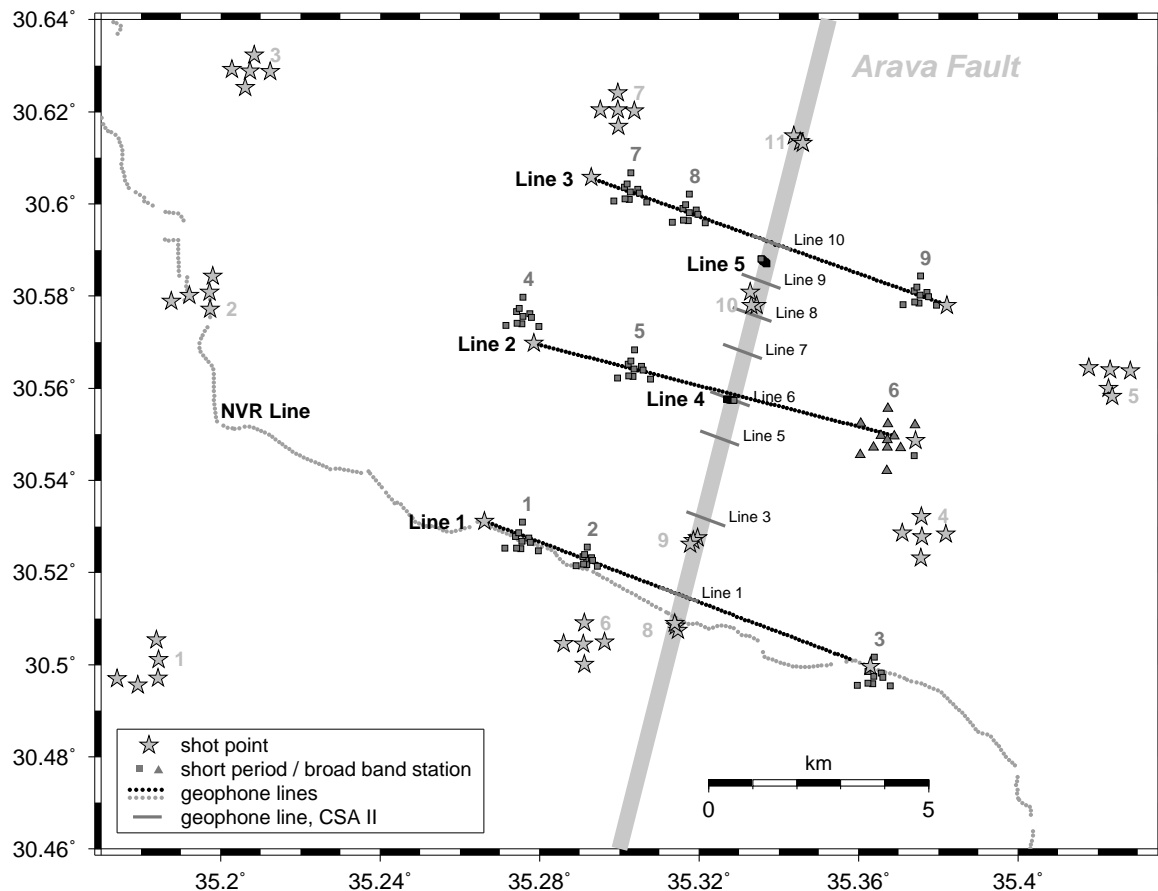
Figure 3.3: *Map of all shot and receiver station locations of the CSA and CSA II experiments with line and array numbers assigned. Line numbers are labelled bold for the CSA and in regular font shape for the CSA II. The NVR geophone line is included for better orientation.*

3.2 Controlled Source Array

This thesis mainly deals with data originating from active seismic experiments conducted in the Arava Valley, along and north of the central part of the NVR profile (figures 3.1 and 3.3). As part of the multidisciplinary DESERT research project (DESERT Group, 2000), the experiments, refered to as Controlled Source Array (CSA) project, were carried out mainly in April 2000. In addition, the CSA II experiment was conducted in the same study area in October and November 2001.

CSA

The CSA project comprises a set of several small-scale seismic experiments in the vicinity of the surface trace of the Arava Fault (AF; see also section 2.2.1). The target region of

Shots

number	shots/array	borehole depth	spacing	charge		note
1–3	5	≤ 20 m		60 kg		
4–7	5	≤ 20 m		45 kg		
8-11	3	≤ 20 m		45 kg		in-fault
	1	≤ 20 m		45 kg		line ends
1,3,5–10	*47–50*	*≤ 1 m*	*≈ 20 m*	*300 g*		*CSA II*

Receiver lines

number	sens./line	type	spacing	sampling	rec. time	note
1	94	1-C, 4.5 Hz	100 m	4 ms	-2…30 s	
2,3	90	1-C, 4.5 Hz	100 m	5 ms	-2…30 s	
4,5	20	3-C, 1.0 Hz	≈ 10 m	5 ms	-2…30 s	
1,3,5–10	*200*	*1-C, 4.5 Hz*	*5 m*	*1/16 ms*	*0…2 s*	*CSA II*

Receiver arrays

number	sens./array	type	aperture	sampling	rec. time	note
1–5,7–9	10	3-C, 1.0 Hz	800 m	5 ms	-2…30 s	©
6	13	3-C, broad band	1500 m	5 ms	-2…30 s	©

Table 3.1: *Acquisition parameters of the CSA and CSA II experiments. Locations of arrays and lines are shown in figure 3.3. The label* 1-C *stands for vertical component geophone groups and* 3-C *for three-component seismometers; the* ©*sign indicates stations, which recorded data continuously for several days.*

these experiments is the AF itself and the upper ∼3 km of the crust surrounding the fault. The CSA aims to image the (velocity) structure in three dimensions around the AF and other faults in the study area (section 4.2), to image shape and location of the AF, and to determine properties of the fault zone itself, such as the width of the damage zone (Haberland *et al.*, 2003b). Furthermore, models and images obtained from CSA data are jointly interpreted with other geophysical results to characterise the various lithologies in the study area (chapter 7). Another aspect is the development of seismic methods to image steeply dipping structures using fault zone reflected waves (section 5.3) and scattered seismic energy (chapter 6 and Maercklin *et al.* (2004)).

To address these aims, the CSA experiment realises various acquisition geometries in an area of about 20×15 km (figure 3.3). This area is located in the Arava Valley and includes the AF, the Qurayqira Fault, the Dana Fault, the Salawan Fault, and a few unnamed fault traces (figure 2.2, page 12). Seismic sources of the CSA are 53 chemical explosions with charge sizes between 45 kg and 60 kg (table 3.1). Most of these shots are arranged in several shot arrays to permit beamforming and stacking techniques in subsequent data processing (see section 5.1.2). The arrays are distributed over the area around and within the receiver spread to get observations from different azimuths (e.g. chapter 6) and crossing ray paths within the entire target volume as required for a tomographic inversion (chapter 4). Some shots are
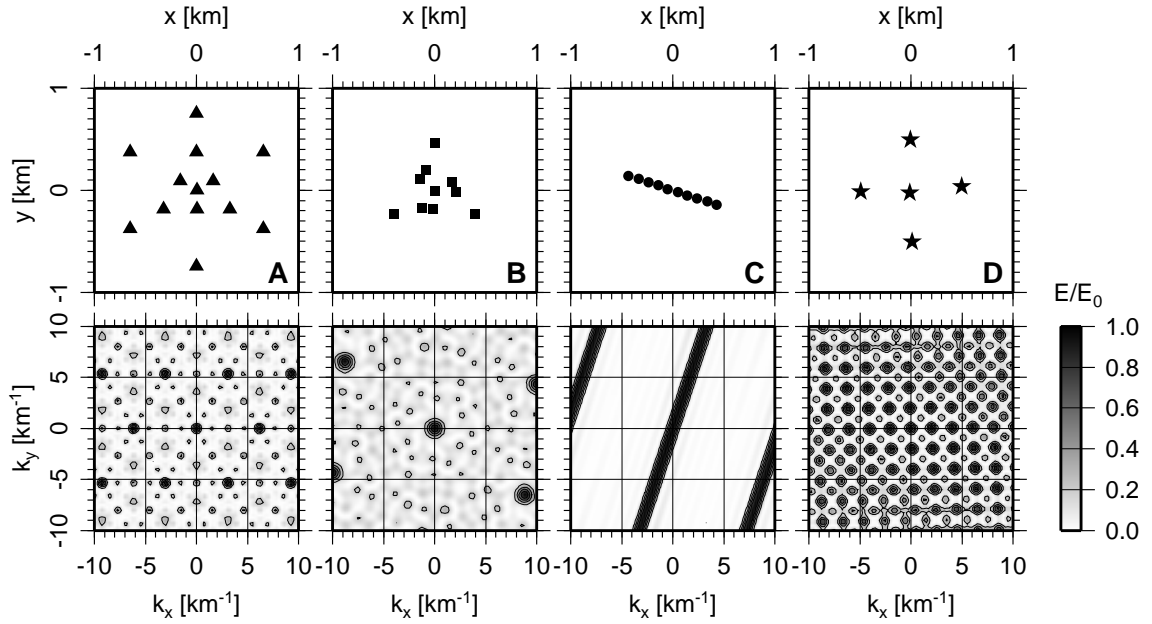
Figure 3.4: *Array configurations (*top*) and their corresponding array transfer functions (*bottom*). A: broad-band array 6, B: short-period arrays, optimal array after Haubrich (1968), C: segment of a geophone line illustrating vanishing resolution in crossline direction, and D: typical shot array included for completeness.*

located along the surface trace of the AF to generate guided waves, trapped in a low-velocity zone related to the fault (Haberland *et al.*, 2003b).

All 404 receiver locations fit into an area of about 10×10 km. Three geophone lines with a length of 9 km each and a receiver spacing of 100 m cross the AF roughly perpendicular. The lines are separated by 3–5 km, and the southernmost line 1 is located along the NVR line (figure 3.3). I use traveltime data obtained along these lines to image the three-dimensional velocity structure around the AF (section 4.2). In addition to these lines, two 200 m profiles of three-component seismometers are centered across the AF. With a station spacing of 10 m these are intended to record fault zone guided waves generated by in-fault shots (Haberland *et al.*, 2003b).

Nine receiver arrays with apertures around 1 km are placed along the geophone lines. Each array is equipped with ten three-component short-period seismometers or with thirteen broad-band stations in case of array 6. Resolution of such arrays is determined by their aperture, and the seismometer distances determine the smallest resolvable wavenumber not affected by spatial aliasing (Harjes and Henger, 1973; Buttkus, 1991; Schweitzer *et al.*, 2002). To visualise these properties, figure 3.4 compares array transfer functions (ATF) of different CSA array configurations. The top row contains array configurations and the row below the corresponding ATF, where k_x and k_y denote the wavenumber components in x and y direction, and E/E_0 the power normalised to the main maximum at $k_x = k_y = 0$. The
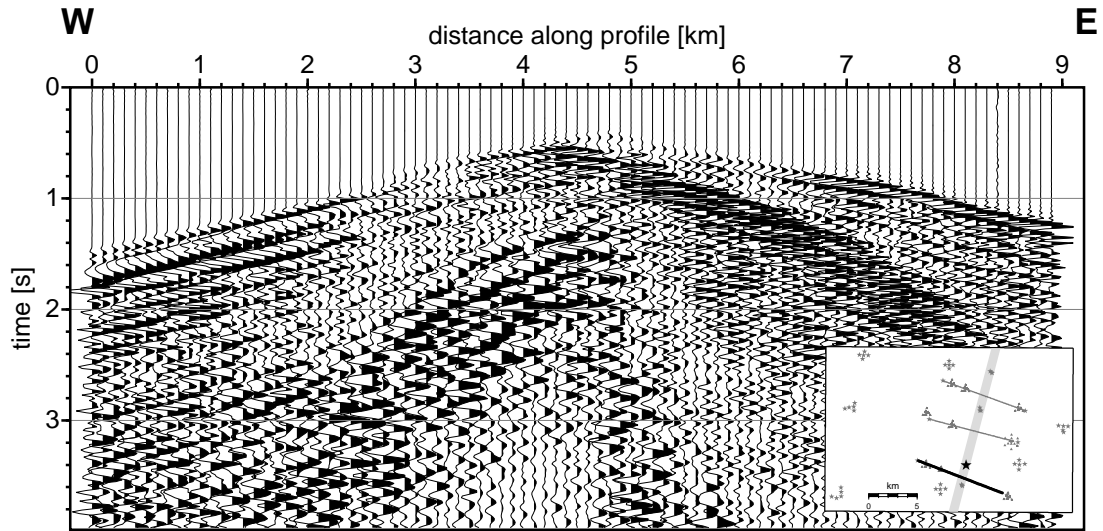
Figure 3.5: *Seismic shot gather recorded along CSA line 1. The shot is located at the surface trace of the Arava Fault, slightly offline 4.8 km along the profie (roughly a split-spread geometry), as indicated on the inset map. The slope of the first P onset between 0.5 s and 1.5 s is steeper west of the Arava Fault, indicating lower subsurface velocities on that side. Evidence for the fault itself comes from a disturbed wavefield at 4.8 km and the different later phases that appear on either side of the fault.*

wavenumber k is the product of frequency f and wave slowness p or reciprocal of apparent velocity: $k = fp = f/v_a$. The receiver arrays (figure 3.4 A,B) are intended mainly for the analysis of secondary seismic phases with initially unknown azimuth and slowness (chapters 5 and 6). Both array configurations are therefore symmetric to achieve the same resolution from all directions, and the variety of realised receiver distances avoids spatial aliasing for a broad range of wavenumbers. In each corresponding ATF, resolution is indicated by a narrow main maximum and low power elsewhere. Aliasing appears in repeating sidelobes, i.e. subsidiary maxima like the main maximum. For comparison with both receiver array configurations, figure 3.4 includes the ATF for a line of receivers (C) and for a typical shot array (D). The broad maximum of the ATF for the line illustrates its vanishing resolution in crossline direction.

All receiver arrays recorded data continuously for up to one week, whereas the geophone lines 2 and 3 ran in pre-defined time windows, which included the shot times. Absolute times were synchronised via satellites of the Global Positioning System (GPS). A cable telemetry system, triggered manually[3] at shot times only, recorded the data of the southernmost line 1. Table 3.1 lists main acquisition parameters of the CSA experiment together with those for the CSA II described at the end of this section.

---

[3] Radio triggers, commonly used in exploration seismics, could not be used there. Via mobile phone, I got shot times, triggered the recorder manually, and saved absolute trigger times for later time corrections.
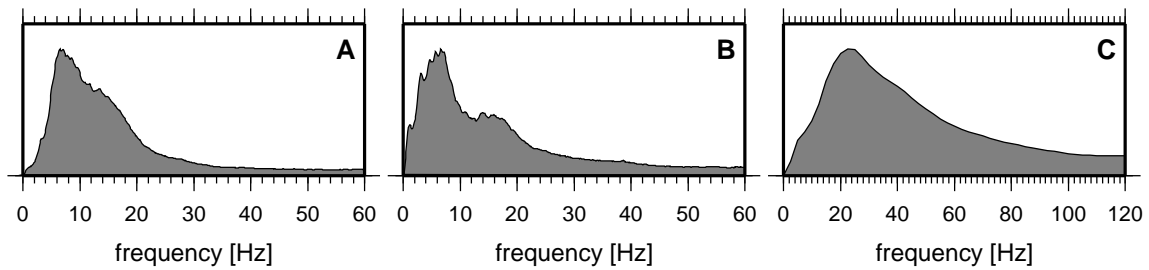
Figure 3.6: *Averaged amplitude spectra of CSA shot records for the first P onset and its coda.* A*: geophone lines,* B*: seismometer arrays, and* C*: complete CSA II dataset.*

The preprocessing of raw field data consisted of conversion from the native file format of instruments to SEG-Y, timing corrections, and subtraction of the arithmetic mean of each trace (debiasing). In general, the data exhibit a high signal-to-noise ratio for the first P onset, but S phases and expected (fault zone) reflections are not clearly visible. As an example, figure 3.5 displays a shot gather recorded on line 1 in split-spread geometry. It illustrates different seismic properties west and east of the AF located at 4.8 km distance along the profile: The steeper dipping P onset indicates lower velocities in the west, and the AF itself appears as interruptions in continuous phases and by diffractions. Surface waves are mostly observed on the western side only. Observed frequencies of the first P onset and its coda range from about 4 Hz to more than 20 Hz, with a peak around 8 Hz (figure 3.6). A shot gather of a distant shot recorded along line 3 is displayed in figure 5.8 (page 69), and figure 5.1 (page 62) shows three-component seismograms of two local earthquakes recorded by receiver arrays.

CSA II

Main aim of the CSA II experiment is a detailed image of the shallow velocity structure of the upper 100 m across the Arava Fault (AF) along several profiles embedded in the CSA area (section 4.3). Additionally, the CSA II provides seismic reflection sections, which help to delineate the exact trace of the fault (section 5.4). Eight parallel profiles of 1 km length cross the AF perpendicularly. They are spaced about 1 km in the northern and 1.5 km in the southern part of the study area (figure 3.3). Each profile consists of 200 vertical geophone groups spaced 5 m, and 47–50 shots with a spacing of about 20 m are fired into this spread. The shots triggered the data acquisition system, and the recorded data were transfered to the control unit via cable telemetry as used for line 1 of the CSA. The initial time sampling rate of the field data is 1/16 ms during a total acquisition length of 2 s (table 3.1). First arrival traveltimes used to derive the P velocity models (section 4.3) are picked from these highly
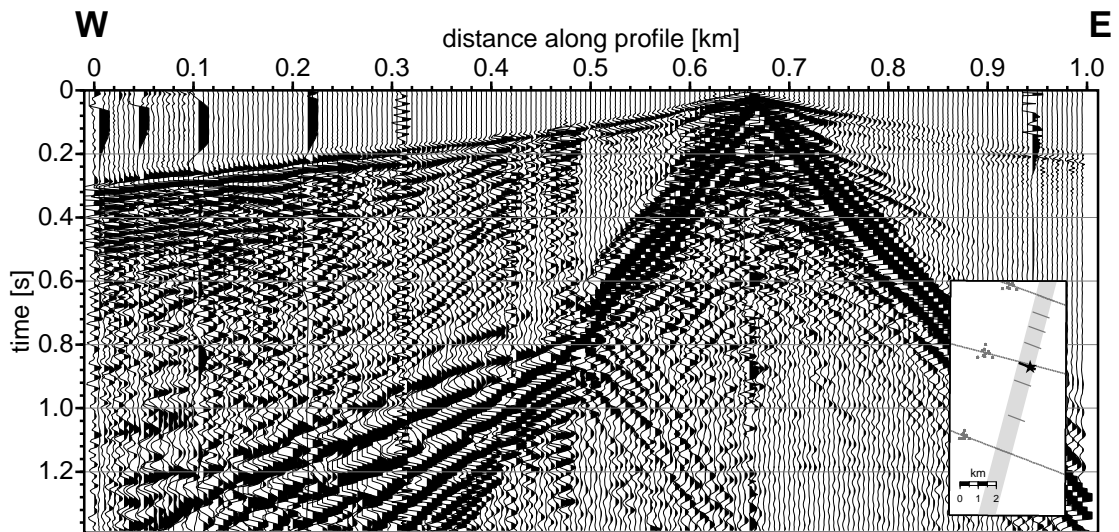
Figure 3.7: *Seismic shot gather recorded along CSA II line 6 (see inset map). The shot is located at 0.66 profile-km, and the Arava Fault at 0.5 km. The first P onset is clearly visible along the entire profile between 0.0 s and 0.28 s. Large-amplitude surface waves generated by the shot and reflected at the fault trace superimpose possible near-vertical reflections.*

sampled shot records, whereas these records are resampled to 1 ms for reflection seismic processing (section 5.4).

Signal frequencies, averaged over the entire CSA II dataset, cover a range up to about 100 Hz (figure 3.6) with a wide peak around 25 Hz. Figure 3.7 displays a shot gather, which shows typical features observed on CSA II profiles. The first *P* onset is clearly visible along the entire section, but again, *S* waves were not excited. As in this example, most shot gathers are dominated by high-amplitude, weakly dispersive surface waves, which were clipped on traces close to a shot during acquisition. These strong waves are due to the relatively large charge in shallow boreholes. The prominent surface wave reflection, correlating with the surface trace of the AF, is a local feature. But in general, that part of the seismogram after the arrival of surface waves is dominated by backscattered energy, which superimposes possible near-vertical reflections (section 5.4).

4. First arrival tomography

First arrival tomography inverts observed first arrival traveltimes for the subsurface P velocity structure. After an introduction to this method, I present its application, results for the whole study area, and higher resolved images across the Arava Fault.

4.1 Tomographic method

Since early works of Aki *et al.* (1977) numerous publications dealt with the inversion of P or S wave first arrival times to produce a subsurface model of the associated velocity distribution, or of perturbations relative to a reference model. Particularly for large sets of traveltime observations using many different source and receiver locations, this inversion is referred to seismic velocity tomography[1] (e.g. Sheriff, 1991). Figure 4.1 sketches the basic principle of velocity tomography. Among others, Nolet (1987), Menke (1989), Iyer and Hirahara (1993), Shearer (1999), and Yilmaz (2001) give general introductions and comprehensive mathematical derivations. Different approaches for the same basic principle were developed for either teleseismic data, local earthquake data, or data from controlled-source experiments. For example, the tomographic inversion method has been implemented in the codes `simulps12` of Thurber (1983) and Evans *et al.* (1994), and `FAST` of Zelt (1998a). A further description is included in section A.1. Because I use explosive sources with known location and origin time, I omit aspects of earthquake location and origin time determination in the following discussion of the method.

4.1.1 Forward and inverse problem

Arrival times shall be calculated for a subsurface velocity structure, such that the difference between observed and modelled times, the traveltime residuals, is made minimum based on a specific norm. As in most geophysical applications, here it is the L_2 norm, in which the residuals are made minimum in a least-squares sense. Hence, the first steps to derive a model are parameterisation of the velocity field and forward calculation of traveltimes.

Commonly, the model is divided into blocks with uniform velocity, or velocities are defined at certain nodes with some kind of interpolation between them. Node spacings or block sizes

---

[1] The word tomography is derived from the Greek $\tau o\mu o\sigma$ (section, slice) and $\gamma\rho\alpha\phi\iota\alpha$ (image, drawing).
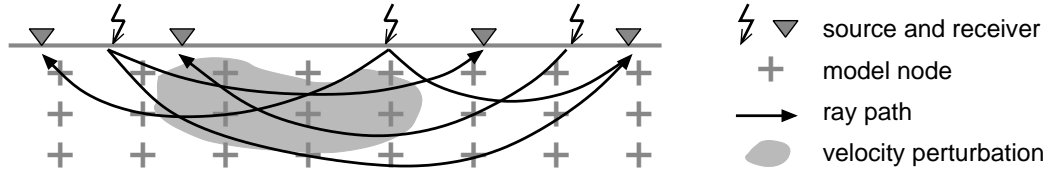
Figure 4.1: *Basic principle of first arrival velocity tomography: First arrival traveltimes of many different source-receiver combinations are inverted at model nodes for velocity perturbations relative to a starting model.*

are always adapted to a specific data set and acquisition geometry. Besides that, the type of parameterisation could be restricted by the forward algorithm of choice (see also Thurber and Eberhart-Phillips, 1999; Kissling *et al.*, 2001).

Thurber (1981, 1983) parameterises the studied volume by grid nodes defined at intersecting lines with variable spacing. Model parameters, here the *P* velocity v_p and optionally the v_p/v_s ratio, are defined at these nodes. At any other location $\mathbf{x} = (x_1, x_2, x_3)$ inside the grid, parameters are interpolated depending on the distances to the eight neighbouring nodes $(p_{1,1}, p_{1,2}, p_{1,3})$, $(p_{1,1}, p_{1,2}, p_{2,3})$, . . ., $(p_{2,1}, p_{2,2}, p_{2,3})$. In a condensed notation of Patzig (1999) the trilinear interpolating function reads as

$$v(\mathbf{x}) = \sum_{i_1=1}^{2}\sum_{i_2=1}^{2}\sum_{i_3=1}^{2} v(p_{i_1,1}, p_{i_2,2}, p_{i_3,3}) \cdot \prod_{j=1}^{3}\left(1 - \left|\frac{x_j - p_{i_j,j}}{p_{2,j} - p_{1,j}}\right|\right). \tag{4.1}$$

Forward calculation of traveltimes is done by tracing rays through the velocity model. A ray-theoretical approximation to the scalar wave equation is the eikonal equation

$$\nabla^2 t(\mathbf{x}) = u^2(\mathbf{x}) = \frac{1}{v^2(\mathbf{x})} \tag{4.2}$$

in which $t(\mathbf{x})$ is the traveltime at $\mathbf{x}$ and u the slowness or reciprocal of the velocity v. Its solution represents wave fronts $\mathrm{t}(\mathbf{x}) = const$ and rays, which are perpendicular to the wave fronts. For example, Aki and Richards (1980) or Yilmaz (2001) provide a detailed mathematical discussion. Introduction of the arc length s along the ray, such that $\mathbf{x} = \mathbf{x}(s)$, leads to the ray equation

$$\frac{\mathrm{d}}{\mathrm{d}s}\left(u\frac{\mathrm{d}\mathbf{x}}{\mathrm{d}s}\right) = \nabla u. \tag{4.3}$$

For each traveltime or traveltime residual, a solution of equation 4.3, that connects source and receiver, must be found. Ray shooting methods sample different take-off angles at the source to converge on the correct receiver location, and ray bending methods deform a nearby ray path slightly to arrive at that receiver (Shearer, 1999; Patzig, 1999; Husen, 1999). These methods are feasible for velocity models with variable node spacing. Finite difference (FD) techniques require a uniform grid of velocity nodes (e.g. Vidale, 1990; Yilmaz, 2001).

Thurber (1983), Um and Thurber (1987), and Eberhart-Phillips (1990) developed a combination of a three-dimensional approximated ray tracer enhanced by pseudo-bending (ART-PB). On planes with varying dip angles they contruct a substantial number of circular arcs of different radii and calculate the traveltimes through the three-dimensional velocity model. Then, pseudo bending for the ray with minimum traveltime adjusts that initial ray path according to the gradient of the velocity field along the ray. Haslinger (1998) implemented a more accurate RKP shooting algorithm after Virieux (1991).[2] But for ray paths shorter than 40 km, as in this study, ART-PB yields reliable results and reduces computational costs significantly.

Vidale (1988, 1990) introduced a method of calculating traveltimes on a uniform square grid by solving the eikonal equation 4.2 using finite-differencing (Zelt and Barton, 1998). With minor modification, this original FD algorithm finds true first arrival times for direct, refracted, or head waves in arbitrarily complex velocity models, even in the presence of sharp velocity contrasts (Hole and Zelt, 1995). Traveltimes are calculated simultaneously for all receivers, and associated rays are found by following the traveltime gradient backward from receivers to the source. Thus, for a large number of receivers such an approach is generally faster than ray tracing.

Calculated traveltimes for each source-receiver pair are subtracted from observed times to form the traveltime residuals $t_{ij}^{obs} - t_{ij}^{cal}$, in which the subscripts denote the observation at the ith receiver for the jth source. Then, model adjustments shall minimise these residuals in a least squares sense. Finding these adjustments is a non-linear problem, because velocity changes affect ray paths and thus modify calculated traveltimes. Therefore, it is usual to linearise the problem and to iterate the inversion procedure, each with an updated set of velocity parameters, ray paths, and traveltime residuals. Iteration terminates, if velocity changes fall below a certain limit, traveltime residuals do not decrease significantly or reach the magnitude of timing errors, or after a maximum number of iterations (Evans *et al.*, 1994; Zelt, 1998a).

The linearised approximation for one observation

$$t_{ij}^{obs} - t_{ij}^{cal} = \sum_{n=1}^{N} \frac{\partial t_{ij}}{\partial v_n} \Delta v_n \qquad (4.4)$$

relates a traveltime residual to changes of the velocity parameters v_n (e.g. Eberhart-Phillips, 1990). Including all M residuals into the data vector $\mathbf{d}$, all N model adjustments into $\mathbf{m}$, and the partial derivatives into the matrix $\underline{\underline{G}}$, equation 4.4 becomes

$$\mathbf{d} = \underline{\underline{G}}\mathbf{m} \qquad (4.5)$$

in vector notation. A direct solution of the model equation 4.5 exist only, if $\underline{\underline{G}}$, the data kernel, is square ($M = N$). But usually seismic tomography problems contain more observations than velocity model parameters. Following Lines and Treitel (1984) this leads to a

---

[2] RKP stands for Runge-Kutta plus (Hamiltonian) perturbation.

least-squares solution for estimated model adjustments

$$\tilde{\mathbf{m}} = (\underline{\underline{\mathbf{G}}}^T \underline{\underline{\mathbf{G}}})^{-1} \underline{\underline{\mathbf{G}}}^T \mathbf{d} \qquad (4.6)$$

in which $\underline{\underline{\mathbf{G}}}^T \underline{\underline{\mathbf{G}}}$ is the data covariance matrix and $(\underline{\underline{\mathbf{G}}}^T \underline{\underline{\mathbf{G}}})^{-1} \underline{\underline{\mathbf{G}}}^T$ is called the generalised linear inverse or least-squares inverse of $\underline{\underline{\mathbf{G}}}$ (Snieder and Trampert, 1999; Yilmaz, 2001). Theoretically, the square matrix $\underline{\underline{\mathbf{G}}}^T \underline{\underline{\mathbf{G}}}$ is invertible. However, a perfect fit cannot be expected. This is due to linearisation of the initial non-linear problem, the discrete velocity model parameterisation, and to errors of observed traveltime data. Moreover, as a result of an irregular ray distribution, some model parameters may be over- and some underdetermined. Introducing a damping factor β to equation 4.6,

$$\tilde{\mathbf{m}} = (\underline{\underline{\mathbf{G}}}^T \underline{\underline{\mathbf{G}}} + \beta \underline{\underline{\mathbf{I}}})^{-1} \underline{\underline{\mathbf{G}}}^T \mathbf{d} \qquad (4.7)$$

with the unit matrix $\underline{\underline{\mathbf{I}}}$, avoids too small or zero eigenvectors of $\underline{\underline{\mathbf{G}}}^T \underline{\underline{\mathbf{G}}}$ and stabilises the solution numerically. The term $(\underline{\underline{\mathbf{G}}}^T \underline{\underline{\mathbf{G}}} + \beta \underline{\underline{\mathbf{I}}})^{-1} \underline{\underline{\mathbf{G}}}^T$ is the stochastic or Levenberg-Marquart generalised inverse. Larger damping values result in smaller model adjustments and vice versa.

Whereas Thurber (1983) follows the approach outlined above, more general regularisation methods are applicable. Typically, a-priori constraints on the model are added to the data to treat the underdetermined part of equation 4.6. For example, penalising roughness of the model, measured by its second order derivatives, leads to a smooth solution. To obtain it, $\underline{\underline{\mathbf{I}}}$ in equation 4.7 has to be replaced by $\underline{\underline{\mathbf{D}}}^T \underline{\underline{\mathbf{D}}}$, if $\underline{\underline{\mathbf{D}}}$ is the matrix of second order spatial derivatives (Scales *et al.*, 2001). The factor β then acts as a tradeoff parameter between data fit and model roughness. Minimising model roughness is justified, because ray methods are valid for smooth models only, and traveltimes constrain only long-wavelength structures since the times represent integrals through the model (Zelt and Barton, 1998). Zelt (1998a) employs a regularised inversion scheme that incorporates a combination of smallest, flattest, and smoothest velocity perturbation constraints. The final model is minimum structure in the sense, that only structure required by the data according to its noise level is included (Scales *et al.*, 1990).

4.1.2   Resolution estimates

Seismic tomography provides formal means to quantify the resolution of model parameters and errors of a solution. These means include measures for ray coverage, formal analysis of the resolution matrix, or quantities derived thereof. Additionally, synthetic models can be tested for the source and receiver distribution of a real experiment.

The distribution of rays in the model volume can be visualised by hit counts and the derivative weighted sum. Hit counts simply sum the number of rays penetrating a block around a certain model node, wheras the derivative weighted sum is a relative measure for the ray density in

the vicinity of the node. Compared to hit counts, it is preferable, because it considers also the spatial distances of rays to a node (Toomey and Foulger, 1989). Regions with large values are considered as well resolved.

The model resolution matrix, also called resolution kernel, relates estimated model adjustments $\tilde{\mathbf{m}}$ and true adjustments $\mathbf{m}$ that solve equation 4.5. With equation 4.7 and the generalised linear inverse abbreviated as $\underline{\underline{\mathbf{G}}}^{-g}$,

$$\tilde{\mathbf{m}} = (\underline{\underline{\mathbf{G}}}^{-g}\underline{\underline{\mathbf{G}}})\mathbf{m} = \underline{\underline{\mathbf{R}}}\mathbf{m} \tag{4.8}$$

determines the resolution matrix $\underline{\underline{\mathbf{R}}}$ (Thurber, 1993; Snieder and Trampert, 1999). Each of its rows includes the resolution of one model parameter. Relative size and pattern of off-diagonal elements illustrate how information is smeared between different model parameters. For an adequately resolved parameter, its resolution peaks on the diagonal and nodes which are not adjacent contribute insignificantly. But the diagonal elements also depend strongly on node spacing and the chosen damping parameter β (Eberhart-Phillips and Michael, 1998). To assess the full resolution matrix $\underline{\underline{\mathbf{R}}}$, Michelini and McEvilly (1991) compress resolution of each parameter j into a single number S_j, the spread function

$$S_j = \log\left[\|R_j\|^{-1}\sum_{k=1}^{N}\left(\frac{R_{jk}}{\|R_j\|}\right)^2 D_{jk}\right]. \tag{4.9}$$

For a node j it is calculated from all elements R_{jk} of the corresponding row of $\underline{\underline{\mathbf{R}}}$, the L_2 norm $\|R_j\|$ of that row, and the spatial distances D_{jk} between nodes. The first factor makes the spread function S_j small for nodes with large diagonal resolution values and the summed terms makes S_j large for nodes that have significant averaging from others, particularly for more distant ones. Perfect resolution is expressed by $S_j = 1$.

Synthetic checkerboard tests are commonly used to estimate the spatial resolution of the entire model independently from formal means such as the resolution matrix (e.g. Hearn and Ni, 1994; Zelt and Barton, 1998). Although varying in details, a checkerboard model consists of an alternating anomaly pattern of positive and negative regions superimposed on the final or on an average one-dimensional velocity model. Relatively small velocity perturbations can be used, so that ray paths through the model are minimally perturbed compared to the background model. But the velocity perturbations must be large enough to yield traveltime perturbations above the noise level. Firstly, synthetic traveltimes are calculated for the real source-receiver geometry, and Gaussian noise with a standard deviation equal to those of the real data is added. Secondly, these data are inverted using the background model of the anomaly pattern as the starting model and the same method as for the real experiment. For each point of the final model, the recovered anomaly pattern indicates the ability to resolve features with a length scale equal to the anomaly spacing (Zelt, 1998b, 1999). The semblance (Neidell and Taner, 1971; Yilmaz, 2001) between exact and recovered checkerboard anomalies provides a quantitative estimate for the resolution:

$$r = \frac{\sum_{i=1}^{N}(\Delta v + \Delta\tilde{v})^2}{2\sum_{i=1}^{N}(\Delta v^2 + \Delta\tilde{v}^2)} \tag{4.10}$$

with exact and recovered anomalies Δv and $\Delta \tilde{v}$. It is calculated using a circular or box-shaped operator centered on each model node. Zelt (1998b) refers to these semblance values as resolvabilities. He states, that a value above 0.7 indicates a well-recovered checkerboard structure and hence a well resolved region in the final model on a length scale given by the anomaly spacing.

To estimate the uncertainty of all model parameters, a procedure called jackknifing can be applied (Wu, 1986; Zelt, 1999). Traveltime data are randomly divided into equal sized subsets, and the complete set without a particular subset is inverted in turn. Each inversion result qualitatively illustrates the importance of the missing data. An alternative approach are bootstrap analyses (Wu, 1986; Nishizawa and Noro, 1995; Lanz *et al.*, 1998), which involve synthetic traveltimes calculated for the final model and the real acquisition geometry. From these times, a large number of replicate data sets are generated by adding random noise. After the inversion of each replicate, using the same procedure as for the real data, model parameter variances can be calculated easily. Compared to the jackknife method, bootstrap analyses do not reduce resolution due to a coarser ray coverage, but strongly increase computational costs.

All resolution estimates mentioned above are relative measures since they depend not only on amount and quality of data, but also on model parameterisation, and forward and inverse solution parameters (Kissling *et al.*, 2001).

4.2   Three-dimensional tomography of the study area

This section describes the application of the tomographic inversion of first arrival traveltimes to determine the three-dimensional *P* velocity structure in the vicinity of the Arava Fault (AF), down to about 3 km depth. I use the inversion code `simulps12` (Thurber, 1983; Evans *et al.*, 1994), which is well-proven in seismological studies and allows an uneven subsurface parameterisation with gradually varying velocities (see sections 4.1.1 and A.1). This study considers *P* arrivals from shots in the central part of the study area and excludes those far outside the receiver spread (shot arrays 1–3, see figure 3.3), because the velocity structure would be very poorly constrained in those areas. Generally, first *P* arrivals are clearly visible on recordings of all shots. These arrivals are interpreted as continuously refracted, diving waves (figure 4.1), which permits a tomographic inversion as outlined in the previous sections. Therefore, in a first step I picked the first *P* traveltimes manually from all recorded shot gathers and excluded only those with a poor signal-to-noise ratio. In a second step prior to an inversion, the inversion parameters have to be determined. These include the subsurface parameterisation, selection of shot and receiver locations to be used, the initial velocity model, and the determination of an appropriate damping value (section 4.1.1).

The ideal acquisition geometry for a tomographic inversion is a uniform distribution of shots and receivers all over the region to be investigated. Additionally, short and long shot-receiver
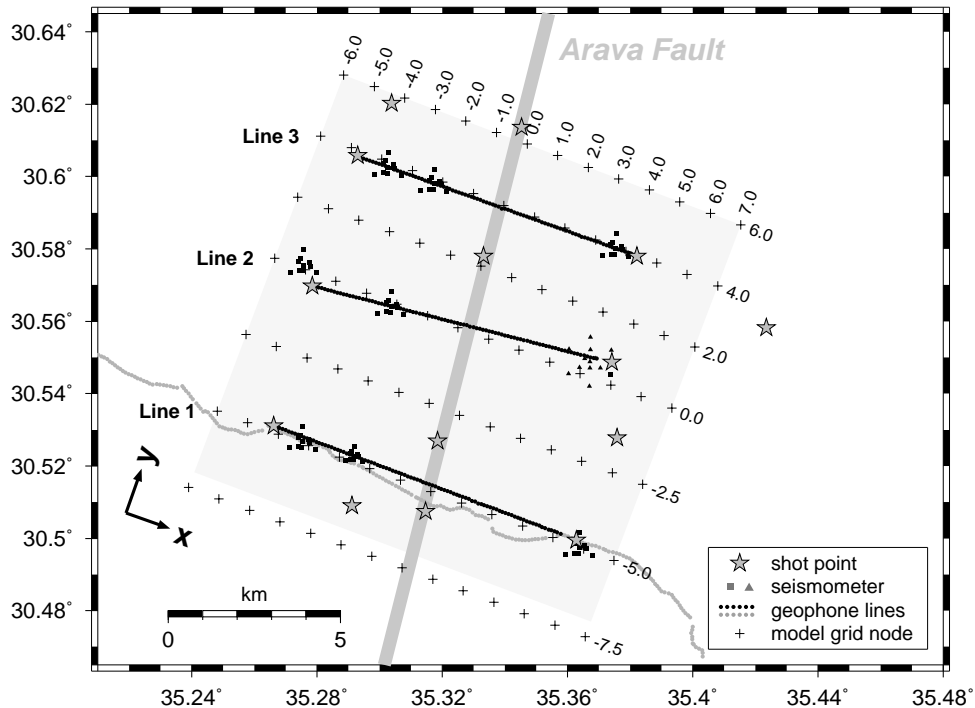
Figure 4.2: *Model node grid and acquisition geometry for three-dimensional tomography. The x-direction is parallel to the receiver lines (inline) and the y-direction perpendicular to them (crossline). Local coordinates at node planes are in km.*

offsets must be realised to ensure ray coverage at all depths. The CSA acquisition geometry is not ideal in this sense. Receivers are located along three lines with a dense spacing of 100 m, but the distances between these lines range between 4 km and 5 km (figure 4.2 and chapter 3.2). Shots are located at the line ends and are arranged in groups along the trace of the AF and at some other locations. Because the ray paths from a group of shots to a certain receiver are essentially the same, I selected a single shot from each of these groups for the inversion. Together with the shots at line ends, this results in 14 used shots (figure 4.2). However, all of these shots were recorded by the entire spread of about 300 receivers leading to a relatively good ray coverage in the study area.

From the geological point of view, the aim of a tomographic experiment is a most detailed resolution of the subsurface velocity structure. A dense spacing of model nodes in all directions and the allowance of a strong heterogeneity complies with this aim. But an inversion of the implied high-dimensional parameter space tends to be unstable. Although this problem can be addressed with an higher damping factor β in the least-squares inversion, from the numerical point of view, a coarse node spacing and a least complex velocity model has to be favoured (see section 4.1.1). The model node grid used in this study reflects the uneven CSA acquisition geometry and the sparse coverage of the area with shots. The grid is based on several tests with different subsurface parameterisations. Node planes are oriented along to
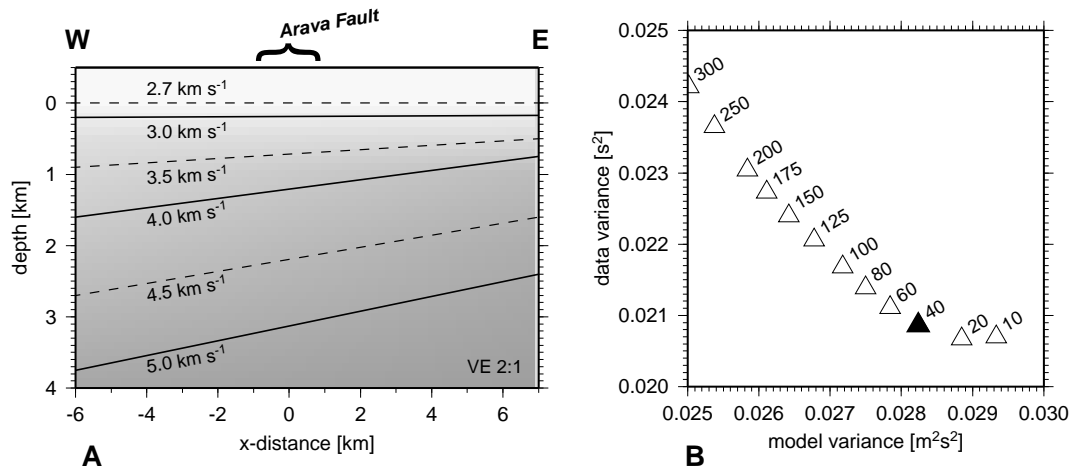
Figure 4.3: A: *Initial P velocity model used for the tomographic inversion.* B: *trade-off between model variance and data variance for several damping factors* β*. The selected value of* $\beta = 40$ *is indicated by a black triangle.*

the receiver lines with additional planes just north and south of the receiver spread and two planes between the lines. The x-direction of the assigned local coordinate system is parallel to the lines (inline) and the y-direction perpendicular to them (crossline). Whereas the inline node spacing of 1 km is constant, the distances between node planes in y-direction are 2 km and 2.5 km, depending on the positions of receiver lines (figure 4.2). In vertical z-direction, nodes are spaced 0.5 km in the depth range of 0 km to 3.5 km, and the model is bounded by nodes in 50 km distance from its centre to avoid that rays hit model boundaries. Velocities between grid nodes are interpolated using the function defined by equation 4.1 (section 4.1.1).

The initial velocity model should be simple to avoid artificial structures related to the initial model in the final result. Often one-dimensional models with increasing velocities with depth are chosen. Increasing velocities ensure that rays from shots at the surface can reach the receivers located also at the surface. However, an examination of the first *P* arrivals and two-dimensional modelling of the picked traveltime curves indicate that the subsurface structure in the study area is in effect two-dimensional with lower velocities in the west. This observation is corroborated by first inversion tests with a one-dimensional initial model. Therefore, I derived the two-dimensional initial model shown in figure 4.3 A. Here, *P* velocities range from 2.7 km s^{-1} at the surface to more than 5 km s^{-1} at 4 km depth. The initial *P* velocities are lowest at the western and highest at the eastern side, and in between they are linearly interpolated. Thus, the velocity structure directly visible in the traveltime curves is approximated without constraining the boundary between regions of higher and lower velocities to a certain position within the model.

As suggested by Eberhart-Phillips (1986) I determined the damping factor β empirically. First, several inversions with one iteration each and with different β are run using the chosen

subsurface parameterisation, initial velocity model, and the observed traveltimes. Second, the reduction of the data variance is compared with the solution or model variance. Figure 4.3 B shows the data variance as a function of the model variance for several β values tested for this experiment. The resulting curve is commonly known as the trade-off curve. For large β the obtained model tends to be smooth (small model variance) and does not fit the data properly (large data variance). Less damping allows a higher model complexity coinciding with a reduction of the data variance. This remains true as long as β is not too small for a stable inversion. Instability is indicated by an increasing or flat trade-off curve for increasing model variance. The optimum value for β is the one that provides both, a small data variance and a small model variance. The models presented below are derived with a constant damping factor of $\beta = 40$.

4.2.1   Resolution

The resolution of the tomographic inversion can be assessed by means discussed in section 4.1.2. Here I present the analysis of the spread function S_j defined by equation 4.9 (Michelini and McEvilly, 1991) and results of synthetic recovery tests. In brief, the spread function describes how much a velocity value obtained at a certain model node is smeared into neighbouring nodes. Good resolution is indicated by small spread function values and poorer resolution by larger ones. The spread function is a relative measure, since its absolute values depend on modelling parameters. Figure 4.4 shows spread function values at five vertical cross-sections through the three-dimensional model volume. The cross-section locations are the same as those illustrating the synthetic tests (figure 4.6) and the final results (figure 4.7). Dark shades of grey correspond to low S_j values, i.e. good resolution, and lighter shades to larger values, i.e. poorer resolution. As expected from the acquisition geometry, the central part is the best resolved region of the model. Along line 2, relatively low S_j values occur down to 3 km, reflecting the deepest penetration of rays due to the largest possible shot-receiver offsets. To the north and to the south, well resolved regions are confined to shallower depths, and variations of S_j are mainly due to the non-uniform coverage of the study area with shots (see figure 4.2). Below the surface trace of the AF, the resolution is generally good.

Calculations with synthetic traveltime data provide another view on the obtainable resolution. A common procedure is the inversion for so-called checkerboard models (section 4.1.2). In a first step, synthetic traveltimes are calculated for the real acquisition geometry and a subsurface model of an alternating pattern of positive and negative velocity anomalies relative to a background model (initial model). Such an anomaly pattern is shown in figure 4.5 as velocity perturbations relative to the background model. Here, each positive or negative anomaly extends over two model nodes in all directions. Their amplitude is $\pm 5\%$ of the background velocity, and synthetic traveltimes used in the inversion are disturbed by additive random noise of ± 50 ms. In a second step, these traveltimes are inverted using the same modelling parameters as for the real data. The inversion demonstrates the resolution of
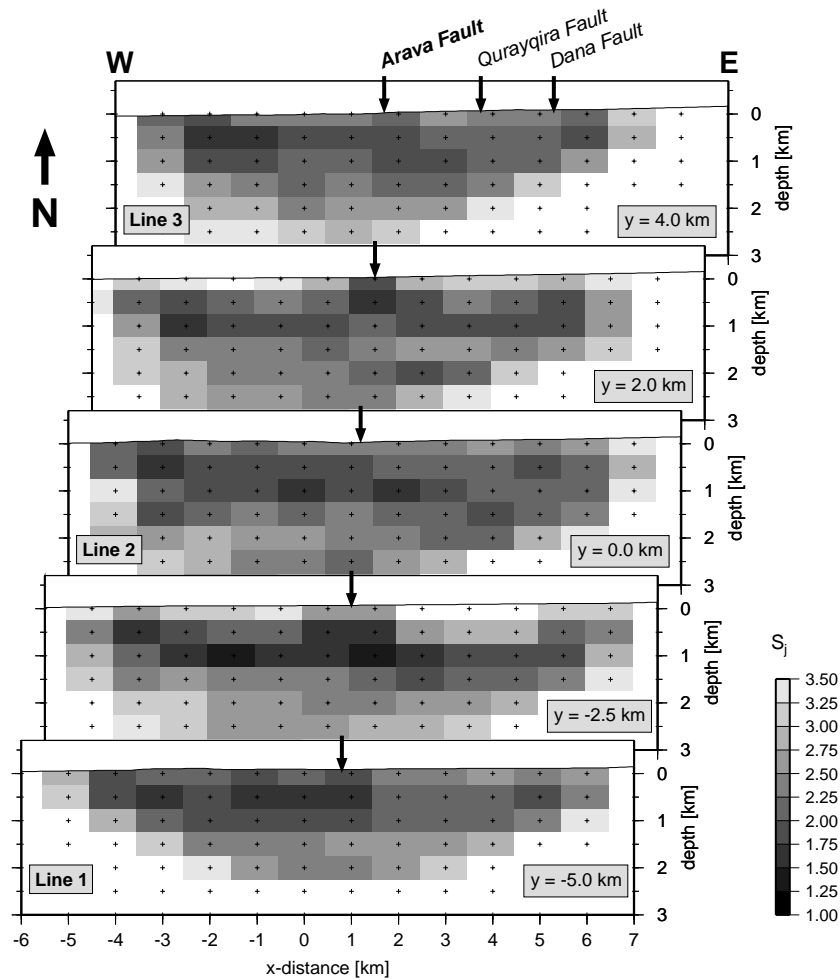
Figure 4.4: *Spread function values for the three-dimensional tomographic velocity model. Low values indicating good resolution are in darker shades of grey (see also section 4.1.2).*

structures with length scales comparable to the anomaly size. Figure 4.6 shows the recovery of the checkerboard pattern test for this study (figure 4.5, again along five cross-sections. The regular checkerboard pattern is well reconstructed along the central section (line 2) down to about 2.5 km depth. With some exceptions, also the neighbouring sections exhibit a good resolution of the anomalies. Well resolved regions along lines 1 and 3, located in the outer parts of the modelled area, occur only in the upper 1.5 km. Despite the good structural resolution of the anomalies, their amplitudes are slightly underestimated. This effect is inherent in the inversion procedure, which favours smooth velocity models. To quantify the resolution of the checkerboard pattern, figure 4.6 includes the boundary of recovered regions according to a resolvability of $r = 0.7$, calculated within a moving box with a correlation length of 1 km in all directions. The resolvability r has been introduced by Zelt (1998b) and is defined by the semblance between the true and recovered anomaly pattern (equation 4.10).

Figure 4.5: *Input anomaly pattern of a synthetic checkerboard test for the three-dimensional tomographic velocity model. The cross-sections shown correspond to those of the model recovery shown in figure 4.6.*

Besides the resolution analysis, I assess the quality of the solution and its reproduceability by a number of inversions with different model parameters and different subsets of the traveltime data. These tests include minor variations of the initial velocity model, shifting of model nodes or a different but not much finer subsurface parameterisation, the use of different shots from shot groups, or the inclusion of all available traveltime data. Essentially, the resulting velocity structures resemble that of the final model presented in the following section 4.2.2. The use of all available traveltime data instead of selected shots from each shot group (see figures 3.3, 4.2), always leads to much smoother models and a higher data variance due to local heterogeneities near shot groups. As stated above, the use of more traveltime observations does not improve the final velocity model, if the corresponding ray paths are essentially the same.

In summary, the resolved regions of the model can be delineated from the spread function values and the checkerboard recovery test (figures 4.4 and 4.6, respectively). In the final *P* velocity model of the study area, I consider regions with spread values larger than $S_j = 3.0$ as unresolved. These regions are therefore clipped (grey-shaded) in all figure representations.
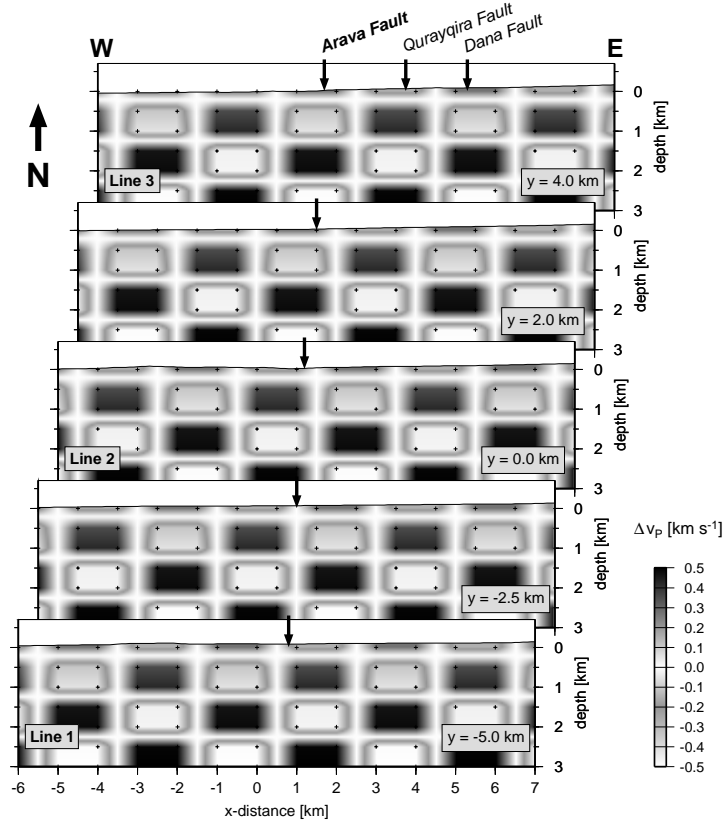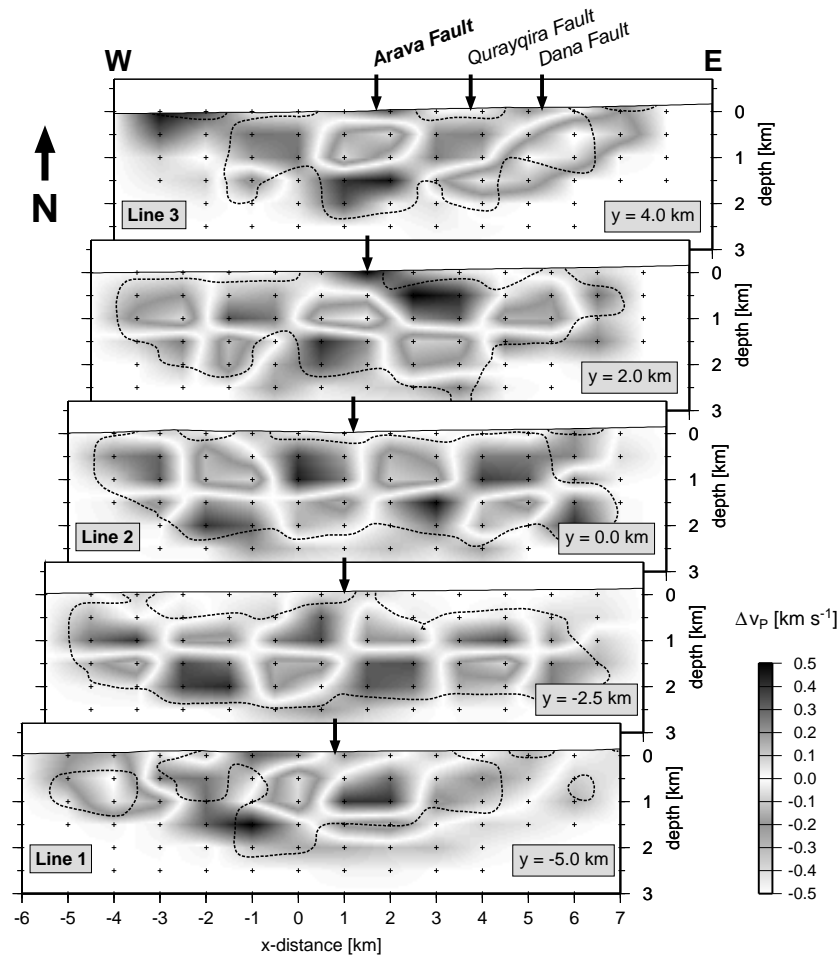
Figure 4.6: *Recovery of the anomaly pattern of a synthetic checkerboard test for the three-dimensional tomographic velocity model. The dashed contour line represents a resolvability of r = 0.7 (equation 4.10).*

4.2.2   Three-dimensional velocity structure

The tomographic inversion of picked first arrival traveltimes reveals the three-dimensional *P* velocity structure in the vicinity of the Arava Fault (AF). The modelled and resolved sub-surface volume extends over an area of up to 13×13 km and down to a maximum depth of about 3 km in the central part of this region. After seven iterations of the inversion algorithm, model adjustments are insignificantly. Therefore, this model constitutes the velocity structure presented below. Table 4.1 summarises the traveltime residuals (data misfit) after each iteration.

Figures 4.7 and 4.9 show the resolved velocity structure along vertical cross-sections roughly perpendicular to the trace of the AF and at horizontal depth slices (map views) through the model volume. Additional cross-sections are shown in figure 7.2, page 98, together with the
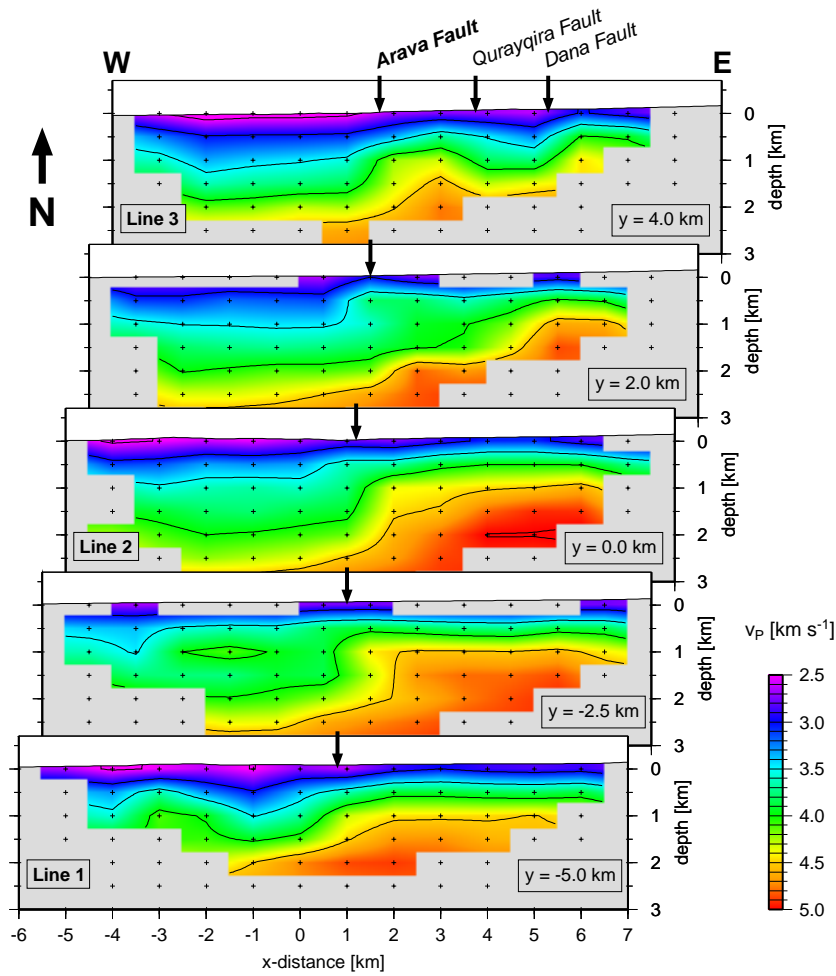
Figure 4.7: *Vertical, roughly E-W oriented cross-sections through the three-dimensional P velocity model around the AF. Model nodes are shown as crosses. Regions of spread values larger than 3 are considered as unresolved and are therefore grey-shaded.*

electrical resistivity structure. Model nodes are marked by small crosses, and the indicated surface traces of faults are adopted from the geological map in figure 2.2 (page 12). For comparison with line 1, figure 4.8 shows the central section of the higher resolved, two-dimensional *P* velocity model along the NVR reflection profile, which coincides roughly with line 1. This model has been determined by Ryberg *et al.* (2001) and is also included in a study of Ritter *et al.* (2003). High *P* velocities always appear in red and yellow, low velocities in violet and blue, and the contour interval is 0.5 km s^{-1}.

P velocities range from slightly less than 2.5 km s^{-1} at the surface in the northwest and west to about 5 km s^{-1} in the lower part of the model east of the AF. The most prominent feature of the velocity structure is a strong contrast across the AF with lower velocities west of the fault and higher velocities east of it. This contrast appears with some variations at all depths
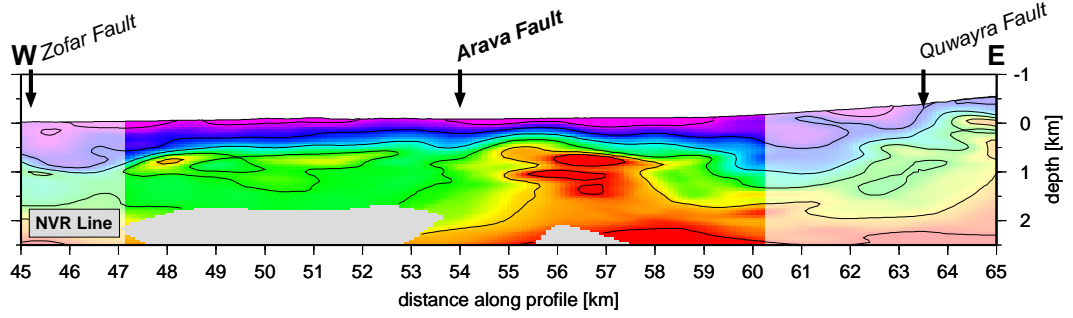
Figure 4.8: *Two-dimensional P velocity model along the NVR line (Ryberg et al., 2001; Ritter et al., 2003), shown here for comparison. Saturated colours indicate the range covered by line 1. Because of the denser shot and receiver spacing, this model is better resolved than the three-dimensional model of my study. The colour scale is the same as in figures 4.7 and 4.9.*

Iteration	1	2	3	4	5	6	7
$\sum(t^{obs} - t^{cal})^2$	119.779	81.917	55.463	38.867	30.434	27.341	26.536
RMS	0.163	0.135	0.111	0.093	0.082	0.078	0.076

Table 4.1: *Sum of squared traveltime residuals in seconds and RMS values for 4518 observations of the three-dimensional tomographic inversion ($RMS = \sqrt{N^{-1} \sum(t^{obs} - t^{cal})^2}$). Model adjustments are insignificantly after the seventh iteration, which thus constitutes the final P velocity structure.*

down to more than 2 km. At 1.5 km depth along line 2, the volocity increases from about 3.5 km s^{-1} to 4.5 km s^{-1}. Whereas this strong contrast appears to be rather smooth due to the cross-fault node spacing of 1 km (figure 4.7), the higher resolved tomographic image in the south of the study area shows a sharp boundary with a complex shape (figure 4.8).

West of the AF, the *P* velocity structure is rather homogeneous with only minor lateral variations (figures 4.7, 4.9). Considering a certain depth level, higher velocities generally occur in the southern region. There, also lense-shaped structures of higher velocities are visible at 1 km depth. These are not just small model artefacts, since they are clearly and reliably resolved along the high-resolution tomographic image (figure 4.8). The eastern side of the AF exhibits a complexer velocity structure. South of line 2 ($y \leq 0$ km) *P* velocities are constanly much higher than west of the AF, contributing to the general two-dimensional appearence of the velocity structure in the study area. Further to the north the model shows a graben-like zone of lower velocities with its centre about 2.5 km east of the AF. This zone leads into the low-velocity region west of the AF around $y = 2$ km (figure 4.9). A perspective view on surfaces of constant *P* velocity further illustrates the described variations of the velocity structure (figure 4.10). Again, the velocity contrast between west and east trends parallel to the trace of the AF, and the graben-like low-velocity zone separates a high-velocity block in the north from the high-velocity region in the southeast.
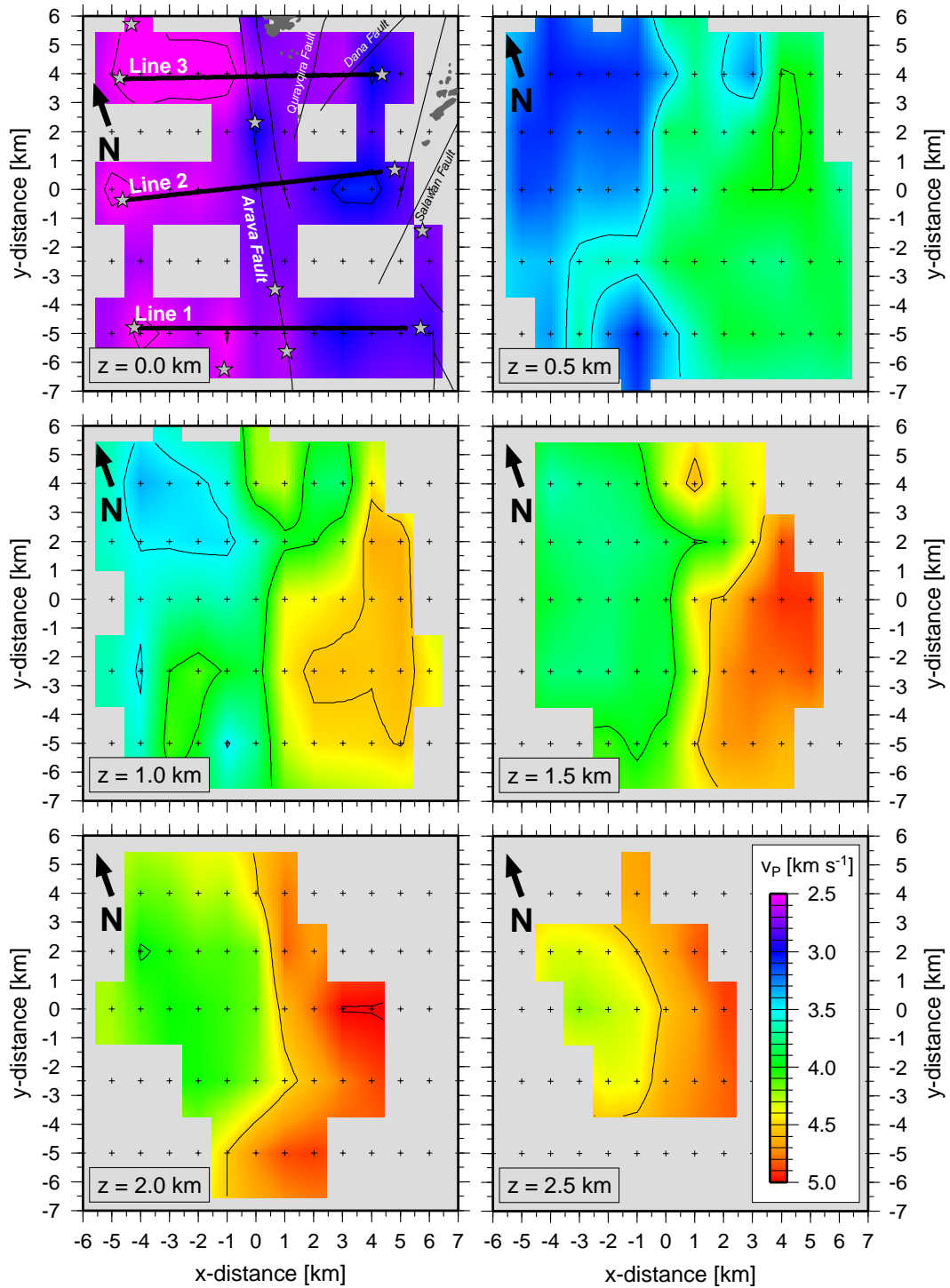
**Figure 4.9:** *Horizontal depth-slices (map views) through the three-dimensional P velocity model around the AF. Model nodes are shown as crosses. Regions of spread values larger than 3 are considered as unresolved and are therefore grey-shaded. The top-left panel shows P velocities at the surface and includes shots and receiver lines, faults (black lines), and outcrops of Precambrian granites (dark grey areas). For details see also the maps in figures 2.2 and 3.3.*
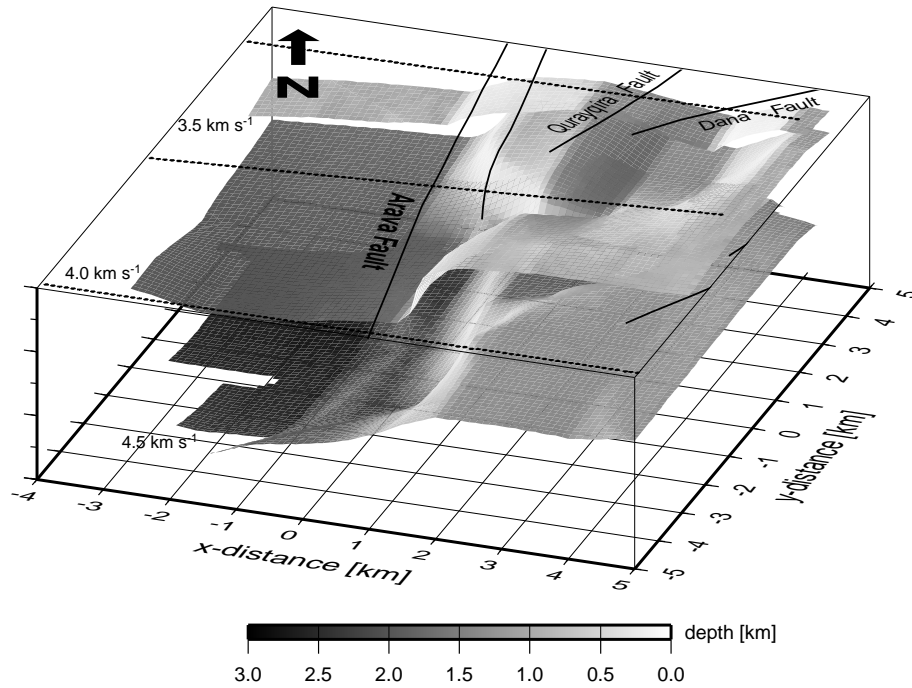
Figure 4.10: *Perspective view northwards on surfaces of constant P velocity. Whereas the surface of $v_p = 4.5 \; km \; s^{-1}$ is clipped only by the resolution limits, the surfaces of $v_p = 4.0$ and $v_p = 3.5 \; km \; s^{-1}$ commence at $y = -3$ and $y = 4 \; km \; s^{-1}$ to enable visibility of lower structures.*

The *P* velocity structure reflects the local geology in this region (section 2.2). The lower velocities west of the AF can be related to the sedimentary fill of the basin west of the fault. In addition, the slight decrease of velocities northwards fits to the observed dip of sedimentary layers towards the Dead Sea (see also figure 3.2, page 20). To the north, this dip leads to successively younger, less consolidated sediments at a certain depth, which are generally characterised by lower velocities. The higher velocities on the eastern side of the AF correspond to different kinds of Precambrian igneous rocks. Commensurate with mapped outcrops, these rocks are predominantely volcanites in the southeast and granites at the high-velocity block in the north (e.g. figure 4.10). The latter seems to reflect the subsurface continuation of the elongated mountain Jebel Hamrat Fidān north of the area covered by the velocity model (see figure 2.2, page 12). The graben-like low-velocity zone correlates with a sagged sedimentary block between the Qurayqira Fault and the Dana Fault (figure 2.3, page 14).

4.2.3 Velocity structure and gravity

The velocity of elastic waves in rocks is controlled primarily by the elastic properties of rock forming minerals, their fractional volume, their contact, cementation, pressure, and temper-

ature. Velocity values, determined in numerous laboratory studies, cover a broad range of values for each rock type. For igneous rocks, these variations are influenced by differences of the rock composition, effects of cracks and fractures, anisotropic effects, temperature and pressure. Additional dominant parameters for sedimentary rocks are the mineralogical composition of the rock matrix, consolidation and cementation of the matrix, as well as porosity, pore shape, and pore content. Schön (1996) reviews these petrophysical effects, lists seismic velocities for different types of rocks, and provides numerous references.

Many authors have developed empirical relations to describe the correlation between the *P* wave velocity v_p and the rock density ρ (e.g. Birch, 1961; Ludwig *et al.*, 1970). Birch (1961) elaborated the linear relation $v_p = a + b\rho$ with the two empirical parameters a and b. A precise conversion of seismic velocities into densities is not possible with such an empirical relation, because the underlying data scatter considerably and laboratory measurements do not cover all combinations of the petrophysical effects named above. However, a linear relation is a good approximation in certain density intervals. Therefore, a velocity-density relation provides an estimate of the subsurface density distribution and thus the gravity effect to be expected at the surface from a two- or three-dimensional velocity model (e.g. Eberhart-Phillips, 1986; Lees and VanDecar, 1991; Graeber, 1997). Calculated gravity anomalies are commonly compared with measured Bouguer anomalies. The Bouguer gravity anomaly is the gravity value obtained from the measured field after latitude, elevation (free-air), and possibly terrain corrections, and the correction for the attraction of masses (Bouguer correction) between the observational location and the reference datum (e.g. Telford *et al.*, 1990; Sheriff, 1991)

A velocity model like that of the study area usually has a limited extent and a finite subsurface parameterisation. Consequently, only some portions of a measured gravity field can be reproduced from the velocity model. Large-scale portions of the gravity field may originate outside the velocity model and poorly resolved regions may cause incorrect calculated gravity values. Small-scale variations of the gravity field are reproducable in principle, if they cover at least the model node spacing and if the corresponding nodes are well resolved. Hence, for a local comparison of calculated and measured gravity anomaly fields, large-scale, regional portions of the measured field have to be eliminated, e.g. by subtraction of the arithmetic mean or a higher-order regional trend in the study area. Furthermore, poorly resolved regions in the velocity model should be down-weighted or excluded from the gravity calculation.

To calculate gravity anomalies from the three-dimensional *P* velocity model (section 4.2.2), I divide the model volume into N blocks with an edge length of 100 m in all directions (Δx, Δy, Δz). Like Graeber (1997) I apply a simple linear relation, adopted from Ludwig *et al.* (1970), between density variations $\Delta\rho$ and velocity perturbations Δv_p relative to a laterally homogeneous background model. Therewith it is straightforward to calculate the vertical component of the residual gravity value Δg_j^z at the model surface as the sum over all blocks:

$$\Delta g_j^z = \gamma \sum_{i=1}^{N} \Delta\rho_i z_i \frac{\Delta x \Delta y \Delta z}{D_{ij}} \qquad (4.11)$$
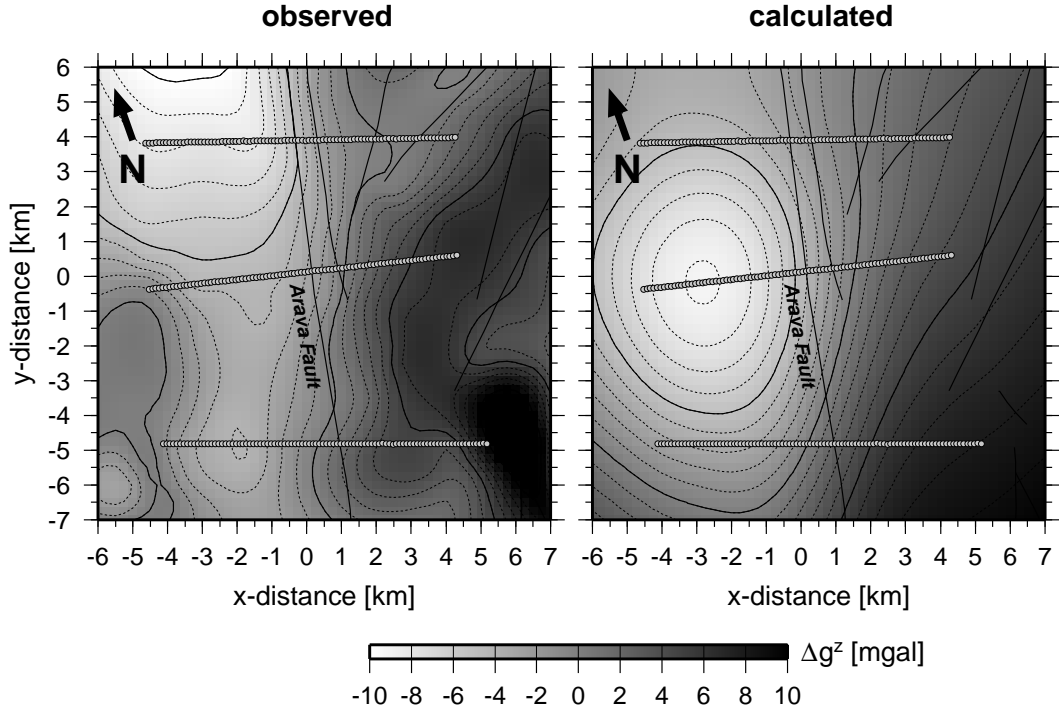
Figure 4.11: *Observed and calculated residual gravity anomalies after subtraction of the arithmetic mean in the area shown. The interval of dashed and solid contour lines in 1 mgal and 5 mgal, respectively.* Left: *Observed residual gravity anomalies extracted from a Bouguer anomaly map of the Dead Sea Transform (ten Brink* et al.*, 2001).* Right: *Residual gravity anomalies calculated from the three-dimensional P velocity model (section 4.2.2).*

with $\Delta\rho = 0.1667\Delta v_p$ for $v_p \leq 6$ km s^{-1}. The velocity perturbation Δv_p is in km s^{-1}, if the density variation $\Delta\rho$ is given in 10^3 kg m^{-3} (equal to g cm^{-3}). Furthermore, γ denotes the gravitational constant[3], z_i the depth of the *i*th block centre, and D_{ij} the distance from this point to the *j*th surface location, where Δg_j^z is calculated. The summation includes resolved regions of the velocity model with a spread function value of $S_j \leq 3$ (section 4.2.1), and the surface sampling of Δg_j^z is 250 m in both directions.

Figure 4.11 compares observed and calculated residual gravity anomalies after subtraction of the arithmetic mean in the area shown. The observed field is an extract of a regional Bouguer anomaly map of the DST (ten Brink *et al.*, 2001). The comparison of observed and calculated anomalies reveals an overall similarity but also small-scale deviations. Residual gravity values vary by some ±10 mgal (equal to 10^{-5} m s^{-2}), and the calculation reproduces the dominant trend from low values in the west to higher values in the east and southeast. In both images, the transition from negative to positive values across the Arava Fault (AF) and adjacent faults is smoother in the northern part. This reflects the lower average density of the sedimentary blocks in the northeastern region than that of the volcanites further south.

---

[3] $\gamma = 6.672 \pm 3 \cdot 10^{-11}$ m^{3}kg^{-1}s^{-2}

The calculated gravity field shows a basin-like negative anomaly. Its shape is caused by the limited extent of the model and poorer resolution outside the receiver spread. Contrarily, a pronounced negative anomaly occurs at the northwestern edge of the observed field. This is the southern tip of an elongated anomaly that stretches towards the Dead Sea basin with successively lower gravity values and reflects the increasing thickness of the sedimentary fill in the Arava Valley (ten Brink *et al.*, 2001; Hassouneh, 2003). However, the calculated negative anomaly is wider in the north, and the 0 mgal contour resembles a trend comparable with the observations.

In summary, the gravity anomalies calculated from the three-dimensional *P* velocity model resemble general trends of the observed field. This fact is an independent corroboration of the modelled velocity contrast at the AF and along-strike variations thereof. The density distribution derived from the seismic velocity structure provides initial constraints for a detailed density modelling in this area. The detailed local gravity survey of Götze *et al.* (2002) covers this study area with a station spacing between 50 m and 300 m, and first results fit well to the velocity model of this study.

4.3 Two-dimensional tomography across the Arava Fault

Eight seismic profiles of 1 km length crossed the Arava Fault (AF) perpendicular (CSA II experiment; figure 3.3, page 21). The shallow *P* velocity structure along these profiles, determined by seismic tomography, aims to delineate the trace of the AF more precisely, to map the pressure ridge at a segment of the fault (section 2.2.1), and to image a vertical low-velocity zone required by observed fault-zone guided waves (see Haberland *et al.*, 2003b). Furthermore, the acquired dataset provides seismic reflection sections across the fault (section 5.4). Each profile consists of 200 vertical-component geophone strings with a spacing of 5 m and up to 50 shots spaced approximately every 20 m along the line. Each shot is recorded along the entire receiver spread of one line (section 3.2). The spacing between profiles is 1 km in the northern part (lines 5–10) and about 2 km in the south (lines 1–5). Lines 1, 6, and 10 concide with the central segments of the longer lines 1, 2, and 3 of the three-dimensional study, respectively (section 4.2 and figure 3.3).

With very few exceptions, *P* wave first arrivals are clearly visible at all offsets along each line. Therefore, up to 10000 manually picked traveltime readings form the database for the two-dimensional tomographic inversion for the *P* velocity structure along a certain line (section 4.1). To invert these traveltimes, I applied a slightly modified version of the tomography code `FAST` developed by Zelt (1998a) and introduced further in section A.1 (see also Zelt and Barton, 1998). The modification of the code affected only the data input and output routines to allow for the densely spaced acquisition geometry. The program `simulps12`, used for the three-dimensional inversion, does not support such a small-scale geometry.

The subsurface parameterisation and model parameters are the same for all eight profiles. The initial *P* velocity model is laterally homogeneous and defined by a constant velocity

gradient from -0.1 km depth (0.1 km above sea level) to 0.5 km depth. The corresponding
P velocities are 0.8 km s^{-1} and 7.0 km s^{-1}, respectively. A value of $v_p = 7.0$ km s^{-1} at
0.5 km depth is not a realistic assumption in the study area. But this strong velocity increase
with depth ensures that rays of the first iteration penetrate deeply into the subsurface and thus
sample a larger region of the model compared to an inversion with initially lower velocities at
the model bottom. This approach with a strong gradient is justified here because of the large
number of rays involved in this investigation and their good spatial coverage. To validate this
statement, I also tested different initial velocity models. Traveltimes are calculated by finite-
differencing (Vidale, 1988) on a grid with a node spacing of 5 m in horizontal and vertical
directions, and ray paths are determined from the subsurface traveltime field. For the damped
least-squares inversion I defined blocks with an edge length of 10 m in both directions. The
models are larger than the presented cross-sections to avoid that rays hit model boundaries.
Each model extends from -0.1 km to 1.1 km in horizontal and from -0.1 km to 0.5 km in
vertical direction. This model parameterisation is the result of several inversion tests run
prior to the final inversion.

The search for an optimum damping parameter β (section 4.1) is implemented in the FAST
inversion algorithm and follows the approach described in section 4.2 for the larger-scale
three-dimensional tomography (Eberhart-Phillips, 1986).[4] Starting from a rather large initial
β, this value is reduced here by a factor of $\sqrt{2}$ several times during preliminary inversions.
For each iteration, the algorithm selects the β value that reduces the data misfit most within
the limits set for model smoothness. Thus, the damping is adjusted for each iteration step,
in contrast to the constant β used for the larger-scale tomographic inversion (section 4.2). In
this study, the initial damping parameter is $\beta = 200$, and the number of preliminary iterations
for each iteration step is limited to 6.

4.3.1   Solution convergence and resolution

At all of the eight profiles the inversion converges rapidly to the final solution of the subsur-
face velocity structure. Dominant features of the final model appear already after the first
iteration. Figure 4.12 shows the evolution of the model at line 9 during four iterations from
the initial laterally homogeneous model to the final solution. Additionally, this figure in-
cludes ray distributions associated with the velocity structure and acquisition geometry. The
ray distribution is represented by ray hit counts for each model grid node. The initial model
(iteration 0) leads to a laterally homogeneous ray coverage in its central part with minor
variations due to geometric effects, i.e. the influence of topography and the distribution of
sources and receivers. The initial model changes to a rather complex velocity structure after
the first iteration. This structure confines the majority of rays to the upper 0.1–0.2 km below
the surface. Iterations after the second step modify some distinct regions of the model, but
they do not change the general appearance of the velocity structure. Ray paths are predomi-
nantly subhorizontal and successively concentrate on regions with a strong vertical velocity

---

[4] Zelt (1998a) refers to the damping parameter β as lambda.
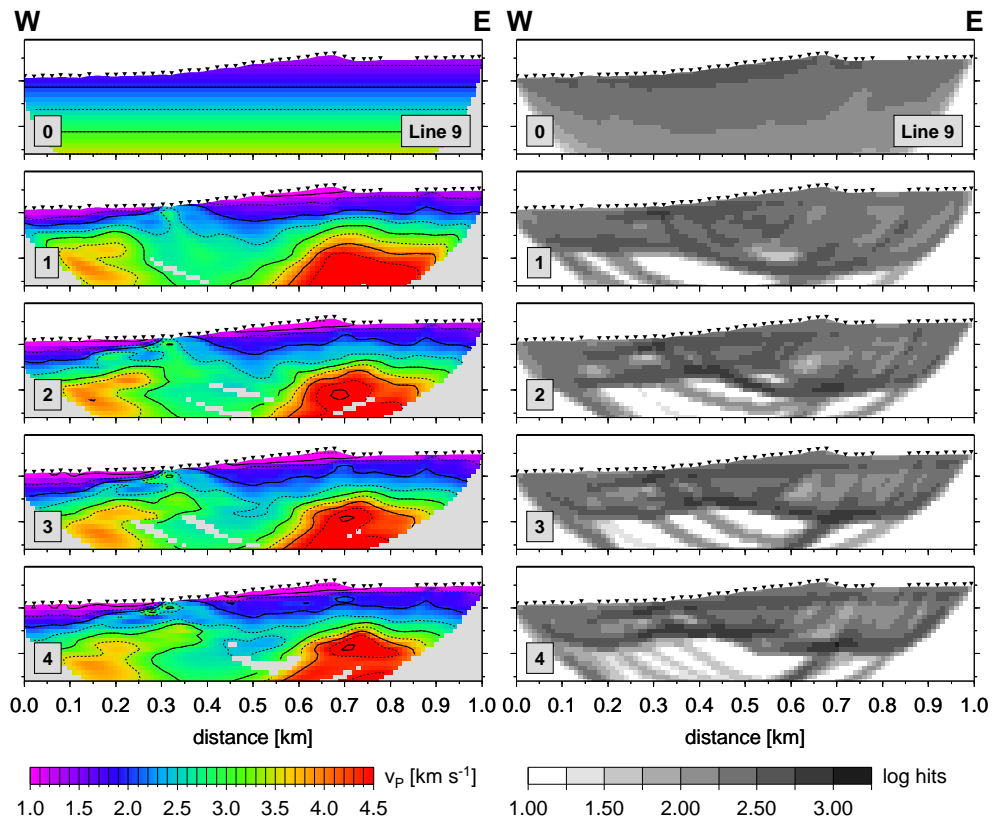
Figure 4.12: *Tomographic inversion results* (left) *and associated ray distribution* (right) *after each iteration step for line 9. The iteration numbers are given in each panel, and the top panel shows the initial, laterally homogeneous P velocity model. The ray distribution is represented by ray hit counts for each grid node. Triangles indicate the shot locations.*

gradient. Possibly, some of these regions comprise true layer boundaries, e.g. just beneath the hill (sand dune) between 0.4 km and 0.7 km model distance. The observed ray pattern is rather typical for near-surface seismic investigations (e.g. Lanz *et al.*, 1998). During the successive model adjustment from one iteration to the next, the concentration of rays favours these regions compared to the remain, where the model is not improved further, significantly.

The evolution of a velocity model during several iterations is also demonstrated by the successive decrease of the (squared) sum of traveltime residuals. Table 4.2 summarises the decrease of RMS traveltime residuals of all eight models. Additionally, the table lists the automatically determined damping values β and the total number of rays involved in the inversions. As expected from the sequence of models shown in figure 4.12, the traveltime residuals decrease most during the first iteration steps. Since modelled velocity structures and traveltime residuals remain almost stable during the last two iterations listed, the models of the fourth iteration contain the relevant subsurface structures and constitute the final *P* velocity structure discussed in the following section 4.3.2.

Iteration	1		2		3		4		1–4
Line	rms	β	rms	β	rms	β	rms	β	N rays
1	40.88	141.42	10.10	141.42	7.00	141.42	6.09	100.00	9760
3	37.52	141.42	8.17	35.36	5.96	35.36	4.39	35.36	9543
5	19.82	200.00	10.69	50.00	7.41	35.36	5.42	35.36	9059
6	21.53	200.00	7.01	70.71	5.46	25.00	4.66	17.68	8410
7	15.99	70.71	7.84	25.00	5.36	25.00	4.58	25.00	8511
8	21.64	35.36	9.26	25.00	6.18	25.00	5.60	25.00	8133
9	20.50	35.36	9.59	25.00	6.27	25.00	5.16	25.00	8657
10	31.92	200.00	12.82	50.00	8.93	50.00	7.92	50.00	8018

Table 4.2: *RMS traveltime residuals in milliseconds for each iteration of the two-dimensional tomographic inversion along the eight CSA II profiles. The residuals are determined by the FAST algorithm (Zelt, 1998a; Zelt and Barton, 1998) for N rays traced successfully. Additionally, damping values β are listed.*

The FAST implementation of the tomographic inversion does not include the computation of the full model resolution matrix (see section 4.1.2). Therefore, the resolution cannot be assessed by means of the spread function S_j of Michelini and McEvilly (1991). Instead of S_j sections for the eight profiles, I analyse ray hit counts like in figure 4.12 and several checkerboard recovery tests as introduced in sections 4.1.2 and 4.2.1.

Figure 4.13 shows the ray hit counts for the model grid nodes of all eight profiles after the final (fourth) iteration. Different shades of grey correspond to different hit count intervals on a logarithmic scale. Darker regions indicate a higher ray coverage. The maximum logarithmic number of rays that hit a certain grid node reaches more than 3, i.e. 1000 rays, but generally the logarithmic hit count values are in the range of 2 to 3 in the upper 0.05–0.1 km below the surface. Because of the high sampling with rays from different source and receiver locations, good resolution can be expected in this depth range. As noticed above, ray paths tend to concentrate at regions with a strong vertical velocity gradient. Strong gradients occur at the base of the near-surface weathering layer (e.g. Cox, 1999) or at the base of sand dunes. An example are the dunes at the eastern ends of lines 5 and 8, and the dune at line 9 (see also section 4.3.2 and figure 4.16). The concentration of rays and subhorizontal ray paths due to layer boundaries limit the resolution for near-vertical, small-scale velocity variations. This is a general limitation of pure surface-based tomographic investigations in such study areas.

For synthetic checkerboard recovery tests as introduced in sections 4.1.2 and 4.2.1, anomaly patterns of different shape and scale are superimposed on the smooth velocity structure obtained after the first iteration. Figure 4.14 shows some of these input patterns (left) and the recovered structure (right) along line 9. The checkerboard patterns in panels A–C consist of squares with an edge length between 40 m and 80 m, and the patterns in panels D–G are horizontally oriented rectangles with an aspect ratio of 2. Their horizontal extent decreases from 100 m in panel D to 40 m in panel G. Anomalies in panel H extend over 40 m in horizontal and 80 m in vertical direction.
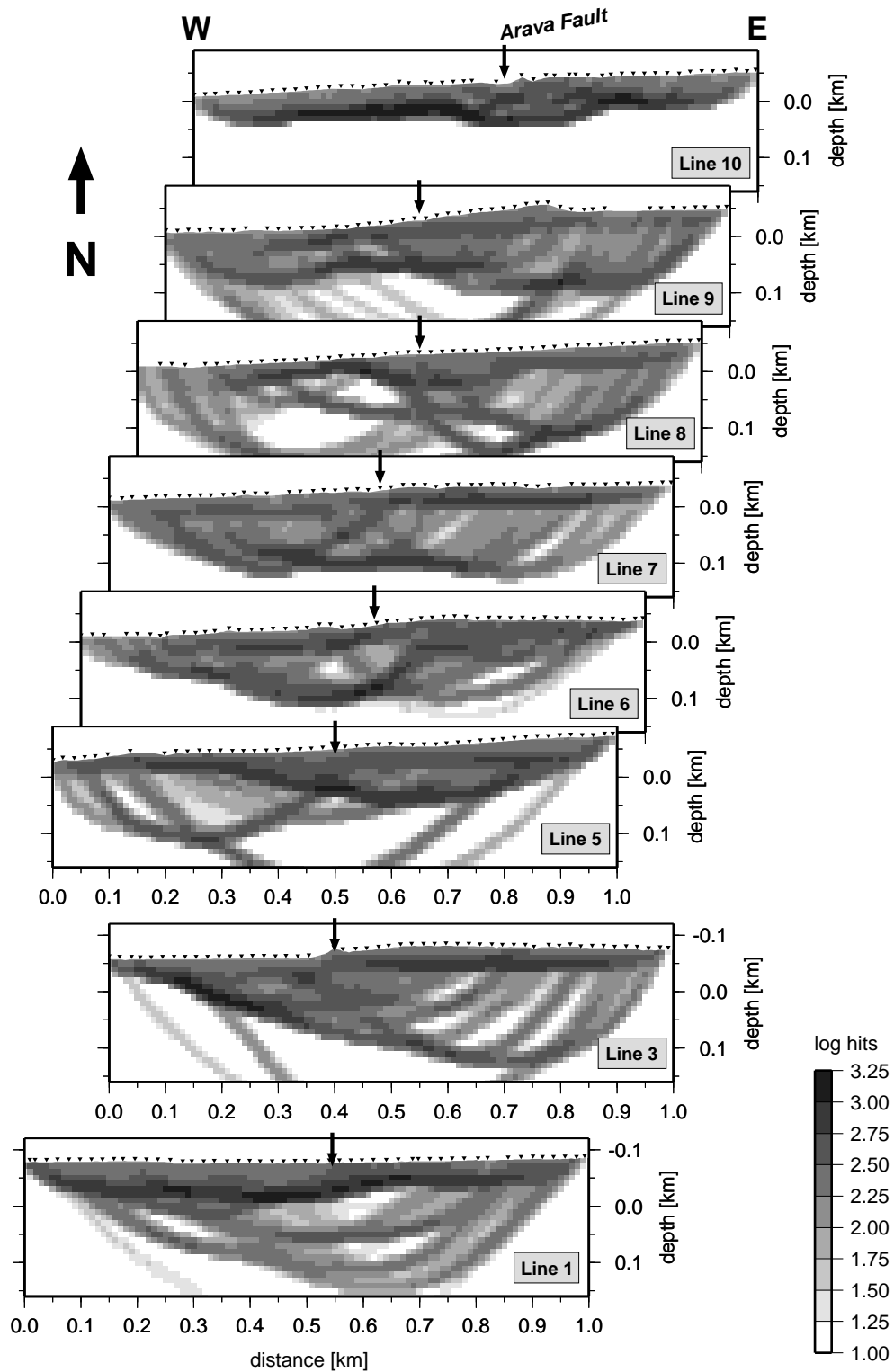
Figure 4.13: *Ray hit counts of the shallow P velocity structure along eight profiles across the Arava Fault. Dark regions indicate a large number of rays (logarithmic scale). Triangles indicate the shot locations and outline the local topography.*

The inversion of synthetic traveltimes, calculated from the checkerboard models (figure 4.14, left), reveals the resolvability of structures with scales and shapes comparable to the input structure. Acquisition geometry and inversion parameters are the same as in the real experiment, and the variable background velocity model ensures that rays follow similar paths as in reality. Generally, the input anomaly patterns are well resolved in the central parts of the models down to depths of up to 100 m below the surface (figure 4.14, right). This is obvious from a visual inspection of the recovered models and quantified by the resolvability measure introduced in section 4.1.2 (Zelt, 1998b). The dashed line in figure 4.14 corresponds to a resolvability of 0.7, always calculated with a correlation length equal to the scale of corresponding anomalies.

Size and shape of checkerboard anomalies affect the maximum depth of good resolution. Large-scale anomalies are recovered down to a greater depth than smaller ones. Furthermore, the resolution of elongated, horizontally oriented anomalies is better than the resolution of squared structures with an edge length equal to the shorter edge of the rectangles. This effect can be explained by the predominantly subhorizontal ray paths in many regions of the models (line 9 in figures 4.12 and 4.13). A checkerboard pattern of rectangular, vertically oriented anomalies leads to an exceptionally poor resolution (panel H in figure 4.14). Again, this is due to predominantly subhorizontal ray paths. Poorer resolution also characterises the western and eastern ends of the models, where the number of crossing rays is lower than in the central parts of the models.

Checkerboard tests as those discussed for line 9 yield comparable results for the other seven lines of this study. Figure 4.15 shows the recovery of the anomaly patterns B and G for all lines across the Arava Fault. Again, larger structures are resolved down to a greater depth than the smaller ones, and the maximum depth of well resolved regions extends to about 100 m below the surface. At line 10, almost the entire depth range covered by rays in the final iteration exhibits a good resolution (see also figure 4.13).

In summary, four iterations of the inversion procedure are sufficiant to reconstruct the subsurface velocity structure from first arrival traveltimes. The ray coverage of this study is generally good down to about 100 m below the surface and enables the inversion for a reliable velocity model. Several checkerboard tests for all eight lines demonstrate a good resolution of velocity perturbations with scales as small as 40 m in horizontal and just 20 m in vertical direction. In most regions, larger structures are resolvable down to 100 m depth below the surface.
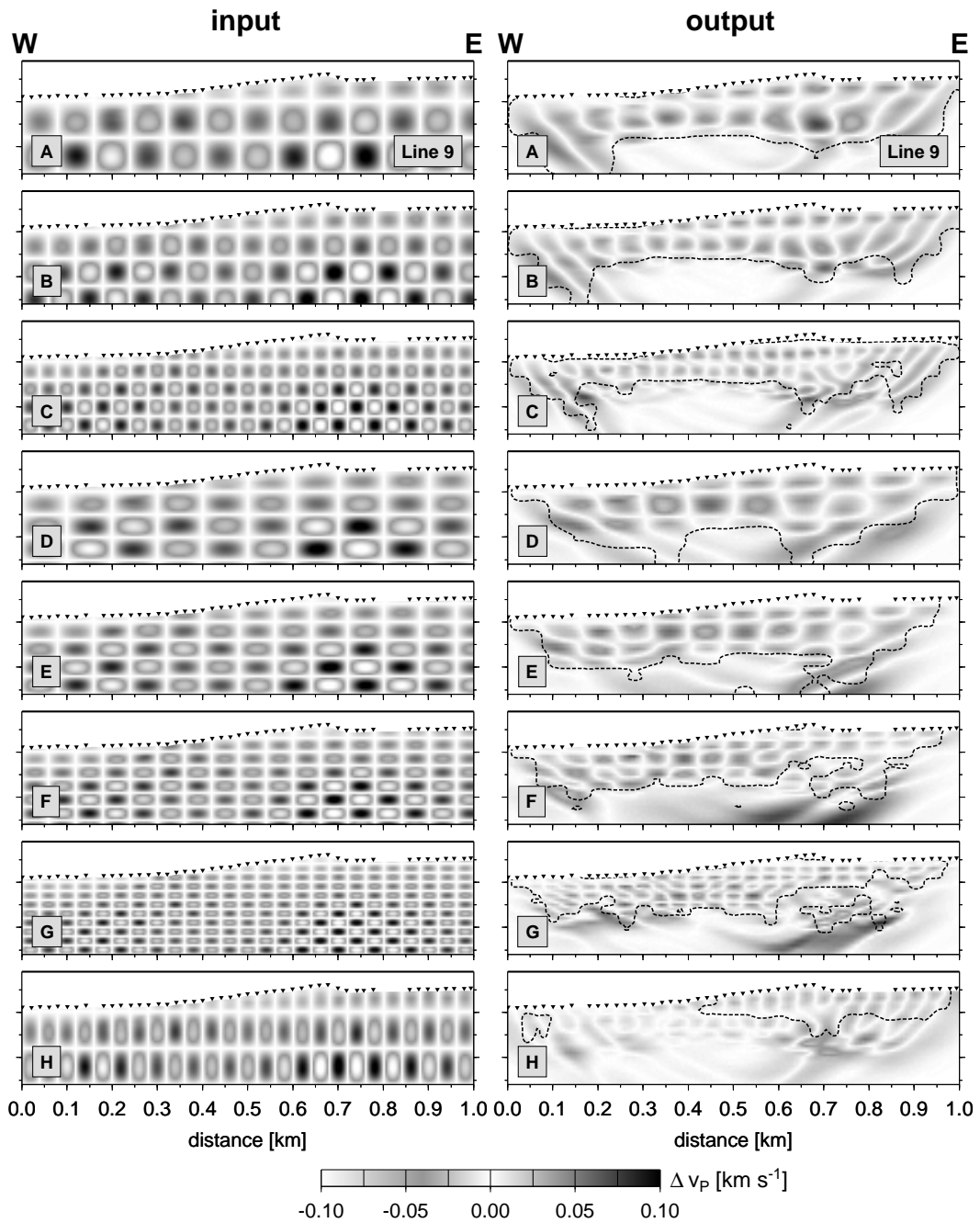
Figure 4.14: *Synthetic checkerboard recovery tests for the two-dimensional tomography along line 9.* Left: *Anomaly patterns of different shape and scale are superimposed on the smooth velocity structure obtained after the first iteration (see figure 4.12).* Right: *Recovered patterns. The dashed contour line represents a resolvability of $r = 0.7$ (equation 4.10), and triangles indicate the shot locations and outline the local topography.*
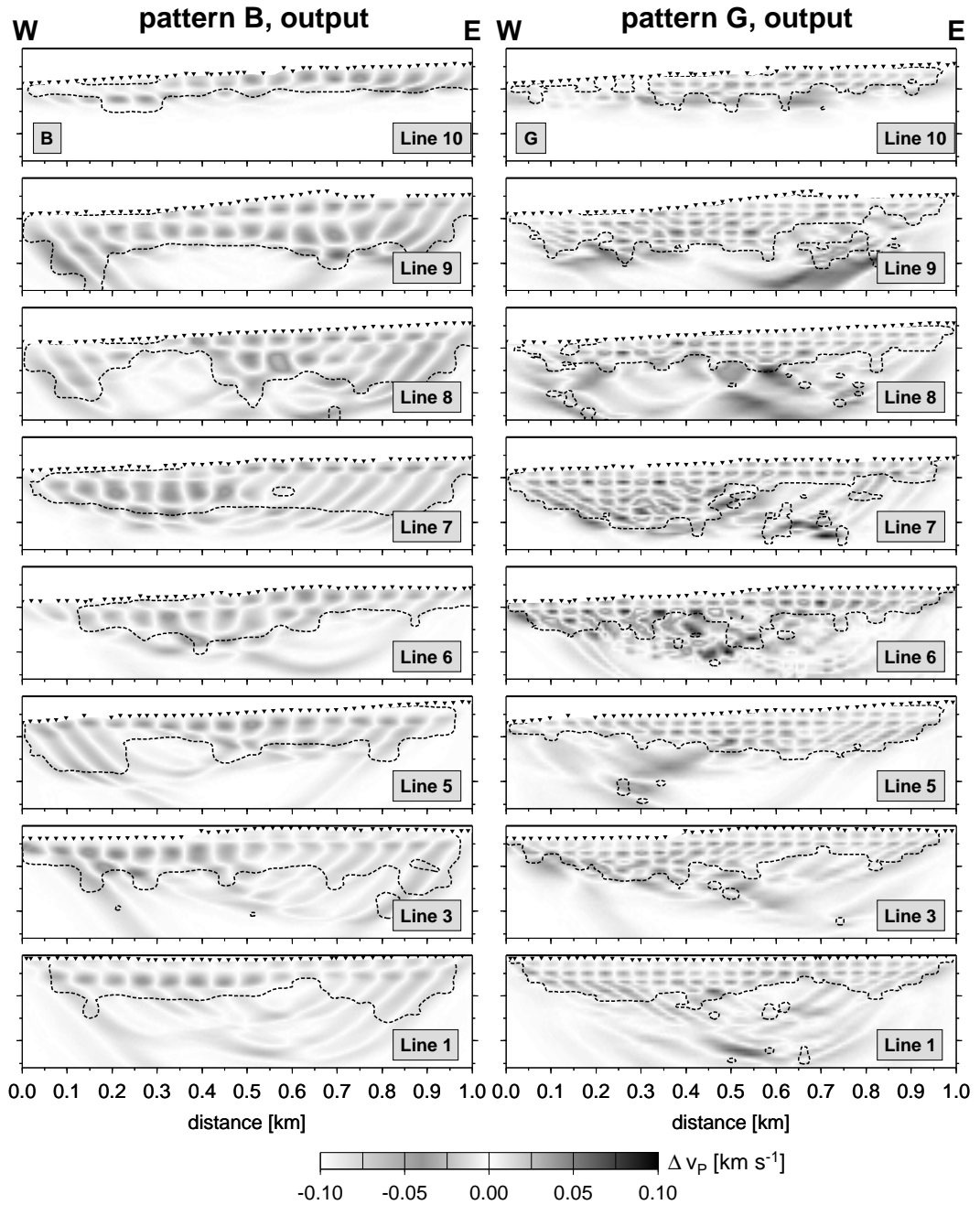
Figure 4.15: *Synthetic checkerboard recovery tests for the two-dimensional tomography along all lines across the Arava Fault. Two different anomaly patterns are superimposed on the smooth velocity structure obtained after the first iteration. The anomaly patterns, indicated by B (left) and G (right), are included in figure 4.14. The dashed contour line represents a resolvability of $r = 0.7$ (equation 4.10), and triangles indicate the shot locations and outline the local topography.*

4.3.2   Shallow velocity structure across the Arava Fault

The two-dimensional tomographic inversion of picked first arrival traveltimes reveals the *P* velocity structure along the eight profiles across the Arava Fault (AF). The resolved subsurface sections extend along the 1 km long geophone spreads of each line and reach maximum depths of about 0.1 km below the surface. Figure 4.16 shows the *P* velocity structure obtained after the final iteration. The distances between sections are 1 km from line 5 northwards and 2 km in the south. Their exact locations are included in figure 3.3 on page 21, and the indicated surface trace of the AF is inferred from geological observations.

In the shallow subsurface, *P* velocities range from less than 1 km s^{-1} at the surface to avarage velocities of 2.5–3 km s^{-1} around 50 m below the surface. Higher velocities between 3.5 km s^{-1} and 4.5 km s^{-1} occur in some regions of the models. Whereas the upper 10–20 m exhibit rather uniform *P* velocities, the deeper structure follows a general trend from simple in the south to more complex in the north. Along many lines, the subsurface in the upper 100 m is characterised by lower velocities east of the AF trace (arrows in figure 4.16). Lower velocities in the east are the opposite of the deeper structure, where these are found west of the AF (section 4.2.2). A pronounced velocity contrast correlating with the AF appears at line 1 at depths greater than some 30 m. The region of lower velocities smaller than 2.5 km s^{-1} extends to the greatest depth of about 150 m. To the north, the thickness of this low-velocity zone decreases, and the contrast near the AF is often less pronounced. Contrary to the laterally almost homogeneous structure in the upper 50–100 m along the eastern sections of a certain profile, the velocities west of the AF feature a patchy pattern, especially at lines 8 and 9. There, *P* velocities of more than 3 km s^{-1} occur at the surface, just west of the AF.

A dominant feature of the northern profiles (lines 6–10) are blocks with *P* velocities higher than 4 km s^{-1}. Except for line 10, these blocks occur at depth greater than about 100 m below the surface. Reminding the discussion in section 4.3.1, this means that the exact shape of these blocks is poorly resolved, but the essentially high velocities in these regions are required to fit the observed traveltime data. High-velocitiy blocks occur west of the AF at lines 6 and 7, whereas such blocks are confined predominantly to the eastern side further north (lines 8 and 9). Along line 10, three rather small but well-resolved blocks of high velocities are found on both sides of the fault, directly beneath the shallow, laterally least-variable portion of the model (upper 20 m).

Regions of certain seismic *P* velocities can be related to certain geological units that are partly observed at the surface. Aeolian and fluviatile sands, and other superficial deposits are characterised by velocities lower than 1 km s^{-1}. Accumulations of aeolian sands with thicknesses of at least 10 m are found at the eastern ends of lines 5 and 8, and at a prominent sand dune in the central part of line 9. The elevation of this dune exceeds the surrounding area by about 20 m, and *P* velocities decrease to 0.5 km s^{-1} at its top. Aeolian sands also occur in the eastern section of line 3 and in the western section of line 10. The low velocities at the surface along line 1 correspond to fluviatile sands, especially west of the indicated AF surface trace (figure 4.16; see also figure 2.2, page 12).
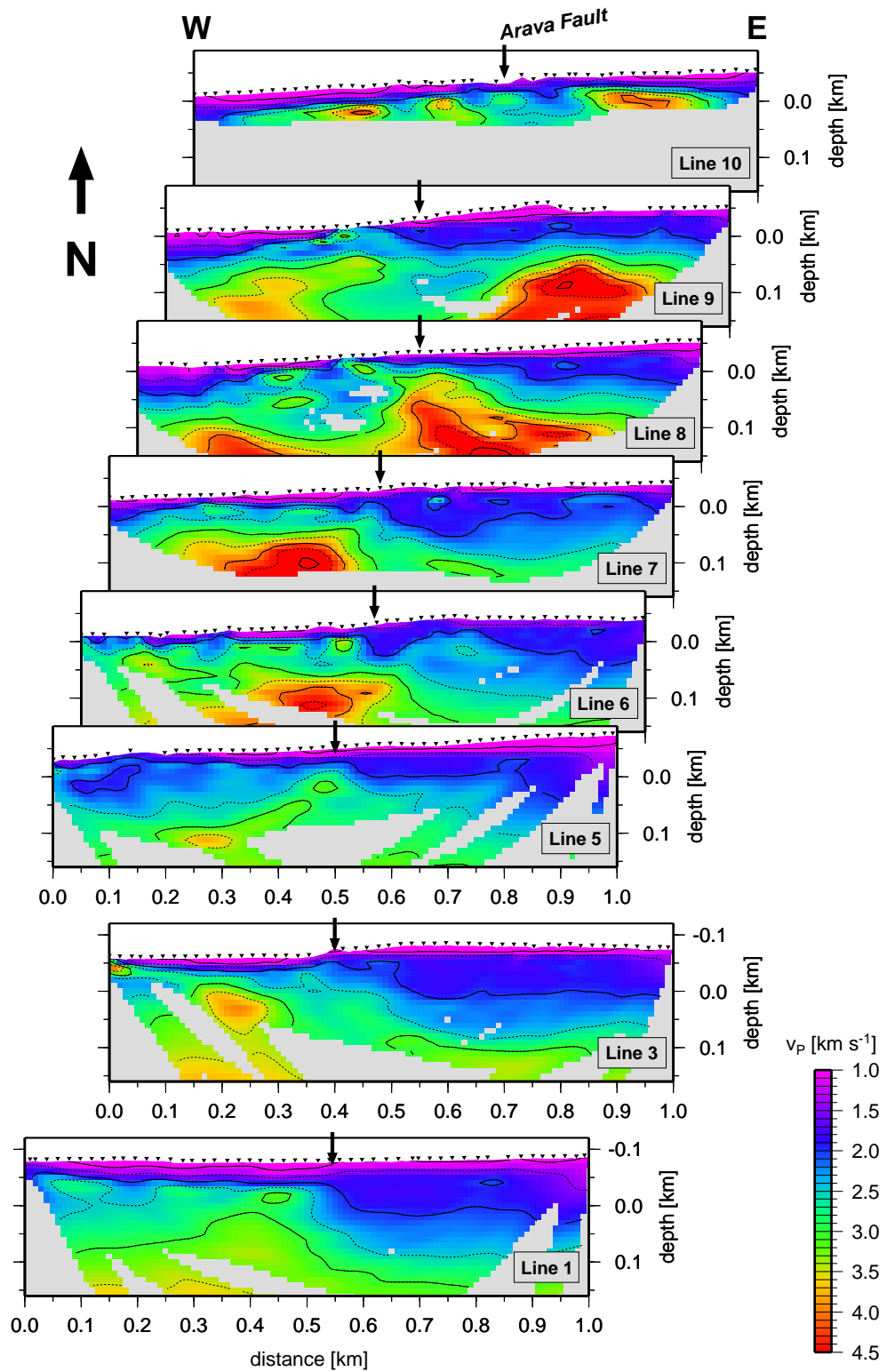
Figure 4.16: *Shallow P velocity structure along eight profiles across the Arava Fault. Only regions penetrated by rays during the final iteration are shown. Triangles indicate shot locations and arrows the surface trace of the Arava Fault inferred from geological observations.*

A pressure ridge, consisting of limestones and located in the northern part of the study area (section 2.2.1), appears as patchy regions of velocities up to 3.5 km s^{-1}. These regions are west of the indicated AF surface trace, mainly at lines 8 and 9 (figure 4.16), but the two lines further south exhibit a rather complex velocity structure in the west, too. The southernmost (small) outcrop of limestones, possibly related to this pressure ridge, is located in the centre of line 6.

Since zones of velocities higher than 4 km s^{-1} occur only in the north of the study area, these zones are probably related to Precambrian granites of Jebel Hamrat Fidān, which are found in small, isolated outcrops east of lines 8–10 (figure 2.2). High-velocity zones occur west of the AF at lines 6 and 7, whereas such zones are predominantly imaged on the eastern side at lines 8 and 9. Assuming that the high-velocity zones between lines 6 and 9 once formed a single unit, this observation would document a left-lateral movement along the AF surface trace of some 2 km. However, except for line 10, boundaries and shape of the high-velocity zones are poorly resolved (section 4.3.1). For a more precise estimation of the slip, the boundaries of these zones should be known as well as their deeper extent.

Fault-zone guided waves have been observed at the surface trace of the AF between lines 6 and 10. These waves are propagated in a low-velocity zone embedded in two regions of higher velocities. To determine the width of the low-velocity waveguide, Haberland *et al.* (2003b) modelled waves that were guided along the AF between lines 8 and 6. The modelled width of just 3–12 m is too small to be resolved by this tomographic study (section 4.3.1). On the other hand, this study confirms that the low-velocity waveguide must be very narrow down to 100 m below the surface.

The trace of the AF as inferred geologically correlates well with subsurface velocity variations along most of the sections (figure 4.16). Between the southernmost lines 1 and 3, the AF trace coincides with the eastern slope of Wadi Qunai at the surface and with a sharp velocity contrast at depth. Further north, a pronounced velocity contrast at the fault location is visible at lines 6 and 7, whereas the remaining sections show a different velocity structure. At line 5, a roughly triangular zone of higher velocities than in surrounding regions correlates with the mapped AF trace. Following this trace from south to north, this high-velocity zone may be the first expression of the pressure ridge that reaches the surface further north. The rather complex velocity structure along lines 6–10 complicates the subsurface delineation of the AF. Whereas its mapped surface trace fits reasonably to subsurface velocity contrasts, the velocity structure along lines 8 and 9 suggests that the AF is located some 50 m west of the mapped trace. However, the AF seems to be split into several, closely spaced branches in this region of the study area. The blocky velocity structure imaged along line 10 supports this assumption. There, branches of the AF are possibly located between 0.3 km and 0.7 km along the profile.

5. Secondary arrivals

Secondary arrivals are those seismic phases that arrive after the first P onset. These phases include shear waves (S waves), reflected waves, guided waves, and scattered seismic energy. After a brief introduction to signal enhancement methods, this chapter begins with the processing and identification of shear wave arrivals, which leads to an estimate of the v_p/v_s ratio and its lateral variation in the study area. The following sections comprise fault-reflected waves and reflection profiles across the Arava Fault. Fault-zone guided waves in the study area are analysed separately by Haberland *et al.* (2003b), and scattered seismic energy is discussed in chapter 6.

5.1 Signal enhancement methods

Whereas P waves are clearly visible in raw or bandpass-filtered CSA shot records, later, secondary arrivals require further processing to be identified. To enhance these arrivals, vector properties of the wavefield can be utilised in case of three-component recordings. A common approach for multichannel (array) data is the correction for different arrival times of a certain phase along the receiver spread (moveout correction, beamforming), followed by a stack of the individual traces.

5.1.1 Three-component processing

The superposition of three monofrequent oscillations that are orthogonal to each other leads to the formation of a polarisation ellipsoid. Its orientation in space depends on phase differences between the oscillations. Seismic signals are not monofrequent but characterised by a frequency band. Therefore, during the transit of a seismic wave, subsurface particles follow a complex trajectory, the hodograph, instead of a simple ellipsoid. For a time window of N samples, this hodograph can be fit to an ellipsoid in a least-squares sense by means of a covariance analysis (Cliet and Dubesset, 1988). The three eigenvectors $\mathbf{V_i}$ of the covariance matrix

$$\underline{\underline{\mathbf{M}}} = \begin{pmatrix} \text{cov}(f^x, f^x) & \text{cov}(f^x, f^y) & \text{cov}(f^x, f^z) \\ \text{cov}(f^y, f^x) & \text{cov}(f^y, f^y) & \text{cov}(f^y, f^z) \\ \text{cov}(f^z, f^x) & \text{cov}(f^z, f^y) & \text{cov}(f^z, f^z) \end{pmatrix} \tag{5.1}$$

with

$$\text{cov}(f^x, f^y) = \text{cov}(f^y, f^x) = \frac{1}{N} \sum_{k=-(N-1)/2}^{N/2} \left[f_k^x - \bar{f}^x \right] \left[f_k^y - \bar{f}^y \right]$$

define the axes of the ellipsoid, if f_k^x denotes the value of sample k on the x-component and $\bar{f}^x$ the arithmetic mean of that trace within the time window analysed. The eigenvectors $\mathbf{V_i}$ and the associated eigenvalues λ_i satisfy the equation

$$\underline{\underline{M}} V_i = \lambda_i \mathbf{V_i}, \tag{5.2}$$

which can be solved by Jacobi iteration (e.g. Press *et al.*, 1996). The eigenvalues are commonly sorted in decreasing order. The eigenvector $\mathbf{V_1}$ associated with the largest eigenvalue λ_1 points into the direction of the principal axis of the polarisation ellipsoid (Kanasewich, 1981). This is the propagation direction of a *P* wave and is perpendicular to it for *S* waves.

The time window N should include one or two mean signal periods. Smaller time windows lead to instabilities and larger ones possibly average over several phases and thus limit the resolution of the analysis. Furthermore, a possible preprocessing has to be applied in the same fashion for all three components, and bandpass filter operators must be zero-phase to avoid artefacts.

Several polarisation attributes can be calculated from the eigenvalues and associated eigenvectors. These attributes describe the degree of linear polarisation, the principal direction of oscillation, and the distribution of energy within the selected time window (e.g. Samson, 1973; Benhama *et al.*, 1986; Kanasewich, 1981, 1990; Jurkevics, 1988; Maercklin, 1999). The direction of polarisation, described by a horizontal azimuth Φ and the incidence angle Θ, is calculated from the components V_{1i} (direction cosines) of eigenvector $\mathbf{V_1}$:

$$\Theta = \arctan\left(\frac{1}{V_{1z}}\sqrt{V_{1x}^2 + V_{1y}^2}\right) \quad \text{with} \quad -90° \leq \Theta \leq 90° \tag{5.3}$$

$$\text{or} \quad \Theta = \arccos\left(|V_{1z}|\right) \quad \text{with} \quad 0° \leq \Theta \leq 90° \tag{5.4}$$

$$\text{and} \quad \Phi = \arctan\left(\frac{V_{1y}}{V_{1x}}\right) \quad \text{with} \quad -90° \leq \Phi \leq 90°. \tag{5.5}$$

The simplest measure of the degree of linear polarisation is the rectilinearity

$$RL = 1 - \left(\frac{\lambda_2}{\lambda_1}\right)^Q \tag{5.6}$$

as defined by Kanasewich (1981, 1990). The exponent Q, refered to as contrast factor, regulates the sensitivity for certain degrees of linear polarisation and is often set to a value of 1.0 or 0.5. In both cases the rectilinearity RL reaches a value of 1 for perfect linear polarisation and of 0 for an undetermined polarisation. Whereas the definition of RL in equation 5.6 evaluates the two largest eigenvalues λ_1 and λ_2 of $\underline{\underline{M}}$, Jurkevics (1988) averages

λ_2 and λ_3 instead of using just λ_2 in the numerator. Other shape attributes of the polarisation ellipsoid include ellipticities, a global polarisation parameter by Samson (1973), a planarity coefficient, and a linearity coefficient (Benhama *et al.*, 1986; Jurkevics, 1988; Meyer, 1988; Maercklin, 1999).

The shape of the polarisation ellipsoid and its orientation in space can be used to construct a polarisation filter refered to as weighted directivity filter (Kanasewich, 1981, 1990). A weighting function $\hat{R}_k$ of the general form

$$\hat{R}_k = F(\lambda_1, \lambda_2, \lambda_3)^J \tag{5.7}$$

is given for each time sample k and calculated in a moving time window along the entire three-component recording. $F(\lambda_1, \lambda_2, \lambda_3)$ can be the rectilinearity RL or some other shape attribute. With the identity $|\mathbf{V_1}| = 1$ the components (direction cosines) of $\mathbf{V_1}$ provide a directivity function

$$D_k^j = (|V_{1j}|)^K \tag{5.8}$$

for each time sample k of component $j = x, y, z$. Finally, with f_k^j denoting the original sample value of component j at time k, the filtered sample g_k^j is given by

$$g_k^j = f_k^j \cdot D_k^j \cdot \hat{R}_k. \tag{5.9}$$

Often it is advantageous to smooth the filter functions to minimise contributions of anomalous spikes. Kanasewich (1981, 1990) suggests smoothing in a time window of $N/2$ samples length. The exponents J and K weight the influences of the filter functions and may be set to 1 and 2, respectively (Kanasewich, 1981, 1990).

5.1.2   Array beamforming and stacking

Seismic arrays are often used in earthquake seismology or controlled-source experiments, because the different arrival times of an incoming wave at each receiver provide information on the azimuth to the seismic source and on wave slowness (reciprocal of the apparent velocity v_a). The geometry and the number of seismometer sites of an array depend on economy and purpose. Details of array configurations and their characteristics are described for example by Haubrich (1968), Harjes and Henger (1973), Buttkus (1991), and Schweitzer *et al.* (2002). Eight of the nine CSA receiver arrays are designed after Haubrich (1968) and have an optimal resolution for incoming waves from all directions (section 3.2; see also chapter 6).

With an array, the signal-to noise ratio of a seismic signal can be improved by stacking the coherent signals from the single seismometer sites after correcting for the different arrival or delay times. For an incoming plane wave and negligible elevation differences between seismometer sites, these time delays t_i are given by

$$t_i = \frac{D_i}{v_a} = -\frac{1}{v_a}\left(x_i \sin\phi + y_i \cos\phi\right) \tag{5.10}$$

(e.g. Schweitzer *et al.*, 2002). Again, D_i denotes the horizontal distance to site i with the coordinates (x_i, y_i), v_a the apparent velocity of the incoming plane wave, and ϕ the backazimuth to the seismic source. In case of too large elevation differences between sites, these differences can be included in equation 5.10 (e.g. Schweitzer *et al.*, 2002), or elevation static corrections may be applied to all recorded traces of the array (see e.g. Sheriff and Geldart, 1995; Cox, 1999; Yilmaz, 2001). Another approach is to calculate delay times t_i by raytracing or a finite-difference solution of the wave equation, if the velocity structure below the array is known and if the incoming wave front cannot be approximated by a plane (see also section 4.1.1 and chapter 6).

After deriving delay times t_i for each seismometer site for a specific backazimuth ϕ and apparent velocity v_a, the individual traces are stacked to form a so-called array beam ("delay and sum process"). The traces can be amplitude-normalised and bandpass-filtered before the summation. In this study, I use beamforming to improve the signal-to-noise ratio of direct *P* or *S* arrivals from known sources (section 5.2). But in general, this technique is also used do detect certain coherent seismic phases or to locate their origin.

A simple stack of N traces suppresses incoherent (random) noise by a factor of $\sqrt{N}$ (e.g. Gimlin and Smith, 1980; Yilmaz, 2001). Some sort of weighted stacking can further improve the signal-to-noise ratio. A common tool in exploration seismics on land is the diversity stacking technique, which down-weights traces with high-amplitude incoherent noise (Naess and Bruland, 1979; Gimlin and Smith, 1980). The weights are calculated in successive time windows. A diversity stack is superior compared to a true-amplitude stack, if the time windows are long enough for a statistical analysis and if the mean signal energy is smaller than the mean energy of the noise. Alternatively, the stack can be weighted by the signal coherency measured within a moving time window along the gather of individual traces. Options for the coherency measure are the semblance as defined by equation 6.1 on page 78 or a phase stack. The latter is the sum of the instantaneous phase of seismic traces (Taner *et al.*, 1979) and is not influenced by signal amplitudes. Thus, a phase stack or a phase-weighted stack permits the detection or enhancement of weak but coherent arrivals (Schimmel and Paulssen, 1997).

5.1.3 Near-vertical reflection seismics

Near-vertical reflection seismics is a standard method in crustal-scale investigations, in the exploration of natural ressources, and in near-surface studies for engineering purposes. Typically, sources and receivers are arranged along lines (profiles), and they are placed in a more or less regular pattern. In three-dimensional surveys, sources and receivers are distributed over the entire target area. A shot gather usually consists of many traces recorded at different offsets to obtain multifold coverage of a single subsurface reflection point and thus to permit signal enhancement by stacking. The basic data processing sequence of a seismic reflection survey includes initial trace editing and signal enhancement, geometrical spreading or gain applications, common-midpoint (CMP) sorting of traces, a moveout correction

(alignment) of reflected arrivals, and finally the stacking of traces belonging to the same CMP (e.g. Telford *et al.*, 1990; Sheriff and Geldart, 1995; Yilmaz, 2001). Additionally, a migration method, applied before or after stacking, can be used to shift seismic arrivals to those times corresponding to a real zero-offset recording or to their true subsurface location. Details on migration methods can be found in the textbooks cited above and in chapter 6.

Bandpass filtering improves the signal-to noise ratio, and a deconvolution can compress the effective source wavelet and thus increases temporal resolution. A geometrical spreading correction removes the amplitude decrease with increasing distance from the source. Another option is to apply a possibly data-adaptive (automatic) gain function to all recorded traces. The preprocessed traces are sorted into CMP gathers. Each of these gathers collects those traces, that have the same central location between source and receiver. In case of subhorizontal reflectors and laterally constant seismic velocities, the CMP coordinates equal those of a common-reflection or common-depth point (CDP) at these subsurface reflectors.[1]

Due to the different source-receiver distances involved in a CMP gather, reflected arrivals do not appear at the same time for all traces. Based on the assumption that, in a CMP gather, reflection traveltimes follow hyperbolic trajectories, a so-called normal moveout (NMO) correction removes the moveout effect and aligns reflected arrivals at the same time across the offset range. However, traces are stretched in a time-varying manner, and signal distortion increases at shallow times and large offsets. Strongly distorted portions of the CMP gather may have to be muted before stacking. Besides that, a dip-moveout correction is required in case of arrivals with conflicting dips (e.g. Sheriff and Geldart, 1995; Yilmaz, 2001).

The NMO process presupposes that arrival times are not influenced by surface topography of the shallow weathering layer, and that the velocities to align the arrivals (stacking velocities) are known. Influences of topography and weathering layer are removed, if static time shifts are applied to all traces such that these recordings correspond to a specified (flat) datum (e.g. Cox, 1999; Yilmaz, 2001). Coherency-based velocity analyses for selected CMP gathers or so-called constant-velocity stacks provide the stacking velocities that best align certain reflections. The first type employs the velocity spectrum, i.e. a coherency image as a function of time and stacking velocity. Local maxima of the velocity spectrum indicate the alignment of a reflection for the corresponding velocity at a specific time, and the velocity-time function for the NMO correction can be picked from these local maxima (e.g. Yilmaz, 2001). The coherency measure commonly used is the semblance (Neidell and Taner, 1971; Yilmaz, 2001) as defined by equation 6.1 on page 78. In the second type of velocity analyses, constant-velocity stacks, several constant velocity values are used to conduct NMO correction and stacking of a large group or all of the CMP gathers. To obtain the velocity-time function, at each specified time the velocity is selected that yields the best (sharpest) reflection image.

The stacked traces of all CMP gathers approximate a zero-offset seismic reflection section of the subsurface. A zero-offset section is the reflection response of a (theoretical) survey with sources and receivers at the same location and ray paths oriented perpendicular to reflectors,

---

[1] In reflection seismics the terms CMP and CDP are often used interchangeably.

i.e. vertical in case of subhorizontal layering. The stacking process can be a simple summation of traces or some type of weighted stacking as mentioned in section 5.1.2. Poststack processing aims to improve the quality of the reflection image and may include additional frequency filtering, deconvolution, and coherence enhancement of reflectors.

5.2   Shear waves

In general, S waves are not clearly visible along the vertical-component geophone lines of the CSA (figure 3.3, page 21). However, three-component receiver arrays recorded two local earthquakes with prominent S arrivals. Additionally, the horizontal components of these receiver arrays recorded sufficient S energy of the CSA shots to get an estimate on the v_p/v_s ratio in the study area.

5.2.1   Data processing and phase identification

All nine three-component receiver arrays (figure 3.3) recorded two local earthquakes, referred to as event 1 and event 2. Event 1 occurred at about 23:00 UTC on 9 April 2000 and event 2 at 2:04 on 12 April 2000. The two three-component receiver lines across the Arava Fault (AF) were not installed at these event times. The epicentres of both events are located near the surface trace of the AF in the study area or slightly south of it (event 1), and their hypocentres are in a depth around 15 km.[2] The dominant frequencies of both events are around 3–4 Hz.

Figure 5.1 shows the three-component recordings of both events. The selected receiver arrays 3 and 8 are located east and west of the AF as indicated in the inset maps. Whereas event 1 exhibits an excellent data quality for both, P and S waves, the data quality of event 2 is generally worse. Therefore, I analysed the polarisation state of these data in detail and applied a three-component polarisation filter to identify the seismic phases and to enhance S arrivals (section 5.1.1). Polarisation attributes are determined in a moving time window of 0.33 s along the entire traces. The filter functions to be multiplied with the original data are the direction cosines of the principal polarisation direction and the rectilinearity RL. Both filter functions are smoothed within a time window of 0.17 s and weighted equally. Because the recordings of event 2 at arrays 1 and 2 are contaminated by strong coherent noise, these data are not included in the subsequent analyses.

First P wave arrivals of both events are linearly polarised in the vertical direction ($\Theta = 0°$) as demonstrated by high rectiliearities RL and small angles Θ (figure 5.2). The polarisation attribute panels for recordings at the receiver arrays 3 and 8 are displayed figure 5.2 in the same trace order as in figures 5.1 and 5.3). The horizontally polarised S waves arrive around 2.5 s after the P onset. Especially the S onset of event 1 is characterised by a sharp

---

[2] C. Haberland (2000), personal communication.
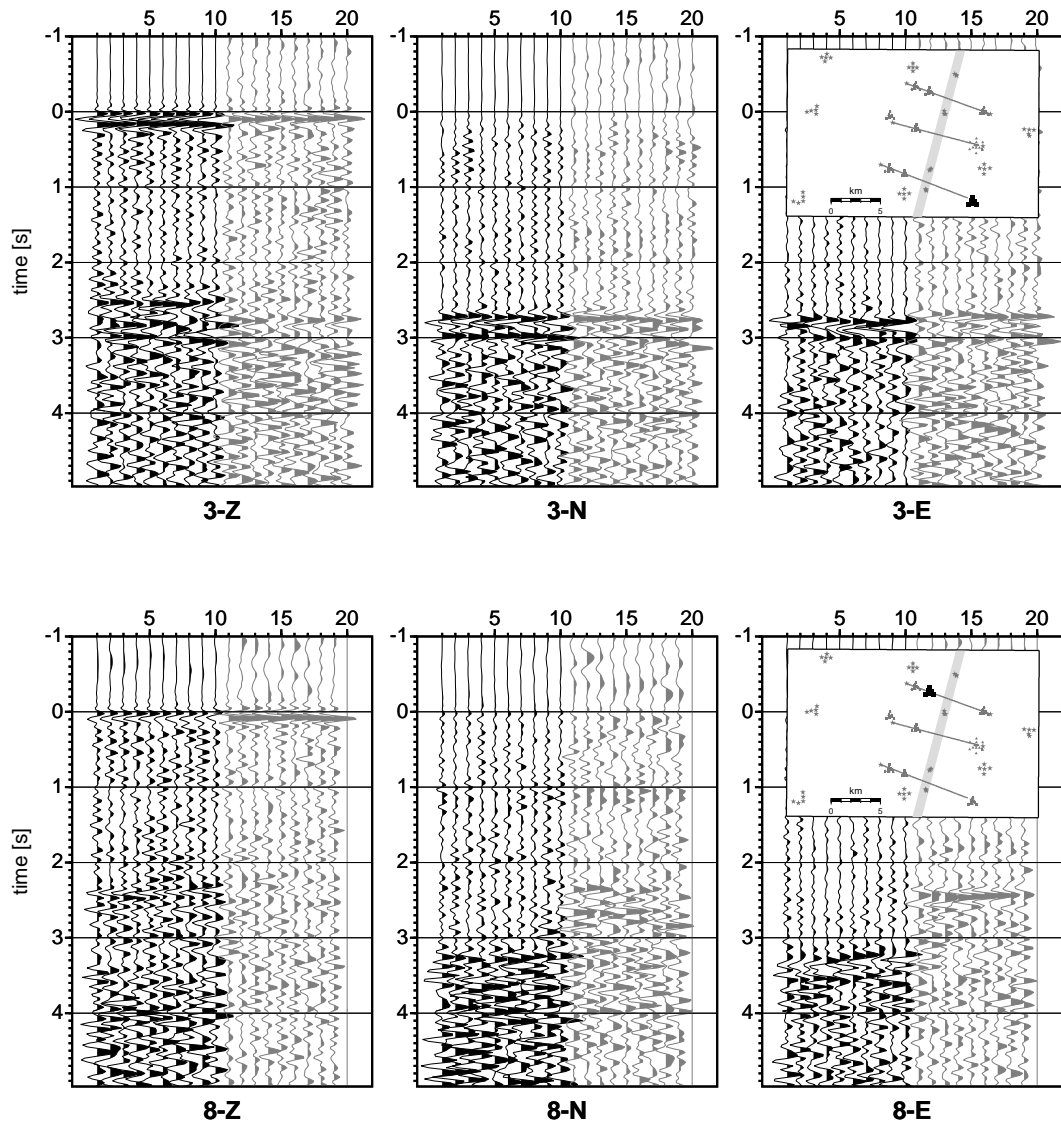
Figure 5.1: *Three-component seismograms of two local earthquakes. The time axis is relative to the first P onset. In each panel, the black traces 1–10 correspond to event 1 and the grey traces 11–20 to event two.* Top: *Seismogram of receiver array 3, east of the Arava Fault.* Bottom: *Seismogram of receiver array 8, west of the Arava Fault.*

Figure 5.2: *Polarisation attributes of two local earthquakes recorded by receiver arrays 3 and 8 (see also figure 5.1). The time axis is relative to the first P onset. A rectilinearity of $RL = 1$ indicates perfect linear polarisation, and Θ denotes the deviation of the principal polarisation direction from the vertical axis ($\Theta = 0°$).*

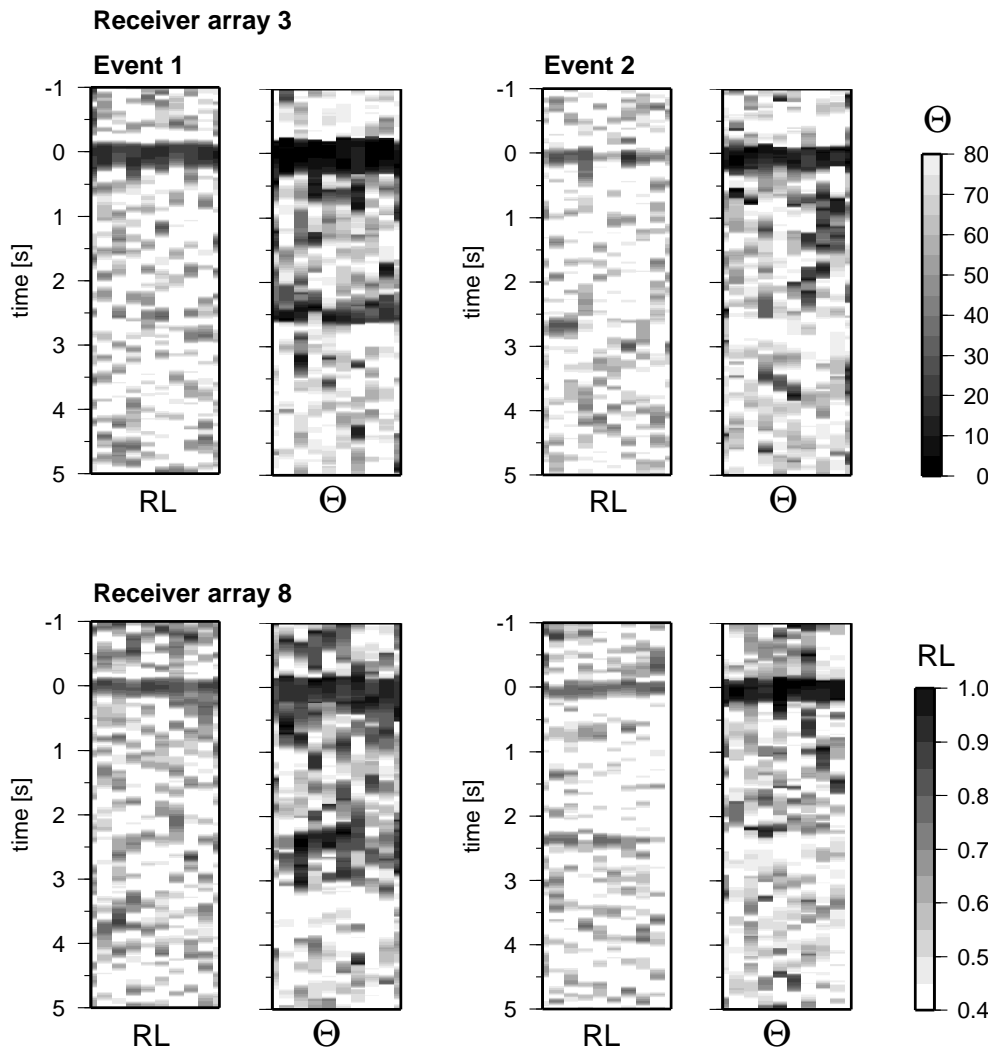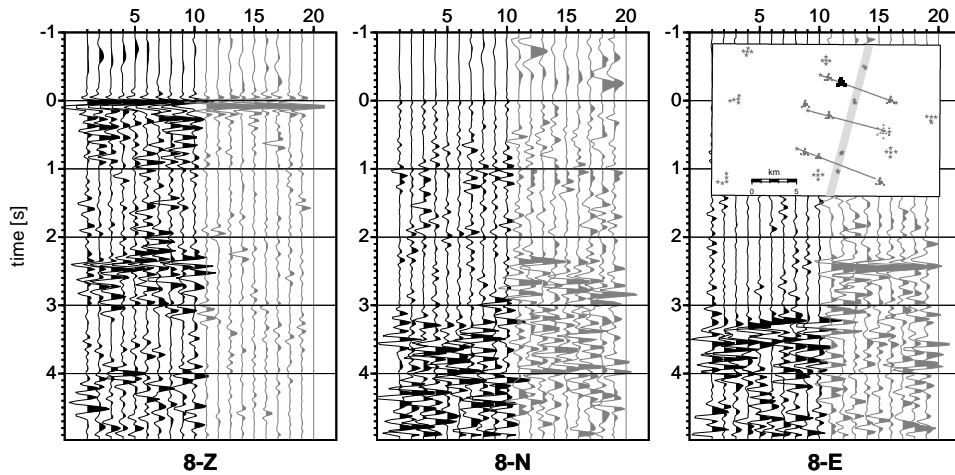***Figure 5.3:** Three-component polarisation-filtered seismograms of two local earthquakes recorded by array 8. The time axis is relative to the first P onset. In each panel, the black traces 1–10 correspond to event 1 and the grey traces 11–20 to event two (see also figure 5.1).*

transition from vertical to horizontal particle movement, and at some receiver sites a linear S polarisation is observed, e.g. event 2 recorded by receiver array 8 (figure 5.2).

Three-component polarisation-filtered data of receiver array 8 are shown in figure 5.3. The filter parameters are those provided above. For most of the local earthquake recordings, the signal-to-noise ratio of P and S arrivals is higher for polarisation filtered data. An example are the S arrivals near 2.5 s on the N-component of array 8 (compare figures 5.1 and 5.3). Therefore, these filtered seismograms are another aid to identify P and S phases clearly.. Finally, I picked the relative P and S arrival times from individual traces to determine an average v_p/v_s ratio in the study area (section 5.2.2).

The data quality of the CSA shots recorded by the three-component receiver arrays is rather good. The dominant frequencies are around 8–10 Hz (section 3.2). Strong P wave first arrivals are observed and can be picked, often without any further processing. But S waves cannot be identified clearly. Furthermore, polarisation analysis and filtering gives good results only for P waves. To improve the signal-to-noise ratio of possible S wave arrivals, I apply several beamforming and stacking techniques for all traces of a single array as described in section 5.1.2. For each receiver array and each shot the selected beam angle is the backazimuth ϕ from the array centre to the shot. With this angle fixed, I adapt the beam velocity v_a to align the P wave first arrival on the vertical component seismogram and reduced v_a by a factor of 1.8–2.0 for the two horizontal components. In general, diversity and phase-weighted stacking proved to emphasize aligned phases better than a simple summation of traces. After stacking, many shot-receiver array combinations still do not show unequivocal S onsets. Nevertheless, I always defined the first strong onset on horizontal components as
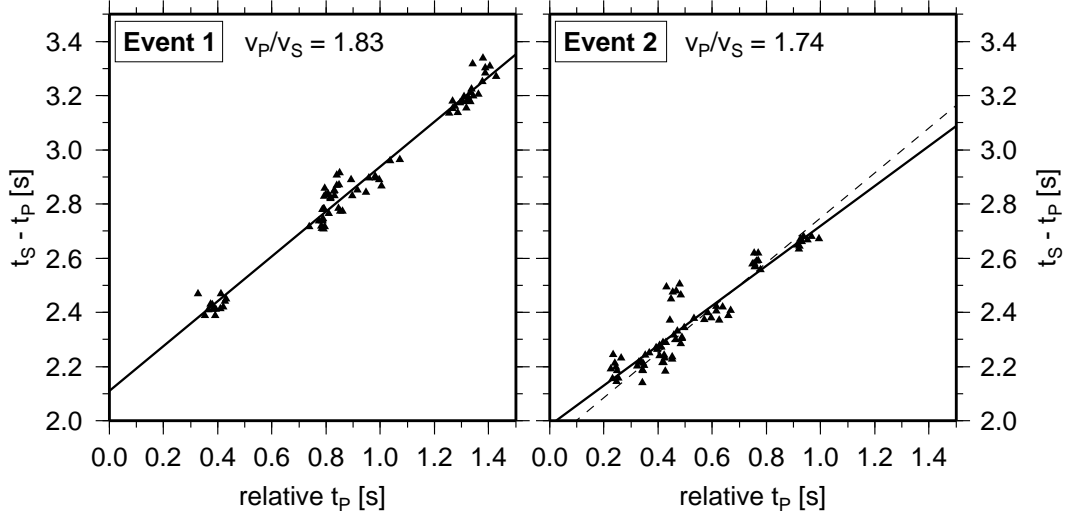
Figure 5.4: *Wadati diagrams for two local earthquakes recorded by the CSA seismometer arrays. Solid lines are least-squares fits of the observations, and their slopes determine the indicated v_p/v_s ratios. The dashed line (right panel) corresponds to $v_p/v_s = 1.83$.*

the S arrival time and picked it in addition to the P onset. These traveltimes provide information of the v_p/v_s ratio and its lateral variation in the shallower portions of the study area, compared to those relative arrival times determined from local earthquakes.

5.2.2 *P*-to-*S* velocity ratio

Together with the P velocity structure, S velocities and the P-to$S$ velocity ratio (v_p/v_s ratio) provide constraints on subsurface lithologies (e.g. Tatham and McCormack, 1991; Bauer *et al.*, 2003). Relative P and S arrival times t_p, t_s determine the average v_p/v_s ratio in the studied subsurface volume. This ratio is commonly derived from a Wadati diagram (Wadati, 1933), i.e. $t_s - t_p$ arrival time differences as a function of relative P arrival times:

$$t_s - t_p = \left(\frac{v_p}{v_s} - 1\right)\left(t_p - t_0\right) \tag{5.11}$$

with an initially unspecified origin time t_0, e.g. as in Quintero and Kulánek (1998); Assumpção *et al.* (2002); Mukhopadhyay *et al.* (2002). The v_p/v_s ratio is directly related to the Poisson's ratio

$$\sigma = \frac{2 - \left(\frac{v_p}{v_s}\right)^2}{2 - 2\left(\frac{v_p}{v_s}\right)^2} \quad, \tag{5.12}$$

which is the ratio of fractional transverse contraction to fractional longitudinal extension (Tatham and McCormack, 1991; Sheriff, 1991).
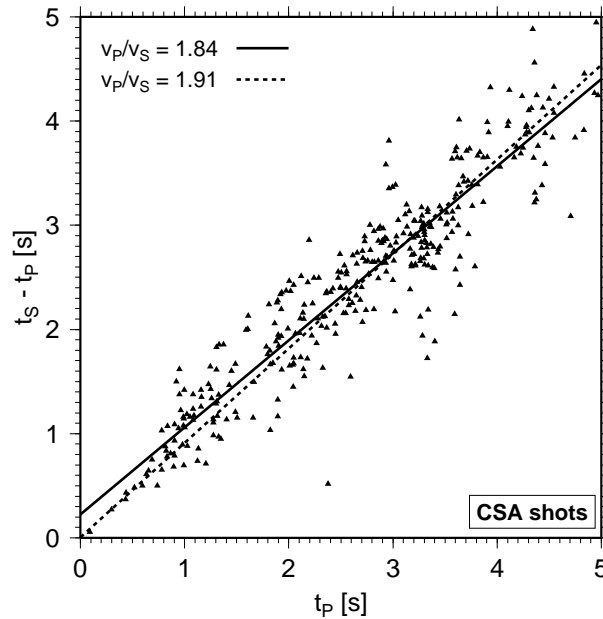
Figure 5.5: *Wadati diagram for observations of all shots recorded by the CSA seismometer arrays. The solid line is least-squares fit without further assumptions, and the dashed one is constrained by the known P origin time $t_0 = 0$ s. The slopes determine the indicated v_p/v_s ratios.*

Figure 5.4 displays Wadati diagrams for the two local events recorded by all receiver arrays. For event 1 *P* wave traveltimes cover a range of 1.2 s and for event 2 of 0.8 s. Linear regression analysis for event 1 yields a v_p/v_s ratio of 1.83 and $\sigma \approx 0.29$. The data scatter around the regression line by up to 0.1 s. This v_p/v_s ratio correlates quite well with results of the WRR experiment in that area ($v_p/v_s > 1.81$). Additionally, modelling results of fault-zone guided waves in the northern part of the study area lead to $v_p/v_s > 1.83$ (Haberland *et al.*, 2003b). The slope of the regression line for event 2 yields a lower v_p/v_s ratio of just 1.74. But a line fitted manually to the data could also have a larger slope. The uncertainty for this event is much higher than for event 1.

All *P* and *S* traveltime picks of the CSA shots are plotted into the Wadati diagram shown in figure 5.5. A linear regression analysis of these data without further assumptions yields a $v_p/v_s = 1.84$ and $\sigma = 0.29$. If the known origin time is fixed, i.e. the regression line has to include the coordinate origin, the v_p/v_s ratio increases to 1.91 and σ to 0.31. In this case it is silently assumed that *P* and *S* waves are excited at the same time by the explosion source. But it is more likely that initial *P* energy is converted to *S* in the close vicinity of the shot location. Anyway, the data scatter much more ($\approx \pm 0.5$ s) then for the local event data. This is due to possible picks of late converted or other phases and to the lateral heterogeneity resolved by the relatively high frequency waves. An average v_p/v_s ratio between 1.84 and 1.91 is still in good agreement with results presented above. A higher v_p/v_s ratio then that derived from local event data is expected for the near surface.
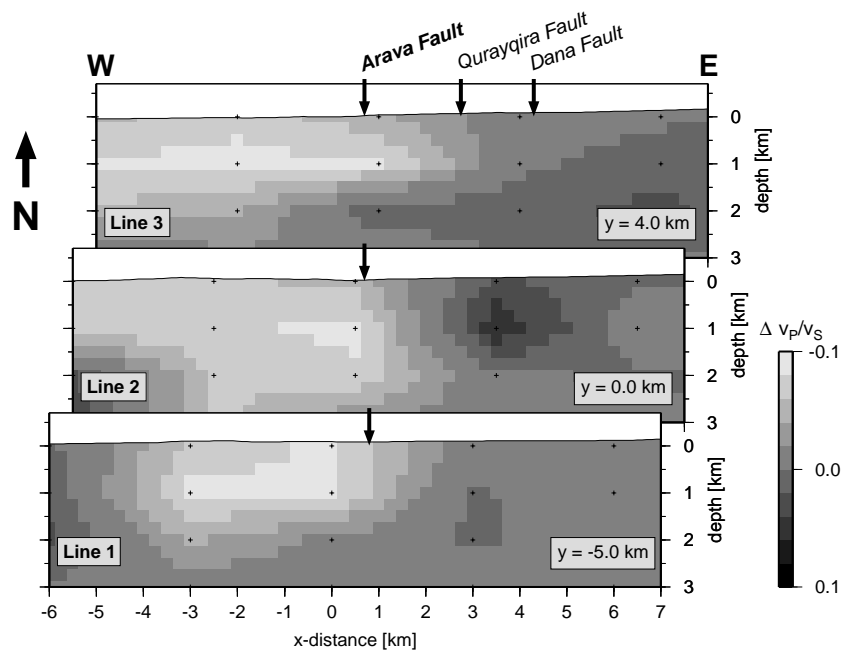
Figure 5.6: *Lateral variation of the v_p/v_s ratio across the Arava Fault. The initial value of this tomographic estimate is $v_p/v_s = 1.86$, and the P velocity model, adopted from the one presented in section 4.2, is held fixed during the inversion. Model nodes (crosses) are spaced 3 km in E-W, in 4 km in N-S, and 1 km in vertical direction.*

Despite of the rather poor quality of t_p, t_s and coarse spatial resolution, lateral variations of v_p/v_s can be estimated. Taking the *P* velocity model from section 4.2 and an initially constant v_p/v_s, an inversion on a coarse node grid shows a tendency to increase v_p/v_s west and to decrease it east of the Arava Fault (figure 5.6). But the inversion is not stable for absolute values of v_p/v_s, and the *S* arrival times might contain too many errors.

Thus, the *S* velocity contrast at the Arava Fault seems to be even higher but is less resolved than the v_p contrast. This observation qualitatively fits to the different lithologies juxtaposed at the Arava Fault: young sedimentary fill in the west and Precambrian volcanites and granites in the east (chapter 2, section 4.2.2, and section 7.3).

5.3 Fault reflections

It is known for a long time that crustal fault planes can act as reflectors (Deacon, 1943; Robinson, 1945). More recently Louie *et al.* (1988) and Hole *et al.* (2001) observed steeply dipping reflections related to the San Andreas Fault zone in California. Furthermore, near-vertical reflections are also known from other geological structures such as flanks of salt diapirs or steeply dipping sedimentary beds (e.g. Allenby, 1962). However, in general, steeply dip-
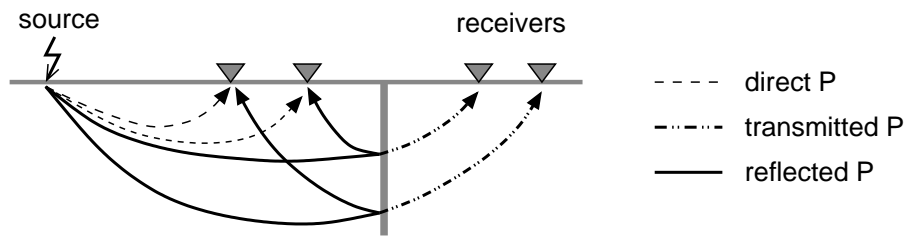
Figure 5.7: *Kinematics of a fault reflection together with raypaths of direct and transmitted waves. Velocities are assumed to increase with depth.*

ping structures are not easily detected by conventional near vertical reflection surveys (e.g. Yilmaz (2001); see also chapter 6).

Figure 5.7 sketches the kinematics of such a fault reflection together with direct and transmitted *P* waves. In this sketch, velocities are assumed to increase with depth, and the fault acting as a reflector is vertical. A seismogram recorded along a profile above this structure would show the first *P* onset with a slope or apparent velocity v_a according to the subsurface velocity structure. Because the reflected waves propagate within the same velocity structure, fault reflected arrivals appear with the same absolute apparent velocity v_a but with the opposite sign. Assuming the same velocity structure, a dip of the reflector towards the source decreases the slope of the reflected onsets (increases v_a), and a dip away from the source increases the slope of the reflected onsets (decreases v_a). Additionally, the reflector dip determines how far away from it a fault reflected arrival can be observed. A dip towards the source decreases this distance.

Figure 5.8 is a seismogram of a shot from array 2 recorded along geophone line 3 (see inset map and figure 3.3, page 21). The minimum and maximum shot-receiver offsets are 10.6 km and 18.6 km, respectively, and the displayed traces are lowpass-filtered (25 Hz) and normalised to their mean energy. The surface trace of the Arava Fault (AF) crosses this profile at about 4.6 km. First *P* arrivals with its positive apparent velocity v_a are clearly visible along the entire profile. An onset with negative v_a originates at about 4.1 s traveltime near 4.6 km distance along the profile and extends backwards to about 3.4 km. Because of the correlation with the surface trace of the AF, this onset can be interpreted as fault-reflected arrivals. The same absolute apparent velocity v_a as the direct *P* onset indicates a nearly vertical fault plane, and ray-based forward modelling of observed traveltimes (Zelt and Smith, 1992) leads to a possible maximum reflector depth of about 1.5–2 km. However, the example shown in figure 5.8 is the only seismogram with a clearly visible fault reflection, except for another shot gather from array 2 and shallow surface wave reflections seen on the short profiles of the CSA II experiment (see figure 3.7, page 26).

Amplitudes of reflected arrivals depend on the impedance contrast at the reflector, i.e. the product of seismic velocity and density (e.g. Tatham and McCormack, 1991; Sheriff and Geldart, 1995; Scales, 1997; Yilmaz, 2001). To answer the question why fault reflections
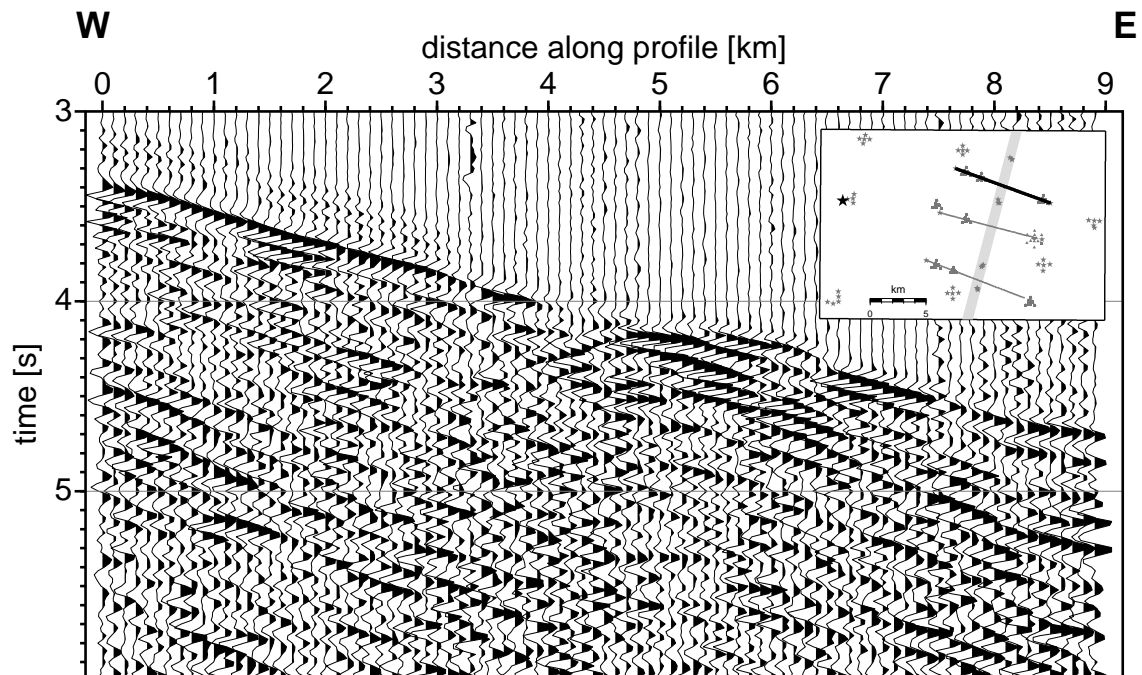
Figure 5.8: *Seismic shot gather with a prominent fault reflection, recorded along CSA line 3. The traces are lowpass-filtered (25 Hz) and normalised to their mean energy. The Arava Fault is located at about 4.6 profile-km, where the reflected onsets with negative slope originate. The inset map shows the acquisition geometry.*

are not recorded more often at the strong velocity and density contrast near the AF (sections 4.2.2, 4.2.3), I model seismic wave propagation and corresponding seismograms in several simplified, two-dimensional subsurface models. For this modelling I use a finite-difference code (Cohen and Stockwell, 2002) that solves the acoustical wave equation, i.e. only *P* wave propagation (e.g. Scales, 1997). Basically, all studied models consist of two quarterspaces in which velocities vary with depth only. These velocity-depth functions approximate the true subsurface velocity structure, and the velocities in the western quarterspace are generally lower than in the eastern one. The two quarterspaces are separated by a transition zone (*fault*) of different width w and shape. Velocities of model grid nodes within the transition zone are determined by linear interpolation of velocities west and east of it. Thus, first-order discontinuities are involved only if $w = 0$ km. All models are rather large to avoid artefacts from model boundaries. They extend from 25 km west of the fault to 13 km east of it and down to 15 km depth. The grid node spacing is 25 m in horizontal and 10 m in vertical direction. The source is located 13 km west of the fault and buried in 20 m depth to approximate roughly the acquisition geometry of figure 5.8. Finally, the seismic source wavelet is a Ricker wavelet (e.g. Sheriff, 1991) with a peak frequency of 8 Hz and a maximum frequency of 20 Hz, again comparable to the real dataset. This results in dominant wavelengths of 0.375 km and 0.5 km for constant velocities of 3 km s^{-1} and 4 km s^{-1}.
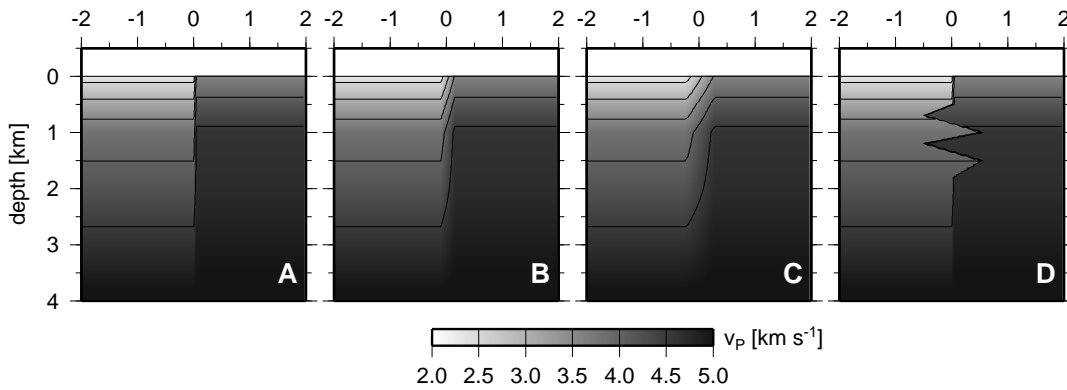
Figure 5.9: *Central parts of velocity models used for finite-difference modelling of fault reflections. The fault is located at 0 km.* A: *Width of the transition zone* $w = 0.0$ *km,* B: $w = 0.25$ *km,* C: $w = 0.5$ *km, and* D: *complex fault structure,* $w = 0$ *km.*

Figure 5.9 shows central sections of four velocity models used to study wave propagation and the generation of fault reflected waves. Additionally, the velocities of the quarterspaces west and east of the fault are included in table 6.1 on page 79. The models A and D (figure 5.9) are characterised by a sharp discontinuity between the two blocks juxtaposed at the fault, whereas the models B and C have a smooth transition. The transition zone is 0.25 km wide in model B and 0.5 km in model C. In model D, the boundary between the two blocks has a complex shape, which approximates the structure resolved by the two-dimensional velocity tomography along the NVR reflection line (figure 4.8, page 40).

Figure 5.10 shows sections of synthetic seismograms calculated for the models presented in figure 5.9. The synthetic traces are normalised to their mean energy for display. Common features in all four seismograms are an easily recognisable first *P* onset with varying apparent velocities according to the different velocities on both sides of the model fault (0 km in figures 5.9 and 5.10), and strong later, linear onsets related to gradient changes at horizontal layer boundaries. Although less pronounced, these features are also visible in real datasets (figure 5.8).

The sharp vertical velocity discontinuity at the fault in model A generates a prominent fault reflection with linear moveout and negative apparent velocity v_a (figure 5.10 A). This reflected onset extends over about 1.4 km until it is obscured by the stronger linear onsets with positive v_a at a traveltime of 4.2 s and -1.6 km cross-fault distance. Whereas model B with a 0.25 km wide transition zone still generates weak fault-reflected arrivals, such arrivals are not visible in the seismogram of model C with its 0.5 km wide transition zone (figure 5.10 B, C). Here, the velocity increase at the fault is apparent only in the v_a decrease of the first *P* onset at 0 km cross-fault distance. The seismogram of model D with its sharp but complex velocity boundary also shows only minor evidence for true fault reflections from this boundary (figure 5.10 D). The weak reflected arrivals are comparable in strength with those of seismogram B. But again, the velocity contrast is apparent in the trend of the first *P*
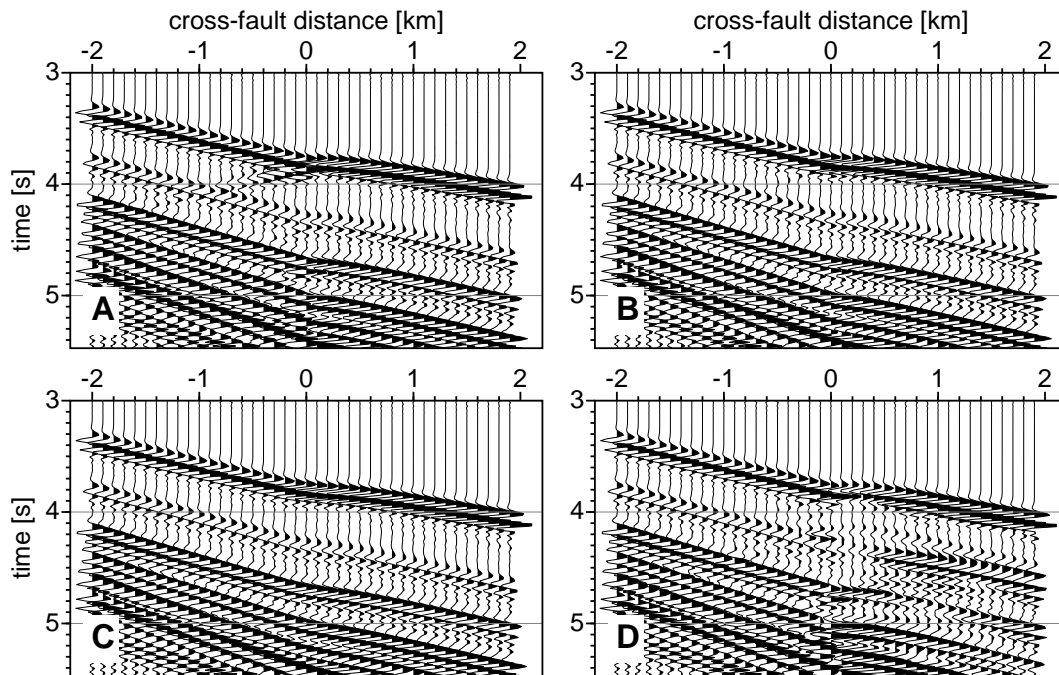
Figure 5.10: *Central parts of synthetic seismograms with fault reflections, generated via finite-difference modelling. The fault is located at 0 km, and the panel labels correspond to those of the input velocity models (figure 5.9). A pronounced fault reflection appears for model* A *with its sharp subvertical velocity contrast, whereas a smoother transition or a sharp but complex boundary reduces the amount of reflected energy (models* B–D*)*

onset, and the disturbed wavefield near 0 km cross-fault distance indicates a narrow transition zone. Furthermore, the weak hyperbolic onsets with their apices near 0 km cross-fault distance are caused by wave scattering at the rough boundary between the two model blocks (see also chapter 6, Müller (2000), and Bohlen *et al.* (2003)).

In conclusion, fault reflections occur at sharp discontinuities with a sufficiently large impedance contrast as used here. If the transition zone between two blocks with different velocities is at least as wide as the dominant wavelength of the incident wave, fault reflections are not observed. Note that the three-dimensional velocity tomography with CSA traveltime data (section 4.2) cannot resolve such sharp discontinuities, and a more detailed velocity model is only available along the NVR reflection line in the southern part of the study area (figure 4.8). As observed for a wide transition zone between blocks of different velocities, a complex shape of a sharp discontinuity can also prevent fault reflections. At boundaries like that in model D, seismic waves are subject of scattering. Because typical fault reflections as in figure 5.10 are rare features in the available dataset, despite of the strong velocity contrast correlating with the AF, I developed and applied a systematic search for scattered seismic energy near the AF fault trace. The method and results are discussed in chapter 6.

Line	CMP	Velocity-time function $v_p(t)$							
		t	v_p	t	v_p	t	v_p	t	v_p
1	1–180	0.10	1.40	0.20	1.80	0.40	2.40		
	220–399	0.10	1.30	0.20	1.50	0.40	2.40		
3	1–160	0.05	1.60	0.10	2.00	0.20	2.00	0.30	2.30
	240–399	0.05	1.40	0.10	1.60	0.20	2.00	0.30	3.00
5	1–160	0.10	1.86	0.20	1.86	0.30	2.40	0.40	3.60
	240–399	0.10	1.50	0.20	1.86	0.30	2.40	0.40	3.60
6–9	1–399	0.10	1.60	0.30	2.50				
10	1–399	0.10	1.80	0.40	2.60				

Table 5.1: *Stacking velocities used for the reflection profiles across the Arava Fault. Line numbers increase from south to north (figure 3.3, page 21). Two-way traveltimes t are in seconds and velocities v in km s^{-1}. Velocities are linearly interpolated between common midpoints (CMP) missing in the table and between times. CMP numbers increase from west to east.*

5.4   Reflection profiles across the Arava Fault

The 1 km long profiles across the Arava Fault (AF) are mainly intended to derive the shallow velocity structure across this fault. These eight lines of the CSA II experiment are included in the map in figure 3.3 (page 21), and the velocity cross-sections along these lines are presented in section 4.3. Nevertheless, the data acquired during this experiment contain reflections from subhorizontal layer boundaries. This section briefly outlines the data processing sequence and obtained results. The results are preliminary in the sense that steep-angle reflections are excluded because of the contamination with strong surface waves (see figure 3.7, page 26) and because precise static time corrections have not been applied.

Each profile consists of 200 vertical-component geophones with a spacing of 5 m, and up to 50 shots spaced about every 20 m were fired into this spread (table 3.1). This leads to 399 common-midpoints (CMP) for each line. The initial processing sequence included bandpass-filtering to suppress random noise, the removal of some traces with too strong noise (trace editing), and first-break muting (e.g. see Sheriff and Geldart, 1995; Yilmaz, 1987, 2001). As mentioned above, most shot gathers are dominated by strong surface wave arrivals, and the sections after these arrivals are characterised by back-and forth travelling (reflected) surface waves and scattered seismic energy. These phases obscur possible reflections from subsurface discontinuities and thus must be filtered out. Because the results from dip and median filters (Yilmaz, 2001) are not satisfactorily, I simply excluded these contaminated sections from subsequent processing (muting). Therefore, the reflection sections presented below are based mainly on wide-angle reflections.

After preprocessing all available data, I apply elevation static corrections with a constant replacement velocity of 1 km s^{-1}. As described in section 5.1.3, the subsurface reflection image is obtained from moveout-corrected and stacked CMP gathers. To determine the required stacking velocities for the normal moveout correction (NMO), i.e. the alignment of

reflected arrivals, I analyse constant-velocity stacks with several different assumed velocities and select those values that yield the sharpest reflection image (section 5.1.3). The used stacking velocities for all eight lines are summarised in table 5.1. Finally, I stack the NMO-corrected traces of each CMP gather, shifted the resulting sections to their final datum, and slightly enhance reflector coherency (Kirlin and Done, 1999; Yilmaz, 2001).

Figure 5.11 shows all eight reflection sections. The indicated times are two-way traveltimes of vertically travelling waves, and 0.0 s corresponds to the mean sea-level (final datum). The topography along the profiles is indicated by solid lines, and arrows mark the surface trace of the AF, determined from geological observations. In such reflection sections, a subvertical fault or a boundary between different lithological units appears as terminating or interrupted subhorizontal reflectors, polarity changes across the fault, or as differences in the reflectivity pattern observed on both sides.

Although the presented reflection sections look rather different, they exhibit many common features. Except for lines 1 and 3, interrupted and disturbed shallow reflectors are visible at the indicated surface trace of the AF. Whereas this simple shallow structure appears on the southern lines 1–7, shallow reflectors on the northern lines 8–10 are more complex. Along line 8, the shallow reflector continuity is disrupted at the AF and additionally about 250 m east of it, at 0.7 km profile distance. At line 9, dipping reflectors occur with a peak near 0.3 km profile distance, west of the AF trace. At later times (greater depths), the general reflectivity pattern is different on both sides of the fault trace. The boundary between these two domains is sometimes offset to the surface trace of the AF, for example slightly to the east at lines 3 and 6.

Shallow subhorizontal reflectors mark the base of the seismic weathering layer, i.e. young, unconsolidated deposits with a high porosity and low seismic velocities (e.g. Sheriff and Geldart, 1995; Yilmaz, 2001). At thick accumulations of aeolian sands or below sand dunes along lines 5, 8, and 9, the first reflector corresponds to the base of this deposits (see also section 4.3.2). Since the surface trace of the AF is often difficult to infer in the study area from surface observations (section 2.2.1), disturbed and offset shallow reflectors corroborate the inferred fault trace and are an evidence for recent activity at this segment of the AF. In the northern part of the study area (lines 7–10), there are indications for more than one fault strand at shallow depths (e.g. line 8). Dipping shallow reflectors west of the AF at line 9 are related to a pressure ridge that crops out north of this line (section 2.2.1). The reflectivity pattern imaged below the northern line 10 suggest a blocky subsurface structure with several fractures within the observed limestones in the vicinity of the AF.

In summary, the reflection sections help to delineate the trace of the AF in the study area and indicate recent activity. The fracture zone of the AF seems to be rather narrow because of the absence of a wide zone of disturbed or vanishing reflectivity there. Dipping reflectors are related to a pressure ridge, a structure also formed by the left-lateral movement along the AF.
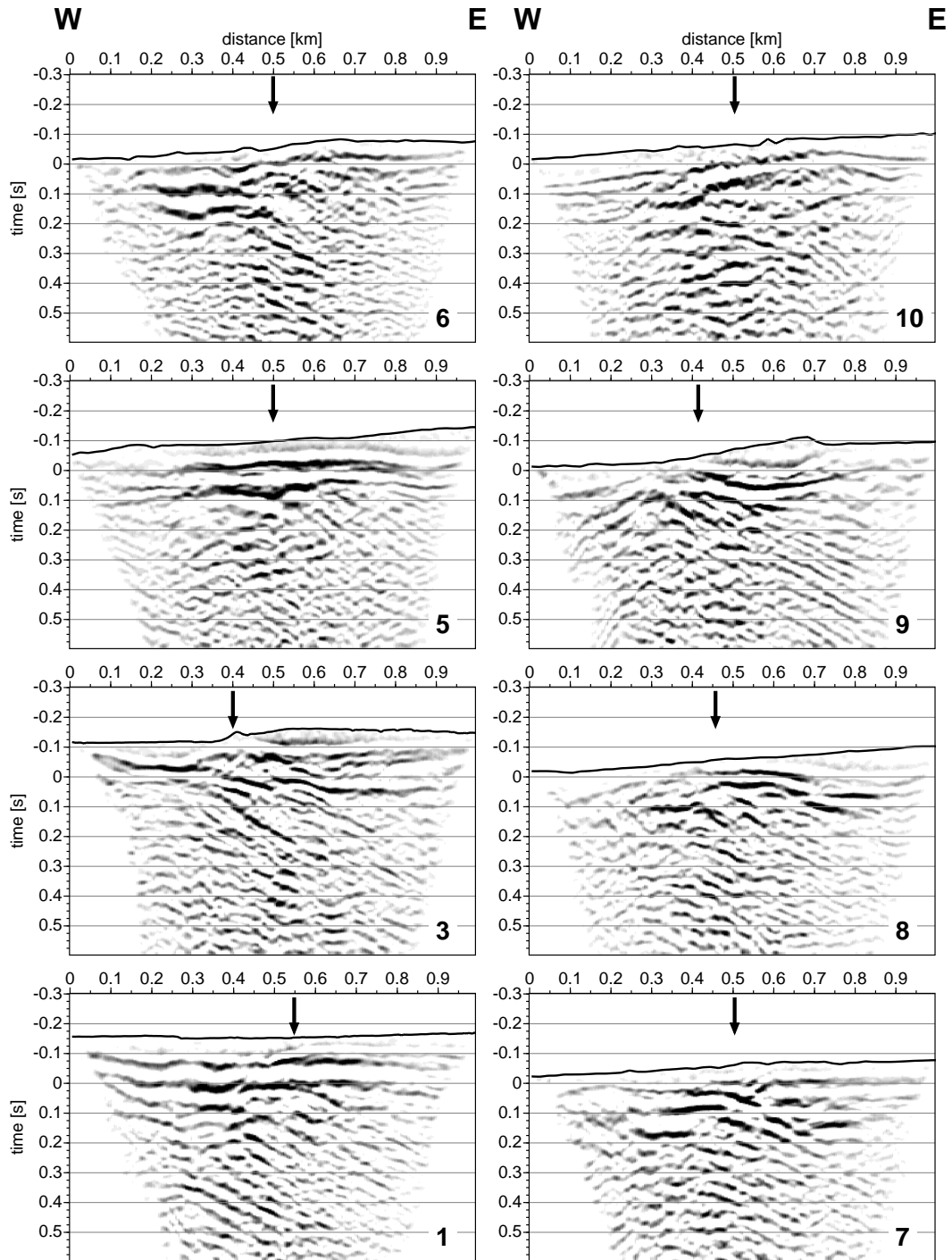
Figure 5.11: *Reflection profiles across the Arava Fault. Arrows indicate the surface fault trace as determined from geological observations, and line numbers increase from south to north (see figure 3.3, page 21).*

6. Imaging of scatterers

Seismic waves are subject to scattering at small inhomogeneities with different elastic properties than the background medium. Here, small means significantly smaller than the dominant wavelength of the incident wave (Rayleigh scattering). The superposition of scattered seismic energy generated by statistical perturbation of elastic parameters is often used to model the seismic coda (e.g. Aki and Chouet, 1975). A complementary approach is to model the subsurface as a layered medium. This approach forms the basis of many seismic processing and migration techniques as described in several textbooks such as Sheriff and Geldart (1995) and Yilmaz (1987, 2001). Models based on single scattering from spatially localised scatterers fill the range between these two end members (Nikolaev and Troitsky, 1987; Lymnes and Lay, 1989; Hedlin *et al.*, 1994; Weber and Wicks, 1996; Belfer *et al.*, 1998; Rietbrock and Scherbaum, 1999; Müller, 2000) and form the basis of diffraction stack or pre-stack Kirchhoff depth migration (e.g. Buske, 1999; Yilmaz, 2001; Louie *et al.*, 2002).

In the study area, sources of seismic scattering are expected to be related to the structure of faults (see also section 5.3). Therefore, an analysis of scatterered waves can lead to images of faults or other steeply dipping structures, which are not easily detected by conventional near-vertical seismic reflection surveys. To image zones of scattering and thus the structure of faults in the upper 4 km of the study area, I use a combination of shots and receiver arrays of the CSA experiment (section 3.2) for a special imaging (migration) technique. This chapter starts with some theoretical considerations on single scattering and continues with the implementation of an imaging technique, the data processing, and the resolution achieved by the method. Section 6.5 presents the imaged distribution of scatterers in the study area. An excerpt of this part of my thesis has been published by Maercklin *et al.* (2004).

6.1   Single scattering

The kinematic behaviour of diffracted and scattered wave fields are similar due to the underlying Huygens's principle. In this concept every point on an advancing wavefront is regarded as a source of secondary waves, and the later wavefront is the envelope tangent of all secondary waves. An omnidirectional point scatterer contributes coherent energy to the entire isochrone that is defined by the arrival times of a specific seismic phase at all traces. For a reflection at a continuous interface, most of the secondary waves are cancelled out and only those satisfying the reflection condition (Snell's law) contribute to the recorded seismogram. The sketch in figure 6.1 illustrates the different kinematic behaviour of reflected
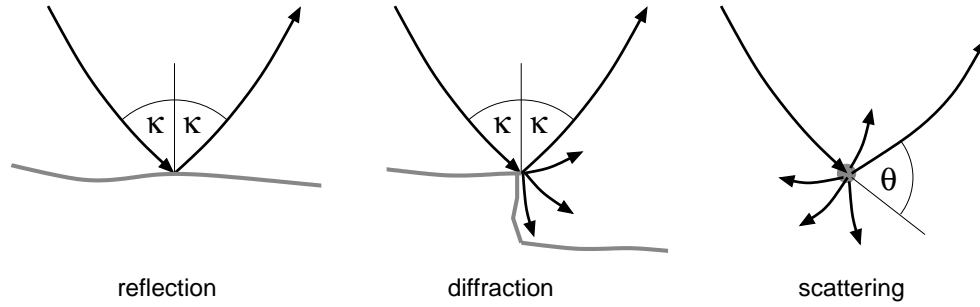
Figure 6.1: *Kinematics of a reflection versus a diffraction and scattering. κ denotes the reflection angle and θ the scattering angle. A reflection at a continuous interface (*left*) occurs, where Snell's law, the reflection condition, is satisfied, whereas a point scatterer (*right*) radiates energy in all directions.*

versus diffracted and scattered waves.

The concept of secondary waves also builds the basis of diffraction summation or Kirchhoff migration, which is widely used in exploration seismology (e.g. Buske, 1999; Yilmaz, 2001; Biondi, 2003) and has been adapted to local earthquake (Louie *et al.*, 2002) or teleseismic data (Hedlin *et al.*, 1994; Aprea *et al.*, 2002). The Kirchhoff migration method not only considers the kinematic, but also the dynamic behaviour of the secondary wave field, i.e. its amplitude and phase. In contrast to an omnidirectional point source with a uniform amplitude response for all angles, a point aperture is assumed, which generates angle-dependent amplitudes. This angle-dependence can be described by the cosine of the scattering angle θ (figure 6.1) and is commonly referred to as obliquity factor (Yilmaz, 2001). Maximum amplitudes of the secondary wave field occur for $\theta = 0°$ and $\theta = 180°$, and they vanish for directions perpendicular to the incident or primary wave field. Besides the obliquity factor, one has to account for spherical divergence, i.e. the amplitude decay with increasing distance to the source, and for angle-dependent phase changes of secondary waves.

The dynamic behaviour of seismic scattering at small inclusions can be described by the Rayleigh scattering theory. Gritto *et al.* (1995) showed that its error is less than 5%, if the length scale of a scatterer is less then roughly one sixth of the wavelength of the incident wave. Applied to CSA data this means scatterer lengths up to a few tens of metres. Amplitudes of scattered P and converted S waves depend on the composition or the elastic constants of the scatterer relative to the background, on the volume of the scatterer, and of its shape (Eaton, 1999; Müller, 2000; Bohlen *et al.*, 2003, and references therein). Generally, scattered P waves show minimum displacement amplitudes between $60° \leq \theta \leq 100°$, which is roughly perpendicular to the incident wave, and maximum values in the forward and backward directions, i.e. $\theta = 0°$ and $\theta = 180°$. In contrast to spherical inclusions, flat-shaped scatterers tend to focus energy in the direction of a reflection from a planar interface with the same dip (see figure 6.1, left). Phase reversals of the first scattered P arrival occur at scattering angles, which are characteristic for the scatterer composition.

The Rayleigh scattering theory is not valid for large complex-shaped scatterers. However,
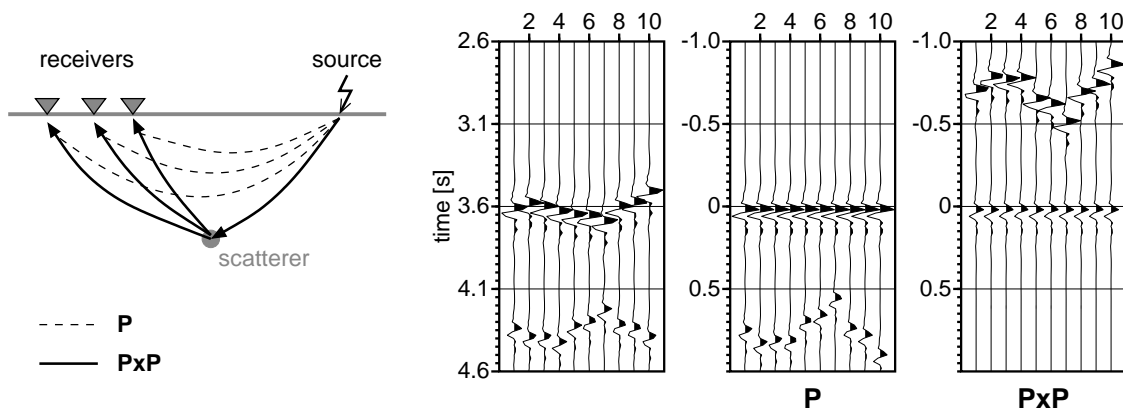
Figure 6.2: left: *Kinematics of the imaging method (beamforming, migration). Dashed lines indicate raypaths associated with direct arrivals (P) and solid lines those imaging the scatterer (PxP).* right: *Synthetic example for beamforming using a single shot and ten receivers. The left panel shows raw data. The right panels show aligned direct arrivals and aligned scattered arrivals shifted to t = 0 s, respectively.*

assuming that scattering there occurs at scattering centres, which lie at areas of strong curvature first reached by the incident *P* wave, the amplitude-versus-angle behaviour of scattered *P* first arrivals still agrees with the Rayleigh theory (Bohlen *et al.*, 2003). For large inclusions the shape dominantly influences the directivity of the scattered wave field, whereas composition effects are less important. Thus, without detailed a priori information on the shape, amplitude-versus-angle analysis of seismic waves scattered from large objects is highly ambiguous.

6.2   Imaging method

Several attempts have been made to image or migrate sources of seismic wave scattering. For example, Krüger *et al.* (1995, 1996) and Scherbaum *et al.* (1997) applied source and receiver array beamforming simultaneously to image inhomogeneities at the Earth's core-mantle boundary. Their method, based on far-field or plane-wave assumptions, became known as double beamforming or double beam imaging (see also section 5.1.2). Rietbrock and Scherbaum (1999) extended this technique to spherical wavefronts to locate sources of scattering, and, among others, Belfer *et al.* (1998) and Müller (2000) worked with controlled-source data and acquisition geometries typical in exploration seismology. To image origins of scattered seismic waves, Müller (2000) discusses different processing and migration techniques applicable to marine and vertical-seismic-profiling acquisition geometries. The imaging method described below incorporates ideas of the authors cited above.

The sketch on the left of figure 6.2 illustrates the basic idea behind the imaging concept. Seismic energy excited by a seismic source is recorded by an array of receivers. The first

arrival is the direct *P* wave, and a second arrival labelled *PxP* is due to scattering from a subsurface inhomogeneity. The first panel of traces in figure 6.2 shows a synthetic example of such a recording with a *P* arrival around 3.6 s and *PxP* around 4.3 s.[1] Direct *P* traveltimes can be applied to these traces as static shifts to align the first onset. This yields the second panel in figure 6.2, labelled *P*. The traveltime of the second arrival, the *PxP* phase, is given for each trace by the sum of the traveltimes of the two legs: from the source to the scatterer and from the scatterer to the corresponding receiver. Applying these moveout times as shifts to the initial recordings aligns the the *PxP* phase as shown in the right panel in figure 6.2. A stack of these aligned traces forms a *PxP* array beam and enhances this phase relative to the *P* phase, because the latter is misaligned and thus cancelled out by summation.

Generally, real data are contaminated with noise, and *PxP* often has small amplitudes compared to *P*. Compared to a simple stack of the traces, coherency measures are superior for the detection of such weak but coherent arrivals, provided that the recording characteristics of the receivers are the same. If this also remains true for different sources of a shot array, it is straightforward to extend the concept to a double beam method. The coherency is measured in a time window centered at the predicted arrival time (0 s in figure 6.2). Assuming coherency of the *PxP* phase within a receiver array gather is justified, because the direct *P* arrivals are always very coherent (see e.g. section 3.2 and figure 6.5) and only a limited range of scattering angles θ is involved in the beamforming process.

Several coherency measures suitable for seismic data are reviewed by Yilmaz (2001). Like Rietbrock and Scherbaum (1999), from these measures I choose the semblance NE (Neidell and Taner, 1971; Yilmaz, 2001), but other measures such as a phase-stack (Schimmel and Paulssen (1997); see also section 5.1.2) could also be used. The semblance is a common coherency measure in seismic velocity analyses (section 5.1.3), or it is employed to detect similarities between different datasets as mentioned in section 4.1.2. The semblance is defined as

$$NE = \frac{1}{M} \frac{\sum_{j=k-N/2}^{k+N/2} \left(\sum_{i=1}^{M} f_{ij} \right)^2}{\sum_{j=k-N/2}^{k+N/2} \sum_{i=1}^{M} f_{ij}^2} \quad , \tag{6.1}$$

in which M aligned traces are analysed in a time window of N samples centered at sample k. Its range of values is $0 \le NE \le 1$ with $NE = 1$ meaning perfect agreement. In this study I use a Hanning time window, in which the semblance NE is calculated. A Hanning window is cosine-tapered and thus downweights data portions further away from the central sample k. A high semblance value observed for *PxP* aligned traces indicates the presence of a scatterer at the corresponding subsurface location. Thus, a discrete scan through a subsurface volume results in an image of regions, where strong sources of scattering are possibly located. The final images presented in sections 6.4 and 6.5 are stacks of such individual semblance images obtained from all source-receiver array combinations of the available dataset. In review, the

---

[1] This example corresponds to a single shot from array 2 recorded by receiver array 8 and a scatterer located 1 km below the surface trace of the Arava Fault south of line 3 (see map on page 21 and the synthetic image in figure 6.6 A).

Data subset			Velocity-depth function $v_p(z)$						
	SA	RA	z = 0.00	0.50	1.00	2.00	4.00	6.50	km
West:	1,2,3,6,7	1,2,4,5,7,8	v_p = 2.30	3.15	3.80	4.19	5.10	6.10	km s^{-1}
East:	4,5	3,6,9	v_p = 3.56	4.15	4.60	4.70	5.10	6.10	km s^{-1}

Table 6.1: *Data subsets and velocity-depth functions $v_p(z)$ used for synthetic calculations and the imaging of scatterers. The locations of shot arrays (SA) and receiver arrays (RA) as well as the model boundaries are shown in figure 6.3.*

use of calculated traveltimes and of a coherency measure brings the outlined imaging method close to the double beam stack migration and diffraction coherency migration described by Scherbaum *et al.* (1997) and Müller (2000), respectively.

The imaging concept for scattered phases outlined above requires a velocity model of the subsurface. The standard plane-wave approach in earthquake array seismology uses a slowness and a horizontal azimuth for the receiver and the source array, respectively (section 5.1.2). I apply this technique to enhance *P* and *S* phases to derive an average v_p/v_s ratio for the study area (section 5.2). In the application presented here possible scatterers may be situated close to source or receiver arrays of the CSA experiment, and therefore, the plane-wave approach cannot be used. Furthermore, the velocity variation in the target area has to be considered for a correct image of the spatial distribution of possible scatterers, especially the known increase of velocity with depth (section 4.2.2), which results in curved ray paths. Therefore, I derived a one-dimensional *P* velocity model and from that build a traveltime table for all possible offsets and depths in the target volume using a finite-difference (FD) scheme (van Trier and Symes, 1991). The FD scheme is based on the geometrical optics or WKBJ approximation[2] of wave propagation (Scales, 1997). The FD grid spacing is 10 m in horizontal and vertical direction, and traveltimes for distances between grid nodes are interpolated linearily. The imaging (migration) algorithm reads *P* and *PxP* traveltimes from this table, which decreases processing times compared to two-point raytracing for each source-scatterer-receiver combination. The dense FD grid ensures accurate traveltimes, which differ less than the time sample rate of the input traces from those times obtained by two-point raytracing.

6.3   Data processing

To image scatterer locations in the study area, I use data recorded by the nine receiver arrays and omit the geophone lines (figure 6.3). As discussed in the following section 6.4, such linear arrays lead to more than one possible location for a single scatterer, and this phenomenon cannot be suppressed by stacking of several different source-receiver combinations. To calculate traveltimes for beamforming, I use one-dimensional velocity models that vary with

---

[2] The letters stand for G. Wentzel, H. Kramers, L. Brillouin, and H. Jeffreys.
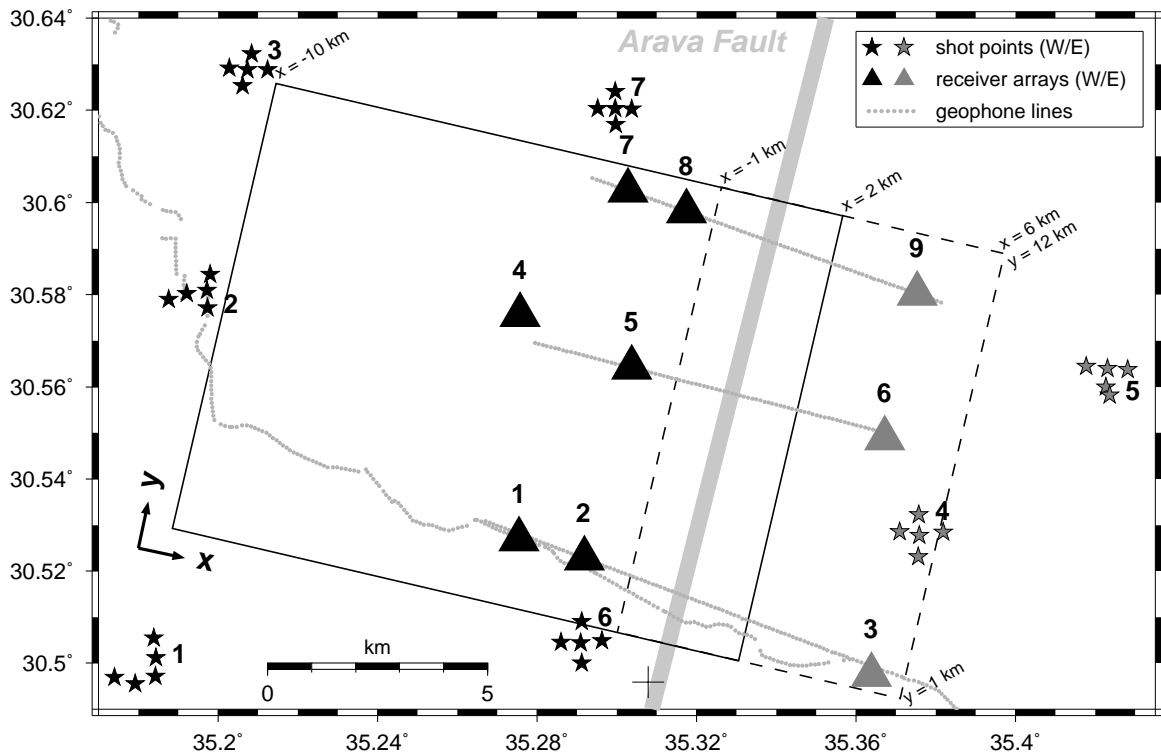
Figure 6.3: *Map of the acquisition geometry for three-dimensional imaging of scatterers. In black are shots and receiver arrays used for the images west of the Arava Fault (solid box), and in grey are those for the images east of it (dashed box). The main target area is the vicinity of the Arava Fault (overlapping region of the two boxes). A cross near 30.5° N, 35.31° E marks the local coordinate origin assigned for this analysis, and the geophone lines are included for better orientation.*

depth only. Because of the prominent velocity contrast correlating with the Arava Fault (section 4.2.2), I split the available data into two subsets (table 6.1). Only those source-receiver combinations that are located on the same side of the fault are included in one subset. Hence, the western subset consists of six receiver arrays and the eastern one of three. For each subset I define a one-dimensional velocity-depth function which yields a good fit with all observed P wave traveltimes (table 6.1). Use of the tomographic three-dimensional velocity model (section 4.2.2) would be reasonable in the well-resolved central areas only. Furthermore, this model shows only minor lateral variations in its western part.

As an example, figure 6.4 shows a vertical-component shot gather of a single shot from array 6 recorded by receiver array 8 (figure 6.3). The direct P wave arrives at about 3.2 s in the panel on the left. The central panel contains the same traces after alignment of the direct P onset (0.0 s), and the traces in the right panel are aligned according to a scatterer in 2 km depth, about 1 km east of the Arava Fault (AF). The relative maximum semblance value for the latter panel corresponds to the coherent arrival at the predicted traveltime (0.0 s). The variation of traveltime differences between P and PxP indicates the different backazimuths
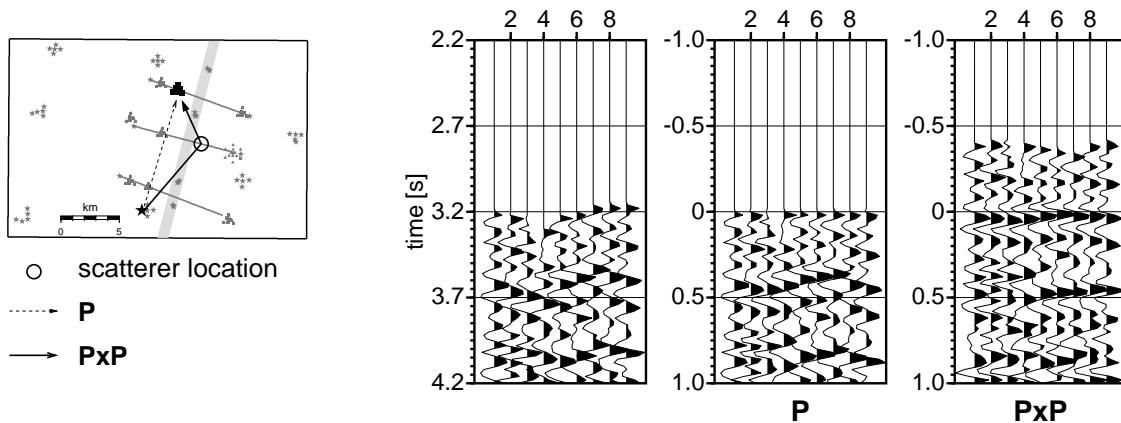
Figure 6.4: *Bandpass-filtered shot record of receiver array 8 (vertical components). The traces are amplitude-normalised, and the noise before the first P onset is muted.* left: *Acquisition geometry of this seismogram. Dashed lines indicate raypaths associated with direct arrivals (P) and solid lines those imaging the scatterer (PxP).* right: *Data example for beamforming using a single shot and ten receivers. The panels show raw data, the aligned direct arrivals, and aligned scattered arrivals.*

to the source regions of these two phases (see also section 5.1.2).

The data processing sequence is the same for both, the western and the eastern data subset. To improve the signal-to-noise level I analyse bandpass-filtered vertical-component data in the frequency range between 4 and 24 Hz (3 db points). To all seismogram traces I apply static time shifts such that the observed direct P phase arrives at the time predicted by the one-dimensional velocity model. Additionally, I calculate residual static corrections individually for each shot-receiver array combination using a technique adopted from Rothman (1986) to refine static time shifts. The procedure, also described by Cox (1999), utilises cross-correlations and simulated annealing to find the maximum stack power around the direct P phase. The approach of using a reference phase (direct P) is known as relative beamforming. This relative beamforming accounts for the influences of topography, near-surface low-velocity layers, and smooth large-scale velocity perturbations in the target volume. The applied static shifts, i.e. the sum of initial and residual corrections, ensure that the direct P wave arrives at the time predicted by the chosen velocity model, and thus enable an alignment of the P phase as in figure 6.2 and figure 6.4.

Figure 6.5 A shows statically corrected traces aligned for the P phase at 0.0 s. The direct P onset and later phases parallel to it dominate the section and may superimpose a scattering signature, which is generally expected to be weak. A difference filter can suppress direct P energy and its multiples. I filter statically corrected data of each combination of a single shot and a receiver array separately. In a first step, a stack of a shot gather with the flattened P phase enhances this phase relative to other arrivals and noise, and in a second step this stack, the direct P beam, is subtracted from each trace in the gather. As seen in figure 6.5 B, the direct P energy is removed effectively from the section, and a comparison with the noise
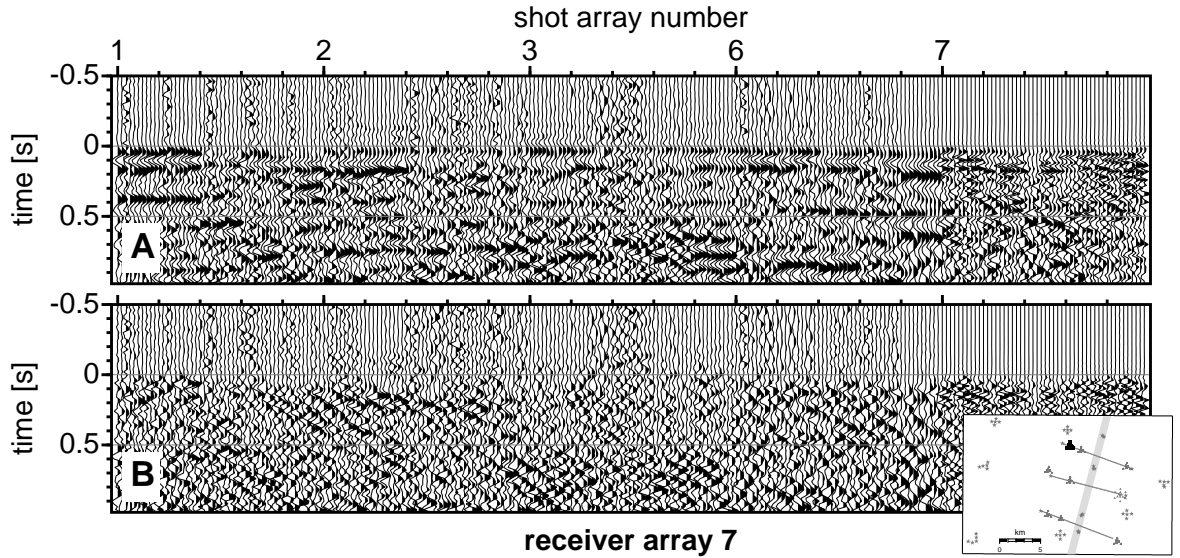
Figure 6.5: *Common receiver array gather of seismometer array 7. The traces are bandpass-filtered and normalised to their mean energy. The ten traces of a single shot are bounded by the small tickmarks, and the inset map shows the location of this array.* A: *Statically corrected traces aligned for the first P onset.* B: *The same traces after application of the difference filter (beam correction) described in the main text.*

level before 0.0 s reveals that there is still a significant amount of energy recorded by the array. To undo the *P* alignment remains as the final step in the filter process.

Obviously, difference filters can be used not only to suppress *P*, but also to suppress other prominent phases. Hedlin *et al.* (1991) designates this technique as beam correction, Müller (2000) adapted it to common-offset gathers of marine seismic profiles, and generally, median filters subtract the weighted moving average from the section instead of a global stack. Difference filters yield best results, if the phase to be removed is aligned perfectly and coherent for all traces included in the stack. Because an accurate *S* velocity model is not available, I cannot remove the influence of possible *S* wave energy in a similar fashion. Therefore, I restrict the semblance analysis to the time window between the direct *P* and the estimated direct *S* traveltime using a constant v_p/v_s of 1.83 (see section 5.2).

For beamforming and semblance analysis, I assign a local coordinate system as indicated in figure 6.3. This system is rotated by 12° to have one axis roughly parallel to the surface trace of the AF (x-axis cross-fault, y-axis parallel). The subsurface is divided into blocks with an edge length of 125 m for beamforming and semblance analysis. The semblance NE is always calculated in a Hanning-tapered time window of 0.25 s, and the one-dimensional velocity models for the two data subsets are listed in table 6.1. After a discussion of the imaging resolution and its implications for the dataset available for this study, section 6.5 continues with results obtained from both data subsets analysed.

6.4 Resolution

Careful resolution testing is necessary, because the target volume is irregularly sampled by rays, especially compared to industry-style three-dimensional exploration surveys (e.g. Yilmaz, 2001; Biondi, 2003). Resolution and imaging ambiguity for single scatterers depend on accuracy of the velocity model, azimuthal coverage of observations, frequency content and time duration of coherent *PxP* energy, and on signal contamination with noise. Influences of near-surface low-velocity layers (see section 4.3) and smooth large-scale velocity perturbations in the imaged volume can be addressed by static time corrections. Then, a reference phase such as direct *P* will arrive at a time predicted by the selected velocity model (relative beamforming). A model with too large velocities images a scatterer at a location further away from sources and receivers, and too small velocities closer to them. In both cases, observed coherency for *PxP* is reduced relative to the true value, i.e. the final image is blurred.

For a given subsurface velocity model, imaging resolution and ambiguity can be assessed with synthetic calculations. To generate a synthetic dataset, I calculate the traveltimes for the direct *P* arrival and for *PxP* of a specified scatterer location, place spikes at these times on synthetic traces, and weight spike amplitudes according to energy decay with increasing distance from the source. These traces are convolved with a synthetic wavelet, which I extract from real CSA data. The extraction algorithm averages the amplitude spectra, maps the average spectrum back into the time domain, and finally transforms the resulting zero-phase wavelet into its minimum-phase representation by twice-repeated Wiener inversion (e.g. see Buttkus, 1991; Yilmaz, 2001).

Figure 6.6 displays imaging responses for a single omnidirectional scatterer embedded in a one-dimensional velocity-depth model. The synthetic seismic wavelet is shown in the legend of the figure. The imaging algorithm assumes that the scatterer is illuminated by a single arrival. But in general, the incoming wave consists of a longer wave train, which results in smearing of energy outward from the actual scatterer location (figure 6.6 A, C, D, and Hedlin *et al.* (1994)). Azimuthal resolution of a point scatterer by a single source and receiver array is inversely proportional to array aperture, because energy is dispersed away from the true location of the scatterer to locations having the same *PxP* traveltime (figure 6.6 A). For a uniform subsurface velocity model, this isochrone describes an ellipsoid with its foci at the source and at the centre of the receiver array (Hedlin *et al.*, 1991, 1994; Müller, 2000). For models with varying velocities, this ellipsoid is distorted as indicated by the shaded areas in figure 6.6, where calculated *PxP* traveltimes t would become smaller than the direct *P* traveltime t_p to the receivers. The influence of array geometry is illustrated by figure 6.6 C and D. A line of receivers has vanishing resolution in crossline direction (see figure 3.4 on page 23). It images the scatterer at more than one location with equal strength, whereas the two-dimensional receiver array design as used in this study reduces energy dispersion and maps the scatterer at the correct location.

Besides that, time averaging (as applied by Hedlin *et al.*, 1994) or a longer analysis time
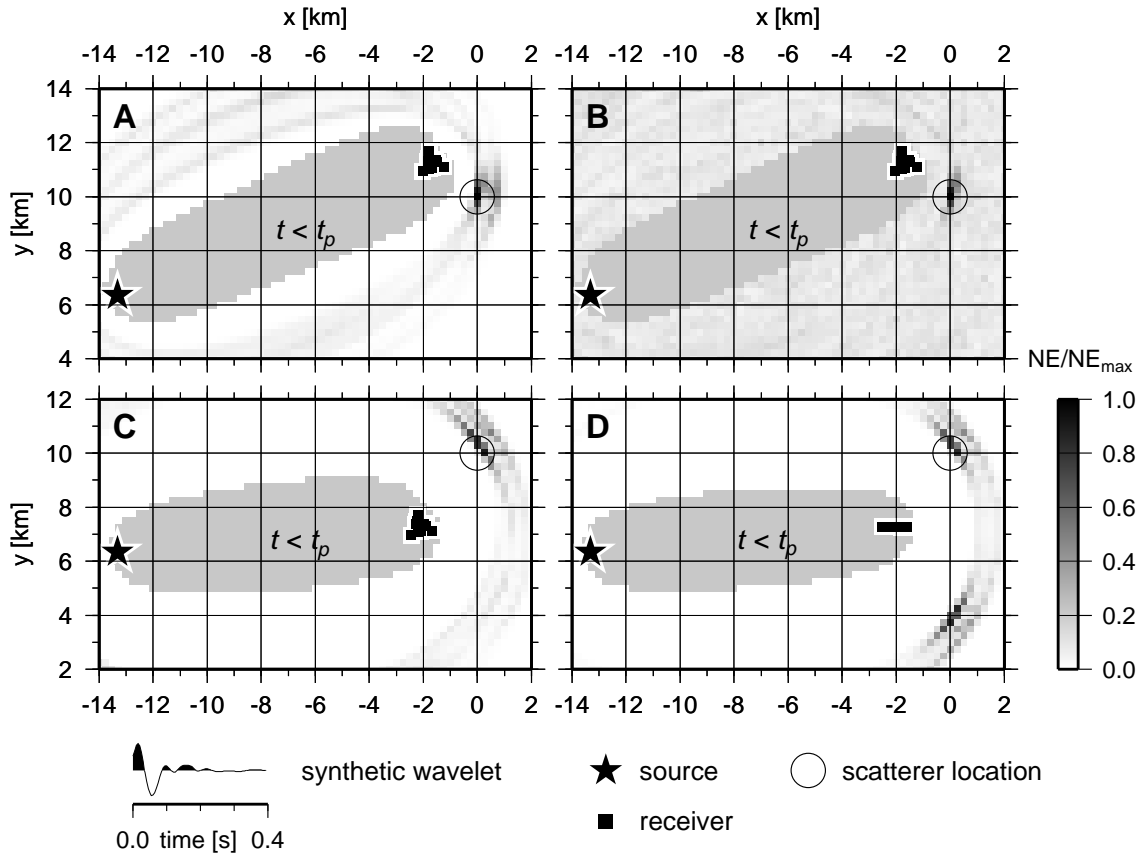
Figure 6.6: *Scatterer imaging responses for synthetic data to assess resolution and ambiguity. Data are generated for a single omnidirectional scatterer in a 1-D $v(z)$ model, 1 km below the indicated location (circle). The synthetic wavelet is extracted from real CSA data.* A, C: *Two different acquisition geometries,* B: *data contaminated with random noise ($S/N = 2$), and* D: *image for a receiver line instead of an array as in C. Energy of the scattered phase (PxP) is indicated by dark areas outside the regions labelled $t < t_p$, which are not reached by this phase.*

window decreases radial resolution. On the other hand, a long time window stabilises the semblance calculation, provided that the window is not much longer than the duration of the coherent *PxP* phase. For the images in figure 6.6 I calculated the semblance in a 0.25 s Hanning window. To increase radial resolution and thus to suppress imaging artefacts, I stack images obtained from different source-receiver combinations. Stacking also suppresses the influence of spatially correlated noise, which would possibly be mapped into an apparent scatterer near the array (Hedlin *et al.*, 1994). In the presence of spatially uncorrelated noise, beamforming combined with semblance analysis seems to be the optimum imaging technique for locating scatterers (figure 6.6 B).

Unlike in seismic velocity tomography (section 4.1), formal quantities describing the resolution of stacked scattering images do not exist. Therefore, several model recovery tests

assist the evaluation of imaging resolution in the study area and for the actual acquisition geometry. Essentially, I conduct two sets of synthetic experiments for the given acquisition geometry and subsurface one-dimensional velocity model. Results of these tests are shown for the western data subset (see section 6.3 and figure 6.3). First, I image single, isolated point scatterers located at various positions in the subsurface volume and analyse energy dispersion. Second, I image planar structures consisting of several point scatterers. The images for synthetic data are obtained using the same local coordinate system, subsurface parameterisation, and velocity model as for the real data (see section 6.3).

For the first set of experiments, I place single point scatterers at locations on a grid within a $12 \times 12 \times 4$ km box. Spacing of scatterers is 1 km in all directions. For each of the 845 scatterers I generate a synthetic dataset as described above and containing only the response of the scatterer itself (*PxP* phase). Using the actual acquisition geometry, I image each scatterer individually. Variations in energy dispersion at all scatterer locations can be visualised by a spread function adopted from that defined by Michelini and McEvilly (1991) for model nodes in seismic tomography (see also section 4.1.2). At each assumed scatterer location j I define a spread function

$$S_j = \log \left[NE_j^{-1} \sum_{k=1}^{N} \frac{NE_k}{NE_j} D_{jk} \right], \tag{6.2}$$

in which k indicates image locations, NE_k the semblance at that point, and D_{jk} the spatial distance between the image location and the assumed scatterer. The normalising factor NE_j is the semblance for the assumed synthetic scatterer location and equals one in this test without preprocessing or random noise. The spread function is a relative measure of dispersion of energy away from a certain scatterer. Its distance term D_{jk} penalises high semblance values mapped at locations far away from the true scatterer locations. Hence, high spread values indicate strong smearing of energy and thus lower resolution of point scatterers than low values. Since it depends on subsurface parameterisation, the spread function is not an absolute measure of imaging resolution. It only indicates variations of resolution for point scatterers in the imaged volume.

Figure 6.7 shows spread values at several depth slices for the selected imaging parameters. Lowest resolution for point scatterers is obtained right beneath the receiver arrays. The lower resolution there is due to the small aperture of the receiver arrays (poor depth resolution) and the coarser spatial sampling of shots and receivers compared to conventional and more expensive three-dimensional acquisition geometries. Highest resolution is achieved in the main target area below the surface trace of the AF.
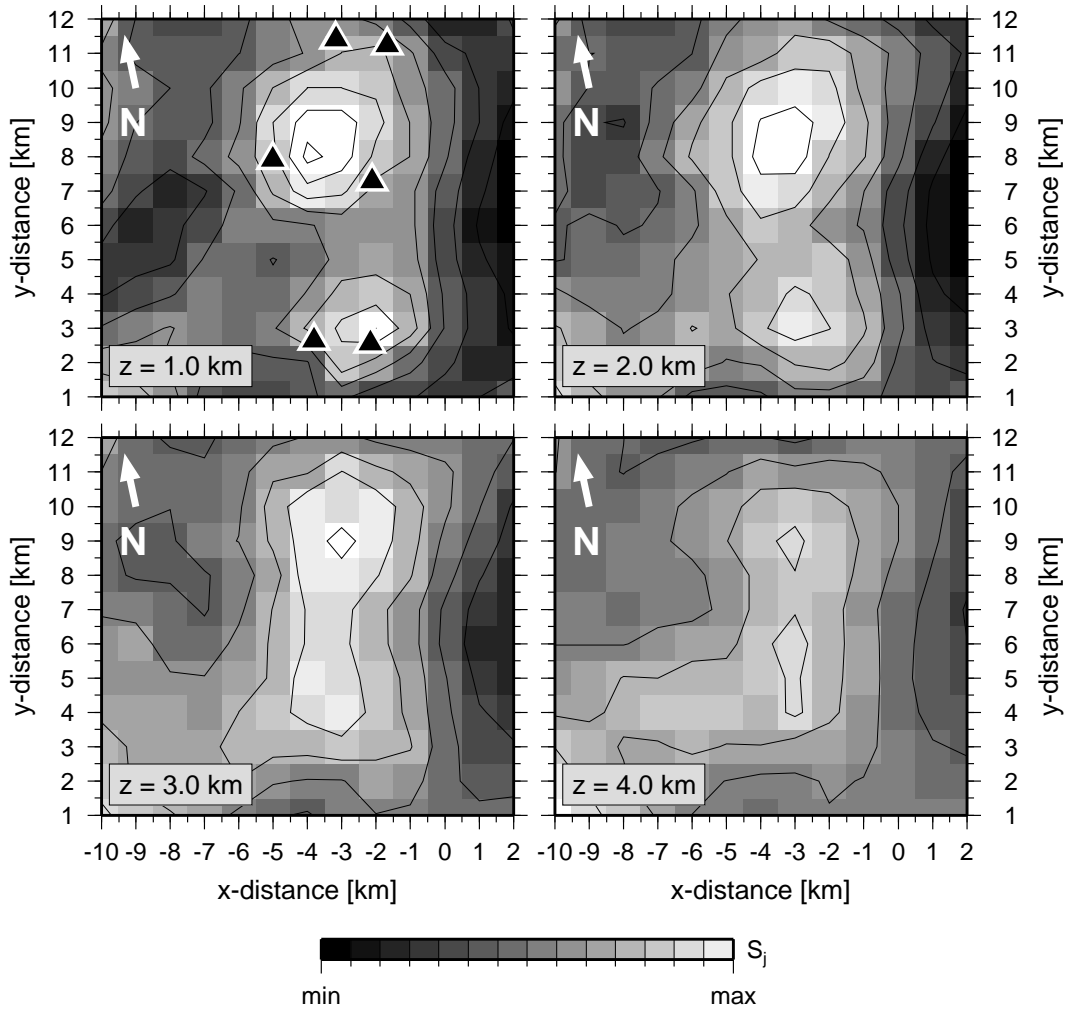
Figure 6.7: *Migration spread function values for the selected imaging parameters at four depth slices. Dark areas correspond to low spread values (better resolution), and the contour line interval corresponds to one tenth of the entire range of spread values. The best resolution at all depth is achieved in the vicinity of the AF trace, stretching at about $x = 0$ km. Triangles in the top left panel indicate receiver array locations.*
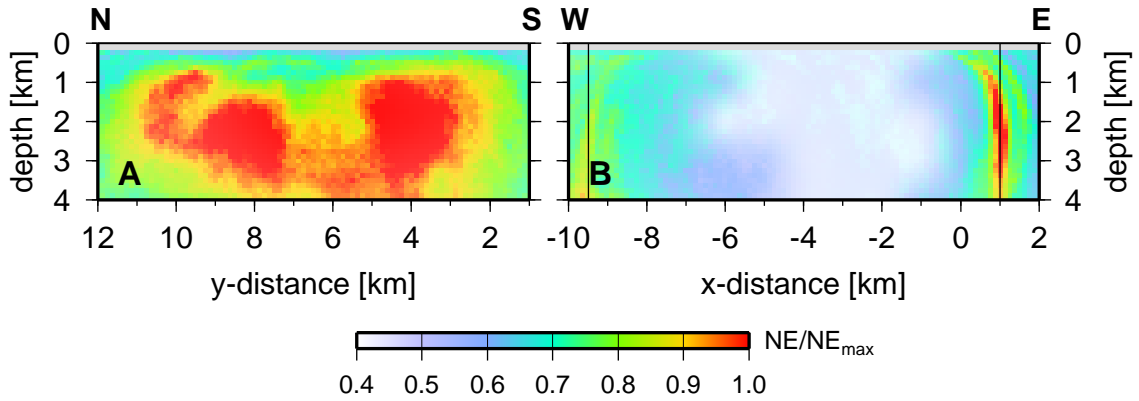
Figure 6.8: Two vertical slices through the imaged volume of a synthetic recovery test for two vertical planes of scatterers located at x = −9.5 km and x = 1 km (solid lines). Large values of the normalised semblance (NE/NE_{max}) indicate the presence of scatterers. The panels A and B represent slices at x = 1 km and y = 8 km, respectively (see map on page 80 and also figure 6.9).

To study the resolution of subvertical zones of scattering related to faults, I conduct the second set of synthetic experiments. I generate a synthetic dataset for two vertical planes of scatterers as described above for single scatterers. The scatterers are placed 0.5 km apart in horizontal and vertical directions down to 4 km depth. Based on indications in the real data, these planes are located under the trace of the Zofar Fault (ZF, $x = −9.5$ km) and about 1 km east of the surface trace of the Arava Fault (AF, $x = 1$ km). Additionally, I add random noise to all synthetic traces (20% of P amplitude) and apply the difference filter described in section 6.3 to include its influence on the imaging result. Figure 6.8 and figure 6.9 show the recovered image along vertical and horizontal slices through the imaged volume. These images are obtained with the same velocity model, acquisition geometry, and subsurface parameterisation as used for spread function calculation and for the real experiment (section 6.3). As expected from the acquisition geometry, scatterers at the ZF, located between several shots and the receiver arrays, can be detected only in a small region in the central part of the studied volume. In contrast to that, the plane of scatterers close to the AF, east of all shots and receivers, is imaged well from about 1 km to about 4 km depth along the segment between 2.5 km and 10.5 km in y-direction (figures 6.8 A, figure 6.9). Segments to the north and to the south are outside the optimum imaging aperture of the receiver array distribution. Like the input plane of scatterers, the imaged scattering zone is very narrow (figure 6.8 B), but it bends towards the receiver array spread. This bend is a migration artefact, because the input plane of scatterers is subvertical at all depths. The upper 1 km is therefore excluded from the presentation and interpretation of the real scatterer distribution imaged. Finally, the analysis of subsets of the data has shown, that the best imaging results are obtained by ray paths with grazing incidence, i.e. from shot array 6 to receiver array 8 or from array 7 to array 2 (see figure 6.3).
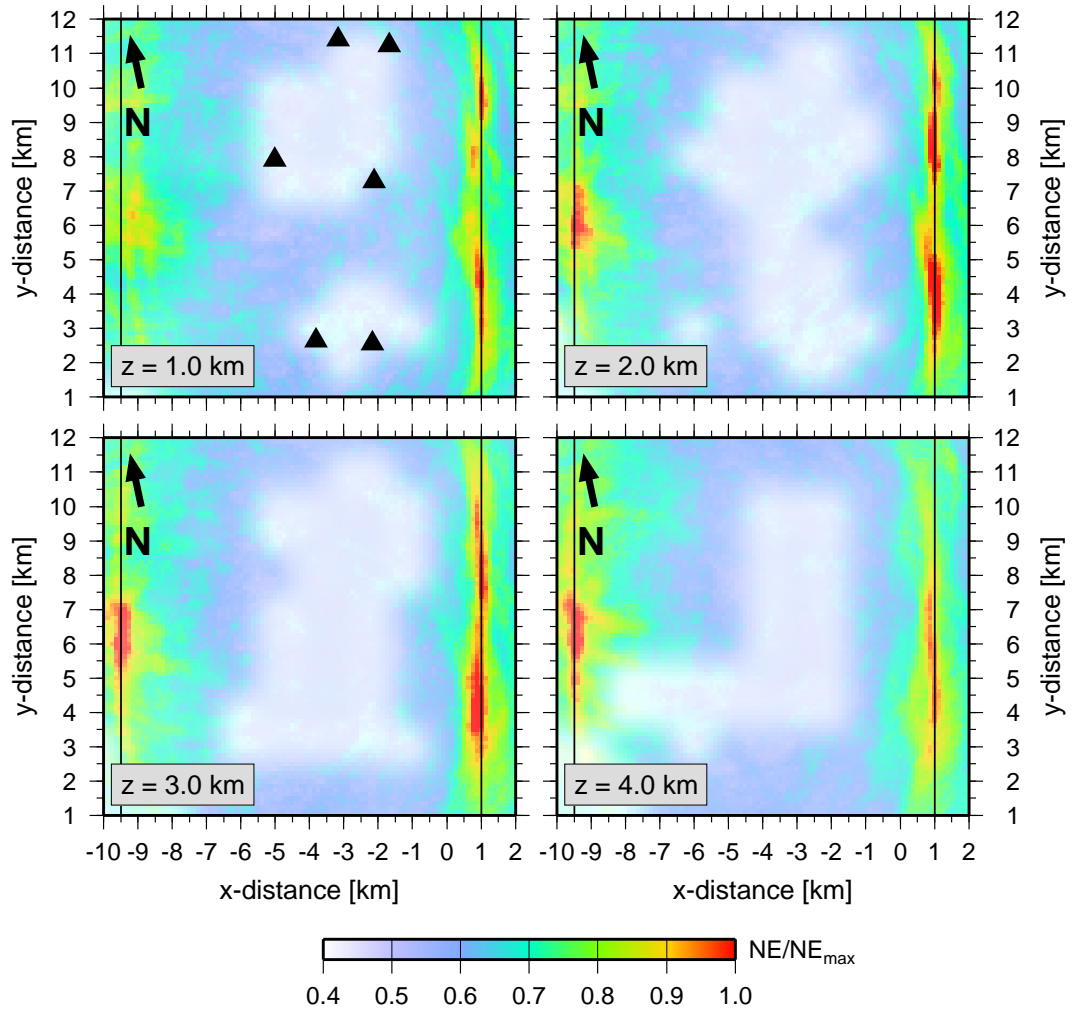
Figure 6.9: *Horizontal depth slices (map views) through the result of a synthetic recovery test for two vertical planes of scatterers located at $x = -9.5$ km and $x = 1$ km (solid lines). Large values of the normalised semblance (NE/NE_{max}) indicate the presence of scatterers, and triangles in the top left panel mark the receiver array locations.*
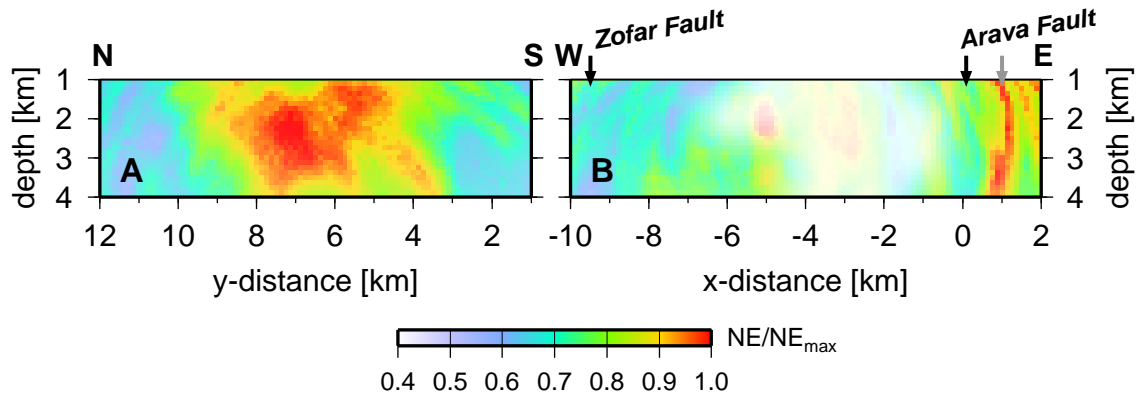
Figure 6.10: Two vertical slices through the scatterer distribution in the vicinity of the Arava Fault, imaged by the western data subset. Zones of strong scattering are indicated by large values of the normalised semblance (NE/NE_{max}), and areas with relatively high spread values (poor resolution) are whitened out. See also the map on page 80 and horizontal depth slices in figure 6.11.

In summary, the scatterer distribution in the main target area around the surface trace of the AF can be well resolved along a 7–8 km long segment in the depth range from 1 km to about 4 km, using the western data subset. With the eastern subset only a limited portion of this region can be imaged as shown in the following section.

6.5 Distribution of scatterers

To image the scatterer distribution in the study area, I assign a local coordinate system with the origin marked in figure 6.3. This system is rotated by $12°$ to have one axis roughly parallel to the surface trace of the Arava Fault (AF, x-axis cross-fault, y-axis parallel). For beamforming and semblance analysis as described in section 6.2, I assign a grid with a spacing of 125 m in all directions. I calculate the semblance in a 0.25 s Hanning-tapered time window, and accept data in the time window from direct *P* to expected direct *S* using a constant v_p/v_s of 1.83 (sections 5.2, 6.3). The one-dimensional *P* velocity-depth function gradually increases with depth, and the precise values used are listed in table 6.1.

Because of the strong velocity contrast near the trace of the AF (section 4.2.2), the available data are split into two subsets: one for imaging the scatterer distribution mainly west of the fault and the other one for the eastern side (see figure 6.3 and table 6.1). Data processing of both subsets includes static corrections and removal of the direct *P* phase (section 6.3). The scanned subsurface volume exceeds that shown here to enable detection of possible artefacts at the boundary of the region reached in the allowed time window.

The final image of the scatterer distribution in the western part is a stack of all 150 individual, normalised images obtained from each shot-receiver array combination west of the

AF. Figure 6.10 shows the scatterer distribution along two vertical cross-sections through the imaged volume and figure 6.10 at six horizontal depth slices. The semblance values in this final image are normalised to the maximum value. Absolute maxima are mostly below $NE \leq 0.5$. Despite these rather low values, the highest semblance values occur always at the times predicted for scattered arrivals (*PxP* phases).

The images reveal a prominent subvertical zone of scattering (*reflector*) trending parallel about 1 km east of the surface trace of the AF and roughly coinciding with another fault strand in the northern part of the study area (grey arrow in figure 6.10 B; see also figure 2.2, page 12). In approximately W-E direction, this structure is horizontally concentrated to about 1–2 subsurface blocks and therefore just up to 250 m wide (figures 6.11, 6.10 B). From south to north the reflector appears between 3 and 10 km in y-direction. Its further extension to the north and to the south remains unresolved as resolution degrades here (section 6.4). The resolved part of the reflector covers a depth range from more than 1 km to about 4 km. Above 1 km depth the image blurs with one branch bending towards the surface trace of the AF. This feature is possibly a migration artefact in this very poorly resolved region (section 6.4) and therefore not included in the figures and in the final interpretation.

Similar to the processing sequence for the western subset, the final image of the scatterer distribution east of the fault is a stack of all 30 individual, normalised images obtained from each shot-receiver array combination involved. Figure 6.12 shows the scatterer distribution at six horizontal depth slices through the imaged volume. Again, the semblance values are normalised to the maximum value. The apparent smearing along circular trajectories, typical for any migration method, is more pronounced in this image compared to the western subset because of the fewer individual images included in the stack. Additionally, some regions of the target volume are not reached within the allowed time window before the arrival of possible *S* energy. This is due to the higher *P* velocities east of the AF and to the acuisition geometry of this data subset. These portions of the target volume are therefore grey-shaded in figure 6.12.

The slices shown in figure 6.12 reveal strong scattering near the fault strand trending parallel to the AF ($x = 1$ km). This zone corresponds to the reflector imaged by the western data subset (figure 6.11). Another zone of scattering is visible around $x = 2$ km and $y = 9$ km. In this region the three-dimensional *P* velocity structure is characterised by high-velocity blocks and a low-velocity, sagged block in between, bounded by the Qurayqira Fault and the Dana Fault (sections 2.2.1 and 4.2.2).
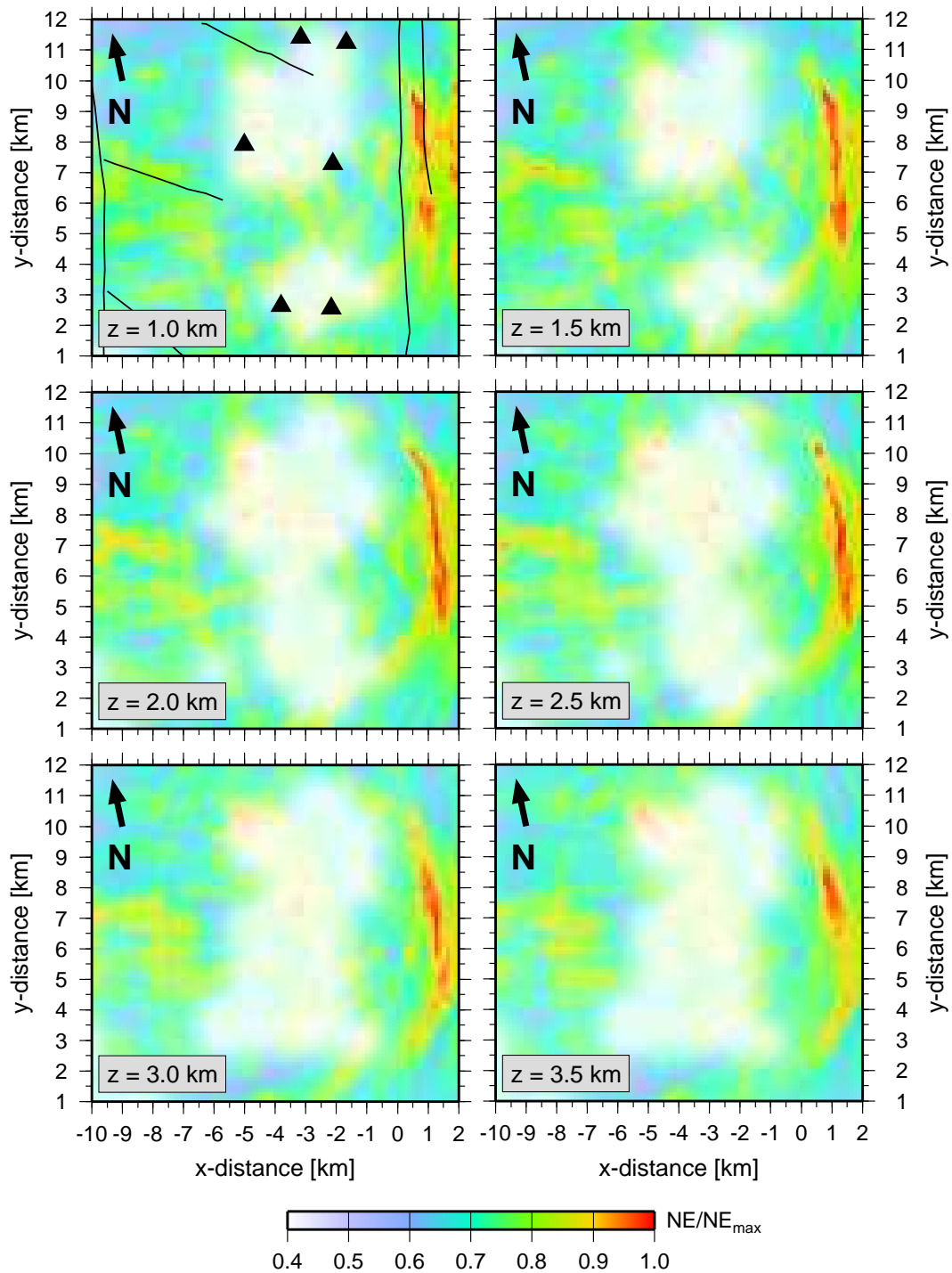
Figure 6.11: *Horizontal depth slices (map views) of the scatterer distribution in the vicinity of the Arava Fault ($x \approx 0$ km), imaged by the western data subset. Zones of strong scattering are indicated by large values of the normalised semblance (NE/NE_{max}), and areas with relatively high spread values (poor resolution) are whitened out. The box orientation is shown in figure 6.3, and triangles in the top left panel mark the receiver array locations.*
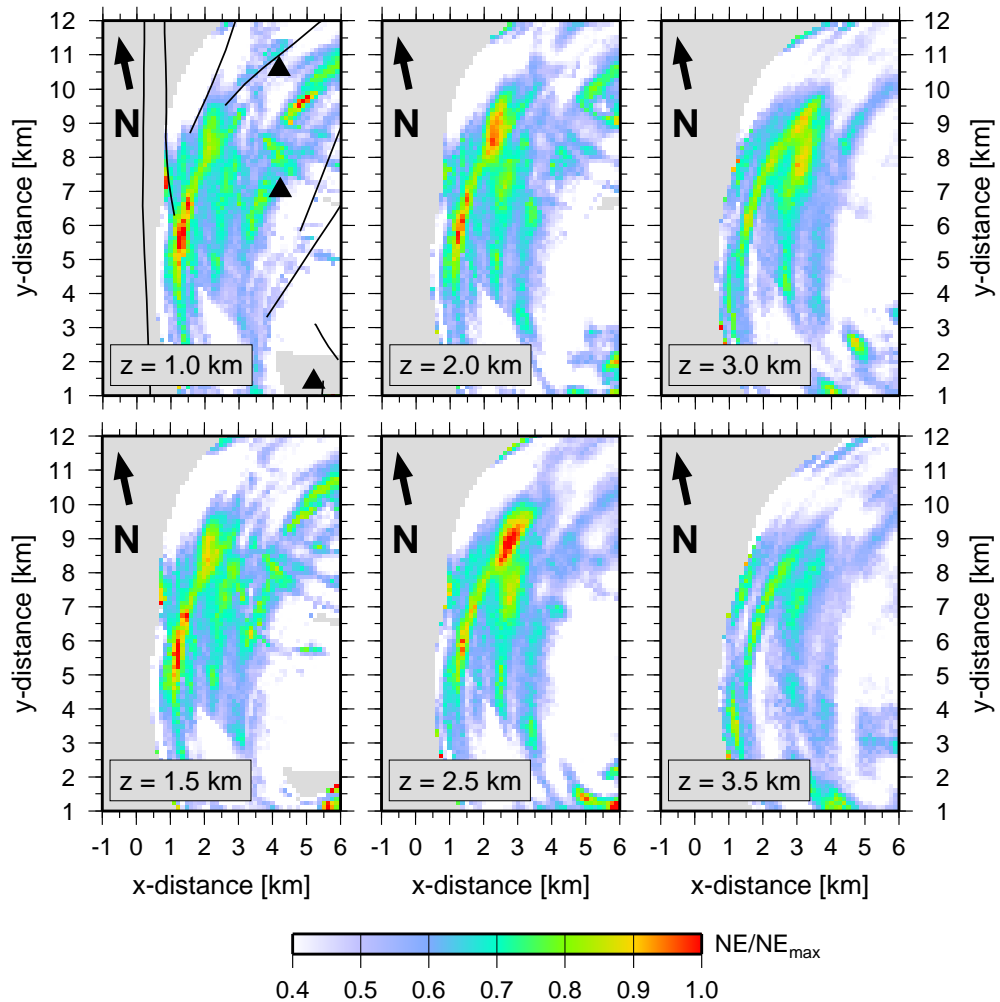
Figure 6.12: *Horizontal depth slices (map views) of the scatterer distribution east of the Arava Fault (x ≈ 0 km), imaged by the eastern data subset. Zones of strong scattering are indicated by large values of the normalised semblance (NE/NEmax), and areas not reached within the allowed time window are grey-shaded. The box orientation is shown in figure 6.3, and triangles in the top left panel mark the receiver array locations.*

7. Velocity and resistivity structure

This chapter combines the velocity structure presented in section 4.2 and the electrical resistivity structure in the CSA study area, derived from magnetotelluric measurements. After an introduction to magnetotelluric methods relevant for this study, subsequent sections describe the magnetotelluric experiment and some results. Finally, I analyse cross-plots of the two parameters seismic velocity and electrical resistivity.

7.1 Magnetotelluric method

The magnetotelluric (MT) method is an electomagnetic prospecting technique in which orthogonal components of horizontal electric and magnetic fields induced by natural primary sources are measured simultaneously as a function of frequency (Sheriff, 1991). Natural electromagnetic fields with frequencies below about 1 Hz and of importance for the MT method originate in the ionosphere and magnetosphere (e.g. Kearey and Brooks, 1991). The time variation results from the interaction of the Earth's magnetic field with the solar wind and from the movement of ionised gases due to tidal and thermal forces. Broad band electromagnetic fields with frequencies above a few Hertz, the *spherics*, are emitted by lightning discharges. The spherics provide a constant source of electromagnetic energy, because those with high energy can travel several times around the Earth and lightning discharges occur constantly on Earth.

Time varying electromagnetic fields penetrate into the subsurface where they induce telluric currents. The induction process is governed by the Maxwell equations and Ohm's law. To adapt these equations to magnetotellurics, several simplifying assumptions are made (Telford *et al.*, 1990; Kaufmann and Keller, 1981). Time variation of the electric field $\mathbf{E}$ and the magnetic field $\mathbf{H}$ is harmonic ($\mathbf{E}, \mathbf{H} \sim e^{i\omega t}$). The incident electromagnetic field is treated as a plane wave and horizontal variations of $\mathbf{E}$ and $\mathbf{H}$ are small compared with their vertical variations. Free charges in the subsurface are not considered; thus, the electromagnetic field is assumed to be source-free. The magnetic permeability of subsurface rocks is small and therefore set to the value for the vacuum. Furthermore, for typical subsurface resistivities of 1–1000 Ωm and the frequency range used here (0.001–1000 Hz) displacement currents are negligible (Telford *et al.*, 1990).

With the assumptions stated above, Weckmann (2002) simplifies the Maxwell equations in

the frequency domain to

$$\nabla \times \mathbf{E} = -i\omega\mu_0\mathbf{H} \tag{7.1}$$
$$\nabla \times \mathbf{H} = \sigma\mathbf{E}$$
$$\nabla \cdot \mathbf{B} = 0,$$

with the angular frequency ω, magnetic permeability of the vacuum μ_0, electrical conductivity σ, the conduction current $\sigma\mathbf{E}$, and the magnetic flux density $\mathbf{B} = \mu_0\mathbf{H}$. Introducing the complex wave number $k = \sqrt{i\omega\mu_0\sigma}$, these equations can be rearranged to two diffusion or Helmholtz equations:

$$\nabla^2\mathbf{H} = k^2\mathbf{H} \quad \text{and} \quad \nabla^2\mathbf{E} = k^2\mathbf{E}. \tag{7.2}$$

A solution of these equations is proportional to $e^{i\omega t - kz}$ with the depth $z \geq 0$. The term e^{-kz} describes the decay of the fields with depth, and the skin or penetration depth δ is defined as the depth where the fields are attenuated to $1/e$ of the surface value. For a homogeneous subsurface it can be estimated as

$$\delta \approx \frac{1}{2}\sqrt{\rho T}, \tag{7.3}$$

with the period $T = 2\pi/\omega$ of an electromagnetic wave and the specific resistivity $\rho = 1/\sigma$.

The ratio of the electric to the magnetic field

$$Z(\omega) = \frac{E(\omega)}{H(\omega)} \quad \text{with} \quad E \perp H$$

is called the magnetotelluric impedance, which is independent of the intensity of the primary field (Telford *et al.*, 1990). For three-dimensional fields the horizontal electric and magnetic components are connected via an impedance tensor (Kaufmann and Keller, 1981):

$$\begin{pmatrix} E_x(\omega) \\ E_y(\omega) \end{pmatrix} = \begin{pmatrix} Z_{xx}(\omega) & Z_{xy}(\omega) \\ Z_{yx}(\omega) & Z_{yy}(\omega) \end{pmatrix} \cdot \begin{pmatrix} B_x(\omega) \\ B_y(\omega) \end{pmatrix} \tag{7.4}$$

or in vector notation

$$\mathbf{E}(\omega) = \underline{\underline{\mathbf{Z}}}(\omega) \cdot \mathbf{B}(\omega).$$

Equation 7.4 is formulated for the magnetic flux density $\mathbf{B} = \mu_0\mathbf{H}$, because this is the measured quantity.

The impedance tensor reflects the dimensionality of the subsurface conductivity structure. In case of a one-dimensional layered half space only electrical and magnetic components perpendicular to each other are correlated. Therefore the diagonal elements of $\underline{\underline{\mathbf{Z}}}(\omega)$ are zero and the off-diagonal elements differ in sign only ($Z_{xy} = -Z_{yx}$). For a two-dimensional structure the conductivity σ varies with depth and one horizontal direction. The diagonal elements of $\underline{\underline{\mathbf{Z}}}(\omega)$ remain zero, but the off-diagonal elements have different values. If the acuisition geometry does not fit a two-dimensional conductivity structure, the impedance tensor $\underline{\underline{\mathbf{Z}}}(\omega)$ can be rotated mathematically by an angle which minimises the squared sum

of the diagonal elements (Swift, 1967; Weckmann, 2002). An alternative measure of the dimensionality is the skewness

$$\chi(\omega) = \frac{|Z_{xx}(\omega) + Z_{yy}(\omega)|}{|Z_{xy}(\omega) - Z_{yx}(\omega)|}. \tag{7.5}$$

A one- or two-dimensional conductivity structure yields $\chi(\omega) = 0$, but values up to $\chi(\omega) \leq 0.2$ or $\chi(\omega) \leq 0.3$ over a broad frequency range are usually accepted for a two-dimensional approximation (e.g. Buttkus, 1991; Hoffmann-Rothe *et al.*, 2001). A true three-dimensional conductivity structure cannot be approximated by two dimensions and all elements of the impedance tensor $\underline{\underline{Z}}(\omega)$ remain non-zero.

The complex impedance tensor $\underline{\underline{Z}}(\omega)$ can be represented as apparent resistivity $\rho_a(\omega)$ and phase $\phi(\omega)$ as functions of frequency ω:

$$\rho_{a,ij}(\omega) = \frac{\mu_0}{\omega} |Z_{ij}(\omega)|^2 \tag{7.6}$$

$$\phi_{ij}(\omega) = \arctan\left(\frac{\mathrm{Im}Z_{ij}(\omega)}{\mathrm{Re}Z_{ij}(\omega)}\right) \tag{7.7}$$

with $i, j = x, y$.

7.2 Magnetotelluric experiment

As part of the DESERT project magnetotelluric measurements in the study area were completed in the years 2000 and 2001 (Ritter *et al.*, 2001). Altogether 101 stations were installed along profiles crossing the Arava Fault roughly perpendicular. Three profiles of 10 km length run along the CSA geophone lines and consist of 33–37 stations each. Seven 4 km profiles are distributed between these lines. Along most of the profiles, the station spacing is 500 m, and it is decreased to 100 m, where the longer profiles cross the surface trace of the Arava Fault. Figure 7.1 shows the locations of all magnetotelluric stations in the CSA study area.

Each station acquired data for a time period of about 48 hours. Schmidt (2002) processed these data to calculate the impedance tensor elements as functions of frequency in a band from 0.001 to 1000 Hz (equation 7.4). He also derived the resistivity models presented below. The following paragraphs outline those parts of his work (Schmidt, 2002), which are relevant for this study.

The data processing included elimination of instrument responses, trace editing, and noise reduction. The data quality, assessed from apparent resistivity and phase curves (equations 7.6, 7.7), is generally high. Examination of the skewness (equation 7.5) justifies a two-dimensional modelling and interpretation. A constant rotation angle of $14°$ N is applied at all stations.
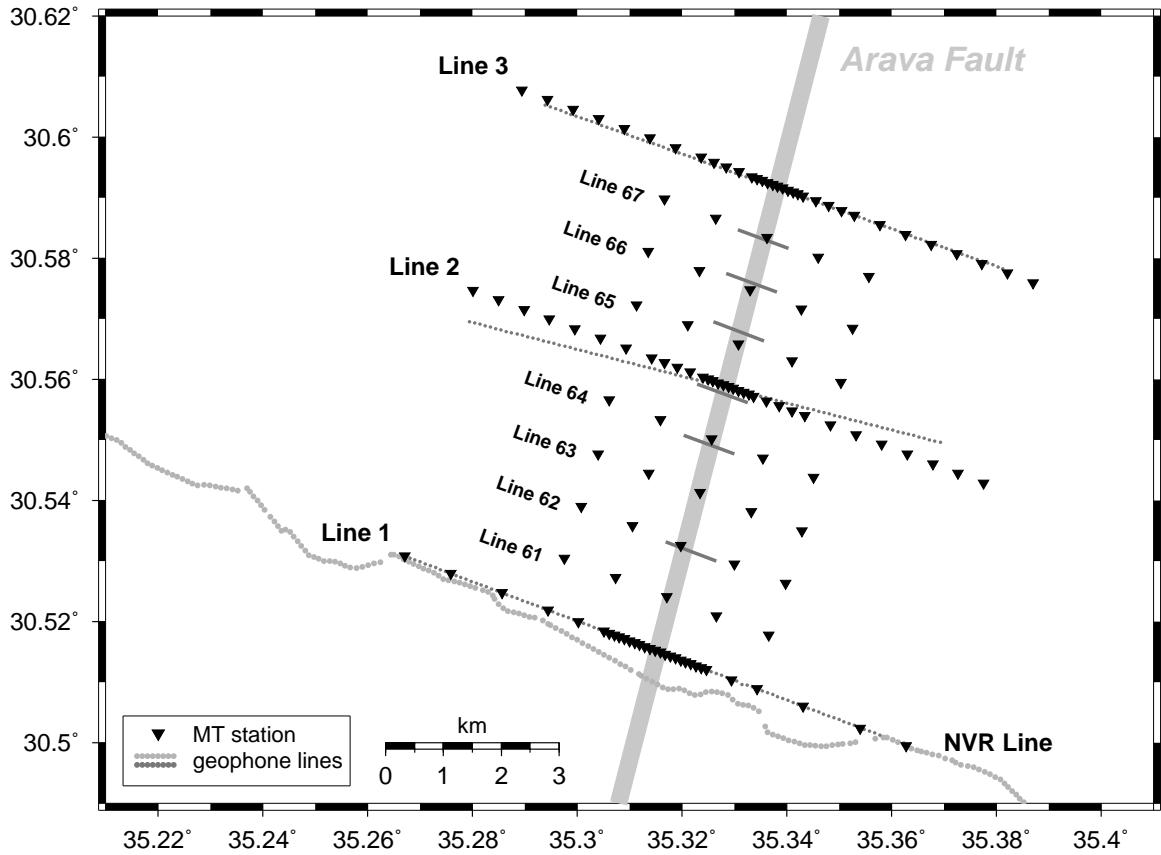
Figure 7.1: *Map showing magnetotelluric stations and the line numbers of model cross-sections. The NVR and CSA geophone lines are included for better orientation.*

The two-dimensional modelling of the subsurface resistivity structure is based on an finite-difference algorithm published by Rodi and Mackie (2001). This algorithm starts from an initial model and seeks a minimum structure model that minimises the least squares misfit between forward modelled and measured data. A regularisation parameter τ controls the compromise between data fit and model constraints; larger values of τ result in smoother, less detailed solutions at the expense of a worse data fit (e.g. Hoffmann-Rothe, 2002).

The inversion for the 10 km profiles 1–3 started as a homogeneous half space with a resistivity of 60 Ωm and a grid of 165 $\times$ 96 nodes each. These are distributed irregularly along the line and to a maximum depth of 5 km. Due to the skin effect (equation 7.3) the minimum frequency considered is about 0.02 Hz, allowing a very conductive subsurface of just 2 Ωm. Errors for the apparent resistivity ρ_a are set constantly to ± 5 % and those for the phase ϕ to ± 2 %. Schmidt (2002) chose the minimum regularisation factor τ, which permits a stable inversion. Several resolution tests with synthetic calculations or different inversion parameters completed this modelling. The 4 km long profiles 61–67 are modelled using a grid of 57 $\times$ 96 nodes and a larger τ, whereas other parameters are the same as for the long profiles.

7.3 Resistivity structure

Electrical resistivity cross-sections for ten profiles in the study area, are a result of the magnetotelluric modelling outlined in section 7.2 (see also Ritter *et al.*, 2003). Figure 7.2 shows the upper 3 km of these models together with corresponding seismic results. Resistivities fall into the range of about 4–260 Ωm.[1] All models have a distinct resistivity contrast in common. It correlates roughly with the surface trace of the Arava Fault (AF). West of the fault, below approximately 1.5 km depth, a conductive layer with resistivities less than 7 Ωm dominates the section. To the north it seems to merge with a shallow conductive layer that also terminates at the AF. The eastern side of the fault is less conductive. There, two resistive structures of more than 100 Ωm are embedded in a quarterspace with uniform resistivities around 40 Ωm. Only the very shallow subsurface is a good conductor east of the AF.

Just a few models deviate from the simple structure described above. At lines 65 and 66 the deeper conductor extents further to the east. Here, the sharp resistivity contrast in 1–2 km depth correlates with a different fault striking parallel to the Arava Fault (figure 2.2, page 12). The model for the northernmost line 3 is rather complex. Schmidt (2002) excludes disturbed stations or model artefacts, but the vicinity of line 3 may be a region, where the assumption of a two-dimensional subsurface resistivity structure is not valid strictly.

The three-dimensional seismic *P* velocity model is described in detail in section 4.2.2. In brief, a velocity contrast correlates roughly with the surface trace of the AF, and the velocities are generally higher on the eastern side than west of the fault.

The seismic velocity structure reflects the different lithologies adjacent at the AF: young sedimentary fill in the west and Precambrian igneous rocks in the east (sections 2.2 and 4.2.2). Effective electrical conductivities or resistivities of many rock types depend mainly on the conductivity of fluids filling pores and fractures (Telford *et al.*, 1990; Schön, 1996). The conductive layer west of the AF is interpreted as sediments filled with saline fluids (Schmidt, 2002; Ritter *et al.*, 2003). Their salinity is in the range of seawater. Since massive, dry igneous rocks generally exhibit much higher resistivities (Schön, 1996) than those modelled east of the AF, it is likely that the igneous rocks there are fractured and filled with (less saline) water. The shallow conductor on the eastern side can be related to meteoric water originating at the eastern valley shoulder and reaching the surface at water holes along the AF (section 2.2.1). Within the entire depth range imaged at line 1, the AF seems to act as an impermeable boundary for fluid flow (Ritter *et al.*, 2003).

---

[1] Resistivities of 4–260 Ωm correspond to electrical conductivities between 250 mS/m and 3.85 mS/m.

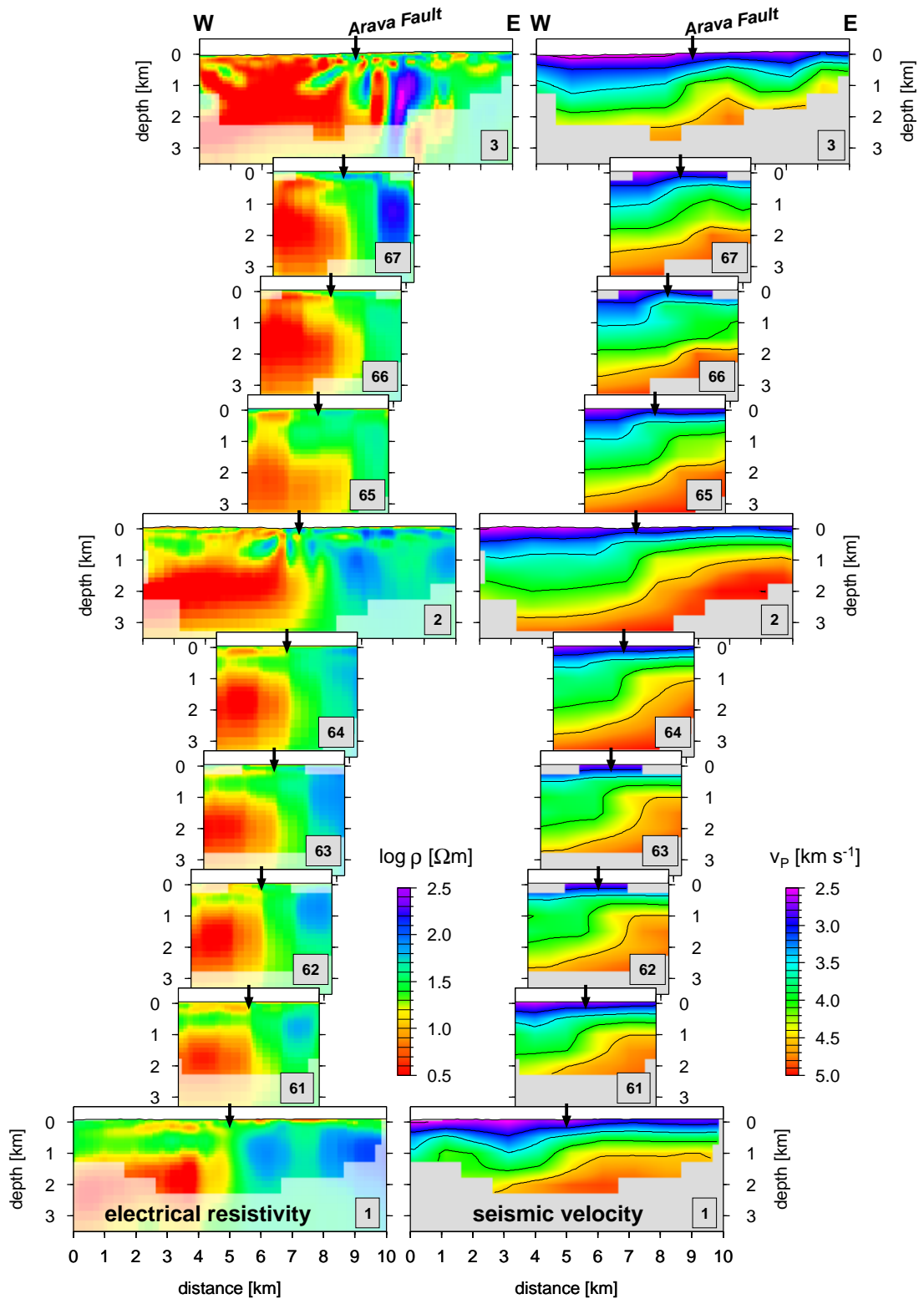**Figure 7.2:** *Electrical resistivity models (Schmidt, 2002) and coincident cross-sections through the three-dimensional P velocity model presented in section 4.2.2. Regions not resolved by seismic velocity tomography are shown in light colours in resistivity profiles on the left. The distance between profiles is about 1 km, and arrows indicate the surface trace of the AF. See also the map on page 96.*

7.4 Correlation of resistivities and velocities

Different geophysical methods are often combined in studies to image and characterise sub-surface lithologies. Coincident seismic and geoelectric or magnetotelluric investigations range from crustal and lithospheric scale (e.g. Eberhart-Phillips *et al.*, 1995; Jones *et al.*, 2002; Bedrosian, 2002) to upper-crustal studies (e.g. Bibby *et al.*, 1995; Unsworth *et al.*, 2000; Dell'Aversana, 2001; Ritter *et al.*, 2003; Haberland *et al.*, 2003a) and engineering applications (e.g. Karastathis *et al.*, 2002). Furthermore, some studies focus on joint inversion methods for seismic and electric data (e.g. Hering *et al.*, 1995; Gallardo and Meju, 2003). In this study, I analyse the resistivity and velocity structure across the Arava Fault (AF) in a similar fashion as Bauer *et al.* (2003), Meju *et al.* (2003), and Haberland *et al.* (2003a). They correlated seismic *P* and *S* velocities, seismic velocities and electrical resistivities, and seismic attenuation and resistivities, respectively.

Qualitatively, the resistivity models and the corresponding *P* velocity sections exhibit a similar subsurface structure (figure 7.2, and Ritter *et al.* (2003)). Correlating with the surface trace of the AF are strong lateral contrasts in electrical resistivity and seismic *P* velocity. Higher values of both arise east of the fault and lower on its western side. Additionally, both methods yield a more complex structure in the northern part of the modelled area.

A problem in combining these independent models of resistivity ρ and *P* velocity v_p is their different physical meaning, acquisition scale, and resolution power (e.g. see Dell'Aversana, 2001). Here, the subsurface resistivity distribution is much higher resolved along the two-dimensional profiles than the tree-dimensional seismic velocity structure. The two-dimensional velocity structure along the NVR reflection line (section 3.1), coincident with line 1 of this study, exhibits a resolution similar to that of the corresponding resistivity model. Furthermore, in this study quantitative resolution measures are available only for the velocity models. Therefore, I analyse only those resistivity-velocity (ρ-v_p) data pairs that belong to regions resolved by seismic tomography. Since the two-dimensional velocity model along the NVR reflection line has a much higher resolution than the three-dimensional model of the study area (section 4.2.2), I compare resistivities and velocities in this region first and then extend the analysis to the tree-dimensional structure of both physical properties.

From an equally spaced grid assigned to the subsurface (50 m spacing), I take the resistivities and corresponding velocities and map these data pairs into a two-dimensional histogram (cross-plot) of *P* velocity versus the logarithm of electrical resistivity ($\log \rho$). Figure 7.3, left, shows the frequency of occurrence of each ρ-v_p data pair modelled along the coincident section of the NVR line and magnetotelluric measurements (line 1). Relative abundances of ρ-v_p pairs are displayed as shades of grey. Black areas indicate most frequent occurrences of ρ-v_p pairs and white areas those pairs not existing in the models.

The ρ-v_p data pairs cluster into several groups with different seismic and electric properties (figure 7.3, left). These groups are apparent as dark patterns separated by white or light-grey areas in the histogram. Ellipses outline four different groups denoted as $\mathbb{A}$, $\mathbb{B}'$, $\mathbb{P}$, and
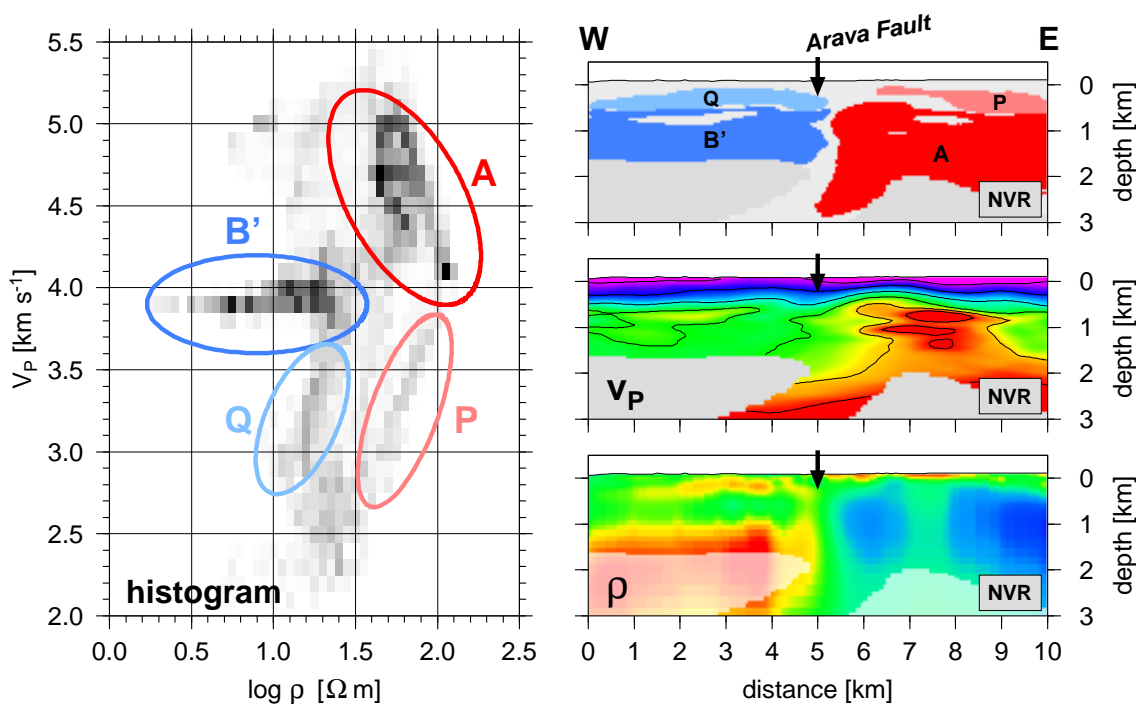
Figure 7.3: *Histogram of resistivities and velocities along the NVR reflection line, and classification of subsurface lithologies.* Left: *Histogram (cross-plot) of seismic velocities v_p versus logarithmic electrical resistivities $\log \rho$. Most abundant ρ-v_p data pairs are in black, and ellipses outline property classes apparent in this histogram.* Right, bottom to top: *resistivity model near the NVR line, corresponding P velocity model, and property classes derived from the histogram and remapped into the subsurface. Colour scales for the ρ and v_p sections are included in figure 7.2.*

$\mathbb{Q}$. Because these groups represent different sets of the physical properties velocity and resistivity, I use the term property class hereafter to refer to a certain group. The term cluster is reserved for a clearly visible and distinct accumulation of ρ-v_p pairs in the histogram. Guided by the pattern of clusters in the histogram, I defined the property classes manually. Hence, the classes are adapted to the modelled subsurface properties in the study area.

Two prominent clusters appear in the ρ-v_p histogram, which belong to the classes $\mathbb{A}$ and $\mathbb{B}'$ (figure 7.3, left). Class $\mathbb{A}$ is defined by high seismic P velocities and high resistivities, whereas $\mathbb{B}'$ comprises almost constant velocities around 3.9 km s^{-1} and a broad range of resistivity values. Both classes and their associated clusters are clearly separated in the histogram. The two remaining classes $\mathbb{P}$ and $\mathbb{Q}$ outline weak ρ-v_p patterns that show a linear relationship between v_p and $\log \rho$. Low seismic velocities and intermediate to high resistivities describe these two classes.

The clustering of ρ-v_p pairs is an indication for different lithologies along the studied profile. To get an image of such different units, I map ρ-v_p from each property class back into the subsurface, i.e. to their original spatial location. Figure 7.3, right, shows a section of the

classified lithologies along the studied segment of the NVR line (top panel) together with the correlated original resistivity and velocity models. Each property class is represented by the same colour as used to delineate its boundary in the ρ-v_p histogram.

Each class covers a distinct region of the subsurface with a pronounced boundary near the surface trace of the AF. The classes $\mathbb{A}$ and $\mathbb{P}$ are confined to the region east of the fault, whereas the classes $\mathbb{B}'$ and $\mathbb{Q}$ occur only on the western side. The separation into different blocks corroborates the qualitative observation of a lithological boundary at the AF in the vicinity of the NVR line (sections 4.2.2 and 7.3). A comparison of the spatial distribution of property classes with the ρ and v_p sections (figure 7.3, right) demonstrates that class $\mathbb{A}$ is associated with rather uniform and high resistivities and mostly high seismic velocities, both related to Precambrian volcanites in this region. Class $\mathbb{B}'$, west of the AF, defines a region of a constant velocity v_p, and the range of resistivity values reflects the increase in conductivities with depth. This observation is an evidence for a possibly homogeneous, fluid-filled sedimentary sequence and an increase of salinity with depth. The classes $\mathbb{P}$ and $\mathbb{Q}$ are associated with the shallow subsurface above 0.5 km depth. These classes exhibit a linear relation of v_p and $\log \rho$ with a coincident increase of both properties with depth. The velocity increase with depth is due to compaction and the closure of pores (e.g. Sheriff and Geldart, 1995). The coincident increase of resistivity (decrease of conductivity) possibly reflects the decreasing pore space and connectivity with depth, because the fractional amount of conductive fluid decreases. The separation of $\mathbb{P}$ and $\mathbb{Q}$ at the AF trace indicates different geological units juxtaposed at this fault.

The same analysis as with the two-dimensional NVR velocity model can be conducted with the ten resistivity models across the AF in the study area and corresponding slices through the three-dimensional P velocity model presented in section 4.2.2. Figure 7.2 shows the corresponding resistivity and velocity sections, and figure 7.4 includes the histogram of velocities v_p and resistivities $\log \rho$. This histogram is calculated for all ρ-v_p data pairs at 50 m spaced grid nodes assigned to all lines and within regions resolved by the tomographic inversion (section 4.2). Again, ellipses define property classes, selected according to various patterns apparent in the histogram. Class $\mathbb{A}$ comprises the same ρ-v_p pairs as defined above, whereas class $\mathbb{B}$ is slightly shifted compared to $\mathbb{B}'$ defined above. The classes $\mathbb{C}$ and $\mathbb{D}$ include ρ-v_p pairs that are mostly missing in the NVR model or the upper part of line 1. The classes $\mathbb{P}$ and $\mathbb{Q}$, associated with the shallow subsurface, are not defined here, because clusters that justify such a definition do not appear in the histogram. The shallow subsurface is represented as a diffuse distribution of relatively low velocities and intermediate resistivities (figure 7.4, top left).

Figure 7.4, right, contains the property classes remapped into the subsurface. This process is also applied to the NVR velocity model for comparison with line 1 (figure 7.4, bottom left). As observed at the southernmost line 1 and the coincident NVR model, the subsurface along the AF is divided into distinct units with a prominent boundary near the AF surface trace. Hence, the defined classes describe the different lithological units in the study area. Class $\mathbb{A}$ is always confined to the region east of the AF. Whereas the western boundary of $\mathbb{A}$ is close

to the AF trace, it is offset to the east at all sections further north. The minimum depth of $\mathbb{A}$ is about 0.5 km. The classes $\mathbb{B}$ and $\mathbb{C}$ dominate the region west of the AF. With the major exception of line 66, their eastern boundary coincides with the fault trace. In the northwest of the study area (lines 66, 67, and 3) a region occurs that is characterised by low velocities and low resistivities and denoted as class $\mathbb{D}$. The gap of unclassified lithologies near the AF may be due to to the limited subhorizontal resolution of the velocity model (section 4.2). But the image of a scattering zone (section 6.5) suggests that the major boundary between the different lithological blocks is in fact offset to the east by about 1 km relative to the surface trace of the AF.

Class $\mathbb{A}$, east of the AF, defines a rather uniform block in the southern region between lines 1 and 2 (figure 7.4). Further north, this unit is more complex. This is the region where the Qurayqira Fault (QF) and the Dana Fault (DF) appear to merge with the AF (figure 2.2, page 12). A sagged block of lower seismic velocities than in the surrounding region, bounded by the QF and DF, separates high velocity regions in the southeast and in the north. These regions are related to Precambrian volcanites and Precambrian granites, respectively (sections 2.2 and 4.2.2).

West of the AF, the classes $\mathbb{B}$ and $\mathbb{C}$ form a layered subsurface structure with $\mathbb{B}$ on top of $\mathbb{C}$ (figure 7.4). This basic structure remains constant throughout the entire study area west of the AF. Class $\mathbb{B}$ extends down to about 1.5 km depth and describes a unit with rather uniform seismic velocities and a minor decrease of resistivities with depth. Following the previous discussion of the NVR line, this resistivity decrease is due to an increase in salinity with depth. A unit described by class $\mathbb{C}$ fills the deep portions of the classified sections. Here, velocities v_p and resistivities ρ increase with depth simultaneously, and the relation between v_p and $\log \rho$ is roughly linear. Assuming that the salinity of subsurface fluids remains constant within unit $\mathbb{C}$, the trend of v_p and $\log \rho$ can be explained by subsequent compaction and porosity reduction with depth.

Both, lowest velocities and resistivities are defined for class $\mathbb{D}$. Corresponding ρ-v_p data pairs are found only in the northwestern corner of the study area (figure 7.4). Furthermore, the relation between v_p and $\log \rho$ follows the opposite trend as within class $\mathbb{C}$, i.e. increasing velocities coincide with decreasing resistivities (increasing conductivities). Here, a possible salinity increase of the pore fluid may superimpose the effect of porosity reduction with depth, which leads to an increase of seismic velocities (e.g. Sheriff and Geldart, 1995). Alternatively, if rather constant porosity is assumed within $\mathbb{D}$, an increase of saturation with depth can explain the observed trend of v_p and ρ. Anyway, the opposite relations of v_p and ρ demonstrate that the classes $\mathbb{C}$ and $\mathbb{D}$ describe different geological layers, whereas the resistivity model of line 3 suggests a uniform conductive layer from the surface to the bottom of the section analysed in this study. Seismic reflection profiles in this area support the interpretation of $\mathbb{C}$ and $\mathbb{D}$ as different layers. Reflections of sedimentary layers, dipping to the north, occur at the boundary of these two classes (see figure 3.2, page 20).
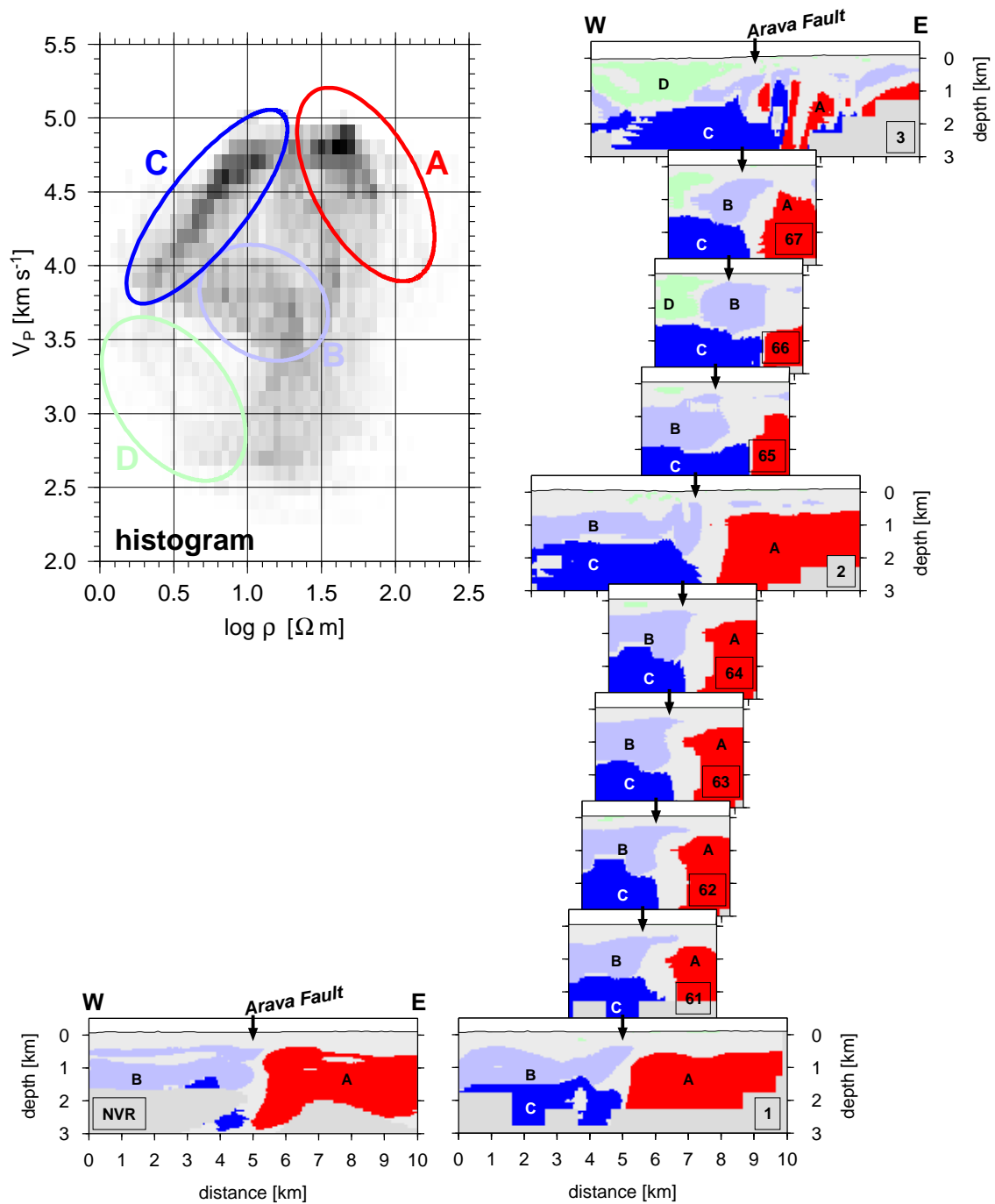
Figure 7.4: *Histogram of resistivities and velocities in the CSA study area, and classification of subsurface lithologies.* Top left: *Histogram (cross-plot) of seismic velocities v_p versus logarithmic electrical resistivities $\log \rho$. Most abundant ρ-v_p data pairs are in black, and ellipses outline property classes apparent in this histogram.* Right: *Property classes derived from the histogram and remapped into the subsurface. The corresponding velocity and resistivity cross-sections are shown in figure 7.2, and line numbers are indicated in figure 7.1. Classes apparent in this histogram are remapped into the velocity structure along the NVR line* (bottom left) *for comparison with line 1* (bottom right).

In summary, independent seismic velocity sections and resistivity models across the AF in the study area reveal a pronounced lithological contrast near the surface trace of the AF. The combined analysis of both parameters and the definition of property classes can be used to map regions of uniform physical properties and thus the different lithologies in the study area. The lithological boundary near the AF is sharp and subvertical (see also Ritter *et al.*, 2003). North of line 1 and below 1 km depth, the boundary appears to be offset to the AF surface trace, as indicated also by scattered seismic waves (section 6.5).

In this study, I defined the classes from visual inspection of ρ-v_p histograms. An application of cluster analysis and pattern recognition algorithms (e.g. Aminzadeh and Chatterjee, 1987) can improve the characterisation of lithologies from different geophysical investigations (see also Bauer *et al.*, 2003). A combined statistical analysis of an approximately 50 km segment of the NVR velocity model and a coincident magnetotelluric resistivity model is in preparation (Ryberg *et al.*, 2003).

8. Discussion and conclusions

Seismic investigations at the Arava Fault (AF), the major fault at the segment of the Dead Sea Transform (DST) between the Red Sea and the Dead Sea, reveal the subsurface structure of the upper 3–4 km of the crust in the vicinity of this fault and of the fault zone itself. Seismic images obtained in this study comprise the three-dimensional velocity structure and shallow velocity sections across the AF from tomographic inversions, the P-to-S velocity ratio (v_p/v_s ratio) from local earthquake and controlled-source data, the distribution of scatterers near the transform trace, and properties of different lithological blocks from seismic and magnetotelluric models. Coincident geophysical studies in the area include modelling of fault-zone guided waves (Haberland *et al.*, 2003b), a combined interpretation of seismic and magnetotelluric profiles (Ritter *et al.*, 2003), and reflection seismic profiles (e.g. DESERT Group (2004); see also section 3.1).

Geophysical observations

Figure 8.1 summarises the geophysical observations of this study and coincident investigations. Structural differences occur between the shallow subsurface, down to one or a few hundreds of metres depth, and at depths greater than about 1 km. The maximum depth considered here is about 4 km below sea level. To avoid repitions, I summarise the principal results in the following paragraphs and refer to individual sections for details.

At depths greater than about 1 km, the three-dimensional tomographic inversion (section 4.2.2) reveals different seismic velocity structures west and east of the AF. A sharp velocity contrast is imaged near the fault trace and correlates with its strike. The western side is characterised by low P velocities and a rather uniform structure with velocities varying with depth only, whereas the eastern side exhibits a blocky structure and higher P velocities (e.g. figure 4.9, page 41). In the southeast the velocity structure seems to be rather simple, and in the northeast a sagged, fault-bounded block of lower velocities, which separates a high-velocity block just south of Jebel Hamrat Fidān from the region of high velocities in the southeast (see figure 8.1). The essentially two-dimensional velocity structure with a contrast near the AF is confirmed by a two-dimensional velocity model along the NVR reflection line, which coincides with line 1 of this study (Ryberg *et al.*, 2001; Ritter *et al.*, 2003). Moreover, there is evidence for a cross-fault variation of the v_p/v_s ratio with a higher v_p/v_s ratio (lower S velocities) west of the AF (section 5.2.2). However, only an average, constant v_p/v_s of 1.83 can be determined from two local earthquake recordings included in the available dataset. Results of regional and local gravimetric measurements are in agreement with the determined velocity structure (ten Brink *et al.*, 2001; Götze *et al.*, 2002).

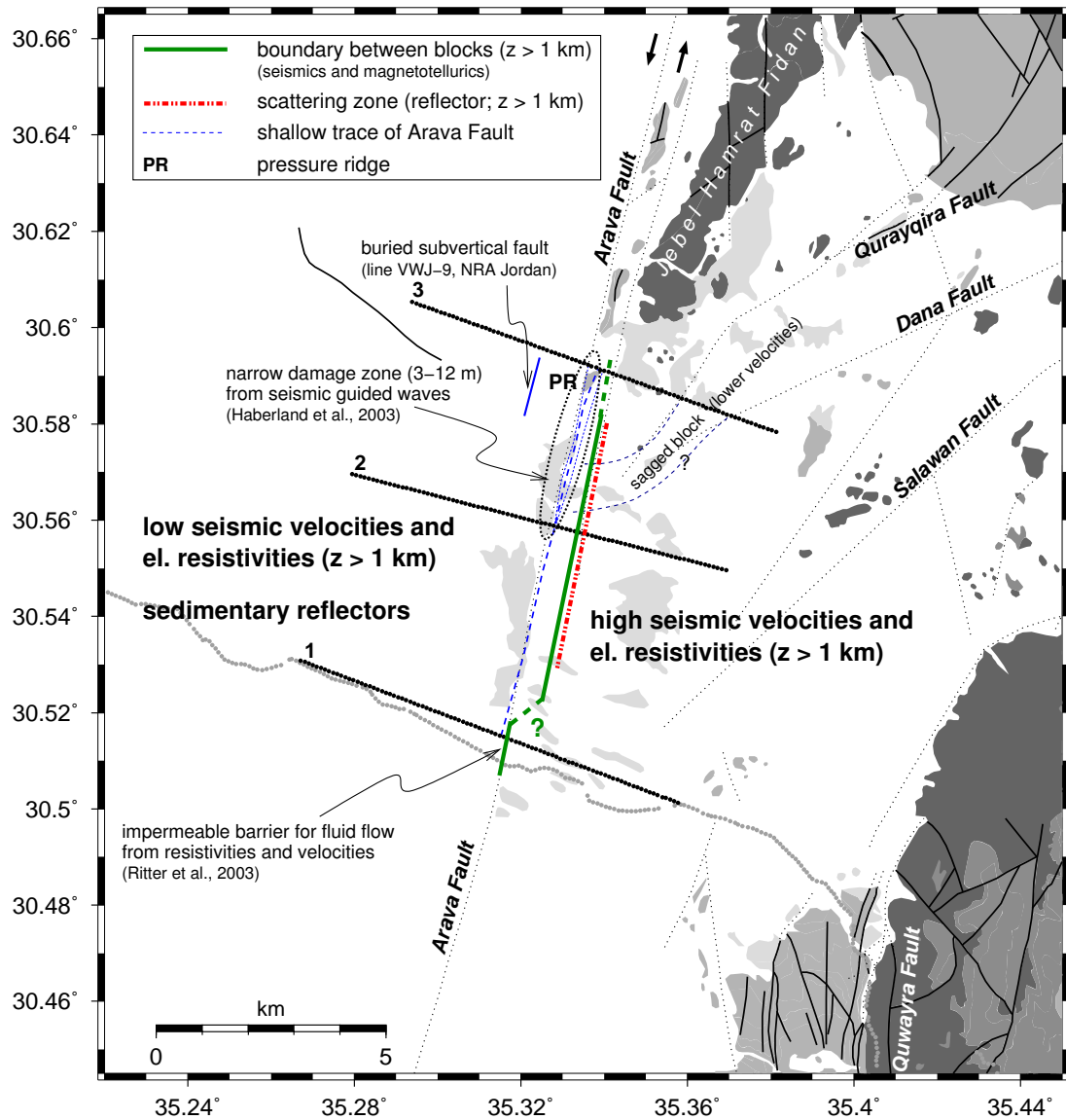***Figure 8.1:*** *Map summarising geophysical observations in the study area. Additionally, Götze* et al. *(2002) inferred higher rock densities east of the Arava Fault than west of it. The NVR and CSA geophone lines are included for better orientation. Surface geology (dark grey to white): Precambrian igneous rocks, Cambrian and Ordovician, Cretaceous, Tertiary, and Quaternary (see figure 2.2, page 12, for details).*

Also seismic reflection profiles in the study area (section 3.1) show two different subsurface structures separated by AF. Whereas the eastern side exhibits a poor reflectivity, the western side is dominated by roughly subhorizontal reflectors related to sedimentary layers (figure 3.2, page 20, and DESERT Group (2004)). These reflectors dip slightly to the north towards the Dead Sea basin, and this trend is indicated by a slight northward decrease in seismic velocities at a certain, constant depth level.

The electrical resistivity models from a local magnetotelluric survey (Ritter *et al.*, 2001, 2003; Schmidt, 2002) reveal a subsurface structure at depths greater than 1 km that is similar to that obtained from the three-dimensional seismic velocity tomography (see figure 7.2, page 98). Here, electrical resistivities are lower on the western side of the AF than on the eastern side, or respectively higher conductivities in the west and lower conductivities in the east. A correlation of both physical parameters, seismic P velocities and electrical resistivities, illustrates similarities in both models and suggest the separation into different lithological units with distinct physical properties on both sides of the AF (section 7.4). Rather uniform physical properties characterise the eastern side of the fault, whereas the western side comprises a layered structure of essentially two units (figure 7.4, page 103). The subvertical boundary between the western units and the eastern one coincides with the surface trace of the AF at line 1 (see also Ritter *et al.*, 2003), and this boundary seems to be offset to the east at the cross-sections further north (figure 8.1 and figure 7.4, page 103).

The spatial distribution of seismic scatterers in the vicinity of the AF (section 6.5) also indicates an offset boundary between the western and the eastern blocks (figure 6.11, page 91). The analysis and migration of scattered seismic phases reveal a 7 km long, subvertical zone of scatterers (reflector) in the depth range from 1 km to 4 km and offset about 1 km to the east of the AF surface trace (figure 8.1). The absence of clearly visible fault-reflected waves indicates a smooth transition between the two blocks or a complex shape of the boundary in the length scale of the dominant wavelength (a few hundreds of metres). Both models are supported by finite-difference modelling of fault reflections (section 5.3), but the shape of the velocity contrast resolved tomographically along the NVR line (figure 4.8, page 40; see also Ritter *et al.* (2003)) suggests the latter model.

The shallow subsurface structure (upper 100 m) as deduced from geophysical investigations correlates well with the surface trace of the AF. Tomographic P velocity models across the AF reveal a contrast near the fault trace with generally lower velocities on the eastern side than in the west (figure 4.16, page 54). Although resolvable theoretically, there is no evidence for a wide (more than 50 m) low-velocity zone beneath the AF trace, which would be related to the fractured damage zone of this fault. Seismic reflection sections along the same profiles (section 5.4; figure 5.11, page 74) show disturbed and terminating reflectors near the AF trace and structures related to a pressure ridge in the northern part of the study area (see figure 8.1). The shallow seismic structure of the AF, deduced in this study, fits to modelling results of seismic guided waves by Haberland *et al.* (2003b). They suggested a narrow damage zone of 3–12 m width for a segment of the AF in the study area (figure 8.1). Besides that, electrical resistivity cross-sections from the local magnetotelluric study show a sharp

resistivity contrast at shallow depths and coinciding with the trace of the AF (figure 7.2, page 98). Here, a shallow conductive layer east of the AF terminates at the fault trace.

Interpretation and comparison with other large fault zones

The modelled P velocity structure reflects the local geology in this region (sections 2.2 and 4.2.2). The lower velocities west of the AF and subhorizontal seismic reflectors (figure 3.2, page 20) can be related to the young sedimentary fill of the basin west of the fault (Bartov *et al.*, 1998; DESERT Group, 2004). This basin fill mainly comprises sediments of the Hazeva Group and Dana conglomerates that were in part synkinematically deposited during the Miocene (section 2.2.2), and also the eastern side is partly covered by thin layers of Hazeva Group strata and younger deposits. At greater depth, the blocky structure with relatively high velocities east of the AF is associated with Precambrian igneous rocks, and the sagged block, bounded by the Qurayqira Fault and the Dana Fault, seems to separate granits of the Jebel Hamrat Fidān from buried volcanics in the southeast of the study area (figure 8.1; see also figure 2.3, page 14). However, the dominant feature is the strong velocity contrast near the surface trace of the AF. Such a velocity contrast has been deduced also at the San Andreas Fault zone, California, in numerous tomographic studies (Lees and Malin, 1990; Michelini and McEvilly, 1991; Eberhart-Phillips and Michael, 1993; Thurber *et al.*, 2003).

Chavarria *et al.* (2003) used scattered seismic waves to image the San Andreas Fault. At the AF, I interpret the imaged subvertical zone of scattering or *reflector* as the boundary between the two different lithological blocks, which were most probably juxtaposed by displacement along the DST. The reflector coincides with a fault strand mapped east of the surface trace of the AF (Rabb'a (1991) and figure 8.1), and its position is in agreement with the three-dimensional P velocity structure. Outcrops of Precambrian granites with high P velocities, mapped only east of the reflector position, support the interpretation that the reflector marks the boundary between the two lithological blocks. Furthermore, there are indications for a correlation of the reflector position with subsurface changes of electrical resistivity as mentioned above. This is illustrated further by the combined analysis of seismic velocity and electrical resistivity cross-sections, where the western boundary of the eastern lithological block seems to correlate with the imaged reflector position along its entire extent (see figure 8.1). South of the imaged reflector segment, the boundary between the two blocks seems to correlate with the surface trace of the AF as indicated by the combined analysis of velocities and resistivities (line 1 in figure 7.4, page 103) and as published by Ritter *et al.* (2003).

On the other hand, surface geological mapping (Bender, 1975; Rabb'a, 1991), neotectonic studies (Klinger *et al.* (2000b); see also section 2.2), and the shallow geophysical investigations in the study area delineate the current surface trace of the AF. At greater depths, below 1 km, the boundary between the two lithological blocks appears to be offset to the east. Such an offset between the boundary of two blocks and the current fault trace at the surface has been suggested by Park and Roberts (2003) also for the San Andreas Fault near

Parkfield, California. At the AF, the relation between very shallow observations and the deeper structure remains unresolved.

The subsurface structure of the AF as inferred from this study and other coincident geophysical investigations (Haberland *et al.*, 2003b; Ritter *et al.*, 2003; DESERT Group, 2004) puts this fault in marked contrast to other major fault zones. Whereas a velocity structure of high and low velocity blocks is also imaged at the San Andreas Fault (e.g. Thurber *et al.*, 2003), this fault also exhibits a 100–170 m wide low-velocity waveguide related to the damage zone (Li *et al.*, 1990), and Ben-Zion *et al.* (2003) reported damage zone widths around 100 m for a segment of the North Anatolian Fault in Turkey. According to Wallace and Morris (1986) the damage zone width appears to proportional to the total slip along a fault (see also Stirling *et al.*, 1996; Scholz and Gupta, 2000). The constant of proportionality is in the range from 10^{-3} to 10^{-1} (Scholz, 1987). Contrarily, Haberland *et al.* (2003b) determined just 3–12 m for the upper 300 m of a segment of the AF (see figure 8.1). Additionally, the shallow velocity models across the AF (section 4.3.2) and the velocity structure along the NVR profile do not reveal a wide, subvertical low-velocity zone correlating with the AF or other faults in the study area.

Resistivity models for other large fault zones often feature a conductive zone beneath their surface expressions. At a segment of the San Andreas Fault, a location described as transitional between locked and creeping, Unsworth *et al.* (2000) found such a fault zone conductor extending to 3 km depth, and they relate it to saline fluids circulating within the fault zone. The maximum depth of the conductor there correlates with the occurrence of small earthquakes, and its width is comparable to the fault-related low-velocity zone determined by Li *et al.* (1990). Generally, a fault zone conductor is a typical feature for active segments of the San Andreas Fault (Bedrosian *et al.*, 2002), whereas it does not appear at a locked and seismically quiet segment (Unsworth *et al.*, 1999). Besides that, Bedrosian (2002) imaged blocks with different physical properties at this fault from combined seismic and magnetotelluric investigations. Another example for a pronounced fault zone conductor is the West Fault Zone in Chile (Hoffmann-Rothe, 2002; Janssen *et al.*, 2002). In contrast, there is no evidence for a fault zone conductor at the studied segment of the AF. Here, subhorizontal conductive layers are confined to either side of the fault. Thus, the boundary between conductive layers on one side and resistive regions on the other side appears to act as an impermeable barrier for fluid flow in the south of the study area (Ritter *et al.*, 2003). Generally, this seems to remain true further north, along the entire segment of the AF in the study area. But whereas the barrier correlates with the trace of the AF at shallow depths, the boundary between the different lithological units seems to be offset eastward below 1 km depth as deduced from the correlation of subsurface resistivities and velocities and supported by the imaged subvertical reflector (see figure 8.1). If a fault zone conductor and a possibly coincident seismic low-velocity layer exists somewhere in the study area, it should be rather narrow, i.e. too small to be resolved by the magnetotelluric or tomographic models.

The whole system of the DST experienced a total slip of about 105 km since Miocene times, some 17 Ma ago (Quennell, 1959; Freund *et al.*, 1970), but there is evidence for activity
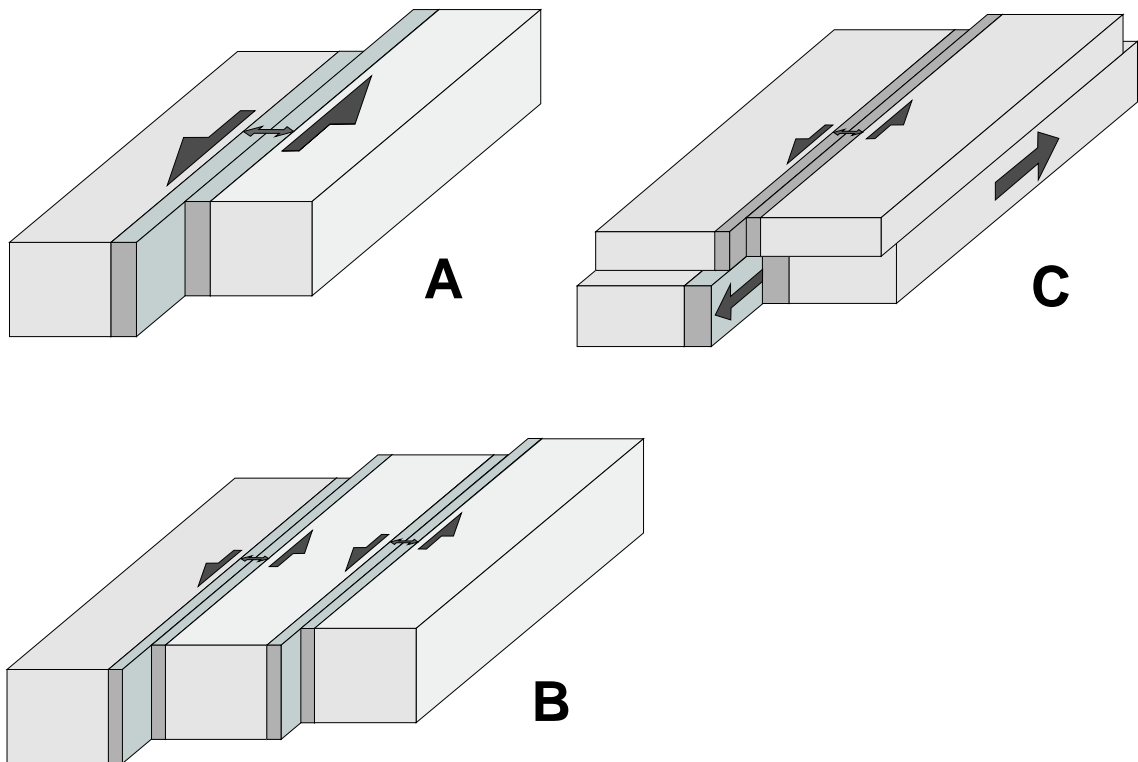
Figure 8.2: *Models of the possible slip history at strike-slip faults in the study area.* A: *Single fault taking all of the slip and characterised by a rather wide damage zone (grey).* B: *Two faults taking half of the total slip each. The damage zone of each fault is narrower than for the single fault model according to the reduced slip at each fault.* C: *Synkinematical deposition of sediments at a single fault. Shallower sedimentary layers experience a reduced amount of slip, and thus, a narrow damage zone is observed near the surface.*

along several subparallel fault strands and thus distributing the total movement spatially (see also chapter 2). Eyal *et al.* (1981) estimated that half of the total movement is distributed over eastern Sinai, and a distribution of the remaining some 50 km of slip over several fault strands is conceivable also in the central Arava Valley. Known fault traces trending parallel to the AF in this region include the Quwayra Fault at the eastern valley escarpment (figure 8.1) and the Zofar Fault in the west (see e.g. Bartov *et al.*, 1998). Additionally, the seismic reflection line VWJ-9, courtesy of the Natural Resources Authority of Jordan, shows a buried and thus recently inactive fault west of the AF, and the offset boundary between the two lithological blocks adjacent in the study area may represent another fault strand (see figure 8.1).

Figure 8.2 sketches the possible slip history at strike-slip faults in the study area and its implication for the damage zone width according to scaling relations. The fault model A consists of o single fault separating two blocks and taking all of the slip. Here, the damage zone is rather wide. A spatial and possibly also temporal distribution of the movement over several fault strands reduces the amount of slip at each individual fault. This situation is

represented by model B. Assuming the same slip behaviour as in the previous model, the observed damage zones at individual faults would be narrower, and the sum of all widths may equal that of model A, according to the scaling relations. A synkinematical deposition of sediments on top of an active fault is assumed for model C in figure 8.2. Shallower and thus younger sedimentary layers experience a reduced slip, which may lead to a narrower damage zone as expected from the total amount of slip at such a fault.

As discussed above, surface geological mapping, neotectonic studies, and shallow geophysical investigations delineate the surface trace of the AF, whereas the boundary between the two lithological units seems to be offset to the east at depths below 1 km. However, the upper 1 km is not resolved in images of the spatial distribution of seismic scatterers and poorly resolved by the combined analysis of resistivity and velocity models. Two possible models of the AF can explain these results. Firstly, the AF could exhibit a rather complex shape, dipping to the east in the upper 1 km and continueing subvertically about 1 km east of its surface trace. Secondly, in my preferred model the AF consists of (at least) two branches spaced ∼1 km apart, where the eastern branch constitutes the main boundary between the different lithological blocks in the upper 4 km of the crust. This situation can be represented by a combination of the sketched fault models B and C in figure 8.2. As documented by the surface trace of the fault (scarps, pressure ridges, rhomb grabens, etc.; see section 2.2.1) and shallow geophysical investigations, the westen strand was probably more recently active. Surface geology with two parallel fault strands in the northern part of the study area (see figure 2.2, page 12) supports the latter model. The buried fault inferred from reflection seismics ∼1.5 km west of the AF may constitute another strand. The total movement along this segment of the DST during the last 17 Ma may be distributed spatially and in time over these two or more branches of the AF and possibly other faults such as the Quwayra Fault or the Zofar Fault.

The fault core and damage zone are distinct structural units that reflect the material properties and deformation conditions within a fault zone (e.g. Ben-Zion and Sammis, 2003). The size of the damage zone depends on localisation and delocalisation processes. These are related to brittle instability of damageable media and related to the long term dynamics of the fault, respectively (Lyakhovsky et al., 1997, 2001). During the organisation of a fault system to form a planar fault zone, some fault strands dominate and take over the movement at the expense of other parallel strands as suggested for the AF. If a fault heals within the period of a seismic cycle, the seismicity is clustered and no characteristic earthquake develops. Geological studies at the DST suggest an ongoing organisation of this fault system (Rotstein et al., 1992), and paleoseismic studies show earthquake clustering over periods of some thousands of years (Marco et al., 1996). The San Andreas Fault, for comparison, shows a characteristic seismic behaviour (Sieh and Jahns, 1984). This fault zone does not heal completely during a seismic cycle, and ruptures preferably repeat on the same smooth trend (Stirling et al., 1996), whereas the AF apparently heals over the longer seismic cycle resulting in a less smooth trace (see also the discussion by Haberland et al., 2003b). This may also be a possible explanation of the spatial distribution of slip over several, closely spaced fault branches at the AF.

Conclusions

Specifically designed seismic experiments, refered to as CSA and CSA II, and in parts newly developed seismic imaging techniques reveal the subsurface structure of the Arava Fault (AF) and its vicinity along a 10 km long segment down to about 3–4 km depth. In the study area, the AF is considered to be the main fault of the southern Dead Sea Transform (DST) system.

A three-dimensional tomographic inversion of first arrival traveltimes provided the seismic *P* velocity structure in the vicinity of this fault trace. The derived model shows a strong velocity contrast near the trace of the AF with higher velocities on the eastern side than on the western side. The western low velocities correspond to the young sedimentary fill, predominantly belonging to the Hazeva Group, in the Arava Valley, and the high velocities in the east reflect mainly Precambrian igneous rocks. A low-velocity zone on the eastern side is related to a sagged sedimentary block bounded by the Qurayqira and Dana Faults. The continuation of the low-velocity zone towards the AF indicates that these two faults merge with the AF in the central part of the study area, although the fault traces cannot be delineated exactly due to the limited resolution of the model.

Additionally, two-dimensional high-resolution velocity models of the upper 100 m and seismic reflection profiles across the AF help to delineate its trace, and most observed features correlate with the surface geology and fault-related structures such as a pressure ridge. An advanced processing and depth migration of the reflection seismic data may reveal the deeper structure of the AF itself.

Electrical resistivity models from magnetotelluric measurements across the AF also show a marked contrast near the fault trace. At depths below 1 km, lower resistivities occur west of the fault and higher resistivities east of it. The low resistivities (high conductivities) in the west are related to saline fluids. The boundary between different resistive regions on either side of the fault appears to act as an impermeable boundary for fluid flow. A correlation of resistivity and velocity cross-sections lead to a characterisation of subsurface lithologies from their physical properties. Whereas the western side of the fault is characterised by a layered structure, the eastern side is rather uniform. The vertical boundary between the western and the eastern units seems to be offset to the east of the AF surface trace, especially in the central and northern part of the study area.

Seismic *S* waves from two local earthquakes provide an average *P*-to-*S* velocity ratio of 1.83, and evidence for a cross-fault variation, consistent with subsurface lithologies, comes from controlled-source data. A modelling of fault-zone reflected waves indicates that the boundary between low and high velocities is possibly rather sharp but exhibits a rough surface on the length scale a few hundreds of metres. This gives rise to scattering of seismic waves at this boundary.

Seismic scatterers are imaged using a combination of controlled sources and specifically designed receiver arrays. The imaging (migration) method is based on array beamforming and coherency analysis of *P*-to-*P* scattered seismic phases. I successfully image a subvertical

reflector along a 7 km long segment of the DST. This is in contrast to conventional near-vertical reflection seismics, where vertical structures are generally inferred indirectly from offsets of more or less subhorizontal reflectors. In the case that the target region is roughly known a priori, the receiver array design used here can lead to three-dimensional subsurface structures with few seismic sources and stations (low-cost 3-D migration). The imaging algorithm can be used without modification for a double beam imaging technique, i.e. a combination of source arrays and receiver arrays, and it is straightforward to implement P-to-S scattering. I propose to carry out similar experiments also at other fault zones, where subvertical structures are expected.

The imaged reflector segment between 1 km and 4 km depth strikes parallel to the AF surface trace and is offset about 1 km to the east. It correlates with surface geological observations and the three-dimensional velocity structure derived independently. The reflector marks the boundary between two lithological blocks juxtaposed most probably by displacement along the DST. This interpretation as a lithological boundary is supported by the combined seismic and magnetotelluric analysis and from a recent study by Ritter *et al.* (2003) south of the resolved structure. This boundary may be another strand of the AF, which is offset from the current, recently active surface trace. The total slip of the DST may be distributed spatially and in time over these two strands and possibly other faults in the area. This interpretation is in agreement with the very narrow damage zone of the AF (3–12 m) deduced by Haberland *et al.* (2003b) and with the seismic behaviour of this fault zone.

Bibliography

Aki, K. and Chouet, B. (1975). Origin of coda waves: Source, attenuation, and scattering effects. *Journal of Geophysical Research*, **80**(23), 3322–3341.

Aki, K. and Richards, P. G. (1980). *Quantitative Seismology*. W. H. Freeman, San Francisco.

Aki, K., Christoffersen, A., and Husebye, E. S. (1977). Determination of the three-dimensional seismic structure of the lithosphere. *Journal of Geophysical Research*, **82**, 277–296.

Al-Zoubi, A. and Ben-Avraham, Z. (2002). Structure of the earth's crust in Jordan from potential field data. *Tectonophysics*, **346**, 45–59.

Allenby, R. J. (1962). The importance of reflected refractions in seismic interpreting. *Geophysics*, **27**, 966–980.

Ambraseys, N. N., Melville, C., and Adams, R. (1994). *The Seismicity of Egypt, Arabia, and the Red Sea*. Cambridge University Press, New York.

Aminzadeh, F. and Chatterjee, S. (1987). Applications of clustering in exploration seismology. In K. Helbig, S. Treitel, and F. Aminzadeh, editors, *Pattern Recognition and Image Processing*, volume 20 of *Handbook of Geophysical Exploration*. Geophysical Press, London, Amsterdam.

Amiran, D. H. K., Arieh, E., and Turcotte, T. (1994). Earthquakes in Israel and adjacent areas: Macroseismic observations since 100 B.C.E. *Israel Exploration Journal*.

Aprea, C. M., Hildebrand, S., Fehler, M., Steck, L., Baldridge, W. S., Roberts, P., Thurber, C. H., and Lutter, W. J. (2002). Three-dimensional Kirchhoff migration: Imaging the Jemez volcanic field using teleseismic data. *Journal of Geophysical Research*, **107**(B10), doi:10.1029/2000JB000097.

Assumpção, M., James, D., and Snoke, A. (2002). Crustal thickness in SE Brazilian Shield by receiver function analysis: Implications for isostatic compensation. *Journal of Geophysical Research*, **107**(B1), doi:10.1029/2001JB000422.

Atallah, M. (1992). Tectonic evolution of northern Wadi Araba, Jordan. *Tectonophysics*, **204**, 17–26.

Avni, Y., Bartov, Y., Garfunkel, Z., and Ginat, H. (2001). The Arava Formation—A Pliocene sequence in the Arava Valley and its western margin, southern Israel. *Israel Journal of Earth Sciences*, **50**, 101–120.

Barjous, M. and Mikbel, S. (1990). Tectonic evolution of the Gulf of Aqaba – Dead Sea transform fault system. *Tectonophysics*, **180**, 49–59.

Barjous, M. O. (1995). Petra & Wadi Al Lahyana, 3050 I & 3050 IV, 1:50000. Geological map, Natural Resources Authority, Geology Directorate, Amman, Jordan.

Bartov, Y. (1974). *A structural and paleogeographic study of the central Sinai faults and domes*. Ph.D. thesis, Hebrew University, Jerusalem. in Hebrew.

Bartov, Y., Avni, Y., Calvo, R., and Frieslander, U. (1998). The Zofar Fault – A major intra-rift feature in the Arava rift valley. *Geological Survey of Israel Current Research*, **11**, 27–32.

Bauer, K., Schulze, A., Ryberg, T., Sobolev, S. V., and Weber, M. H. (2003). Classification of lithology from seismic tomography; a case study from the Messum igneous complex, Namibia. *Journal of Geophysical Research*, **108**(B3), doi:10.1029/2001JB001073.

Bedrosian, P. A. (2002). *Electromagnetic Imaging of Active Fault Zones*. Ph.D. thesis, University of Washington.

Bedrosian, P. A., Unsworth, M., and Egbert, G. (2002). Magnetotelluric imaging of the creeping segment of the San Andreas Fault near Hollister. *Geophysical Research Letters*, **29**, doi:10.1029/2001GL014119.

Belfer, I., Bruner, I., Keydar, S., Kravtsov, A., and Landa, E. (1998). Detection of shallow objects using refracted and diffracted seismic waves. *Journal of Applied Geophysics*, **38**, 155–168.

Ben-Avraham, Z., Ginzburg, A., Makris, J., and Eppelbaum, L. (2002). Crustal structure of the Levant basin, eastern Mediterranean. *Tectonophysics*, **346**, 23–43.

Ben-Zion, Y. (1998). Properties of seismic fault zone waves and their utility for imaging low-velocity structures. *Journal of Geophysical Research*, **103**(B6), 12567–12585.

Ben-Zion, Y. and Sammis, G. (2003). Characterization of fault zones. *Pure and Applied Geophysics*, **160**, 677–715.

Ben-Zion, Y., Peng, Z., Okaya, D., Seeber, L., Armbruster, J. G., Ozer, N., Michael, A. J., Baris, S., and Aktar, M. (2003). A shallow fault-zone structure illuminated by trapped waves in the Karadere-Duzca branch of the North Anatolian Fault, western Turkey. *Geophysical Journal International*, **152**, 699–717.

Bender, F. (1968). *Geologie von Jordanien*, volume 7 of *Beiträge zur regionalen Geologie der Erde*. Gebrüder Borntraeger, Berlin, Stuttgart.

Bender, F. (1975). Geological Map of Jordan, 1:500000. Government of Jordan and Geological Survey of the FRG, Bundesanstalt für Bodenforschung, Hannover.

Benhama, A., Cliet, C., and Dubesset, M. (1986). Study and applications of spatial directional filterings in three component recordings. *Geophysical Prospecting*, **36**, 591–613.

Bibby, H. M., Caldwell, T. G., Davey, F. J., and Webb, T. H. (1995). Geophysical evidence on the structure of the Taupo Volcanic Zone and its hydrothermal circulation. *Journal of Volcanology and Geothermal Research*, **68**, 29–58.

Biondi, B. L. (2003). 3-D Seismic Imaging. Technical report, Stanford University. http://sepwww.stanford.edu/sep/biondo/Lectures/index.html.

Birch, F. (1961). The velocity of compressional waves in rocks to 10 kilobars (Part II). *Journal of Geophysical Research*, **66**, 2199–2224.

Bohlen, T., Müller, C., and Milkereit, B. (2003). Elastic seismic wave scattering from massive sulfide orebodies: on the role of composition and shape. In D. W. Eaton, B. Milkereit, and M. H. Salisbury, editors, *Hardrock Seismic Exploration*, volume 10 of *Geophysical Developments Series*. Society of Exploration Geophysicists, Tulsa.

Bonnet, E., Bour, O., Odling, N. E., Davy, P., Main, I., Cowie, P., and Berkowitz, B. (2001). Scaling of fracture systems in geological media. *Reviews of Geophysics*, **39**(3), 347–383.

Buske, S. (1999). Three-dimensional pre-stack Kirchhoff migration of deep seismic reflection data. *Geophysical Journal International*, **137**(1), 243–260.

Buttkus, B. (1991). *Spektralanalyse und Filtertheorie in der angewandten Geophysik*. Springer Verlag, Berlin.

Caine, J. S., Evans, J. P., and Forster, C. B. (1996). Fault zone architecture and permeability structure. *Geology*, **24**, 1025–1028.

Calvo, R. and Bartov, Y. (2001). Hazeva Group, southern Israel: New observations, and their implications for its stratigraphy, paleogeography, and tectono-sedimentary regime. *Israel Journal of Earth Sciences*, **50**, 71–99.

Chaimov, T. A., Barazangi, M., Al-Saad, D., Sawaf, T., and Gebran, A. (1990). Crustal shortening in the Palmyride fold belt, Syria, and implications for movement along the Dead Sea fault system. *Tectonics*, **9**, 1369–1386.

Chavarria, J. A., Malin, P., Catchings, R. D., and Shalev, E. (2003). A look inside the San Andreas fault at Parkfield through Vertical Seismic Profiling. *Science*, **302**, 1746–1748.

Chester, F. M., Evans, J. P., and Biegel, R. L. (1993). Internal structure and weakening mechanisms of the San Andreas Fault. *Journal of Geophysical Research*, **98**, 771–786.

Cliet, C. and Dubesset (1988). Polarization analysis in three-component seismics. *Geophysical Transactions*, **36**.

Cohen, J. K. and Stockwell, J. W. (2002). *CWP/SU: Seismic Unix Release 36: a free package for seismic research and processing.* Center for Wave Phenomena, Colorado School of Mines. http://www.cwp.mines.edu/cwpcodes/index.html.

Cox, M. (1999). *Static Corrections for Seismic Reflection Surveys*, volume 9 of *Geophysical Reference Series*. Society of Exploration Geophysicists, Tulsa.

Deacon, L. E. (1943). An analysis of abnormal reflexions. *Geophysics*, **8**, 3–8.

Dell'Aversana, P. (2001). Integration of seismic, MT and gravity data in a thrust belt interpretation. *First Break*, **19**(6), 335–341.

DESERT Group (2000). Multinational geoscientific research kicks off in the Middle East. *EOS Transactions, American Geophysical Union*, **81**(50), 609, 616–617.

DESERT Group (2002). The DESERT passive seismic experiment 2000/2001 in the Middle-East. *ORFEUS Electronic Newsletter*, **4**(1). http://orfeus.knmi.nl/newsletter/vol4no1/-vol4no1.pdf.

DESERT Group (2004). The crustal structure of the Dead Sea Transform. *Geophysical Journal International*, **156**(3), 655–681.

Eaton, D. W. (1999). Weak elastic-wave scattering from massive sulfide orebodies. *Geophysics*, **64**(1), 289–299.

Eberhart-Phillips, D. (1986). Three-dimensional structure in northern California coast ranges from inversion of local earthquake arrival times. *Bulletin of the Seismological Society of America*, **76**, 1025–1052.

Eberhart-Phillips, D. (1990). Three-dimensional P and S velocity structure in the Coalinga region, California. *Journal of Geophysical Research*, **95**(B10), 15343–15363.

Eberhart-Phillips, D. and Michael, A. J. (1993). Three-dimensional velocity structure, seismicity, and fault structure in the Parkfield region, central CA. *Journal of Geophysical Research*, **98**, 15737–15758.

Eberhart-Phillips, D. and Michael, A. J. (1998). Seismotectonics of the Loma Prieta, California, region determined from three-dimensional V_P, V_P/V_S, and seismicity. *Journal of Geophysical Research*, **103**(B9), 21099–21120.

Eberhart-Phillips, D., Stanley, W. D., Rodriguez, B. D., and Lutter, W. J. (1995). Surface seismic and electrical methods to detect fluids related to faulting. *Journal of Geophysical Research*, **100**(B7), 12919–12936.

El-Isa, Z. H., Mechie, J., Prodehl, C., Makris, J., and Rihm, R. (1987). A crustal structure study of Jordan derived from seismic refraction data. *Tectonophysics*, **138**, 235–253.

Evans, J. R., Eberhart-Phillips, D., and Thurber, C. H. (1994). *User's Manual for SIMULPS12 for Imaging V_P and V_P/V_S: A derivative of the "Thurber" tomographic inversion SIMUL3 for local earthquakes and Explosions*. U. S. Geological Survey. Open File Report 94-431.

Eyal, M., Eyal, Y., Bartov, Y., and Steinitz, G. (1981). The tectonic development of the western margin of the Gulf of Elat (Aqaba) rift. *Tectonophysics*, **80**, 39–66.

Freund, R., Garfunkel, Z., Zak, I., Goldberg, M., Weissbrod, T., and Derin, B. (1970). The shear along the Dead Sea rift. *Philosophical Transactions of the Royal Society of London*, **267**, 107–130.

Gallardo, L. A. and Meju, M. A. (2003). Characterization of heterogeneous near-surface materials by joint 2D inversion of dc resistivity and seismic data. *Geophysical Research Letters*, **30**(13), doi:10.1029/2003GL017370.

Galli, P. (1999). Active tectonics along the Wadi-Araba-Jordan Valley transform fault. *Journal of Geophysical Research*, **104**(B2), 2777–2796.

Gardosh, M., Reches, Z., and Garfunkel, Z. (1990). Holocene tectonic deformation along the western margins of the Dead Sea. *Tectonophysics*, **180**, 123–137.

Garfunkel, Z. (1981). Internal structure of the Dead Sea leaky transform (rift) in relation to plate kinematics. *Tectonophysics*, **80**, 81–108.

Garfunkel, Z. (1997). The history and formation of the Dead Sea basin. In T. M. Niemi, Z. Ben-Avraham, and J. R. Gat, editors, *The Dead Sea – The Lake and its Setting*, volume 36 of *Oxford Monographs on Geology and Geophysics*, pages 36–56. Oxford University Press, Oxford.

Garfunkel, Z. and Ben-Avraham, Z. (1996). The structure of the Dead Sea basin. *Tectonophysics*, **266**, 155–176.

Gimlin, D. R. and Smith, J. W. (1980). A comparison of seismic trace summing techniques. *Geophysics*, **45**(6), 1017–1041.

Ginat, H., Enzel, Y., and Avni, Y. (1998). Translocated Plio-Pleistocene drainage systems along the Arava fault of the Dead Sea transform. *Tectonophysics*, **284**, 151–160.

Ginzburg, A., Makris, J., Fuchs, K., Prodehl, C., Kaminski, W., and Amitai, U. (1979). A seismic study of the crust and upper mantle of the Jordan – Dead Sea Rift and their transition toward the Mediterranean Sea. *Journal of Geophysical Research*, **84**, 1569–1582.

Girdler, R. W. (1990). The Dead Sea transform fault system. *Tectonophysics*, **180**, 1–13.

Gomez, F., Meghraoui, M., Darkal, A. N., Hijazi, F., Mouty, M., Suleiman, Y., Sbeinati, R., Darawcheh, R., Al-Ghazzi, R., and Barazangi, M. (2003). Holocene faulting and earthquake recurrence along the Serghaya branch of the Dead Sea fault system in Syria and Lebanon. *Geophysical Journal International*, **153**, 658–674.

Götze, H., Ebbing, J., Hese, F., Kollersberger, T., Schmidt, S., Rybakov, M., Hassouneh, M., Hrasha, M., and El-Kelani, R. (2002). Gravity field analysis and 3D density modeling of the lithosphere along the Dead Sea Transform. In *EOS Transactions, American Geophysical Union*, volume 83. Fall Meeting Supplement, abstract S61A-1105.

Graeber, F. (1997). *Seismische Geschwindigkeiten und Hypozentren in den südlichen Anden aus der simultanen Inversion von Laufzeitdaten des seismologischen Experiments PISCO 94 in Nordchile*. Ph.D. thesis, Freie Universität Berlin. Scientific Technical Report STR97/17, GeoForschungsZentrum Potsdam.

Gritto, R., Korneev, V. A., and Johnson, L. R. (1995). Low-frequency elastic-wave scattering by an inclusion: limits of applications. *Geophysical Journal International*, **120**, 677–692.

Gutenberg, B. and Richter, C. F. (1954). *Seismicity of the Earth and Associated Phenomena*. Princeton University Press, Princeton.

Haberland, C. (1999). *Die Verteilung der Absorption seismischer Wellen in den westlichen Zentralen Anden*. Ph.D. thesis, Freie Universität Berlin. Berliner Geowissenschaftliche Abhandlungen, Reihe B, Band 35.

Haberland, C., Rietbrock, A., Schurr, B., and Brasse, H. (2003a). Coincident anomalies of seismic attenuation and electrical resistivity beneath the southern Bolivian Altiplano plateau. *Geophysical Research Letters*, **30**(18), doi:10.1029/2003GL017492.

Haberland, C., Agnon, A., El-Kelani, R., Maercklin, N., Qabbani, I., Rümpker, G., Ryberg, T., Scherbaum, F., and Weber, M. (2003b). Modeling of seismic guided waves at the Dead Sea Transform. *Journal of Geophysical Research*, **108**(B7), doi:10.1029/2002JB002309.

Harjes, H.-P. and Henger, M. (1973). Array-Seismologie. *Zeitschrift für Geophysik*, **39**, 865–905.

Haslinger, F. (1998). *Velocity Structure, Seismicity and Seismotectonics of Northwestern Greece between the Gulf of Arta and Zakynthos*. Ph.D. thesis, ETH Zürich.

Hassouneh, M. (2003). *Interpretation of Potential Fields by Modern Data processing and 3-dimensional gravity Modeling of the Dead Sea Pull-Apart Basin / Jordan Rift Valley (JRV)*. Ph.D. thesis, Universität Würzburg. http://opus.bibliothek.uni-wuerzburg.de/opus/volltexte/2003/483/.

Hatcher, R. D., Zeiz, I., Reagan, R. D., and Abu-Ajameh, M. (1981). Sinistral strike-slip motion of the Dead Sea rift: confirmation from new magnetic data. *Geology*, **9**, 458–462.

Haubrich, R. A. (1968). Array design. *Bulletin of the Seismological Society of America*, **58**, 977–991.

Hearn, T. M. and Ni, J. F. (1994). P_n velocities beneath continental collision zones: the Turkish-Iranian Plateau. *Geophysical Journal International*, **117**, 273–283.

Hedlin, M. A. H., Minster, J. B., and Orcutt, J. A. (1991). Beam-stack imaging using a small aperture array. *Geophysical Research Letters*, **18**(9), 1771–1774.

Hedlin, M. A. H., Minster, J. B., and Orcutt, J. A. (1994). Resolution of prominent crustal scatterers near the NORESS small-aperture array. *Geophysical Journal International*, **119**, 101–115.

Hering, A., Misiek, R., Gyulai, A., Dobroka, M., and Dresen, L. (1995). A joint inversion algorithm to process geoelectric and surface wave seismic data. Part I: basic ideas. *Geophysical Prospecting*, **43**, 135–156.

Hoffmann-Rothe, A. (2002). *Combined structural and magnetotelluric investigation across the West Fault Zone in nothern Chile*. Ph.D. thesis, Mathematisch-Naturwissenschaftliche Fakultät, Universität Potsdam. http://pub.ub.uni-potsdam.de/2002/0025/ahoro.pdf.

Hoffmann-Rothe, A., Ritter, O., and Haak, V. (2001). Magnetotelluric and geomagnetic modelling reveals zones of very high electrical conductivity in the upper crust of Central Java. *Physics of the Earth and Planetary Interiors*, **124**, 131–151.

Hole, J. A. and Zelt, B. C. (1995). Three-dimensional finite-difference reflection travel times. *Geophysical Journal International*, **121**, 427–434.

Hole, J. A., Catchings, R. D., St. Clair, K. C., Rymer, M. J., Okaya, D. A., and Carney, B. J. (2001). Steep-dip seismic imaging of the San Andreas fault near Parkfield. *Science*, **294**, 1513–1515.

Husen, S. (1999). *Local Earthquake Tomography of a Convergent Margin, North Chile*. Ph.D. thesis, Mathematisch-Naturwissenschaftliche Fakultät, Universität Kiel.

Iyer, H. M. and Hirahara, K., editors (1993). *Seismic Tomography: Theory and practice*. Chapman and Hall, London.

Izzeldin, A. Y. (1987). Seismic, gravity and magnetic surveys in the central part of the Red Sea: Their interpretation and implications for the structure of the Red Sea. *Tectonophysics*, **141**, 269–306.

Janssen, C., Hoffmann-Rothe, A., Tauber, S., and Wilke, H. (2002). Internal structure of the Precordilleran fault system (Chile) — insights from structural and geophysical observations. *Journal of Structural Geology*, **24**, 123–143.

Jarrar, G., Bauman, A., and Wachendorf, H. (1983). Age determination in the Precambrian basement of the Wadi Araba area, southwest Jordan. *Earth and Planetary Science Letters*, **63**, 292–304.

Joffe, S. and Garfunkel, Z. (1987). The plate kinematics of the circum Red Sea — A reevaluation. *Tectonophysics*, **141**, 5–22.

Jones, A. G., Snyder, D., Hanmer, S., Asudeh, I., White, D., Eaton, D., and Clarke, G. (2002). Magnetotelluric and teleseismic study across the Snowbird Tectonic Zone, Canadian Shield: A Neoarchean mantle suture? *Geophysical Research Letters*, **29**(17), doi:10.1029/2002GL015359.

Jurkevics, A. (1988). Polarization analysis of three-component array data. *Bulletin of the Seismological Society of America*, **78**(5), 1725–1743.

Kanasewich, E. R. (1981). *Time Sequence Analysis in Geophysics*. The University of Alberta Press.

Kanasewich, E. R. (1990). *Seismic Noise Attenuation*, volume 7 of *Handbook of Geophysical Exploration*. Pergamon Press, Oxford.

Karastathis, V. K., Karmis, P. N., Drakatos, G., and Stavrakakis, G. (2002). Geophysical methods contributing to the testing of concrete dams. Application at the Marathon Dam. *Journal of Applied Geophysics*, **50**, 247–260.

Kaufmann, A. A. and Keller, G. V. (1981). *The Magnetotelluric Sounding Method*, volume 15 of *Methods in Geochemistry and Geophysics*. Elsevier Scientific Publishing Company, Amsterdam, Oxford, New York.

Kearey, P. and Brooks, M. (1991). *An Introduction to Geophysical Exploration*. Blackwell Scientific Publications, Oxford, 2 edition.

Kearey, P. and Vine, F. J. (1995). *Global Tectonics*. Blackwell Science, Oxford.

Ken-Tor, R., Agnon, A., Enzel, Y., and Stein, M. (2001). High-resolution geological record of historic earthquakes in the Dead Sea basin. *Journal of Geophysical Research*, **106**(B2), 2221–2234.

Kesten, D., Stiller, M., Schulze, A., Frieslander, U., Bartov, Y., Qabbani, I., and DESERT Group (2000). Crossing the Dead Sea Fault System – First results of the near-vertical seismic reflection study within project DESERT 2000. In *EOS Transactions, American Geophysical Union*, volume 81. Fall Meeting Supplement, abstract T12C-08.

Kirlin, R. L. and Done, W. J. (1999). *Covariance Analysis for seismic Signal Processing*, volume 2 of *Geophysical Developments Series*. Society of Exploration Geophysicists, Tulsa.

Kissling, E., Husen, S., and Haslinger, F. (2001). Model parametrization in seismic tomography: a choice of consequence for the solution quality. *Physics of the Earth and Planetary Interiors*, **123**, 89–101.

Klinger, Y., Avouac, J. P., Dorbath, L., Karaki, N. A., and Tisnerat, N. (2000a). Seismic behaviour of the Dead Sea fault along the Araba valley, Jordan. *Geophysical Journal International*, **142**(3), 769–782.

Klinger, Y., Avouac, J. P., Karaki, N. A., Dorbath, L., Bourles, D., and Reyss, J. L. (2000b). Slip rate on the Dead Sea transform fault in northern Araba valley, (Jordan). *Geophysical Journal International*, **142**(3), 755–768.

Krüger, F., Weber, M., Scherbaum, F., and Schlittenhardt, J. (1995). Evidence for normal and inhomogeneous lowermost mantle and core-mantle boundary structure under the Arctic and northern Canada. *Geophysical Journal International*, **122**, 637–657.

Krüger, F., Scherbaum, F., Weber, M., and Schlittenhardt, J. (1996). Analysis of asymmetric multipathing with a generalization of the double-beam method. *Bulletin of the Seismological Society of America*, **86**(3), 737–749.

Lanz, E., Maurer, H., and Green, A. G. (1998). Refraction tomography over a buried waste disposal site. *Geophysics*, **63**(4), 1414–1433.

Lees, J. and VanDecar, J. (1991). Seismic tomography constrained by Bouguer gravity anomalies: Applications in western Washington. *Pure and Applied Geophysics*, **135**, 31–52.

Lees, J. M. and Malin, P. E. (1990). Tomographic images of P wave velocity variation at Parkfield, California. *Journal of Geophysical Research*, **95**, 21793–21804.

LePichon, X. and Gaulier, J. M. (1988). The rotation of Arabia and the Levant fault system. *Tectonophysics*, **153**, 271–294.

Li, Y.-G., Leary, P., Aki, K., and Malin, P. (1990). Seismic trapped modes in the Oroville and San Andreas fault zones. *Science*, **249**, 763–765.

Lines, L. R. and Treitel, S. (1984). Tutorial: A review of least-squares inversion and its application to geophysical problems. *Geophysical Prospecting*, **32**, 98–118.

Louie, J. N., Clayton, R. W., and Le Bras, R. J. (1988). 3-D imaging of steeply dipping structure near the San Andreas fault, Parkfield, California. *Geophysics*, **53**, 176–185.

Louie, J. N., Chávez-Pérez, S., Henrys, S., and Bannister, S. (2002). Multimode migration of scattered and converted waves for the structure of the Hikurangi slab interface, New Zealand. *Tectonophysics*, **355**, 227–246.

Ludwig, J. W., Nafe, J. E., and Drake, C. L. (1970). Seismic refraction. In A. E. Maxwell, editor, *The Sea*, volume 4, pages 53–84. Wiley, New York.

Lyakhovsky, V., Ben-Zion, Y., and Agnon, A. (1997). Distributed damage, faulting, and friction. *Journal of Geophysical Research*, **102**, 27635–27649.

Lyakhovsky, V., Ben-Zion, Y., and Agnon, A. (2001). Earthquake cycle, fault zones, and seismicity patterns in a rheologically layered lithosphere. *Journal of Geophysical Research*, **106**, 4103–4120.

Lymnes, C. S. and Lay, T. (1989). Inversion of P coda for isotropic scatterers at the Yucca Flat test site. *Bulletin of the Seismological Society of America*, **79**, 790–804.

Maercklin, N. (1999). Polarisationsanalyse refraktionsseismischer Daten vom Vulkan Merapi, Indonesien. Master's thesis, Institut für Geowissenschaften, Abteilung Geophysik, Universität Kiel.

Maercklin, N., Haberland, C., Ryberg, T., Weber, M., Bartov, Y., and DESERT Group (2004). Imaging the Dead Sea Transform with scattered seismic waves. *Geophysical Journal International*, **158**, 179–186.

Makris, J., Ben-Avraham, Z., Behle, A., Ginzburg, A., Giese, P., Steinmetz, L., Whitmarsh, R. B., and Eleftheriou, S. (1983). Seismic refraction profiles between Cyprus and Israel and their interpretation. *Geophysical Journal of the Royal Astronomical Society*, **75**, 575–591.

Marco, S., Stein, M., and Agnon, A. (1996). Long-term earthquake clustering: A 50,000-year paleoseismic record in the Dead Sea Graben. *Journal of Geophysical Research*, **101**, 6179–6191.

McClusky, S., Balassanian, S., Barka, A., Demir, C., Ergintav, S., Georgiev, I., Gurkan, O., Hamburger, M., Hurst, K., Kahle, H., Kastens, K., Kekelidze, G., King, R., Kotzev, V., Lenk, O., Mahmoud, S., Mishin, A., Nadariya, M., Ouzounis, A., Paradissis, D., Peter, Y., Prilepin, M., Reilinger, R., Sanli, I., Seeger, H., Tealeb, A., Toksöz, M. N., and Veis, G. (2000). Global Positioning System constraints on plate kinematics and dynamics in the eastern Mediterranean and Caucasus. *Journal of Geophysical Research*, **105**(B3), 5695–5719.

McClusky, S., Reilinger, R., Mahmoud, S., Ben-Sari, D., and Tealeb, A. (2003). GPS constraints on Africa (Nubia) and Arabia plate motions. *Geophysical Journal International*, **155**, 126–138.

McKenzie, D. P., Davies, D., and Molnar, P. (1970). Plate tectonics of the Red Sea and East Africa. *Nature*, **224**, 125–133.

Mechie, J., Weber, M., Abu-Ayyash, K., Ben-Avraham, Z., El-Kelani, R., and DESERT Group (2000). A wide-angle profile across the Jordan-Dead Sea Rift (Transform). In *EOS Transactions, American Geophysical Union*, volume 81. Fall Meeting Supplement, abstract T12C-09.

Meju, M. A., Gallardo, L. A., and Mohamed, A. K. (2003). Evidence for correlation of electrical resistivity and seismic velocity in heterogeneous near-surface materials. *Geophysical Research Letters*, **30**(7), doi:10.1029/2003GL016048.

Menke, W. (1989). *Geophysical Data Analysis: Discrete Inverse Theory*. Academic Press, San Diego.

Meyer, J. H. (1988). *First Comparative Results of Integral and Instantaneous Polarization Attributes for Multicomponent Seismic Data*. Institut Français du Petrole, F-92506 Rueil Malmaison Cedex.

Michelini, A. and McEvilly, T. (1991). Seismological studies at Parkfield. I. Simultaneous inversion for velocity structure and hypocenters using cubic B-splines parameterization. *Bulletin of the Seismological Society of America*, **81**, 524–552.

Mohsen, A., Bock, G., Abdel-Hafes, W., Hofstetter, R., Rümpker, G., and Wylegalla, K. (2000). A passive seismic array across the Dead Sea Transform. In *EOS Transactions, American Geophysical Union*, volume 81. Fall Meeting Supplement, abstract T12C-11.

Mukhopadhyay, S., Kayal, J. R., Khattri, K. N., and Pradhan, B. K. (2002). Simultaneous inversion of the aftershock data of the 1993 Killari earthquake in Peninsular India and its seismotectonic implications. In *Proceedings of the Indian Academy of Sciences (Earth and Planetary Sciences)*, volume 111.

Müller, C. (2000). *On the Nature of Scattering from Isolated Perturbations in Elastic Media and the Consequences for Processing of Seismic Data*. Ph.D. thesis, Mathematisch-Naturwissenschaftliche Fakultät, Universität Kiel. http://e-diss.uni-kiel.de/diss_384/.

Naess, O. E. and Bruland, L. (1979). Stacking methods other than simple summation. In A. A. Fitch, editor, *Developments in Geophysical Exploration Methods*, volume 6. Applied Science Publications, London.

Neidell, N. and Taner, M. T. (1971). Semblance and other coherency measures for multichannel data. *Geophysics*, **36**, 482–497.

Nikolaev, A. V. and Troitsky, P. A. (1987). Lithospheric studies based on array analysis of P-coda and microseisms. *Tectonophysics*, **140**, 103–113.

Nishizawa, O. and Noro, H. (1995). Bootstrap statistics for velocity tomography: application of a new information criterion. *Geophysical Prospecting*, **43**, 157–176.

Nolet, G. (1987). Seismic wave propagation and seismic tomography. In G. Nolet, editor, *Seismic Tomography*, pages 1–24. D. Reidel Publishing Company, Dordrecht.

Park, S. K. and Roberts, J. J. (2003). Conductivity structure of the San Andreas fault, Parkfield, revisited. *Geophysical Research Letters*, **30**(16), doi:10.1029/2003GL017689.

Patzig, R. (1999). *Lokalbebentomographie des Gebietes um Antofagasta (Nordchile) sowie Betrachtungen zu den Magnituden-Häufigkeits-Parametern in dieser Region*. Ph.D. thesis, Freie Universität Berlin. http://www.agg.dkrz.de/people/Patzig/tomotheo.htm.

Pe'eri, S., Wdowinski, S., Shtibelman, A., Bechor, N., Bock, Y., Nikolaidis, R., and van Domselar, M. (2002). Current plate motion across the Dead Sea Fault from three years of continuous GPS monitoring. *Geophysical Research Letters*, **29**(14), doi:10.1029/2001GL013879.

Press, W. H., Teukolsky, S. A., Vetterling, W. T., and Flannery, B. P. (1996). *Numerical Recipes in C – The Art of Scientific Computing*. Cambridge University Press, Cambridge. http://www.nr.com.

Quennell, A. M. (1958). The structural and geomorphic evolution of the Dead Sea rift. *Quarterly Journal of the Geological Society of London*, **114**, 1–24.

Quennell, A. M. (1959). Tectonics of the Dead Sea rift. In *20th International Geological Congress, Association of African Geological Surveys*, pages 385–405.

Quintero, R. and Kulánek, O. (1998). P_n-wave observations in Costa Rica. *Geofísica Internacional*, **37**(3), 171–182.

Rabb'a, I. (1991). Al Qurayqira, 3051 II, 1:50000. Geological map, Natural Resources Authority, Geology Directorate, Amman, Jordan.

Rabb'a, I. (1994). Geology of the Al Qurayqira (Jabal Hamra Fadan Area), Map Sheet No. 3051 II. 1:50000 Geological Mapping Series, Geological Bulletin No. 28, Natural Resources Authority, Geology Directorate, Amman, Jordan.

Rietbrock, A. and Scherbaum, F. (1999). Crustal scattering at the KTB from combined microearthquake and receiver analysis. *Geophysical Journal International*, **136**, 57–67.

Ritter, O., Schmidt, J., Weckmann, U., Thoss, H., Abueladas, A., and Haak, V. (2001). A 3D magnetotelluric study of the Dead Sea Transform Fault in Jordan. In *EOS Transactions, American Geophysical Union*, volume 82. Fall Meeting Supplement, Abstract S41A-0582.

Ritter, O., Ryberg, T., Weckmann, U., Hoffmann-Rothe, A., Abueladas, A., Garfunkel, Z., and DESERT Group (2003). Geophysical images of the Dead Sea Transform in Jordan reveal an impermeable barrier for fluid flow. *Geophysical Research Letters*, **30**(14), doi:10.1029/2003GL017541.

Robinson, W. B. (1945). Refraction waves reflected from a fault zone. *Geophysics*, **10**, 535–545.

Rodi, W. and Mackie, R. L. (2001). Nonlinear conjugate gradients algorithm for 2D magnetotelluric inversion. *Geophysics*, **66**(1), 174–187.

Rothman, D. H. (1986). Automatic estimation of large residual statics corrections. *Geophysics*, **51**, 332–346.

Rotstein, Y., Bartov, Y., and Frieslander, U. (1992). Evidence for local shifting of the main fault and changes in the structural setting, Kinarot basin, Dead Sea Transform. *Geology*, **20**, 251–254.

Rümpker, G., Ryberg, T., Bock, G., and DESERT Seismology Group (2003). Boundary-layer mantle flow under the Dead Sea transform fault inferred from seismic anisotropy. *Nature*, **425**, 497–501.

Rybakov, M., Goldschmidt, V., and Rotstein, Y. (1997). New regional gravity and magnetic maps of the Levant. *Geophysical Research Letters*, **24**(1), 33–36.

Ryberg, T., Garfunkel, Z., Qabbani, I., and El-Kelani, R. (2001). Shallow, high-resolution velocity structure across the Dead Sea transform fault, Dead Sea rift valley, from Vibroseis data – project DESERT 2000. In *EOS Transactions, American Geophysical Union*, volume 82. Fall Meeting Supplement, abstract S41A-0586.

Ryberg, T., Bedrosian, P. A., Maercklin, N., Ritter, O., Weckmann, U., and DESERT Group (2003). Combined seismic and magnetotelluric imaging of the Dead Sea Transform. In *EOS Transactions, American Geophysical Union*, volume 84. Fall Meeting Supplement, abstract T51D-0195.

Salamon, A., Hofstetter, A., Garfunkel, Z., and Ron, H. (1996). Seismicity of the eastern Mediterranean region: Perspective from the Sinai subplate. *Tectonophysics*, **263**, 293–305.

Salamon, A., Hofstetter, A., Garfunkel, Z., and Ron, H. (2003). Seismotectonics of the Sinai subplate – the eastern Mediterranean region. *Geophysical Journal International*, **155**, 149–173.

Samson, J. C. (1973). Description of the polarisation states of vector processes: application to ULF electromagnetic fields. *Geophysical Journal*, **34**.

Scales, J. A. (1997). *Theory of Seismic Imaging*. Samizdat Press, Center for Wave Phenomena, Colorado School of Mines, Golden, 2.2 edition. http://samizdat.mines.edu.

Scales, J. A., Docherty, P., and Gersztenkorn, A. (1990). Regularisation of nonlinear inverse problems: Imaging the near-surface weathering layer. *Inverse Problems*, **6**, 115–131.

Scales, J. A., Smith, M. L., and Treitel, S. (2001). *Introductory Geophysical Inverse Theory*. Samizdat Press, Center for Wave Phenomena, Colorado School of Mines, Golden. http://samizdat.mines.edu.

Scherbaum, F., Krüger, F., and Weber, M. (1997). Double beam imaging: Mapping lower mantle heterogeneities using combinations of source and receiver arrays. *Journal of Geophysical Research*, **102**(B1), 507–522.

Schimmel, M. and Paulssen, H. (1997). Noise reduction and detection of weak, coherent signals through phase-weighted stacks. *Geophysical Journal International*, **130**, 497–505.

Schmidt, J. (2002). Auswertung flächenhafter magnetotellurischer Messungen an der Dead Sea Transform in Jordanien. Master's thesis, Institut für Geowissenschaften, Universität Potsdam.

Scholz, C. H. (1987). Wear and gouge formation in brittle faulting. *Geology*, **15**, 493–495.

Scholz, C. H. and Gupta, A. (2000). Fault interactions and seismic hazard. *Journal of Geodynamics*, **29**, 484–492.

Scholz, C. H., Dawers, N. H., Yu, J. Z., Anders, M. H., and Cowie, P. A. (2000). Fault growth and fault scaling laws: Preliminary results. *Journal of Geophysical Research*, **98**(B12), 21951–21961.

Schön, J. H. (1996). *Physical Properties of Rocks. Fundamentals and Principles of Petrophysics*, volume 18 of *Handbook of Geophysical Exploration*. Pergamon Press, Oxford.

Schulz, S. E. and Evans, J. P. (2000). Mesoscopic structure of the Punchball Fault, Southern California and the geologic and geophysical structure of active strike-slip faults. *Journal of Structural Geology*, **22**, 913–930.

Schweitzer, J., Fyen, J., Mykkeltveit, S., and Kværna, T. (2002). Seismic arrays. In P. Bormann, editor, *IASPEI New Manual of Seismological Observatory Practice*, chapter 9. GeoForschungsZentrum, Potsdam.

Shapira, A. and Feldmann, L. (1987). Microseismicity of three locations along the Jordan Rift. *Tectonophysics*, **141**, 89–94.

Shearer, P. M. (1999). *Introduction to Seismology*. Cambridge University Press, Cambridge.

Sheriff, R. E. (1991). *Encyclopedic Dictionary of Exploration Geophysics*. Society of Exploration Geophysicists, Tulsa, 3 edition.

Sheriff, R. E. and Geldart, L. P. (1995). *Exploration Seismology*. Cambridge University Press, Cambridge.

Sieh, K. E. and Jahns, R. H. (1984). Holocene activity of the San Andreas Fault at Wallace Creek. *Geological Society of America Bulletin*, **95**, 883–896.

Snieder, R. and Trampert, J. (1999). Inverse problems in geophysics. In A. Wirgin, editor, *Wavefield Inversion*. Springer Verlag, New York.

Sobolev, S. V., Babeyko, A. Y., Garfunkel, Z., and DESERT Group (2003). Thermo-mechanical model of the Dead Sea Transform. submitted to *EPSL*.

Stacey, F. D. (1992). *Physics of the Earth*. Brookfield Press, Brisbane, Australia.

Stern, R. J. (1994). Arc assembly and continental collision in the Neoproterozoic East African orogen: Implications for the consolidation of Gondwanaland. *Annual Reviews of Earth and Planetary Sciences*, **22**, 319–351.

Stirling, M. W., Wesnousky, S. G., and Shimazaki, K. (1996). Fault trace complexity, cumulative slip, and the shape of the magnitude-frequency distribution for strike-slip faults: a global survey. *Geophysical Journal International*, **124**, 833–868.

Stockwell, J. W. (1999). The CWP/SU: Seismic Unix package. *Computers and Geosciences*, **25**, 415–419.

Stockwell, J. W. and Cohen, J. K. (2002). *The New SU User's Manual*. Center for Wave Phenomena, Colorado School of Mines, Golden, USA, 3.2 edition. http://www.cwp.mines.edu/cwpcodes/index.html.

Stoeser, D. B. and Camp, V. E. (1985). Pan-African microplate accretion of the Arabian Shield. *Geological Society of America Bulletin*, **96**, 817–826.

Swift, C. M. (1967). *A Magnetotelluric Investigation of an Electrical Conductivity Anomaly in the Southwest United States*. Ph.D. thesis, Massachusetts Institute of Technology, Department of Geology and Geophysics, Cambridge.

Taner, M. T., Koehler, F., and Sheriff, R. E. (1979). Complex seismic trace analysis. *Geophysics*, **44**(6), 1041–1063.

Tatham, R. H. and McCormack, M. D. (1991). *Multicomponent Seismology in Petroleum Exploration*, volume 6 of *Investigations in Geophysics*. Society of Exploration Geophysicists, Tulsa.

Telford, W. M., Geldart, L. P., and Sheriff, R. E. (1990). *Applied Geophysics*. Cambridge University Press, Cambridge, 2 edition.

ten Brink, U., Al-Zoubi, A., and Rybakov, M. (2001). Bouguer gravity anomaly map of the Dead Sea fault system, Jordan, and Israel. Open file report 01-216, U. S. Geological Survey. http://pups.usgs.gov/of/of01-216.

ten Brink, U. S., Schoenberg, N., Kovach, R. L., and Ben-Avraham, Z. (1990). Uplift and a possible Moho offset across the Dead Sea transform. *Tectonophysics*, **180**, 71–85.

Thurber, C. and Eberhart-Phillips, D. (1999). Local earthquake tomography with flexible gridding. *Computers and Geosciences*, **25**, 809–818.

Thurber, C., Roecker, S., Roberts, K., Gold, M., Powell, M., and Rittger, K. (2003). Earthquake locations and three-dimensional fault structure along the creeping section of the San Andreas fault near Parkfield, CA: Preparing for SAFOD. *Geophysical Research Letters*, **30**(3), doi:10.1029/2002GL016004.

Thurber, C. H. (1981). *Earth structure and earthquake locations in the Coyote Lake area, central California*. Ph.D. thesis, Massachusetts Institute of Technology, Cambridge.

Thurber, C. H. (1983). Earthquake locations and three-dimensional crustal structure in the Coyote Lake area, central California. *Journal of Geophysical Research*, **88**(B10), 8226–8236.

Thurber, C. H. (1993). Local earthquake tomography: velocities and V_P/V_S-theory. In H. M. Iyer and K. Hirahara, editors, *Seismic Tomography: Theory and practice*, chapter 20. Chapman and Hall, London.

Toomey, D. and Foulger, G. (1989). Tomographic inversion of local earthquake data from the Hengill-Grensdalur central volcano complex, Iceland. *Journal of Geophysical Research*, **94**, 17497–17510.

Um, J. and Thurber, C. H. (1987). A fast algorithm for two-point ray tracing. *Bulletin of the Seismological Society of America*, **77**, 972–986.

Unsworth, M. J., Egbert, G., and Brooker, J. (1999). High-resolution electromagnetic imaging of the San Andreas fault in central California. *Journal of Geophysical Research*, **105**, 1131–1150.

Unsworth, M. J., Bedrosian, P., Eisel, M., Egbert, G., and Siripunvaraporn, W. (2000). Along strike variations in the electrical structure of the San Andreas Fault at Parkfield, California. *Geophysical Research Letters*, **27**(18), 3021–3024.

van Eck, T. and Hofstetter, A. (1989). Microearthquake activity in the Dead Sea region. *Geophysical Journal International*, **99**, 605–620.

van Eck, T. and Hofstetter, A. (1990). Fault geometry and spatial clustering of microeartquakes along the Dead Sea – Jordan rift fault zone. *Tectonophysics*, **180**, 15–27.

van Trier, J. and Symes, W. W. (1991). Upwind finite-difference calculation of traveltimes. *Geophysics*, **56**(6), 812–821.

Vidale, J. E. (1988). Finite-difference calculation of traveltimes. *Bulletin of the Seismological Society of America*, **78**, 2062–2076.

Vidale, J. E. (1990). Finite-difference calculation of traveltimes in three dimensions. *Geophysics*, **55**, 521–526.

Virieux, J. (1991). Fast and accurate ray tracing by Hamiltonian perturbation. *Journal of Geophysical Research*, **96**, 579–594.

Wadati, K. (1933). On the travel time of earthquake waves. *Geophysical Magazine*, **7**, 101–111.

Wallace, R. and Morris, H. (1986). Characteristics of faults and shear zones as seen in deep mines. *Pure and Applied Geophysics*, **124**, 107–126.

Walley, C. D. (1988). A braided strike-slip model for the northern continuation of the Dead Sea Fault and its implication for Levantine tectonics. *Tectonophysics*, **145**, 63–72.

Wdowinski, S. and Zilberman, E. (1997). Systematic analyses of the large-scale topography and structure across the Dead Sea Rift. *Tectonics*, **16**, 409–424.

Weber, M. and Wicks, C. W. (1996). Reflections from a distant subduction zone. *Geophysical Research Letters*, **23**(12), 1453–1456.

Weckmann, U. (2002). *Entwicklung eines Verfahrens zur Abbildung krustaler Leitfähigkeitsstrukturen anhand von Magnetotellurikdaten aus Namibia*. Ph.D. thesis, Freie Universität Berlin. http://www.diss.fu-berlin.de/2002/24/index.html.

Weckmann, U., Ritter, O., Hoffmann-Rothe, A., Abueladas, A., and Haak, V. (2003). The electrical image of the Dead Sea Transform on a regional scale. In *EOS Transactions, American Geophysical Union*, volume 84. Fall Meeting Supplement, abstract GP11A-0251.

Weissbrod, T. and Sneh, A. (2002). Sedimentology and paleogeography of the Late Precambrian – Early Cambrian arkosic and conglomeratic facies in the northern margins of the Arabo-Nubian Shield. *Geological Survey of Israel Bulletin*, **87**.

Wessel, P. and Smith, W. H. F. (1998). New, improved version of Generic Mapping Tools released. *EOS Transactions, American Geophysical Union*, **76**, 579.

Wessel, P. and Smith, W. H. F. (2002). *The Generic Mapping Tools (GMT) version 3.4.2, Technical Reference & Cookbook*. SOEST/NOAA, USA. http://gmt.soest.hawaii.edu.

Wu, C. F. J. (1986). Jackknife, bootstrap and other resampling methods in regression analysis. *Annals of Statistics*, **14**, 1261–1295.

Yilmaz, Ö. (1987). *Seismic Data Processing*, volume 2 of *Investigations in Geophysics*. Society of Exploration Geophysicists, Tulsa.

Yilmaz, Ö. (2001). *Seismic Data Analysis*, volume 10 of *Investigations in Geophysics*. Society of Exploration Geophysicists, Tulsa.

Zelt, C. A. (1998a). *FAST – Program package for First Arrival Seismic Tomography*. Rice University, Houston, USA.

Zelt, C. A. (1998b). Lateral velocity resolution from three-dimensional seismic refraction data. *Geophysical Journal International*, **135**, 1101–1112.

Zelt, C. A. (1999). Modelling strategies and model assessment for wide-angle seismic traveltime data. *Geophysical Journal International*, **139**, 183–204.

Zelt, C. A. and Barton, P. J. (1998). Three-dimensional seismic refraction tomography: A comparison of two methods applied to data from the Faeroe Basin. *Journal of Geophysical Research*, **103**, 7187–7210.

Zelt, C. A. and Smith, R. B. (1992). Seismic traveltime inversion for 2-D crustal velocity structure. *Geophysical Journal International*, **108**, 16–34.

List of Figures

List of Tables

A. Appendix

The appendix comprises an overview on relevant computer program packages, tables of coordinates of the data acquisition layout and presented results, an overview of used abbreviations and symbols, and a list of DESERT Group members.

A.1 Software

This section provides an overview on program packages used to process and analyse data, and to present the results. Discussions on underlying processing or inversion methods are included in the chapters 4, 5, and 6. Freely available packages are the tomography codes `simulps12` (Thurber, 1983; Evans *et al.*, 1994) and `FAST` (Zelt, 1998a; Zelt and Barton, 1998), the seismic data analysis package `Seismic Unix`, (Stockwell, 1999; Cohen and Stockwell, 2002, or previous releases), and the `Generic Mapping Tools` (Wessel and Smith, 1998, 2002). Additionally, I worked with the commercial `ProMAX` processing package to pick traveltimes and to process reflection profiles. This document is typeset with LaTeX 2_ε.

The `simulps` code family executes a simultaneous inversion of three-dimensional *P* and *S* velocity structure and hypocentral parameters of local earthquakes. Since the first version developed by Thurber (1983) `simulps` has experienced many modifications (e.g. Eberhart-Phillips, 1986; Um and Thurber, 1987; Haslinger, 1998; Thurber and Eberhart-Phillips, 1999). One of these modified versions is `simulps12` (Evans *et al.*, 1994), which I used to derive the *P* velocity structure around the Arava Fault (section 4.2). Compared to `FAST`, `simulps12` provides greater flexibility in subsurface model parameterisation. The velocity model is defined on nodes at the intersections of a possibly unevenly spaced rectangular grid. Between grid nodes, velocities are interpolated trilinearily (equation 4.1). A more recent version also allows linking of grid nodes to form blocks of constant velocity or gradient in the inversion (Thurber and Eberhart-Phillips, 1999). Traveltimes are calculated by approximate raytracing and pseudo-bending (ART-PB), and the damped least-squares solution of velocity model equations is obtained by Cholesky decomposition (e.g. Press *et al.*, 1996). Haslinger (1998) implemented a precise shooting raytracer, and Husen (1999) introduced the concept of fat rays. Besides that, some versions can invert for seismic absorption (e.g. see Haberland, 1999). If desired, `simulps` computes the full resolution and model covariance matrices. The code to compute the spread function (equation 4.9) was provided by C. Haberland[1].

The program package `FAST` is a collection for two- and three-dimensional first arrival traveltime tomography (Zelt, 1998a). The inversion is restricted to either v_p or v_s and initally known source

---

[1] Program `res2spread`, C. Haberland, GeoForschungsZentrum Potsdam, Germany, 2000.

locations. But the algorithm is generally much faster than `simulps`, and the model parameterisation is more suitable for smaller-scale seismic experiments. Velocity models are parameterised on a uniform square grid, and inversion is cell-based with possibly different but constant cell sizes in each direction. Forward calculation of traveltimes and ray paths uses finite-differencing (Vidale, 1988, 1990; Hole and Zelt, 1995). The tomographic method is a regularised inversion incorporating a combination of smallest, flattest, and smoothest perturbation constraints with their weights being allowed to vary with depth. The linear system of equations is solved by a variant of the conjugate gradient method described by Nolet (1987). To allow a layer stripping procedure, an interface may be specified above which the model is held fixed. Unlike `simulps`, `FAST` cannot compute the full resolution matrix. Therefore, resolution has to be assessed for example by hit counts and the resolvability of checkerboards (Zelt, 1998b). The original version of `FAST` reads and writes locations in an accuracy of 1 m and times of 1 ms. To invert the higher resolved data of the CSA II experiment (section 4.3), I modified in- and output routines to increase the accuracy.

`Seismic Unix` (`SU`) is a seismic processing and modelling environment for Unix-based systems (Stockwell and Cohen, 2002). Each task is executed by a single program, and these programs can be connected via Unix pipes or shell scripts to build up a processing flow. Besides standard processes, such as filtering, stacking, and plotting of data, `SU` includes tools for three-component processing (section 5.1.1), and for finite-difference modelling of the acoustic or elastic wave equation (section 5.3). Since `SU` supports non-regular acquisition geometries, I used its code libraries to develop my own processing and imaging tools for CSA data (e.g. chapter 6). C. Haberland[2] implemented residual static correction adopted from Rothman (1986) (section 6.3).

The `Generic Mapping Tools` (`GMT`) is a software package to manipulate tabular or gridded data and to display these data in a variety of forms ranging from simple x-y plots to maps and color, perspective, and shaded-relief illustrations (Wessel and Smith, 2002). It supports a variety of geographic projections as well as linear or logarithmic plots, and it includes several tools for gridding data in two dimensions. Like `SU`, `GMT` follows a modular design, which offers great flexibility for its use in Unix shell scripts. Most figures in this thesis are generated using `GMT`, `SU`, or a combination of these two program packages.

A.2   Coordinates

This section lists centroid coordinates of shot and seismometer arrays, coordinates of seismic and magnetotelluric profiles (first sensor in the west and last sensor in the east), and coordinates of presented cross-sections and horizontal depth slices. The values provided correspond to geographical coordinates, refered to as lon. and lat., to the Universal Transverse Mercator grid (UTM, zone 36), refered to as x and y, and to local coordinates used for this study and labelled x and y. The reference is the World Geodetic System 1984 (WGS-84).

Two different local coordinate systems with units of length in all directions are defined for this study. The first system, associated with the three-dimensional velocity tomography (section 4.2), has its origin at $30.55833°$ N, $35.32500°$ E and is rotated clockwise by $19.4694°$ to have the x-axis parallel to the geophone line 1. The second system is used to image seismic scatterers (chapter 6). Its origin is at $30.49588°$ N, $35.30784°$ E, and the rotation angle is $12.0°$ clockwise to orient the y-axis roughly

---

[2] Program `surest`, C. Haberland, GeoForschungsZentrum Potsdam, Germany, 2000.

parallel to the trace of the Arava Fault. Locations in seismogram sections or other two-dimensional cross-sections are given by the distance along the profile (profile-km).

Centroid coordinates of shot and seismometer arrays

Shot arrays						Seismometer arrays					
#	lon. [°]	lat. [°]	x [m]	y [m]	z [m]	#	lon. [°]	lat. [°]	x [m]	y [m]	z [m]
1	35.18115	30.49923	709331	3376129	34	1	35.27549	30.52686	718325	3379371	91
2	35.19448	30.58032	710435	3385143	-13	2	35.29183	30.52278	719903	3378950	79
3	35.20742	30.62888	711571	3390551	-46	3	35.36380	30.49749	726869	3376289	114
4	35.37603	30.52801	727972	3379698	117	4	35.27572	30.57560	718238	3384774	26
5	35.42303	30.56207	732401	3383570	213	5	35.30367	30.56417	720946	3383562	56
6	35.29115	30.50460	719878	3376934	132	6	35.36724	30.54884	727079	3381989	93
7	35.29959	30.62042	720426	3389790	-46	7	35.30274	30.60258	720769	3387818	-22
8	35.31423	30.50827	722085	3377386	88	8	35.31745	30.59802	722190	3387342	-19
9	35.31864	30.52690	722466	3379460	80	9	35.37538	30.58016	727787	3385477	92
10	35.33346	30.57894	723769	3385258	23						
11	35.34504	30.61383	724800	3389149	11						
12	35.26614	30.53117	717418	3379831	59						
13	35.36287	30.49956	726775	3376517	110						
14	35.27849	30.56973	718517	3384129	36						
15	35.37422	30.54866	727750	3381983	102						
16	35.29296	30.60581	719823	3388157	-36						
17	35.38211	30.57800	728438	3385252	97						

The shot arrays 12–17 represent single shots.

Coordinates of seismic and magnetotelluric profiles

Geophone and seismometer lines (CSA)

#	lon. [°]	lat. [°]	x [m]	y [m]	z [m]	lon. [°]	lat. [°]	x [m]	y [m]	z [m]
1	35.26709	30.53084	717510	3379796	64	35.35775	30.50126	726279	3376695	106
2	35.27943	30.56956	718608	3384112	42	35.36929	30.54964	727274	3382082	94
3	35.29390	30.60530	719915	3388103	-33	35.38127	30.57833	728357	3385287	92
4	35.32679	30.55763	723178	3382883	22	35.32869	30.55735	723361	3382855	33
5	35.33548	30.58810	723942	3386278	25	35.33695	30.58696	724085	3386154	36

Geophone lines (CSA II)

#	lon. [°]	lat. [°]	x [m]	y [m]	z [m]	lon. [°]	lat. [°]	x [m]	y [m]	z [m]
1	35.30997	30.51677	721657	3378320	78	35.31968	30.51368	722597	3377997	85
3	35.31685	30.53321	722280	3380156	59	35.32651	30.53007	723215	3379826	74
5	35.32030	30.55078	722571	3382110	26	35.33002	30.54768	723511	3381786	73
6	35.32286	30.55927	722798	3383057	8	35.33260	30.55617	723739	3382732	39
7	35.32597	30.56951	723072	3384198	12	35.33570	30.56640	724013	3383873	39
8	35.32842	30.57756	723289	3385096	10	35.33815	30.57447	724229	3384772	51
9	35.33062	30.58475	723483	3385897	7	35.34035	30.58165	724424	3385572	49
10	35.33319	30.59324	723711	3386843	8	35.34292	30.59014	724651	3386518	52

Magnetotelluric lines (MT)

#	lon. [°]	lat. [°]	x [m]	y [m]	lon. [°]	lat. [°]	x [m]	y [m]
1	35.26709	30.53084	717510	3379796	35.36276	30.49953	726764	3376513
2	35.28009	30.57474	718659	3384688	35.37759	30.54292	728086	3381354
3	35.28948	30.60782	719485	3388373	35.38701	30.57598	728913	3385038
61	35.29757	30.53049	720436	3379816	35.33656	30.51777	724207	3378483
62	35.30076	30.53909	720723	3380776	35.33975	30.52636	724494	3379442
63	35.30395	30.54769	721009	3381736	35.34294	30.53496	724780	3380402
64	35.30616	30.55660	721201	3382728	35.34516	30.54387	724972	3381394
65	35.31131	30.57227	721660	3384475	35.35032	30.55954	725431	3383141
66	35.31352	30.58119	721851	3385468	35.35253	30.56845	725623	3384133
67	35.31671	30.58978	722138	3386427	35.35572	30.57705	725909	3385093

Coordinates of presented cross-sections and depth slices

Reflection profiles and NVR velocity model (figures 3.2 and 4.8)

#	profile-km	lon. [°]	lat. [°]	x [m]	y [m]	lon. [°]	lat. [°]	x [m]	y [m]
a	44.99–65.01	35.22587	30.54721	713519	3381531	35.41096	30.45661	731493	3371853
b	43.52–58.52	35.21359	30.55520	712323	3382394	35.35891	30.49398	726408	3375890
c	27.50–40.50	35.31746	30.61818	722145	3389577	35.28429	30.50449	719220	3376908
d	1.50–10.50	35.27822	30.59377	718437	3386794	35.37010	30.57754	727287	3385177

a = NVR v_p, b = NVR, c = VWJ-6, and d = VWJ-9

Coincident velocity and resistivity sections (figures 7.2 – 7.4)

#	profile-km	lon. [°]	lat. [°]	x [m]	y [m]	lon. [°]	lat. [°]	x [m]	y [m]
1	0.00–10.00	35.26709	30.53084	717510	3379796	35.36276	30.49953	726764	3376513
2	0.00–10.00	35.28009	30.57474	718659	3384688	35.37759	30.54292	728086	3381354
3	0.00–10.00	35.28948	30.60782	719485	3388373	35.38701	30.57598	728913	3385038
61	-0.25–4.25	35.29513	30.53129	720200	3379900	35.33900	30.51698	724443	3378400
62	-0.25–4.25	35.29832	30.53988	720487	3380859	35.34218	30.52556	724729	3379358
63	-0.25–4.25	35.30152	30.54849	720774	3381819	35.34537	30.53416	725015	3380318
64	-0.25–4.25	35.30373	30.55739	720966	3382811	35.34760	30.54307	725208	3381310
65	-0.25–4.25	35.30887	30.57306	721424	3384558	35.35276	30.55875	725667	3383058
66	-0.25–4.25	35.31109	30.58199	721616	3385552	35.35496	30.56765	725858	3384050
67	-0.25–4.25	35.31427	30.59057	721902	3386510	35.35815	30.57625	726144	3385010

Velocity models across the Arava Fault (figures 4.12 – 4.16)

#	profile-km	lon. [°]	lat. [°]	x [m]	y [m]	lon. [°]	lat. [°]	x [m]	y [m]
1	0.00–1.00	35.30997	30.51677	721657	3378320	35.31974	30.51366	722603	3377995
3	0.00–1.00	35.31685	30.53321	722280	3380156	35.32660	30.53004	723223	3379823
5	0.00–1.00	35.32030	30.55077	722571	3382110	35.33008	30.54766	723517	3381784
6	0.00–1.00	35.32285	30.55927	722797	3383057	35.33264	30.55616	723742	3382731
7	0.00–1.00	35.32596	30.56951	723071	3384198	35.33574	30.56639	724016	3383872
8	0.00–1.00	35.32842	30.57756	723289	3385096	35.33820	30.57445	724234	3384770
9	0.00–1.00	35.33061	30.58475	723483	3385897	35.34040	30.58163	724428	3385571
10	0.00–1.00	35.33319	30.59324	723711	3386843	35.34297	30.59012	724656	3386517

Three-dimensional velocity structure (figures 4.4 – 4.7, 4.9 – 4.11, and 5.6)

x [km]	y [km]	lon. [°]	lat. [°]	x [m]	y [m]	x [km]	lon. [°]	lat. [°]	x [m]	y [m]
-6.0	-7.5	35.23896	30.51404	714848	3377880	7.0	35.36566	30.47275	727105	3373550
-6.0	-5.0	35.24813	30.53517	715681	3380240	7.0	35.37485	30.49387	727938	3375910
-6.0	-2.5	35.25731	30.55630	716515	3382600	7.0	35.38404	30.51490	728771	3378260
-6.0	0.0	35.26648	30.57734	717348	3384950	7.0	35.39325	30.53602	729605	3380620
-6.0	2.0	35.27383	30.59426	718015	3386840	7.0	35.40060	30.55293	730271	3382510
-6.0	4.0	35.28117	30.61109	718681	3388720	7.0	35.40797	30.56975	730938	3384390
-6.0	6.0	35.28852	30.62801	719348	3390610	7.0	35.41533	30.58666	731604	3386280
0.0	0.0	35.32500	30.55833	723005	3382957					

Distribution of scatterers (figures 6.7 – 6.12)

x [km]	y [km]	lon. [°]	lat. [°]	x [m]	y [m]	x [km]	lon. [°]	lat. [°]	x [m]	y [m]
-10.0	1.0	35.18848	30.52925	709970	3379470	2.0	35.33049	30.50053	723664	3376560
-10.0	12.0	35.21451	30.62587	712257	3390230	2.0	35.35665	30.59712	725951	3387320
-1.0	1.0	35.30007	30.50676	720730	3377190	6.0	35.37105	30.49231	727577	3375730
-1.0	12.0	35.32620	30.60335	723017	3387950	6.0	35.39724	30.58889	729864	3386490
0.0	0.0	35.30784	30.49588	721500	3376000					

A.3 Abbreviations and symbols

General	AF	Arava Fault (Araba Fault, Wadi Arava Fault)
	CSA	Controlled Source Array (experiment) of DESERT
	DESERT	Dead Sea Rift Transect
	DST	Dead Sea Transform
	GPS	Global Positioning System
	MT	magnetotelluric(s)
	N, E, S, W	north, east, south, and west
	N, M	numbers
	NRA	Natural Resources Authority, Amman, Jordan
	NVR	Near-Vertical Reflection (profile) of DESERT
	VE	vertical exaggeration of cross-sections
	WRR	Wide-angle Reflection-Refraction (experiment) of DESERT
	x,y,z	coordinates
Seismics	ART-PB	approximate ray tracing and pseudo bending
	ATF	array transfer function
	β	damping factor for a damped least-squares solution
	CMP	common-midpoint, common-midpoint stacking technique
	$\underline{\underline{\mathbf{D}}}$	matrix of second order spatial derivatives
	$\overline{D}_{ij}$	spatial distance between two model nodes
	D_k^j	directivity (polarisation filter function based on direction cosines)
	$\mathbf{d}$	data vector of travel time residuals
	FD	finite difference (modelling technique)
	$\underline{\underline{\mathbf{G}}}$	matrix of spatial derivatives (equation 4.5)
	$\underline{\underline{\mathbf{G}}}^{-g}$	(Levenberg-Marquart) generalised linear inverse
	$\overline{k}, k_x, k_y$	wave number and its horizontal components
	κ	reflection angle
	$\underline{\underline{\mathbf{M}}}$	covariance matrix of three-component data
	$\tilde{\mathbf{m}}, \mathbf{m}$	estimated and true model adjustment vector
	NE	semblance (coherency measure)
	NMO	normal-moveout (correction)
	ϕ	backazimuth
	P, S	seismic compressional or longitudinal wave, and seismic shear wave
	PxP	P-to-P scattered seismic wave (single scattering)
	$\underline{\underline{\mathbf{R}}}, R_{ij}$	model resolution matrix and its elements
	$\tilde{\overline{\hat{R}}}_k$	generic weighting function (polarisation filter)
	RKP	Runge-Kutta plus perturbation (ray tracing)
	RL	rectilinearity (polarisation attribute)
	r	resolvability of a checkerboard model
	ρ	rock density
	S_j	spread function value for one model node or scatterer location
	SKS	teleseismic S wave that passed the Earth's core as P
	S/N	signal-to-noise ratio

s	arc length of a seismic ray
σ	Poisson's ratio
Θ, Φ	incident angle and azimuth of principal polarisation direction
θ	scattering angle
$t_{ij}^{obs}, t_{ij}^{cal}$	observed and calculated traveltimes
t_0	shot or event origin time
t, t_p, t_s	arrival or travel times (of P and S)
u, v, v_a, v_p, v_s	slowness and (apparent) velocity (of P and S)
v_p/v_s	seismic P-to-S velocity ratio
$\mathbf{V_i}, \lambda_i$	eigenvector of matrix $\underline{\underline{M}}$ and corresponding eigenvalue
$\Delta v, \Delta \tilde{v}$	true and recovered velocity perturbations
WKBJ	geometrical optics approximation of wave propagation
Z, N, E	vertical, north-south, and east-west (seismometer) component

MT		
	$\mathbf{B}$	magnetic induction (magnetic flux density)
	$\mathbf{E}, \mathbf{H}$	electric and magnetic field
	χ	skewness
	i	imaginary unit ($i^2 = -1$)
	k	complex wave number
	μ_0	magnetic permeability of the vacuum
	ω	angular frequency
	σ, ρ	specific electrical conductivity and resistivity
	τ	regularisation (smoothness) parameter
	$\underline{\underline{Z}}, Z_{ij}$	impedance tensor and its elements

A.4 DESERT Group

Members of the DESERT Group are K. Abu-Ayyash[1], A. Abueladas[1], A. Agnon[2], H. Al-Amoush[3], A. Babeyko[3,12], Y. Bartov[4], M. Baumann[5], Z. Ben-Avraham[6], G. Bock[3], J. Bribach[3], R. El-Kelani[7], A. Förster[3], H.-J. Förster[5], U. Frieslander[8], Z. Garfunkel[2], S. Grunewald[3], H. J. Götze[9,10], V. Haak[3], Ch. Haberland[3,5], M. Hassouneh[1], S. Helwig[11], A. Hofstetter[8], K.-H. Jäckel[3], D. Kesten[3], R. Kind[3], N. Maercklin[3,*], J. Mechie[3], A. Mohsen[3], F. M. Neubauer[11], R. Oberhänsli[5], I. Qabbani[1], O. Ritter[3], G. Rümpker[3], M. Rybakov[8], T. Ryberg[3], F. Scherbaum[5], J. Schmidt[3], A. Schulze[3], S. Sobolev[3,12], M. Stiller[3], H. Thoss[3], M. Weber[3,5], U. Weckmann[3], and K. Wylegalla[3].

⋆ Author of this thesis, now at NORSAR, Kjeller, Norway; 1 Natural Resources Authority, Amman, Jordan; 2 Hebrew University, Jerusalem, Israel; 3 GeoForschungsZentrum, Potsdam, Germany; 4 National Ministry of Infrastructure, Jerusalem, Israel; 5 University of Potsdam, Germany; 6 Tel Aviv University, Israel; 7 An-Najah University, Nablus, Palestine Territories; 8 Geophysical Institute of Israel, Lod, Israel; 9 Free University of Berlin, Germany; 10 now at Christian-Albrechts University Kiel, Germany; 11 University of Köln, Germany; 12 Institute of Earth Physics, Moscow, Russia.

Acknowledgements

Curriculum vitae

Name	Nils Maercklin
Date and place of birth:	6 March 1972 in Hannover, Germany
Citizenship:	German

School

1978–1982	Elementary School in Tellingstedt and Hennstedt (Dithmarschen), Germany
1982–1983	Gymnasium Heide-Ost in Heide, Germany
1983–1991	Freie Waldorfschule Rendsburg, Germany Degree: Abitur

Social service

1991–1992	Social service as a kindergarten teacher at the Kindertagesstätte Mastbrook in Rendsburg, Germany

University

1992–1999	Christian-Albrechts-University (CAU) Kiel, Germany; Institute of Geosciences, Geophysical section Degree: Diploma in Geophysics Diploma thesis (CAU Kiel, September 1999): *Polarisationsanalyse refraktionsseismischer Daten vom Vulkan Merapi, Indonesien* (Advisor: Prof. Dr. W. Rabbel, CAU Kiel)
2000–2003	Ph.D. student at the University of Potsdam, Germany; Geoscience Institute

Scientific career

2000–2003	Scientist at the GeoForschungsZentrum (GFZ) Potsdam, Germany; section 2.2 *Deep Geophysical Sounding* (Prof. Dr. M. Weber)
since 02/2004	Scientist in the seismology section at NORSAR, Kjeller, Norway (Prof. Dr. H. Bungum)

Eidesstattliche Erklärung

Ich erkläre hiermit an Eides statt, dass ich die vorliegende Arbeit selbständig und ohne Benutzung anderer, als der angegebenen Hilfsmittel angefertigt habe. Die aus fremden Quellen direkt übernommenen Gedanken sind kenntlich gemacht.

Diese Arbeit wurde in gleicher oder ähnlicher Form keiner anderen Prüfungsbehörde vorgelegt oder veröffentlicht.

Potsdam im Januar 2004   Nils Maercklin